CHARLES UNIVERSITY

Faculty of Science

Study programme: Inorganic Chemistry

Jan Havlík

DESIGN AND SYNTHESIS OF SURFACE ARCHITECTURES ON FLUORESCENT NANODIAMONDS

Design a syntéza povrchových architektur na fluorescenčních nanodiamantech

Doctoral Thesis

Supervisor: Doc. RNDr. Jan Kotek, Ph.D

Consultant: Mgr. Petr Cígler, Ph.D.

Praha, 2017

DESIGN AND SYNTHESIS OF SURFACE ARCHITECTURES ON FLUORESCENT NANODIAMONDS

Jan Havlík

Prohlášení

Prohlašuji, že jsem závěrečnou práci zpracoval samostatně a že jsem uvedl všechny použité informační zdroje a literaturu. Tato práce ani její podstatná část nebyla předložena k získání jiného nebo stejného akademického titulu.

V Praze dne 24. listopadu, 2017

Váží si taky Sovy, a kdo by si jí taky nevážil,
když umí napsat MYSLIVEC, třebas ne správně;
ale pravopis není všecko. Jsou dni, kdy ti
vůbec nepomůže, že umíš napsat MYSLIVEC

Alan A. Milne

Poděkování

Tato práce mohla spatřit světlo světa pouze díky podpoře několika lidí, kterým bych chtěl touto cestou vyjádřit svůj vděk:

Na prvním místě děkuji svým školitelům, *Petrovi Cíglerovi* a *Honzovi Kotkovi*, za jejich péči, cenné rady a skvělé vedení během celého doktorského studia.

Poděkovat bych chtěl také všem svým spolupracovníkům: *Vlaďce Petrákové*, *Janu Štursovi*, *Martinu Hrubému*, *Ondrovi Pačesovi*, celému současnému i minulému osazenstvu Laboratoře syntetické nanochemie na UOCHB a ostatním kolegům.

I would also like to thank *Stephanie Krueger* for her help with the tricky aspects of the English language and *Alexandra Elbakyan* for "removing barriers in the way of science."

Speciální dík patří i *Zuzi* a *Makouškovi* za jejich neutuchající morální podporu. @->->--

Největší dík však patří mé milé rodině:

Děkuji své přítelkyni, *Maruš*, která po celou dobu stála při mém boku a trpělivě snášela všechny související strasti.

Děkuji také svým *rodičům*, kteří mi umožnili dokončit studium, aniž bych se musel potýkat s jakýmikoliv existenčními překážkami.

Abstract

Thanks to their unique properties and high biocompatibilities, fluorescent nanodiamonds are promising representatives of modern carbon nanomaterials with a broad range of applications. Nevertheless, their wider use is limited because of weak fluorescence intensity and low colloidal stability in the biological environment. The optimization of treatment procedures and development of new suitable surface designs is therefore critically needed.

In this study, several key steps for fluorescent nanodiamond treatment have been optimized, leading to both a substantial increase in fluorescence intensity and to significantly lower surface damage caused by graphitization. Further, a new high-throughput irradiation technique was developed. The influence of surface chemistry on the fluorescence parameters was studied using partial fluorination of the functional groups on the nanodiamond surface. A novel method which significantly affects the interaction of nanodiamonds with biological systems by increasing of the homogeneity and circularity was developed. The potential of nanodiamonds for future medical and biological research was demonstrated on particles with complex surface architectures that enabled targeting and therapy of tumor cells. Moreover, a strong and highly selective affinity of fibroblast growth factors to diamond surfaces was discovered and demonstrated using both *in vitro* and *ex vivo* models.

Abstrakt

Díky svým unikátním vlastnostem a vysoké biokompatibilitě patří fluorescenční nanodiamanty mezi slibné zástupce uhlíkatých nanomateriálů s potenciálně širokým spektrem uplatnění v mnoha odvětvích. Jejich nízká intenzita fluorescence a koloidní nestálost v biologickém prostředí však doposud brání jejich širšímu využití. Optimalizace jejich přípravy spolu s vývojem nových vhodných povrchových architektur tak představuje významnou výzkumnou výzvu.

V rámci této práce byly navrženy a optimalizovány jednotlivé kroky přípravy fluorescenčních nanodiamantů, díky čemuž bylo dosaženo řádového zvýšení intenzity jejich fluorescence spolu s omezením poškození jejich povrchu grafitizací. Dále byla vyvinuta metoda ozařování nanodiamantů umožňující dramatické navýšení jejich produkce. S využitím částečné fluorace funkčních skupin na povrchu nanodiamantů byla demonstrována možnost ovlivnění parametrů jejich fluorescence. Byla také vyvinuta metoda zvyšující homogenitu a cirkularitu nanodiamantů, což významně ovlivnilo jejich interakci s biologickými strukturami. Možná uplatnění tohoto materiálu v medicíně a biologickém výzkumu byla demonstrována na přípravě částic s komplexní povrchovou architekturou umožňujících cílení a terapii nádorových buněk. Bylo také objevena a na *in vitro* a *ex vivo* modelech demonstrována vysoká a selektivní afinita fibroblastových růstových faktorů k povrchu nanodiamantů.

Table of Contents

1. List of abbreviations

AFM – Atomic-force microscopy

CVD – Chemical vapor deposition

DI – Deionized

DMEM – Dulbecco's modified Eagle's medium

DNDs – Detonation nanodiamonds

EGF – Epidermal growth factor

ERK – Extracellular signal–regulated kinases

FGF – Fibroblast growth factor

FNDs – Fluorescent nanodiamonds

F-TEDA – 1-chloromethyl-4-fluoro-1,4-diazoniabicyclo[2.2.2]octane

HBS – Heparin-binding site

HeLa – Commonly used immortal cervical cancer cell line

HPHT – “High pressure–high temperature” synthesis method

IFN – Interferon

IL – Interleukin

NDs – Nanodiamonds

MCF7 – Commonly used breast cancer cell line

NEXAFS – Near edge X-ray absorption fine structure

NGF – Nerve growth factor

NIR – Near–infrared

PEG – Poly(ethylene oxide)

PGNS – Plasmonic gold nanoparticles

PGNS-Tf – Plasmonic gold nanoparticles with transferrin-modified surface

FLI – Fluorescence intensity

RCS – Rat chondrosarcoma cells

SKBR3 – Adenocarcinoma cell line

TGF – Transforming growth factor

Tf – Transferrin

TfR – Transferrin receptor

XPS – X-ray photoelectron spectroscopy

ZPL – Zero-phonon line

2. Preface

Nanomaterials based on carbon allotropic modifications are perennial stars of scientific research. Over the last few years, many such materials have found their way from laboratories into commercial applications, and some have even become an inspiration for artists and popular culture. This thesis is dedicated to the study of lesser-known members of this "carbon nanozoo" known as nanodiamonds – remarkable materials with the same crystalline structure as macroscopic diamonds. However, in contrast to macroscopic diamonds, the size of individual nanodiamond crystallites ranges from units to hundreds of nanometers. This small particle size imbues them with many unique physical and chemical properties. Once secret byproducts of explosives research, nanodiamonds now show promise in addressing the challenges of medicine, science, and technology.

3. Introduction

3.1. Carbon allotropes

Carbon has several forms with different crystal lattice arrangements. The most well-known allotropes are amorphous carbon, graphite with a planar structure, and diamond with a cubic geometry. Other, more exotic forms of carbon include hexagonal lonsdaleite[1] and complex structures created by pyrolysis or laser

ablation such as fibers, foams, or glassy carbon. In recent decades, the list of carbon structural modifications has been further extended into a broad family of nanocarbons.[2] The most prominent of them are fullerenes, discovered by Kroto, Smalley, and Curl[3] in 1985; nanotubes, prepared by Ijima[4] in 1991; and graphene, obtained by Geim and Novoselov[5] in 2007.

The substantial influence of allotrope crystalline structures on material properties can be illustrated with the examples of graphite and diamond (**Tab. 1**). Graphite consists of planar sheets of sp^2-hybridized carbon atoms stacked upon each other, weakly bound by van der Waals forces. Each layer has a honeycomb structure with a C–C bond length of 1.4210 Å.[6] Each carbon atom is linked by three localized σ bonds to its neighboring atoms with an angle of 120º. The fourth available valence electron is delocalized in π molecular orbitals. In the more stable hexagonal arrangement of graphite (α-graphite), carbon atoms of adjacent layers lie above and below the middle of the same hexagonal carbon ring with a layering sequence ABABAB. In less stable rhombohedral form (β-graphite), the layers are arranged in a layering sequence ABCABC. In both cases, the interlayer distance is 3.354 Å (**Fig. 1**). [6]

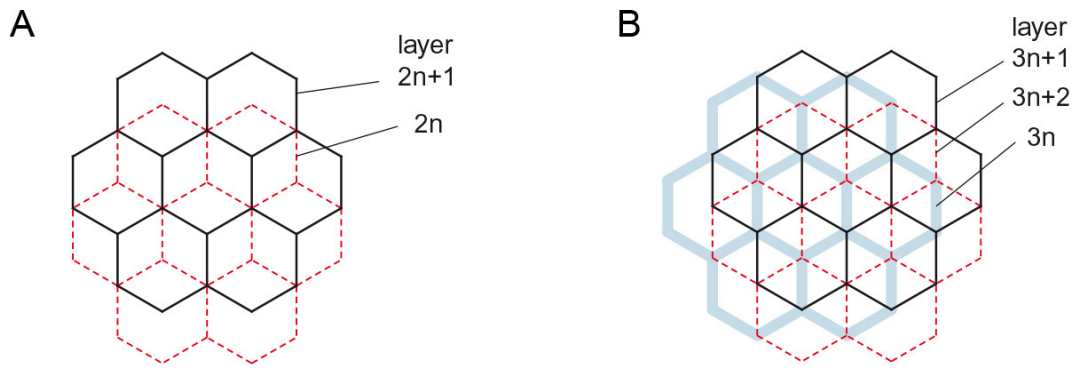

Figure 1. Lattice structures of (A) ABA-stacked hexagonal graphite and (B) rhombohedral ABC-stacked graphite. *Adapted from Ref.*[7]

A diamond lattice consists of sp^3 hybridized carbon atoms connected by four identical covalent bonds in a covalent network, where each atom is surrounded

by four other carbon atoms with tetrahedral symmetry at the same distance of 1.5445 Å and bond angles of 109.28°.[6] Due to the strength of the C–C bonds (cohesive energy of diamond is 717 kJ/mol) and the absence of free electron pairs, diamond forms extraordinarily hard and inert colorless crystals which have an extremely high melting temperature (~5000 K).[8]

Table 1. The comparison of the properties of diamond and graphite.[9,10]

PROPERTY	DIAMOND	GRAPHITE
CRYSTALLINE SYSTEM	Cubic – ($m\bar{3}m$)	Hexagonal – (6/mmm)
DIPHANEITY	Transparent to translucent	Opaque
DENSITY [g·cm^{-3}]	3.50–3.53	2.09–2.23
ELECTRICAL CONDUCTIVITY	Insulator	Conductor
MOHS SCALE HARDNESS	10	1
THERMAL CONDUCTIVITY [W·cm^{-1}·K^{-1}]	23.0	Anisotropic 0.057(⊥), 19.5 (∥)

3.2. Diamond classification

At the beginning of the twentieth century, researchers discovered that most natural diamonds absorb in the infrared region at 6.5–15 μm.[11] Diamonds with this optical feature, which was later linked to the presence of nitrogen in the crystal lattice, have been classified as type **I**.[12] Rare, relatively nitrogen-free diamonds have been classified as type **II**.

Type **I** diamonds contain N atoms as their main impurity in sufficient amounts to be measured by infrared (IR) spectroscopy techniques. They can be further divided according to the forms in which nitrogen is present in their crystal lattice.[13,14] Most natural diamonds belong to a subtype **Ia**, with aggregated nitrogen atoms in high concentration up to 3000 ppm. The nitrogen atoms in

these aggregates can be either present in pairs (**IaA**), large even-numbered clusters (**IaB**), or as a combination of both (**IaAB**). In contrast, in the less common **Ib** diamond type, nitrogen is present in the form of single substitutional atoms with one order of magnitude lower concentration than in the case of **Ia**. Most synthetic diamonds produced by high pressure–high temperature (HPHT) methods belong to the **Ib** subtype.

Natural type **II** diamonds are extremely rare. These diamonds can be divided into clear, nitrogen-, and boron-free **IIa** subtype, which is typical for diamonds produced by chemical vapor deposition (CVD) methods, and semiconducting boron-doped subtype **IIb**, with very low resistivity.[15] The schematic representation of different diamond subtypes is summarized in **Fig. 2**.

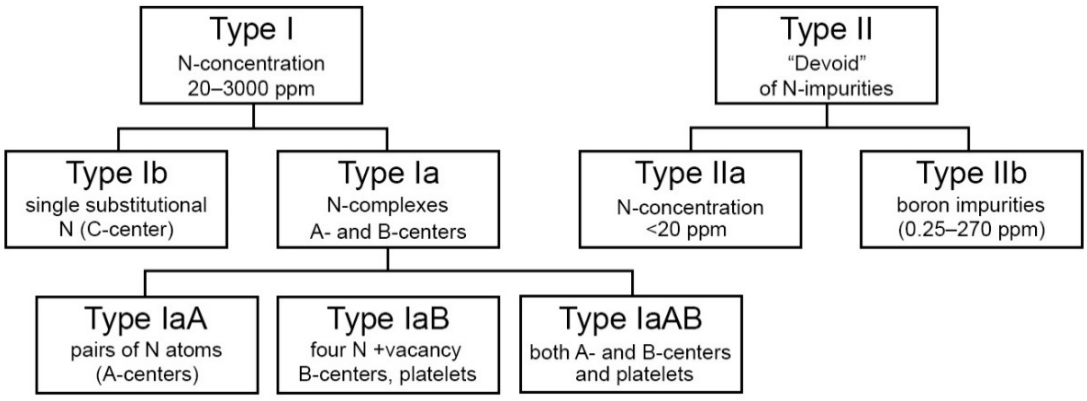

Figure 2. Schematic representation of different diamond subtypes. *Adapted from Ref.*[16]

3.3. Synthesis and stability of diamond-based materials

As a result of high cohesive and activation energies, metastable carbon allotropes tend to persist at pressures and temperatures far distant from their stability regions. For this reason, a diamond might exist under room conditions, even though graphite is the most thermodynamically stable form of carbon with

a stability boundary ranging from 1.7 GPa at 0 K to the graphite/diamond/liquid triple point of 12 GPa at 5000 K (**Fig. 3**).[8] Similarly, rhombohedral graphite can be reversibly compressed up to approximately 80 GPa before it transforms into diamond (**Fig. 3, conditions "E"**).[17]

Commercial diamond synthesis techniques therefore employ a combination of high pressures and temperatures (**Fig. 3, conditions "A"**). The first successful experiments with the preparation of small synthetic diamonds using this approach were performed in 1955, when Bundy et al. prepared diamond crystals with sizes up to 1 mm.[18] Their high pressure–high temperature (HPHT) synthesis method required producing pressure of approximately 10 GPa at 2300 °C and a metal alloy which served both as a solvent and a catalyst. The first HPHT diamonds were yellow in appearance due to the natural contamination of the metal catalyzers with traces of nitrogen impurities. The method for the preparation of nitrogen free, colorless crystals with HPHT was developed during the 1970s, utilizing nitrogen getters (Zr, Al or Ti).[19,20] However, the removal of nitrogen during synthesis slowed down the growth process. Industrial-grade HPHT diamonds are therefore still produced with nitrogen impurities.[21] For use in nanotechnology, the obtained micron-sized particles are further processed by grinding to obtain monocrystalline nanoparticles.

Another approach to diamond synthesis takes into account the fact that the difference between graphite and diamond standard Gibbs free energies of formation is negligible (2.9 kJ/mol) in comparison to the standard Gibbs free energy of carbon vapor (671.3 kJ/mol).[10] The condensation of carbon vapor at low pressure is therefore controlled mainly by the presence of suitable crystallization nuclei. In the case of the chemical vapor deposition (CVD) method developed in the 1980s, diamonds are grown on a diamond substrate from microwave plasma containing C_2 molecules (**Fig. 3, conditions "D"**).

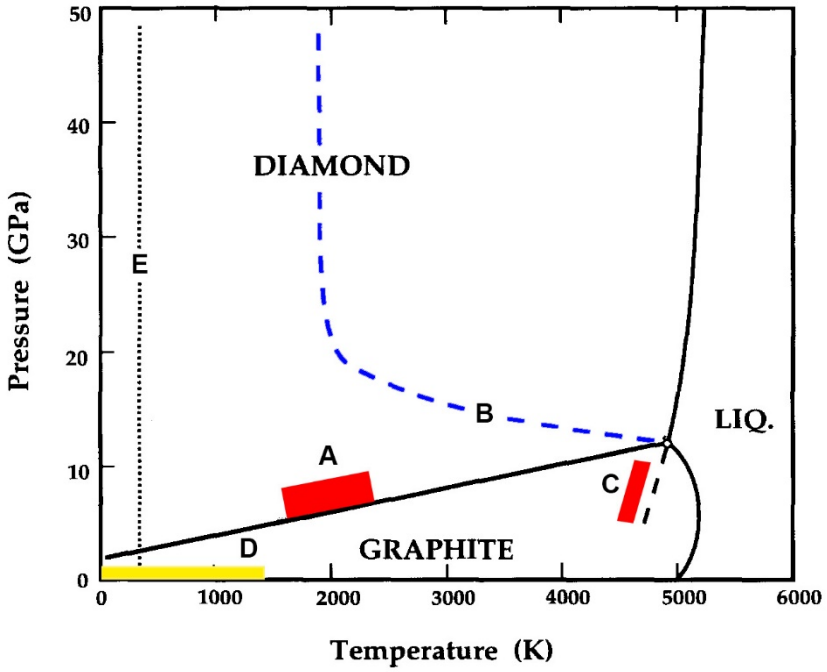

Figure 3. Phase and transition diagram for carbon (p,T). Equilibrium phase boundaries are represented by solid lines. (**A**) Typical conditions for commercial HPHT diamond synthesis with catalyst. (**B**) Threshold for very fast graphite/ diamond transformations. (**C**) Threshold for very fast diamond to graphite transformation. (**D**) Typical conditions for nonequilibrium CVD diamond synthesis. (**E**) Path along which compressed graphite reversibly loses some characteristics and acquires some properties of diamond-like polytypes. *Adapted from Ref.*[8]

Plasma discharge is typically generated with a methane/hydrogen gas mixture (1–20% of methane) at 900–1200 ºC in contrast to the high pressures required for the HPHT method, with which CVD growth occurs under non-equilibrium conditions in a low vacuum (20–200 Torr).[22] Depending on the deposition parameters, CVD-produced diamonds may vary in morphology, type of structural defects, and crystallinity, with grain sizes from 2–5 nm to several millimeters.[23]

The third commonly-used synthetic method, which produces nano-sized diamonds, dates back to the early 1960s, when DeCarli and Jamieson discovered that microscopic diamonds could be formed from graphite by exposure to an explosive shock.[24] At about the same time, in the summer of 1963, Volkov and Danilenko in the former Soviet Union discovered that soot residues resulting from the detonation of explosives contain a significant amount of

nanodiamonds. Unfortunately, all experimental methods for diamond synthesis were strictly classified at that time, which led to repeated rediscovery of approaches at different research institutions across the Soviet Union during the subsequent 25 years.[25]

The abovementioned "detonation method" utilizes explosives as a source of both carbon and energy. A synthetic explosion occurs in a metallic detonation chamber filled with an oxygen–deficient mixture of explosives such as 1,3,5-trinitro-1,3,5-triazinane (RDX) and 2,4,6-trinitrotoluene (TNT) together with an inert gas or water in form of ice, which serves as a coolant. During the 0.5 μs detonation, both temperature and pressure increase sharply, reaching the conditions for the formation of liquid carbon.[26] With their subsequent decrease, small carbon nanoclusters are formed followed by condensation and crystallization into a diamond lattice. During the further decrease of pressure below the diamond/graphite equilibrium, the growth of diamonds is replaced by the formation of graphitic and amorphous sp^2 carbon. The resulting detonation soot contains up to 75% detonation nanodiamonds (DNDs) with a 4–6 nm diamond core surrounded by 0.4–1.0 nm layer of amorphous sp^2 structures.[27] However, these core particles always form extremely tight "grape shaped" aggregates with a diameter range of 100–200 nm.[28]

Nanodiamonds can also be synthesized using other, less common methods such as laser ablation,[29] electron irradiation of graphite,[30] and chlorination of metal carbides.[31]

The thermodynamic properties, phase equilibria, and phase transitions of nanomaterials are strongly influenced by size and temperature and may significantly differ from the bulk state. This characteristic feature of nanosystems is a consequence of their high surface-to-volume ratio, because of which surface stresses and surface free energies become increasingly important with decreasing size.[32] This nano-thermodynamic phenomenon can be observed in the existence of many metastable high-pressure phases of materials such as CdSe, ZnS, or Fe which have not been found in a bulk state but can be easily

formed at the nanoscale.[33] In the case of nanocarbons, the relative stability of diamond lattices increases with decreasing size and temperature, making NDs smaller than 5 nm more stable than graphite.[34] Larger NDs are usually covered with a thin discontinuous layer of disordered sp^2-carbon structures. Further phase transformation is effectively inhibited by high activation energy. For this reason, distinctive NDs graphitization starts to occur on the particle surface only above approximately 900 °C, creating core-shell structures with highly defective and curved graphitic surfaces. This process deteriorates the properties of NDs during annealing treatment.[35] The sp^2/sp^3 phase ratio gradually increases with rising temperature up to 1500 °C, when a continuous onion-shell structure wrapped around a small diamond core is formed.[36]

3.4. Spectral characteristics of common diamond defects

Diamond crystallographic defects are the result of substitutional or interstitial impurities (extrinsic defects) or irregularities (intrinsic defects) in the crystal lattice. Crystal defects strongly affect a broad spectrum of material and spectral properties and therefore play a crucial role in the design of new materials based on the diamond lattice. Many impurities of foreign elements, such as H, He, Li, B, N, O, Ne, P, Si, As, Ti, Cr, Ni, Co, Zn, Zr, Ag, W, Xe, and Tl can be introduced into a diamond crystal lattice during growth or by ion implantation methods.[16,37] These elements can produce a broad spectrum of more than 500 known electronic optical centers. The most common among them are various kinds of nitrogen impurities which result in diamond classification (vide supra). The classification system of diamond crystal defects is still not fully settled and may in some cases be confusing, primarily for historical and customary reasons. The list below is an overview of the most common optically active defects with their alternative symbols, meanings of abbreviations, short structural descriptions, and spectral characteristics.[38–41] Center energies listed

here correspond to the energies of zero-phonon line (ZPL) transitions or to the spectral position of their maxima.

A-nitrogen center (A-aggregate, *N=N*)

This defect is a very common in natural **IaA** diamonds. It consists of two neighboring nitrogen atoms. The A-center has an absorption continuum above 3.4 eV at 310 nm. In the IR spectrum, the A-center has an absorption peak of 1282 cm^{-1}, which can be used to estimate its concentration.

B-nitrogen center (*B1, B-aggregate, N4–V*)

The B-center consists of a vacancy directly surrounded by four nitrogen atoms. It is a naturally occurring defect in **Ia** diamonds. Diamonds in which this form of nitrogen distribution predominates are classified as **IaB**. It does not induce ultraviolet (UV) nor visible absorption. In the IR spectrum, the B-center has a characteristic sharp peak at 1332 cm^{-1} and the most intensive absorption peak at 1175 cm^{-1}.

GR1 center (V^0*, general radiation 1*)

This defect is a neutral, single, isolated vacancy in the diamond lattice. It is the main optical feature of irradiated diamonds and one of the most heavily studied defects. It is created by almost any high-energy irradiation. However, it might be influenced by impurities. This center is annealed out normally at temperatures above 600 °C due to the migration and annihilation of vacancies. Its characteristic feature is a Zero phonon line (ZPL) doublet at 1.673 and 1.665 eV (740.9 and 744.4 nm).

3H center

The transition at 2.462 eV (503.4 nm) corresponding to this center is observed in all types of diamonds after irradiation. Its intensity is proportional to the nitrogen content and usually occurs in conjunction with GR1 defects. The center anneals out at temperatures above 500 °C. Even though several structure models

have been proposed, its nature is unclear. The center is probably related to interstitial carbon atoms in the diamond lattice.

H2 center *(heat treatment 2, N-V-N^-)*

An H2 center with a ZPL at 1.256 eV (986.3 nm) can be observed in **I** type diamonds after irradiation and subsequent annealing at temperatures above 500ºC or in synthetic type **Ib** diamonds after annealing at 1700 ºC. A possible model of the H2 center consists of two nitrogen atoms sandwiching a vacancy along the [110] direction.

H3 center *(heat treatment 3, N-V-N^0)*

This uncharged center with ZPL at 2.463 eV (503.2 nm) is the most common naturally occurring optical feature of nitrogen-containing diamonds. The H3 center is formed from the A-aggregate of nitrogen and vacancies which probably form an N-V-N or V-N-N-V complex (A-nitrogen center bound to two vacancies). It can be created in type **I** diamonds with any irradiation and subsequent annealing. In synthetic diamonds, the H3 center may be created by annealing at 1100 ºC at normal pressure; however, the annealing behavior varies according to the irradiation condition and diamond type.

H4 nitrogen center (*heat treatment 4, 3N-V-V-N*)

This center can be found naturally in **IaB** diamonds, producing their yellow color with ZPL at 2.498 eV (496.2 nm). It can be induced by any irradiation and subsequent annealing at temperatures above 600ºC. It consists of 4 nitrogen atoms separated by 2 vacancies.

N3 nitrogen center *(naturally occurring 3, N3-V)*

The N3 defect is common in most **Ia** natural diamonds with B-nitrogen aggregates. It is made up of a vacancy surrounded by the 3 nearest substitutional nitrogen atoms in the [111] plane. This center is paramagnetic and can produce blue fluorescence at 2.985 eV (415.2 nm).

NV^- center (*nitrogen-vacancy, N-V^-*)

This center is a naturally occurring feature of nitrogen-containing diamonds. However, its concentration is usually negligible. The center consists of a nitrogen atom in a pair with a vacancy and is suppressed with boron doping. The ZPL is pronounced at 1.945 eV (638 nm), resulting in a purple coloration of synthetic diamonds.

NV^0 center (*nitrogen-vacancy, T_1, N-V^0*)

This neutral charged center is closely related to the NV^- center and differs because of an extra electron located at the vacancy site. Both centers can be mutually converted by a change of the Fermi level position. The ZPL is pronounced at 2.156 eV (575.5 nm).

3.5. Nitrogen-vacancy (NV) centers

From the perspective of optical and magnetic properties, diamond represents an unique material with a broad spectrum of applications in quantum computing,[42–44] bioimaging,[45,46] and single-spin magnetometry.[47,48] Over 500 types of electronic color centers are hosted by the diamond lattice and the NV center belongs to the most extensively studied. This center was first described experimentally in 1976.[49] Nevertheless, such centers came into the focus of scientific investigation only with the discovery of their perfect photostability and ability to serve as a bright single-photon source.

The NV center is a crystal lattice point defect consisting of the nearest-neighbor pair of a nitrogen atom and a lattice vacancy oriented along the [111] crystal direction (**Fig. 4**).[51] Their natural concentration in diamonds is negligible; thus, they must be prepared artificially through the recombination of nitrogen atoms and vacancies. In the case of the HPHT **Ib** diamond type, nitrogen atoms occur in the crystal lattice naturally as an impurity in

concentration up to 300 ppm.[52] Vacancies are subsequently created by irradiation with high-energy particles.[46]

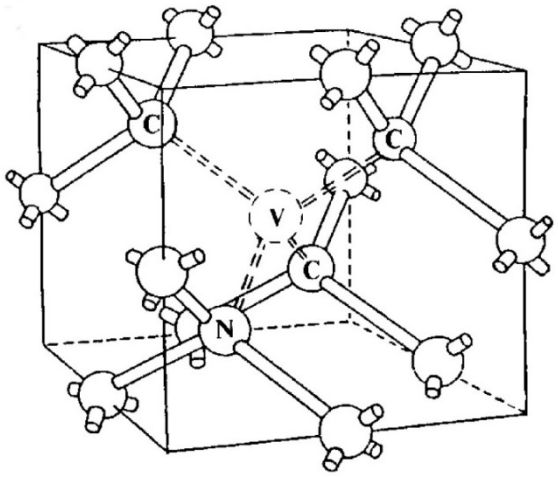

Figure 4. The structure of a nitrogen-vacancy center in diamond. *Adapted from Ref.*[50]

In NDs, the NV centers are produced by annealing of irradiated material at 600–900 °C in an inert atmosphere. During this process, vacancies migrate in their neutral form (V^0) through the diamond lattice and recombine with nitrogen atoms with energetically favorable aggregation.[53,54] The activation energy of vacancy migration in natural, type **I** diamonds is 2.30–2.45 eV.[55]

NV centers exist in two charge states with different photoluminescence and spin properties: neutral NV^0 and negative NV^-, with ZPL at 575 nm (2.156 eV) and 638 nm (1.945 eV), respectively.[56] A typical excitation and emission spectrum for NV^- is depicted in **Fig. 5A**. The ZPL has vibronic bands which are generated by the interactions of electronic and vibrational degrees of freedom extending from ZPLs to lower energy.[57] This effect, related to the Franck-Condon principle, is also co-responsible for different positions of excitation and emission maxima. For NDs larger than 5 nm, NV^- centers are resistant to photobleaching and photoblinking[58,59] and their photoluminescence occurs at longer timescales than biological autofluorescence (≈17 ns for NDs and 11.6 ns

for bulk diamond).[60] Their photoluminescence spectrum can be also altered by applying a magnetic field,[61] electric field,[62] microwave radiation,[63] or by modifying the diamond surface.[56]

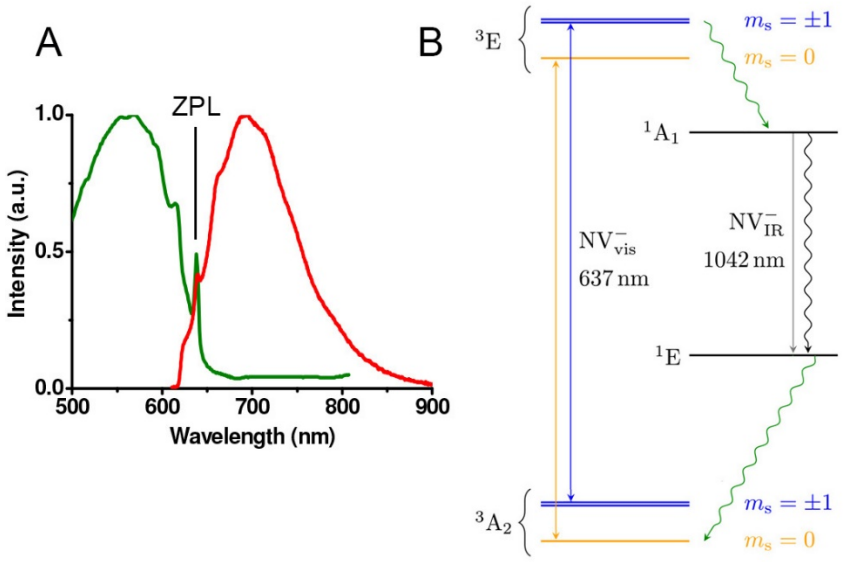

Figure 5. (**A**) Excitation (green) and emission (red) spectrum of NV⁻ center with zero phonon line at 638 nm.[64] (**B**) Electronic energy level scheme for the NV⁻ transitions. *Adapted from Ref.*[65]

NV⁻ centers contain a three-level emission system with a parallel decay channel through a metastable state with a long emission time (**Fig. 5B**). Two of the six electrons of the center are unpaired. Thus, both the ground and the first excited states, are spin triplets.[66] Due to the magnetic interaction between the two unpaired electrons, the electronic spin states are split into $^3A_2$ ($m_s = 0$) and doubly degenerate $^3A_2$ ($m_s = \pm 1$) sublevels with an energy gap of 2.87 GHz. The smaller splitting for ^3E sublevels (1.42 GHz) is caused by larger electron–electron separation in the excited state. The primary transition between triplet ground and excited states is predominantly spin conserving.[65] The course of optical excitation differs according to involved spin sublevels: While excitation from $^3A_2$ ($m_s = 0$) to ^3E ($m_s = 0$) results in radiative decay, excitation from $^3A_2$ ($m_s = \pm 1$) can either be followed by radiative deexcitation to ^3E ($m_s = \pm 1$), or by intersystem crossing through the intermediate singlet states ($^1A_1$ and ^1E). This

might play an important role in the quenching of photoluminescence. This deexcitation is predominantly nonradiative, although it may be accompanied by feeble infrared emission (1042 nm).[65,49,67]

The $m_s = \pm 1$ states can be split by an external magnetic field. The position of their lines in the electron spin resonance (ESR) spectrum allows for calculations of the external field magnitude. According to this principle, highly sensitive scanning probe magnetometers, which can detect fields of single electrons in nanometer scale, can be constructed.[48,68] If the magnetic field oriented along the axis of the defect splits the ^3E or $^3A_2$ states with energies of 1.42 GHz or 2.87 GHz, respectively, the corresponding $m_s = -1$ and $m_s = 0$ sublevel states become energetically equal. This interaction results in spin polarization observable as a drop in luminescence intensity.[69] In a similar fashion, splitting can be modulated by applying a static electric field.[70] Another approach for the modulation of luminescence intensity is based on changing the electron populations between $m_s = 0$ and $m_s = \pm 1$ states using microwave radiation.[71] In addition to static perturbations, numerous dynamic effects, such as Rabi oscillations or spin echo, have been also studied.[72–74]

3.6. Generation of vacancies in the ND lattice

The fraction of pristine nitrogen-rich HPHT NDs particles which naturally contain NV centers is negligible. To increase their concentration, sufficient amount of vacancies in a crystal lattice of **Ib** NDs (naturally containing nitrogen impurities) must be generated with high-energy particles such as $^4He^+$ particles,[46,75] protons,[60,76] and electrons.[77,78] Another approach, suitable for thin diamond films, uses the direct implantation of N^+ ions which serve both as vacancy-generating particles and as a source of nitrogen in the lattice.[79,80,42] The efficiency of ionizing particles in the generation of crystal lattice defects is determined by their mass, energy, and charge. For charged particles, coulombic

interactions are the dominant cause of ionization damage. In the case of energetic electrons, their interactions occur predominantly with other electrons as an elastic (Rutherford) scattering resulting in considerable change of particle direction in accordance with the laws of conservation of momentum and energy.[81] This type of interaction produces mainly single vacancies in the crystal lattice.

Heavier charged particles, such as protons, deuterons, or alpha particles, tend to scatter the significantly lighter electrons without considerable energy loss. Their deflection in the collision is negligible and therefore, their penetration paths have substantially straighter trajectories. Heavy ions traversing matter lose energy primarily through the ionization and excitation of atoms. During collisions, they may also transfer sufficient momentum to produce "knock-on" atoms which may further displace other surrounding atoms, causing a cascade of collisions within a small distance. The result is extensive lattice damage with clusters of vacancies.[82]

The effect of neutron irradiation on a diamond lattice differs from other heavy particles mainly due to the absence of charge. Neutrons do not interact with orbital electrons and their main interaction is limited to a ballistic one, where neutrons collide with atom nuclei.[83] The cross-section of this reaction is small for thermal and epithermal neutrons, but complex and significant for fast neutrons, producing a cascade of "knock-on" atoms and damage occurs in the form of vacancy clusters.[84] The thermal and epithermal neutrons typically interact with neutron capture, producing heavier isotopes which can undergo radioactive decay and form different elements.[81] This phenomenon can be utilized for neutron activation analysis or doping.[85]

The rate of energy loss in the material is called stopping power. For non-relativistic heavy charged particles, it can be described using the Bethe formula as a function of atomic number, velocity, and environmental parameters (**Fig. 6**).

$$-\frac{dE}{dx}=\frac{5.08\,x10^{-31}\,z^2 n}{\beta^2}[F(\beta)-\ln I_{ev}] \quad \text{MeV cm}^{-1}$$

$$\text{where,} \quad F(\beta)=\ln\frac{1.02\,x10^6\,\beta^2}{1-\beta^2}-\beta^2$$

Figure 6. The Bethe formula for stopping power of a uniform medium for a heavy charged particle, where z = atomic number of the heavy particle, n = density of electrons in medium, $\beta = v/c$ = speed of the particle relative to c, and I = mean excitation energy of the medium. *Adapted from Ref.*[86]

With decreasing particle velocity, the factor in front of the bracket increases as $\beta \rightarrow 0$ causing a peak at the point when the kinetic energy of a particle starts to be comparable to the energy of the orbital electrons of the surrounding atoms. After this point, the particle can acquire electrons, rapidly lose energy, become uncharged, and the curve tails off.[87] This peak in energy loss function, the Bragg peak, allows for the delivery of a significant fraction of energy at the end of the particle range (**Fig. 7**).

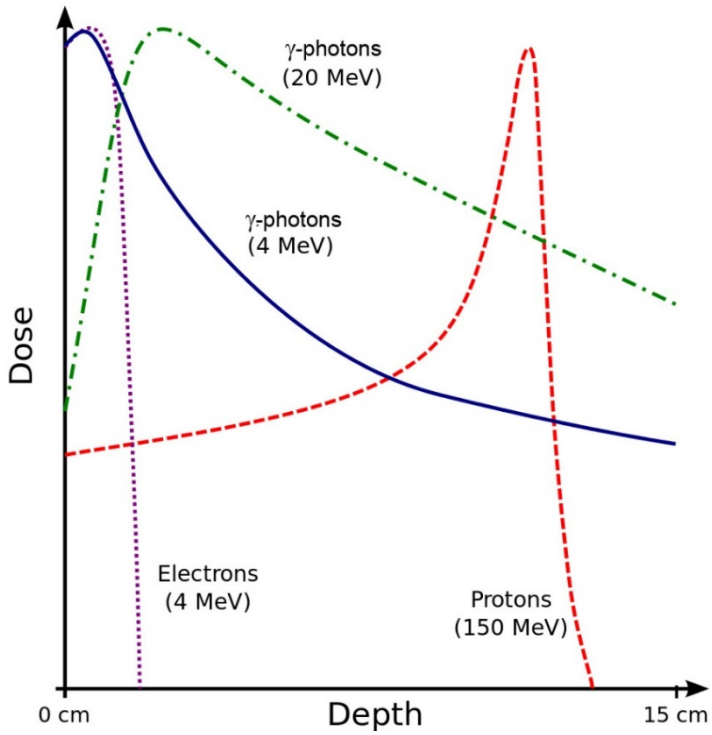

Figure 7. Relative energy loss rate of different types of particles in tissue (normalized). Unlike electrons and γ-photons, the dose from protons to tissue is maximal just over the last few millimeters of the particle range, forming a Bragg peak (red dashed line). *Adapted from Ref.*[89]

This feature is crucial for applications which require energy focused in a precisely defined position, such as proton radiation therapy of cancer.[88]

An effort to produce sufficient amounts of highly fluorescent nanodiamonds by homogeneous irradiation inevitably brings with it many technical challenges. The most prominent are limited particles range, spatial and energetic inhomogeneity of particle distribution, uneven rate of energy loss in irradiation targets, and sample overheating. These issues are especially significant in the case of irradiation by heavy ions with short range and considerable Bragg peaks. Traditional solid-state irradiation techniques usually compensate for these obstacles with irradiation of thin layers of samples. This significantly limits the amount of irradiated material and increases the cost (**Fig. 8**).[46,90]

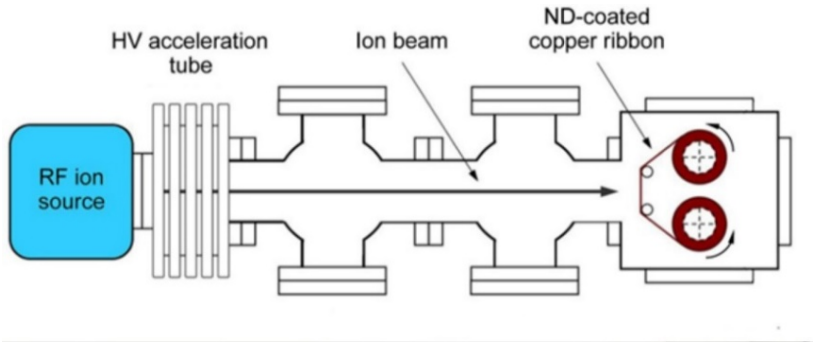

Figure 8. Schematic diagram of a 40-keV He^+ ion beam facility for routine production of FNDs. A thin diamond film is prepared on a copper ribbon which rolls in a vacuum to allow continuous exposure of the nanoparticles to the ion beam for irradiation. *Adapted from Ref.*[91]

3.7. Colloidal properties and surface structures on NDs

Perfect colloidal stability is a key prerequisite for the use of NDs in bioapplications. The behavior of solid nanoparticles in solution is determined by the sum of all repulsive and attractive forces among them. The intensity of these forces is influenced by many factors, such as the size, shape and surface charge

of the nanoparticles; the composition of chemical groups on their surfaces; and the solvent composition. One of the most important measurable indicators of colloidal stability is zeta-potential, which is closely related to the electrophoretic mobility and surface charge. Its magnitude indicates the degree of electrostatic repulsion between similarly charged particles in solution. Colloids with an absolute value of zeta-potential higher than 30 mV are generally considered to be electrically stabilized, whereas colloids with lower zeta-potentials tend to aggregate and require further steric stabilization.[92]

The zeta-potential of NDs varies significantly according to the synthesis method and subsequent purification treatment. These differences are especially prominent for DNDs. Particles obtained by de-aggregation of pristine aggregates by milling with zirconia microbeads and sonication have a positive zeta–potential at 45–50 mV.[93] After treatment with ozone or with a mixture of H_2SO_4-$KMnO_4$, particles, a strong negative zeta-potential is obtained.[94–96] Subsequent annealing at 700 °C in a vacuum can change the zeta-potential of DNDs back to positive values. This behavior can be explained since the negative charge of thermally sensitive functional groups on DNDs and because of partial surface graphitization. The chemical structure of groups responsible for negative zeta-potential is still not fully understood. However, it has been suggested that the surface of negatively charged DNDs is covered with a mixture of oxidic functional groups such as phenols, pyrenes and carboxylic groups.[97–99] For positively charged surfaces, the chemical origin of zeta-potential values is understood even less, and several surface models are under consideration. The most probable explanation of their basic properties is the presence of pyrone-like structures on the edges of the polyaromatic layers connected in a π-conjugated system.[100,101]

Unlike “bottom-up” DNDs synthesis, HPHT and CVD NDs are prepared according to a “top-down” approach in which bulk crystals are milled and consequently size-sorted with centrifugation. Their surface structure therefore differs from DNDs. The surface of commercially produced HPHT NDs is usually

covered with residues of graphitic carbon which reduces their colloidal stability and worsens their photoluminescence properties. For these reasons, high-temperature oxidation with air followed by wet oxidation with a mixture of oxidizers and strong acids is usually performed prior to further use.[97] According to X-ray photoelectron spectroscopy (XPS) and Near edge X-ray absorption fine structure (NEXAFS) analysis, the surface of oxidized HPHT NDs is occupied predominantly with hydroxyl groups together with a small fraction (~2%) of carboxyl groups. This corresponds more to the typical surface of a bulk diamond crystals than to the surface of DNDs.[102]

The most important environmental factors which affect NDs colloidal stability are solvents and their ionic strength. Bare NDs with an oxidic surface are usually stable only in very polar solvents such as water or dimethyl sulfoxide. Unlike HPHT NDs, DNDs can be also dispersed in alcohols and glycols.[93] The stabilization in less polar solvents is possible only with surface modification using hydrophobic functional groups.[103] As typical colloidal dispersions, NDs lose their colloidal stability and start to aggregate at ionic strengths higher than 50 mM due to contractions in the stabilizing electric double layer.[104] This behavior limits direct use of bare NDs for bioapplications on account of the high concentration of salts in media and biological fluids, e.g. normal saline solution with ionic strength of 154 mM. This weakness can be overcome by chemical modification of the surface with hydrophilic and bulky molecules.[105]

The behavior of particles in solution is also influenced by their size and density. While single digit ND particles cannot be quantitatively separated from a solution without a use of ultracentrifuges, particles larger than approximately 100 nm tend to sediment slowly even at laboratory conditions. This effect is even more distinct in the case of ND hybrid particles with metal shells, due to their density.[106]

3.8. Chemical properties of NDs

In comparison to bulk diamonds, nanodiamonds are significantly more reactive. This feature might be explained by their large surface/volume ratio, larger number of surface and crystal lattice defects, and changes of sp^3/sp^2 carbon thermodynamic equilibrium in nanoscale.[33] These effects increase the number of reactive groups on ND surfaces and facilitate their transformation into other forms of carbon.[107] The chemical properties of NDs also vary significantly based on the production methods. For both historical and practical reasons, DNDs belong to the most thoroughly studied systems. Unfortunately, due to their higher reactivity compared to NDs produced by other synthetic methods, functionalization strategies used on this material are generally not directly transferable. This difference is usually not emphasized in the literature and comprehensive comparative studies have not yet been undertaken.

The chemistry of NDs is affected by extreme steric hindrance of functional groups on their surfaces and by the heterogeneous nature of nanoparticles. These factors, together with the limited spectrum of available methods for surface analysis, make even common organic reactions synthetically very challenging.

As it was outlined in the previous chapter, the surface of commercially available NDs varies according to their manufacturing processes. They usually involve treatment with strong oxidizing agents in order to obtain a heterogeneous mixture of functional groups such as carboxyls, hydroxyls, lactones, ketones, and ethers together with a certain amount of heterogeneous sp^2 residues.[108] To ensure reproducibility and selective high-yield functionalization, standardized homogenization methods are required. Initial homogenization strategies include surface oxidation, graphitization, reduction, and halogenation. These approaches are summarized in **Fig. 9**.

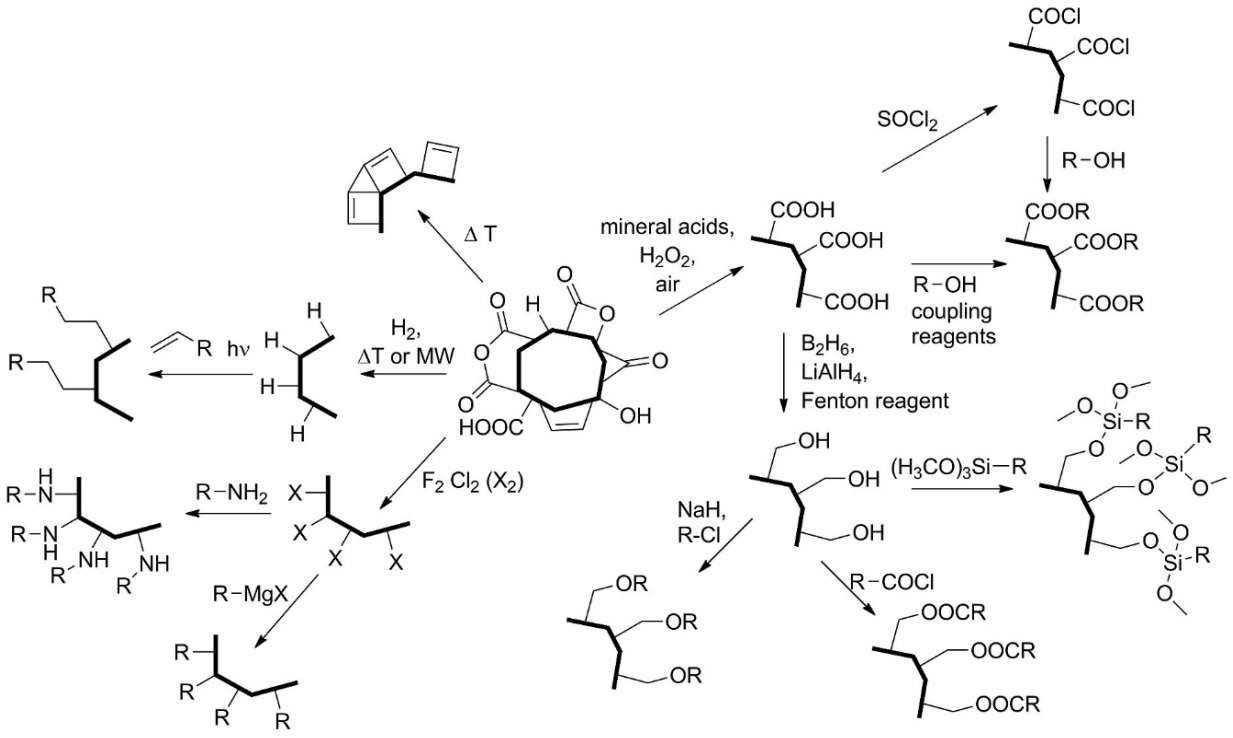

Figure 9. Common NDs surface modification pathways.

Probably the most frequently used approach is oxidation, which transforms surface moieties into a combination of carboxyl and hydroxyl groups. It can be performed with various mixtures of sulphuric, nitric, hydrofluoric, and perchloric acids[109,110] in a piranha solution (freshly prepared mixture of hydrogen peroxide with sulphuric acid),[111] air,[97] or ozone.[96] Except for ozone treatment, these reactions are performed at high temperatures and occasionally also at elevated pressures. They are also usually applicable for both DNDs and HPHT NDs.

Partially reduced (hydroxylated) NDs can be obtained from carboxylated NDs by reduction with lithium aluminum hydride[112] or borane-THF complex.[113] Another approach uses oxidative decarboxylation with Fenton's reagent.[114] Hydrogen-terminated NDs can be produced by the reaction with hydrogen at elevated temperatures[115] or in a CVD plasma reactor.[116]

Commonly used halogenation methods for sp^2-nanocarbon materials are difficult to apply to sp^3-diamond surfaces because of their fundamentally

different chemical natures and lower reactivities. A halogenated diamond surface can be obtained by treatment with elemental gas or halogenating reagents.[117] The fluorination approaches for nanodiamond surfaces typically involve highly corrosive gasses such as fluorine,[118,119] chlorine trifluoride,[120,121] fluorine-containing plasmas,[117,122,123] or an ultrahigh-vacuum fluorine atomic beam.[124]

3.9. Surface modification using polymers and biomolecules

The surface of an ND can be further modified with grafting of polymers. Typically, this kind of modification is intended to achieve colloidal stability in a high ionic strength environment (buffers, cell culture media or blood plasma); to increase particle homogeneity; and in the case of *in vivo* use, to significantly reduce the immune response. Appropriately selected side functional groups of the polymer also allow subsequent conjugation with other moieties. Both grafting-from[104,125] and grafting-to[109,126] approaches are used to produce NDs with surface polymers. Another approach employs a non-covalent grafting of polymers to ND surfaces.[127] Relatively newer techniques include coating of NDs with a porous silica layer that allows the use of well-known chemical methods based on silica chemistry.[128,129] The advantage of this method is higher monodispersity and sphericity of silica-coated NDs in comparison to the starting materials.

Various types of biomolecules such as peptides,[130] enzymes,[131] antibodies, or nucleic acids are often attached to an ND surface by both covalent and non-covalent interactions in order to obtain the desired properties and behaviors. Non-covalent linkage can be typically accomplished by the simple incubation of nanoparticles in a solution of biomolecules. However, the disadvantages of non-covalent absorption are low surface specificity and low stability to an exchange with other biomolecules in solution. These issues can be solved using covalent

grafting employing coupling reactions. Another common solution is a reaction of isocyanate with amine and Cu(I)-catalyzed alkyne-azide cycloaddition (“click reaction”). The conjugated molecules are sometimes separated from the nanoparticles by a linker in order to preserve bioactivity, to avoid steric hindrance, and to limit nonspecific interactions.

4. Scope of the thesis

Fluorescent nanodiamonds represent a promising material with unique properties. Unfortunately, their possible use is limited by many factors, such as low fluorescence intensity of individual nanoparticles, heterogeneity of surface functional groups, poor colloidal stability in biological environment, and broad size distribution of nanoparticles. The experimental part of this thesis is focused on the improvement of FND material properties to overcome the above-mentioned obstacles and to demonstrate potential applications of the improved NDs.

The aims of this work are following:

1. To develop procedures for the large-scale production of FNDs with improved fluorescent properties in terms of fluorescence intensity and fluorescence homogeneity of individual nanoparticles.

2. To modify ND shape, size distribution and surface chemistry in order to facilitate their use in bio-applications.

3. To demonstrate novel use of developed architectures on NDs in medicinal or biological applications.

The results obtained from experiments undertaken for this thesis are divided into three sections:

The first section (Chapter 5.1.) summarizes the obtained results related to the improvement of fluorescent properties. It is dedicated to the boosting of fluorescence intensity, homogeneity of NV centers in nanoparticles, removal of surface graphitized structures, and scale-up of FNDs production. All related results are covered by two publications and a manuscript appended as Appendices A, C, and E.

The second section (Chapter 5.2.) deals with ND surface and shape modifications. It describes the fluorination of surfaces and the adjustment of size distribution and circularity of nanoparticles. All related data are included in the publications and manuscript reprinted in Appendices D and G.

The third section (Chapter 5.3.) encompasses biological and medicinal applications for NDs. Two different approaches demonstrate the versatility of NDs. First, a complex architecture on an ND surface allows selective targeting, detection, and therapy of cancer cells. Second, a specific surface chemistry of NDs is utilized for selective inhibition of cell signaling. The topic is completed by the paper and manuscript reprinted in Appendices B and F.

5. Results and discussion

5.1. Boosting of ND fluorescence intensity and production optimization

FND production represents a technological challenge in terms of fluorescence intensity, achievable yields and of production costs. Surprisingly, only limited attention was paid to this subject in the literature to date. This section focuses on the development and optimization of new production methods that meet the requirements for the possible use in bio-applications.

Development of a novel method for direct homogeneous irradiation of NDs in colloidal solution[1]

*The vacancies in ND crystals are created by a coulombic interaction of carbon atoms with accelerated particles during their path through an irradiation target. The penetration depth of heavy charged ions is relatively low and energy deposition is uneven, with a maximum at the Bragg peak at the end of the particle path. This problem is usually compensated with irradiation of thin ND layers on a flat surface such as long metallic tape (**Fig. 8**) or a pellet target (**Fig. 10**). Both methods significantly limit the achievable amount of NDs per one irradiation. Further technological challenges arise from various types of irradiation-dose uncertainties caused by the technical design of systems such as the energy spread of particles in an*

[1] **Published as**: Stursa, J.; Havlik, J.; Petrakova, V.; Gulka, M.; Ralis, J.; Zach, V.; Pulec, Z.; Stepan, V.; Zargaleh, S. A.; Ledvina, M.; Nesladek, M.; Treussart, F.; Cigler, P.; *Mass Production of Fluorescent Nanodiamonds with a Narrow Emission Intensity Distribution.* Carbon 2016, 96, 812–818.

accelerated beam or the differences in the density of solid sample pellet. Moreover, the particle beam from the accelerator must be defocused before it reaches a target in order to irradiate a sufficient amount of NDs. All of these effects influence particle energy and density distribution in the cross-section of a beam, resulting in changes of the Bragg peak position. This significantly affects irradiation dose homogeneity. Another technical complication is the risk of local sample overheating causing ND graphitization and deterioration of colloidal properties.

The aims of this study were to develop a new type of irradiation target which would reduce the negative influence of the above-mentioned factors and experimentally compare properties of this design with a traditionally used pellet target (**Fig 10A**). The proposed liquid target design allows direct irradiation of NDs in the form of a colloidal solution (**Fig 10B**).

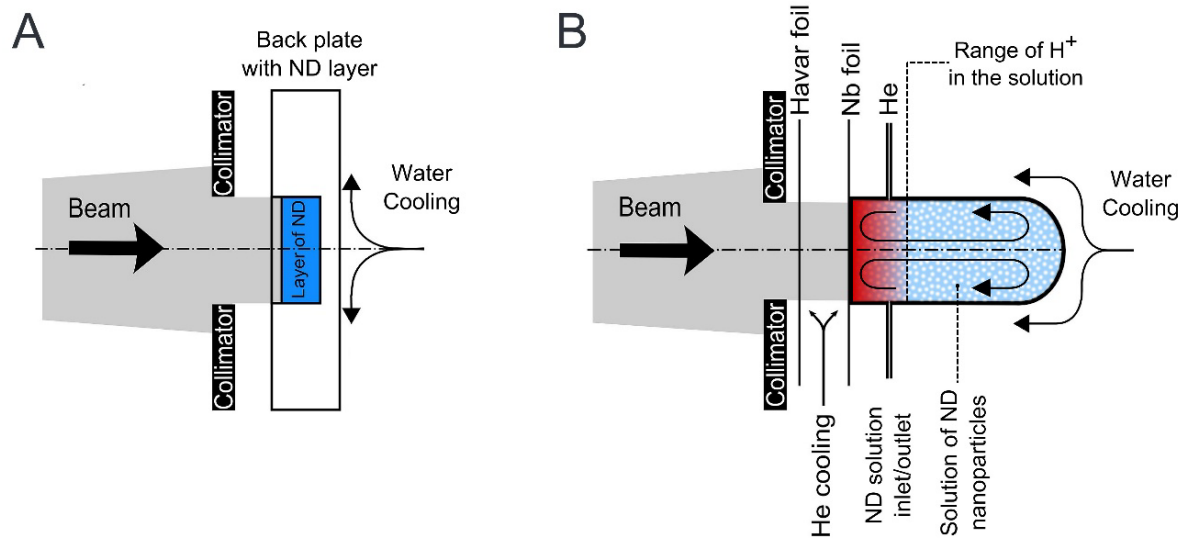

Figure 10. ND pellet target (**A**) and liquid target (**B**) irradiation configurations. The pellet target contains a compressed solid ND pellet. The liquid target is filled with a 5% ND aqueous solution. The "active stopping zone" for protons in the liquid target is outlined by the proton range (red area). *Adapted from Ref.*[132]

The proposed target consists of a niobium chamber separated from the irradiation site with a combination of thin niobium and Havar foils which are easily penetrable for the proton beam arriving from the accelerator. The chamber

can be filled with a 5% NDs colloidal solution through an inlet and outlet system using pressurized helium gas. The whole target is cooled during irradiation with a combination of water and helium gas.

In order to assess the suitability of liquid target design, energy deposition during irradiation was simulated for both target designs using Geant4 software. Obtained depth-dose distribution curves for 16 MeV protons show that the maxima of energy deposition (Bragg peaks) are at a depth of approximately 1.5 mm and 2.7 mm for pellet and liquid targets, respectively (**Fig. 11**). For the solid target, this value limits the possible thickness of the pellet to ~1.6 mm. In the liquid target is the actual irradiated amount significantly increased by thermal convection of the liquid. The ND solution in a ~2.8 mm layer behind the niobium foil is heated by the beam stopping energy and mixes with the rest of the solution with convective currents. Thanks to this effect, all nanoparticles in the solution are continuously exchanged in an active irradiation zone which allows for more uniform irradiation in comparison with the solid target.

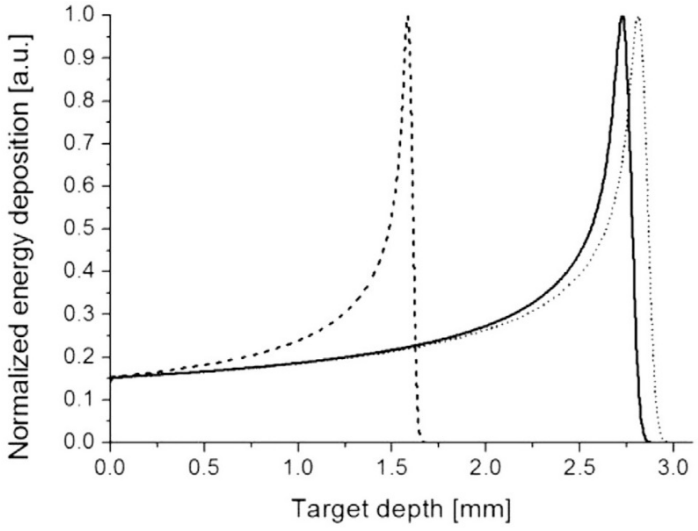

Figure 11. Normalized depth-dose distribution of a 16 MeV proton beam in a compressed solid ND pellet (dashed line), 5% ND aqueous solution (solid line) and water (dotted line). *Adapted from Ref.*[132]

To prove the superiority of a liquid target over a pellet target and to quantitatively assess material properties, HPHT NDs were irradiated using both

targets and compared. Surface graphitization caused by irradiation damage and local overheating were evaluated using Raman spectroscopy. The measured spectra show a significantly lower intensity of the so-called G-band[133] at ~1600 cm^{-1} for the liquid target in comparison with the pellet target. This indicates reduced surface graphitization damage (**Fig. 12**). This effect can be explained by the colloidal state of the sample, in which nanoparticles surrounded by water are effectively protected against local overheating.

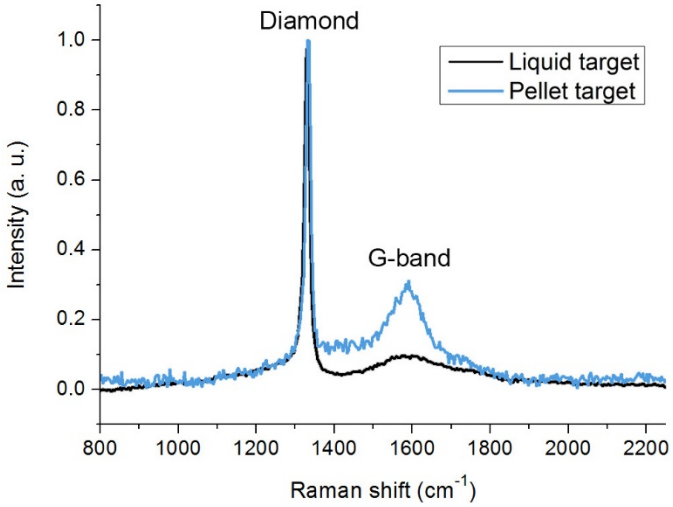

Figure 12. Raman spectra of NDs from the pellet target and liquid target after irradiation. The liquid target shows significantly lower intensity of the G-band at ~1600 cm^{-1} indicating lower surface graphitization. *Adapted from Ref.*[132]

To create fluorescent NV^- centers, the irradiated material was processed by annealing at 900 °C for 1 hour in an argon atmosphere followed by air oxidation at 510 °C for 4 hours. The fluorescent properties of FNDs obtained from both types of targets were evaluated using simultaneous atomic force microscopy (AFM) and confocal fluorescence spectroscopy techniques at the single particle level, which allowed the simultaneous comparison of both size and fluorescence intensity. The results of the analysis show a significantly larger fraction of fluorescent particles in the sample for the liquid target (77%) compared to the pellet target with only 24% of fluorescent particles (**Fig. 13**). In contrast, NDs

from the pellet target exhibited higher mean brightness with a small fraction of exceptionally fluorescent particles. This observation is in accordance with the expected random motion of particles in a solution through an active irradiation zone, leading to lower but more homogenous irradiation in comparison with the stationary particles in a pellet target.

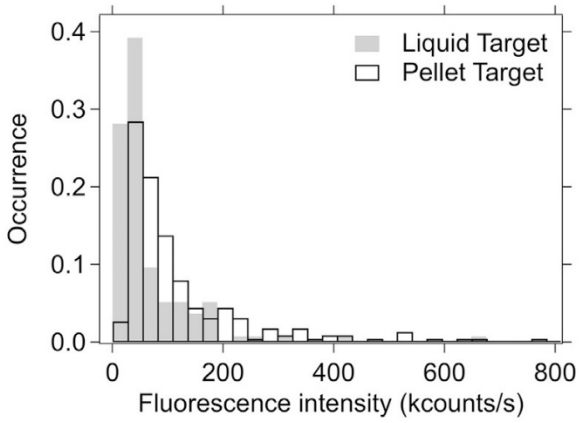

	Pellet target	Liquid target
Fraction of fNDs (%)	24	77
Mean fluorescence intensity (kcounts/s)	122 ± 8	66 ± 7
Median intensity (kcounts/s)	75	38
Standard deviation (kcounts/s)	123	80

Figure 13. Normalized distribution of single FND fluorescence intensity and single particle analysis of fluorescence intensity for pellet and liquid targets. These results were obtained from 175 and 950 NDs analyzed by AFM for liquid and pellet targets respectively. *Adapted from Ref.*[132]

In summary, a new method of FND production using direct irradiation in a colloidal solution was developed. NDs prepared with this approach substantiate lower damage with regards to surface graphitization in comparison with particles from a solid pellet target. Moreover, the analysis of the fluorescence intensity distribution showed more homogeneous distribution of NV centers per particle for new target design. This feature is important for applications in bioimaging and physics.

Boosting nanodiamond fluorescence: optimization of annealing and post-annealing treatment[2]

Fluorescent nanodiamonds represent a promising photoluminescent material with exceptional biocompatibility. Thanks to the properties of NV centers, FNDs are distinguished because of extreme photostability, no photobleaching or photoblinking (for nanocrystals bigger than 5 nm), and suitable emission wavelengths located in NIR windows of biological tissues. However, their broader applications are limited by relatively insufficient particle brightness in comparison with probes such as quantum dots. Optimization of NV center formation in FNDs is therefore critically needed.

In contrast to the relatively well-described formation of NV centers for bulk single crystal diamonds, a systematic study of ND annealing parameters has been missing from the research literature to date. One of the unanswered questions was whether the commonly used annealing parameters (700–800 ºC for 1–2 hours) are in the thermal and kinetic optimum of the annealing treatment. To shed light on this problem, mapping of optimal annealing parameters was performed in this study with two sizes of HPHT proton-irradiated NDs (45 nm and 140 nm in diameter). The set of FNDs, containing 24 samples for each ND size, was prepared with annealing in an argon atmosphere with a variation of temperature and time conditions (700–950 ºC, 0.5–8 h). All samples were subsequently treated with a mixture of H_2SO_4 and HNO_3 to oxidize sp^2 structures on the ND surfaces.

The photoluminescence spectroscopy measurements showed significant differences in fluorescence intensity (FLI) among the samples (**Fig. 14**). The FLI

[2] **Published as**: Havlik, J.; Petrakova, V.; Rehor, I.; Petrak, V.; Gulka, M.; Stursa, J.; Kucka, J.; Ralis, J.; Rendler, T.; Lee, S.-Y.; Reuter, R.; Wrachtrup, J.; Ledvina, M.; Nesladek, M.; Cigler, P.; *Boosting Nanodiamond Fluorescence: Towards Development of Brighter Probes*. Nanoscale 2013, 5, 3208–3211.

of 140 nm NDs was approximately tenfold higher in comparison with 45 nm NDs. This result is in agreement with previously observed behaviors and can be explained by the higher volume-to-surface ratio of bigger particles. In larger nanoparticles, migrating vacancies are more likely to be captured by a nitrogen atom before their termination on the ND surfaces.

In accordance with these observations, measurements of NV concentration in single nanodiamond particles with anti-bunching time-correlation spectroscopy have shown that an average 45 nm particle contains ~1.7 NV centers, whereas approximately 360 NV centers were present in 140 nm particles.

For both 45 nm and 140 nm NDs, discrete FLI maxima were identified for the conditions of 1 hour of annealing at 900 ºC. Under these conditions, FLI is approximately three times higher when compared to the commonly used parameters (700 ºC, 2 hours).

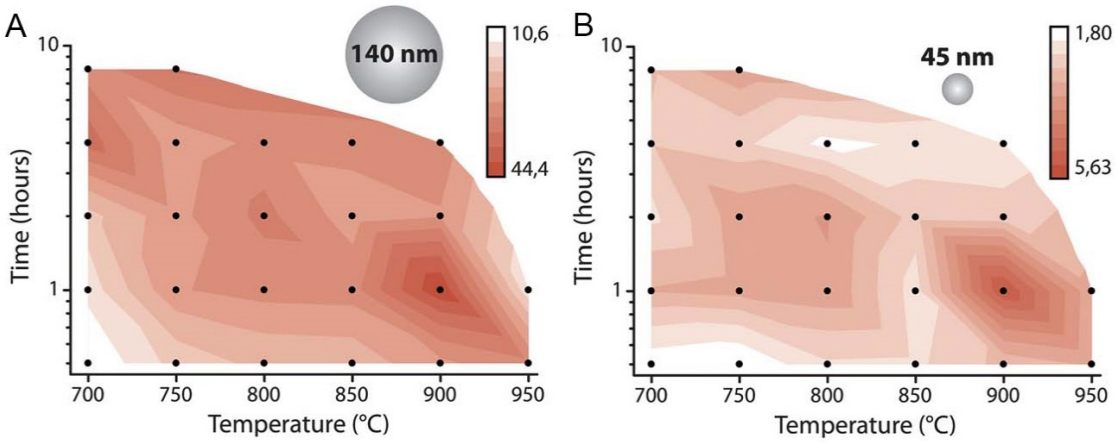

Figure 14. Normalized total FLI of NV centers (NV^- + NV^0) for (**A**) 140 nm and (**B**) 45 nm ND particles as a function of annealing time and temperature. Black dots represent the individual points of the matrix of annealing conditions. Darker colors represent brighter samples.[134]

The evolution of sp^2 structures on ND surfaces during thermal annealing was analyzed using Raman spectroscopy measurements normalized to the diamond Raman signal at 1332 cm^{-1}. The occurrence of amorphized sp^2 carbons is markedly higher for smaller (45 nm) particles, probably due to a higher surface

to volume ratio. The formation of sp^2 impurities is caused by a rearrangement of the surface at high temperature and it negatively affects both particle FLI and colloidal stability in aqueous solutions. To remove sp^2 carbons and increase the FND brightness, different oxidation treatments with air, oxygen plasma, and melted potassium nitrate were studied (**Fig. 15**). Oxidation with air at 510 °C for 4.5 hours shows results comparable to oxygen plasma treatment, with approximately twofold higher FLI when compared to an untreated sample. The most significant result was achieved with a novel treatment of NDs in molten KNO_3 at 560 °C for 10 minutes, producing 2.5-fold brighter FNDs with excellent colloidal properties. The thermal and kinetic formation optimum of NV centers in FNDs was identified. A new oxidation method using molten potassium was developed. The combination of these approaches allows the preparation of particles one order of magnitude brighter in comparison to commonly treated FNDs.

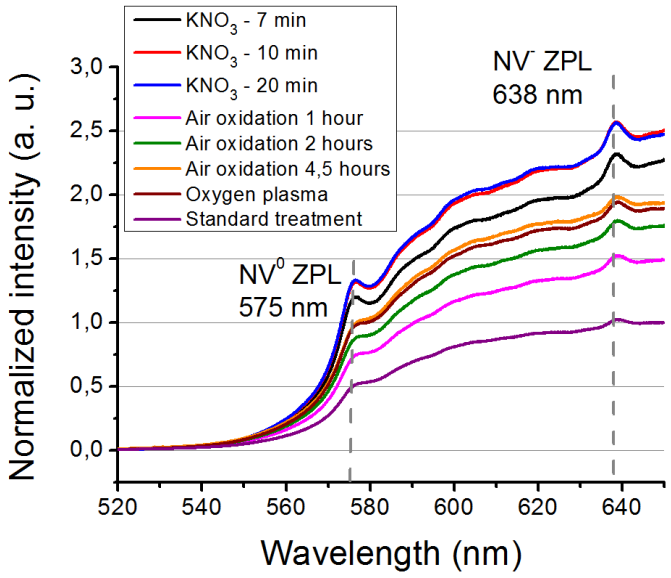

Figure 15. Normalized fluorescence spectra of fNDs oxidized under various conditions.[134]

Rapid irradiation of large ND quantities with ions generated *in situ* by a nuclear reaction[3]

From the viewpoint of material throughput and production costs, the irradiation of NDs constitutes the most limiting step in the manufacturing of FNDs. Traditional methods using direct irradiation with charged particles are limited in penetration depth, inhomogeneity of deposition energy, and long irradiation times. These factors make the potential scale-up of FNDs production very challenging. Development of novel mass production methods is therefore critically needed for the potential broad use of FNDs.

To fulfill these requirements, a new approach for nanoparticle irradiation was suggested. It utilizes a dispersion of NDs in ^{10}B-isotopically enriched boron(III) oxide in the form of a pulverized glassy melt. After placing the mixture in a nuclear reactor channel, captured thermal neutrons induce a nuclear reaction on ^{10}B with a high absorption cross section of 3869 barn (10^{-24} cm^2), forming an all-directional localized flux of charged ions. The mixture of *in situ* generated α-particles and ^{7}Li ions uniformly irradiates the surrounding NDs and creates vacancies in their crystal lattices (**Fig. 16**). This approach combines the advantages of a long penetration depth for uncharged neutrons together with a high ionization potential of heavy ions generated homogeneously in the whole sample volume.

To quantitatively assess the irradiation efficiency, the trajectories of alpha and $^{7}_{3}$Li particles in glassy melt were simulated using a Geant 4 toolkit. Projected range, energy deposition, and average number of ND particle hits per one alpha or $^{7}_{3}$Li particle were calculated from 10^6 simulated particle trajectories. The

[3] **Manuscript submitted as**: Havlik, J.; Kucka, J.; Raabova, H.; Petrakova, V.; Stepan, V.; Zlamalova Cilova, Z.; Kucera, J.; Hruby, M.; Cigler, P.; *Extremely rapid irradiation of nanoparticles with ions generated in situ by a nuclear reaction*

simulation results confirmed the efficiency of this approach. The results of calculations for alpha particles show that one alpha particle interacts on average with 37 nanodiamond particles per along the ~4.0 µm trajectory. Similarly, $^{7}_{3}$Li ion interacts along its ~1.7 µm trajectory with another 19 NDs (**Fig. 17**).

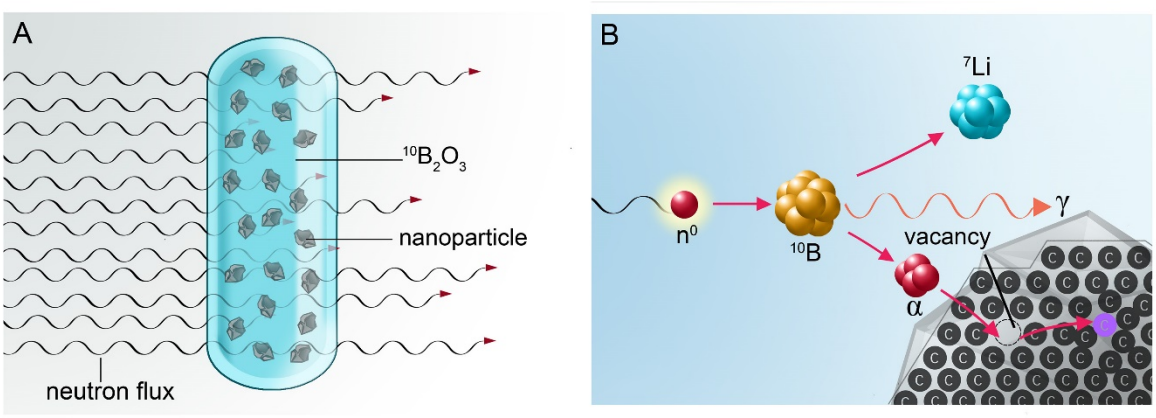

Figure 16. General scheme of the implantation of energetic ions into NDs generated *in situ* by ^{10}B neutron capture. (**A**) A capsule containing nanoparticles embedded in a glassy melt of $^{10}B_2O_3$ is exposed to a neutron flux. (**B**) Schematic representation of alpha and $^{7}Li^{+}$ particles formation mechanism and subsequent creation of a vacancy in a nanodiamond.

These values indicate that particles generated from a single ^{10}B split can create vacancies in tens of individual surrounding NDs. If the reactions of ^{10}B atoms with neutrons occur randomly in the entire volume of the melt, the creation of vacancies can be homogenous and efficient.

To experimentally confirm the abovementioned simulations, the glass melts containing 33% dispersion of 35 nm and 150 nm NDs in $^{10}B_2O_3$ were irradiated in a nuclear reactor at various time intervals ranging from 3–100 minutes. After the dissolution of the B_2O_3 glassy matrix, NDs were processed with annealing and subsequent oxidation treatment. Zeta potentials of obtained colloidal solutions were –46.7 mV for 35 nm particles and –41.0 mV for 150 nm particles. This indicates strong stabilization of the surface with the negative charge of deprotonated carboxylates on cleaned NDs. The absence of major aggregates and unchanged particle size distribution after treatment was also confirmed by TEM image analysis.

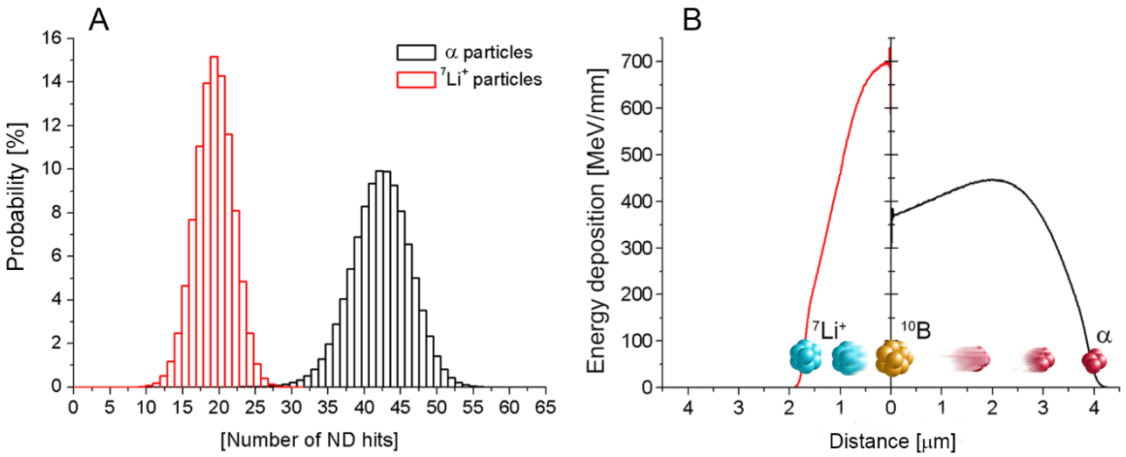

Figure 17. Compared to $^{7}Li^{+}$ particles, α particles interact with a higher number of ND particles and deposit lower energy over larger distances in 33 wt.% dispersion of 35-nm spherical NDs in $^{10}B_2O_3$. (**A**) The number of ND hits per one α particle and $^{7}Li^{+}$ ion and (**B**) energy deposition of these α particles (**black**) and $^{7}Li^{+}$ ions (**red**) along their trajectory.

To find the optimal ratio between ND brightness and the necessary irradiation time, FLIs of NDs irradiated for 3–100 minutes were analyzed and compared (**Fig. 18**). Surprisingly, FLIs of NDs irradiated for the shortest technically available time (3 minutes) are fully comparable to both NDs irradiated for longer irradiation times (**Fig. 18C**). The possibility of substantial irradiation time reduction provides enables an increase in daily production output of FNDs by a factor of approximately 10^3.

Further analysis of crystal lattice damage using Raman spectroscopy confirmed an expected increase in sp^2 carbon content with increasing irradiation time related to lattice degradation (**Fig. 18A, B**). This correlates with an observed decrease in FLI for NDs irradiated for more than 20 minutes. The spectral characteristic of FNDs prepared in a nuclear reactor is similar to FNDs produced by direct cyclotron irradiation (**Fig 18D**). The single particle fluorescence homogeneity is increased by a factor of 2.6 in comparison with solid pellet target (49% vs. 19% of fluorescent particles fraction). These values are close to the results achieved for a homogeneous liquid target.

In summary, a novel method for the production of FNDs was developed. It utilizes indirect irradiation of NDs with ions generated *in situ* from ^{10}B-enriched boron oxide in neutron flux. This method provides a material with a high fraction of bright FNDs. Moreover, the demonstrated approach opens the doors to the large-scale production of FNDs for more affordable applications in bioimaging, nanomedicine, and quantum sensing.

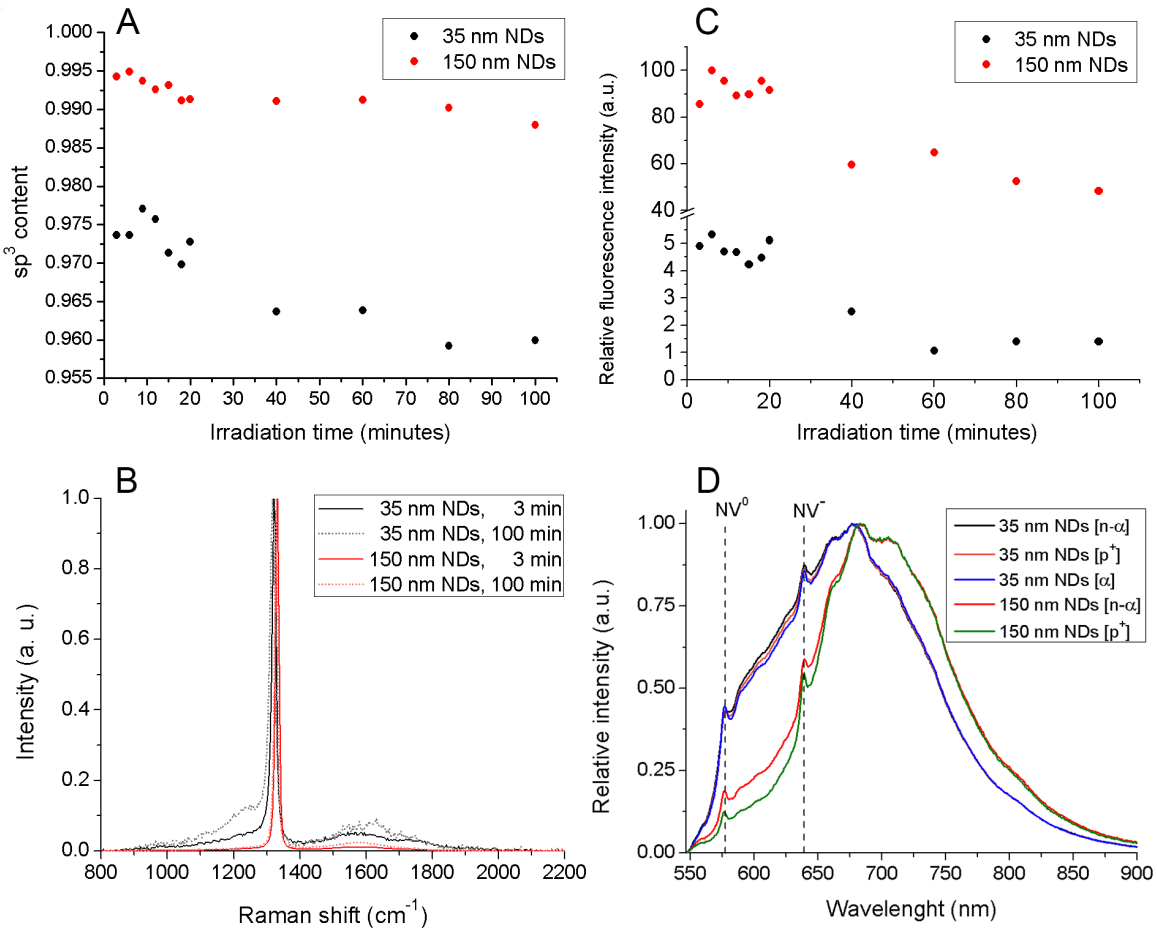

Figure 18. Spectral characterization of irradiated 35-nm and 150-nm NDs reveals how increased radiation damage (**A, B**) lowers relative fluorescence intensities (**C**) with increasing irradiation time in a nuclear reactor. (**A**) Content of sp^3 carbon in irradiated samples. (**B**) Raman spectra showing increasing amount of sp^2 impurities (below and above a diamond signal at 1332 cm^{-1}). (**C**) Relative fluorescence intensity of irradiated samples. (**D**) Comparison of photoluminescence spectra of samples irradiated in a nuclear reactor [n-α] with samples irradiated in a cyclotron with protons [p^+] or with α particles [α]. The spectra in (**D**) are normalized at their maxima.

5.2. Surface and shape modification of NDs

The nature of surface groups significantly affects not only colloidal stability but also the fluorescence properties of NDs. Unfortunately, due to steric hindering, low reactivity, and the limitations of conventional analytical methods, the chemistry of ND surfaces still represents a challenging and relatively poorly understood field of synthetic chemistry. In addition to surface chemistry, the *in vivo* behavior of nanoparticles is also substantially influenced by their shapes and size distribution. The following section is focused on the development of effective methods for ND surface functionalization and shape and size modifications.

Benchtop fluorination of FNDs on a preparative scale[4]

Carbon nanomaterial fluorination methods have attracted considerable interest over the last two decades thanks to the ability of a C–F bond to shift optical, electromagnetic, and mechanical properties of nanomaterials and increase their hydrophobicity. In the case of FNDs, surface fluorination can stabilize the negatively charged form of fluorescent NV centers (NV^-). Whereas traditionally used fluorination methods typically require harsh and technically demanding treatment conditions, the preparative method described in this study can be carried out on a benchtop using modest synthetic equipment.

[4] **Published as**: Havlik, J.; Raabova, H.; Gulka, M.; Petrakova, V.; Krecmarova, M.; Masek, V.; Lousa, P.; Stursa, J.; Boyen, H.-G.; Nesladek, M.; Cigler, P.; *Benchtop Fluorination of Fluorescent Nanodiamonds on a Preparative Scale: Toward Unusually Hydrophilic Bright Particles*. Adv. Funct. Mater. 2016, 26, 4134–4142

To utilize the effect of surface fluorination while maintaining the colloidal stability of nanoparticles in water, a surface modification method based on dual functionality involving both fluorine and hydrophilic oxygen-containing groups has been proposed. Functional groups on the surface of nanodiamonds are represented primarily by hydroxyl, carbonyl, and ether groups, while carboxyl groups represent only about 2–7%. We assumed that even a limited number of fluorine atoms on the surface of nanoparticles would suffice to affect the spectral properties of NV centers. For this reason, the recently described selective partial substitution of carboxyls for fluorine groups was used to modify the surface, while hydroxyl groups, together with the remaining carboxyls, would keep the fluorinated NDs hydrophilic and colloidally stable in an aqueous environment. The procedure is based on a silver-catalyzed decarboxylative fluorination reaction utilizing the electrophilic fluorinating reagent Selectfluor (F-TEDA$^+$ BF_4^-). The complex reaction mechanism is shown in **Fig. 19**.

The reaction was tested at various temperatures and duration times. The fluorination yield of the reaction was determined by combustion of the samples in an oxygen atmosphere followed by an analysis of fluoride anion content using ion exchange chromatography. The highest fluorine content (0.13 wt%) was obtained for 2 days of fluorination at 95 °C. The conversion of the reaction was determined from the following estimate of the maximum fluoride content on the ND surfaces. The total number of available terminal carbon atoms on the ND surfaces was calculated from the size distribution of nanoparticles, obtained with a precise image analysis of NDs using TEM images. Assuming a [111] diamond surface, the maximal theoretical load of fluorine on a perfluorinated NDs surface is 3.7 mmol g^{-1}. Considering the experimentally determined coverage of NDs with carboxyl groups as 2 % of all surface functionalities, the maximal total theoretical fluorine content is ≈0.14 wt%, which corresponds to a 94% reaction conversion for the most fluorinated sample. Although this result is strongly affected by the accuracy of the input value of carboxyl content, the fluorination proceeds with a high conversion.

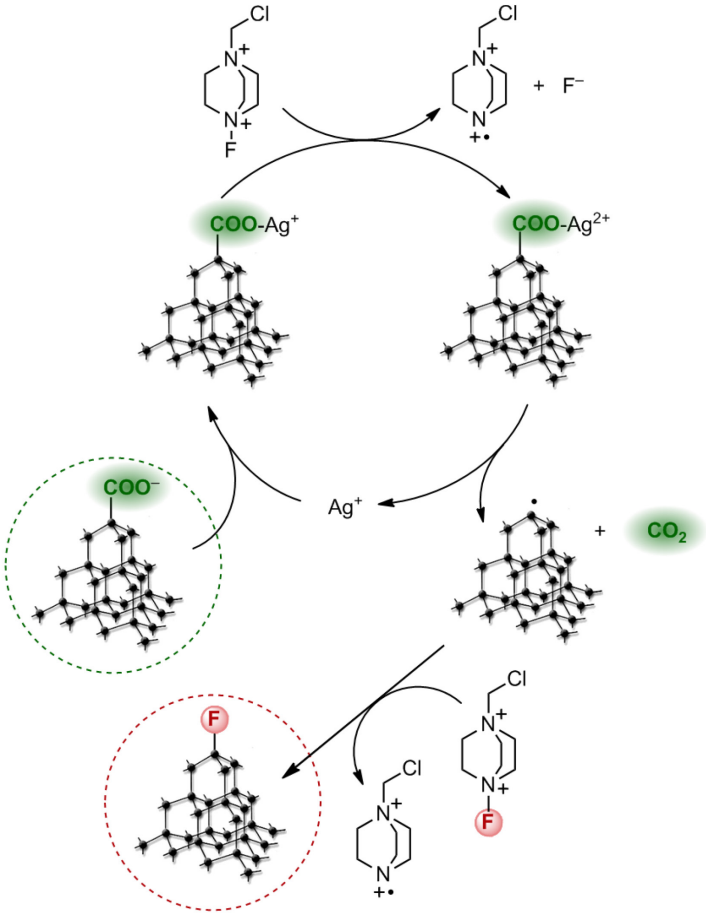

Figure 19. Simplified scheme showing the catalytic cycle for decarboxylative fluorination of NDs. The ND is represented by a fragment of the diamond lattice.[135]

Fluorinated NDs were analyzed using XPS to obtain information about the chemical environment of fluorine atoms from binding energy shifts of appropriate core levels. A single line centered at 687.3 eV, corresponding to a transition of C–F bonds (687.5 eV), confirmed stable attachment of fluorine atoms to ND surfaces. A semiquantitative analysis of surface coverage resulted in an intensity ratio of C–C (sp^3) peak at 285.3 eV and C–F shoulder at 287.4 eV (4.3% of line intensity). This observation confirms that the ND surfaces were partially functionalized.

The colloidal behavior of fluorinated particles in water was analyzed using DLS and zeta-potential measurements. Both fluorinated and non-fluorinated control NDs have an average particle diameter of 38 nm and typical size distribution for HPHT NDs. This confirms that colloidal stability was not affected

by fluorination. The zeta-potential of fluorinated diamonds (–46 mV) differs by only 2 mV from the non-fluorinated diamonds (–48 mV), most likely due to stabilization of the surface with the remaining unreacted carboxyl groups. Structural and morphological analysis with TEM further confirmed that ND fluorination does not affect the size distribution or circularity. This observation indirectly confirms that, unlike other fluorination methods, radical fluorination proceeds without a loss of particle mass by surface etching.

C–F termination is currently considered to be the most powerful surface termination for stabilization of NV^- charge state. To assess the effect of surface fluorination on the spectral shape and NV^-/NV^0 ratio, fluorescence spectra measured in colloidal aqueous solution were quantitatively compared (**Fig. 20**). A ≈5% increase in emission intensity of the NV^- state upon fluorination of oxidized NDs was observed. This change can be considered significant since the fluorine surface coverage is relatively low and the presence of oxidic groups already contributes to a strong inversion of surface dipole polarity.

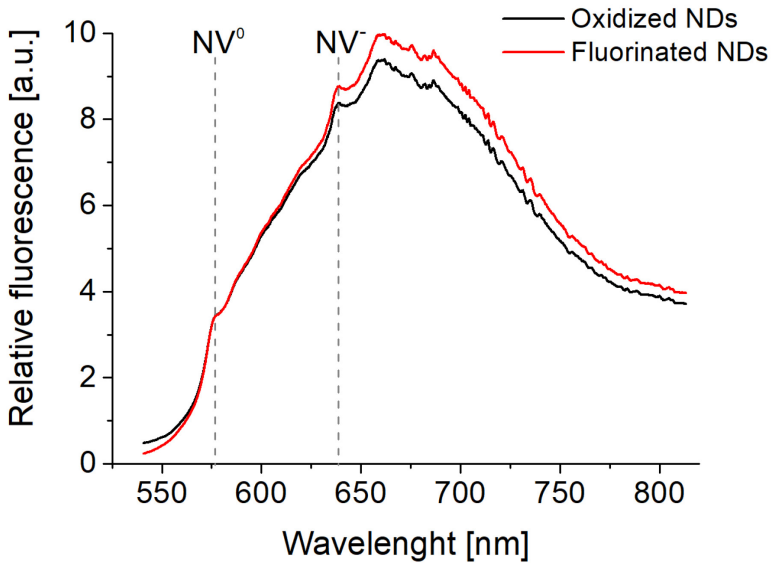

Figure 20. Fluorescence spectra of oxidized and fluorinated FNDs measured in aqueous colloidal solutions and normalized to NV^0 intensity.[135]

In conclusion, a synthetic pathway for the selective substitution of ND surface carboxyl groups with fluorine atoms was developed. Mixed oxygen-fluorine termination on the surface of sterically demanding NDs was synthesized. In contrast to the traditional harsh fluorination procedures, this procedure can be easily performed on the benchtop under mild conditions in an aqueous environment. The decarboxylative fluorination boosts the fluorescence intensity of treated fNDs while maintaining their colloidal stability, shape, and size distribution.

Production of rounded monodisperse nanodiamonds[5]

Small FNDs of suitable size for bio-applications are produced from larger HPHT microcrystals by grinding and rough size separation. Industrially-produced material prepared in this manner is relatively non-uniform in size and shape. Moreover, the nanoparticles contain sharp edges and spike vertexes which negatively affect their properties, such as the distribution in living systems or single particle fluorescence homogeneity. Recent studies have also shown that spiky particles may induce cytotoxicity in cells. The development of a simple and large-scale technique for the preparation of pseudospherical monodisperse nanodiamonds is thus an important step in the production of new diagnostic fluorescent probes or biosensors.

Based on a review of available methods, etching in the melt of potassium nitrate was chosen as the most promising way to influence the size and shape of NDs. Preliminary studies have shown that short exposure of NDs to the oxidation environment of KNO_3 melt at temperatures between 500–580 °C results in rounded NDs (RNDs) with shifted size distributions. A large systematic study has been proposed in order to find the optimal conditions for a maximal yield of maximum RNDs. In the initial experiments with a small amount of NDs, it was found that for yield enhancement, higher temperatures and shorter etching times were favored. Reaction times were therefore set in a range of 3–8.5 minutes. To prevent aggregation and to achieve rapid homogenization even for a large-scale reaction with 0.5 g raw NDs, small changes were made in the treatment procedure. Instead of slowly heating the whole mixture in a furnace, NDs were first homogenized with a small amount of KNO_3 and then added to an excess of preheated KNO_3 melt set to 567 °C, slightly above the KNO_3

[5] **Manuscript in preparation as**: Rehor, I.; Raabova, H.; Havlik, J.; Fiserova, A.; Richter, J.; Turner, S.; Van Tendeloo, G.; Stursa, J.; Petrakova, V.; Dai, L.; Cigler, P.; *Rounded monodisperse nanodiamonds: properties and mass production*

decomposition temperature. Several parameters, such as RND yield, particle size distribution, sp^2 carbon content, and colloidal stability have been measured for the etched particles. The obtained data were used to determine optimal etching conditions, primarily considering particle circularity and reaction yield.

The rounding effect was evaluated using image analysis of TEM pictures. The analysis shows that for a very short treatment time, the rounding effect increases at the expense of yield; however, after 6 minutes, this effect reaches its maximum and further etching only causes material loss without additional rounding (**Fig. 21**).

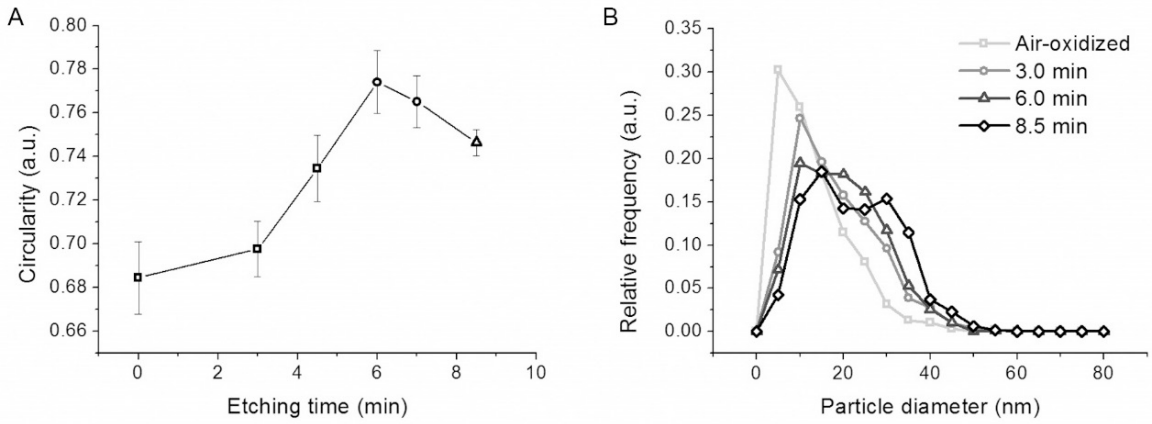

Figure 21. Polydisperse HPHT nanodiamonds are etched in molten potassium nitrate in order to round the particles while maintaining maximal reaction yield. (**A**) The whole etching process is illustrated with a series of etching times at a fixed starting temperature (567 °C); the optimum etching time is found at 6 minutes. (**B**) Number-weighted particle size distributions are shifted to larger particles since the small particle fractions are reduced and digested by a prolonged etching process.

A more detailed image of surface morphology was obtained from a high-resolution TEM (HRTEM) analysis. The surface of NDs treated by etching represents a multitude of atomic steps with preferential exposure of the [111] planes and a small amount of remaining sp^2 impurities. It was also found that etching, unlike conventional oxidation by air, significantly affects particle size distribution. Although the etching process resulted in increased roundness and reduced non-diamond carbon content, the samples have remained relatively

polydisperse, with two major particle size populations (<10 nm and 20–50 nm). The fractions containing larger particles were separated to achieve brighter NDs for the possible application as fluorescent probes. A method involving several consecutive centrifugation separations was developed to remove both very small diamonds and large aggregates with possible impurities. An analysis of the obtained colloids showed an average particle size 35–40 nm and the almost complete removal of particles with size below 10 nm. The dispersity of particles (for details see Appendix G) also significantly dropped from 2.5 for original RNDs to 1.6 for NDs after separation (**Fig. 22**).

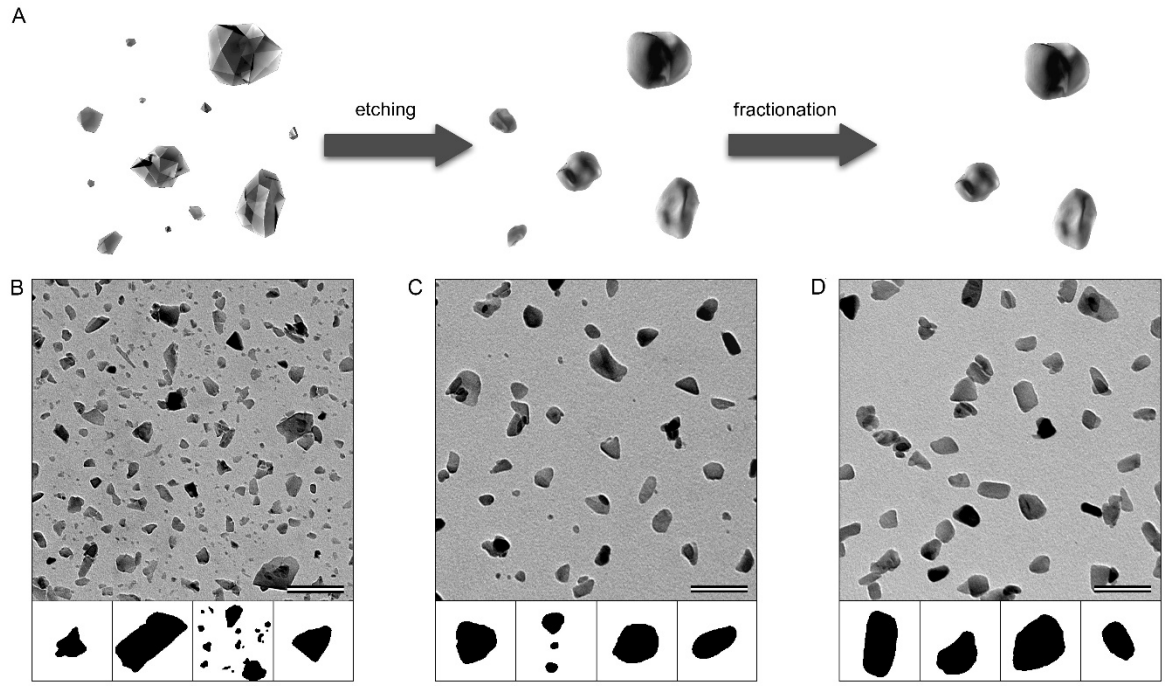

Figure 22. Preparation and appearance of monodisperse RNDs. (**A**) Particles from a manufacturer are rounded by etching and consequently separated by centrifugation to obtain particles of narrow size distribution, approximately 40 nm. The NDs drawings shown here are illustrative. (**B**) TEM micrographs of air-oxidized diamonds before etching, (**C**) rounded diamonds after etching, and (**D**) rounded diamonds separated by ultracentrifugation. The insets show examples of particles in the form of a binary image, used for image analysis. The scale bar corresponds to 100 nm for TEM microphotography and to 50 nm for the inset.

The obtained RNDs were irradiated in a cyclotron, resulting in the production of FNDs. The measurements of FLI using Raman spectroscopy confirm similar fluorescent behavior in comparison to non-rounded NDs irradiated under same conditions. RNDs produced by this method can therefore be used as a source for FNDs.

The etching of NDs in molten potassium nitrate can be used as a rounding and surface oxidation procedure in the scale of grams. The optimal compromise etching condition between the etching yield and particle circularity was found, and the method for a significant decrease in material polydispersity using centrifugal fractionation was developed. Overall, the results show that the combination of etching and subsequent fractionation is an effective way towards the production of a monodisperse material which can be transformed into a fluorescent material for bio-applications.

5.3. Medicinal and bio-applications

A key area for the modification of nanoparticle surfaces is the design of surface architectures. Materials such as amorphous silica, polymers, gold, proteins, nucleic acids, or fluorescent molecules are often combined in a non-orthodox way to achieve the desired properties of the particles. The surface of NDs contains a broad spectrum of functional groups. The knowledge of their interactions with living systems together with appropriately chosen surface design can utilize the enormous specific surface of NDs to scavenge large signalizing molecules and effectively influence their metabolic functions.

Plasmonic nanodiamonds for cancer cell thermoablation[6]

Plasmon nanoparticles represent a unique structural system that allows the construction of nanosensors and nanoparticles with theranostic (therapeutic and diagnostic) properties. Their specific quantum properties are illustrated by a resonant oscillation of conduction electrons associated with the strong absorption of certain wavelengths. This occurs in structures of precious metals and their composites with dimensions corresponding to the wavelength of the incident photons. The absorbed energy is effectively converted to heat by plasmon nanoparticles. This enables possible applications for the design of selective theranostic agents in cancer therapy by thermoablation.

[6] **Published as**: Rehor, I.; Lee, K. L.; Chen, K.; Hajek, M.; Havlik, J.; Lokajova, J.; Masat, M.; Slegerova, J.; Shukla, S.; Heidari, H.; Bals, S.; Steinmetz, N. F.; Cigler, P.; *Plasmonic Nanodiamonds: Targeted Core-Shell Type Nanoparticles for Cancer Cell Thermoablation*. Adv. Healthcare Mater. 2015, 4, 460–468.

To create plasmonic gold nanoparticles (PGNS), a core-shell design with multistep encapsulation based on ND diamagnetic cores was proposed, serving as a suitable dielectric and optically transparent material, covered with functional layers using multistep encapsulation (**Fig. 23**). In this study, the irregular shape of a 35-nm diamagnetic diamond core was normalized first with an approximately 20 nm thick silica shell. Thereafter, small gold nanoparticles (2–3 nm) were electrostatically attached to the layer of silica and served as nucleation centers for the subsequent growth of a gold shell in the reductive environment containing Au(III), yielding a deep blue solution with a broad plasmonic band and an absorption maximum at 675 nm.

To employ the particles in biological applications, it was necessary to protect them against aggregation caused by high ionic strength and to prevent undesirable interactions with the immune system. This was achieved using polyethylene glycol (PEG) polymer nanointerface functionalization, consisting of PEG terminated with lipoic acid at one end and aliphatic alkyne at the other. The lipoic acid served as an anchor with a strong affinity to the gold surface. The alkyne groups allowed the subsequent connection of the requested biomolecules by a “click reaction”: Cu(I)-catalyzed alkyne-azide cycloaddition. The functional design was confirmed with subsequent colloidal stability tests. These tests showed high colloidal stability in PBS, the physiological solution, and even in the cell growth media.

To obtain fluorescent particles for flow cytometry and confocal microscopy analysis, the alkyne-bearing surface was conjugated with an Alexa Fluor 647-azide dye. After this step, human holotransferrin (Tf) was conjugated to the remaining alkynes with a ”click reaction” under similar conditions. This glycoprotein was recognized by the corresponding receptor (TfR) expressed in an increased amount on the surface of cancer cells and may thus serve as a targeting ligand for internalization through clathrin-mediated endocytosis.

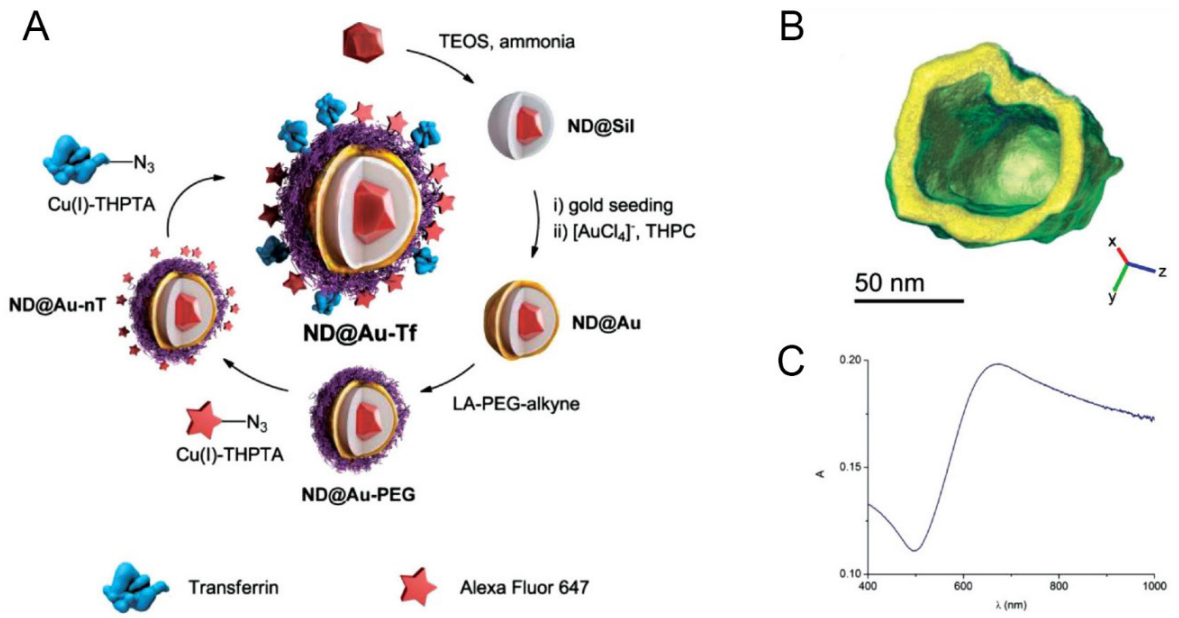

Figure 23. (**A**) Schematic representation of PGNS preparation. The particles contain a diamond core encapsulated in a silica layer, which is then covered with a gold plasmonic shell and protected by a PEG surface modification. (**B**) A slice through the 3D representation of the gold shell demonstrating its homogeneity. (**C**) The absorption spectrum of PGNS in water at 15 μM concentration. *Adapted from Ref.*[106]

Target-specificity and cellular uptake of particles were evaluated in TfR-expressing SKBR3 cells (a human breast cancer cell line) using flow cytometry. The analysis indicated that PGNS with attached transferrin (PGNS-Tf) was targeted to 26% of the cell population, while non-specific uptake of PGNS without transferrin (PGNS-nTf) was attributed to 18% of the cells. The fate of the particles in cells was investigated by confocal microscopy. The data confirmed that even though both formulations can bind to cellular membranes, only PGNS-Tf is internalized. Moreover, after 24-hour incubation, the cells with PGNS did not show any significant differences in cell viability compared to non-treated cells. This indicates that PGNS are not cytotoxic.

The ability of PGNS to kill cancer cells with thermoablation was demonstrated *in vitro*. HeLa cells were incubated with PGNS-Tf, washed, and irradiated with a Ti:Sapphire pulse laser (37W/cm^2). After one minute of irradiation, cells were incubated for 24 hours and their viability was estimated. The viability of HeLa

cells exposed to laser radiation alone or PGNS-Tf alone was not affected. Only the cells exposed to both nanoparticles and laser irradiation were affected and almost completely ablated (**Fig. 24**).

A novel plasmonic nanomaterial consisting of nanodiamond core coated with a silica layer and encapsulated in a thin gold nanoshell was synthesized. The attached PEG chains were modified with Alexa Fluor 647 dye and transferring by "click chemistry". The ability of PGNS-Tf to bind and internalize into an SKBR3 human breast cancer cell was observed with no toxic effects. The ability of internalized PGNS-Tf to kill cancer cells upon 750 nm pulse laser irradiation while leaving cells without PGNS-Tf treatment viable was demonstrated *in vitro*.

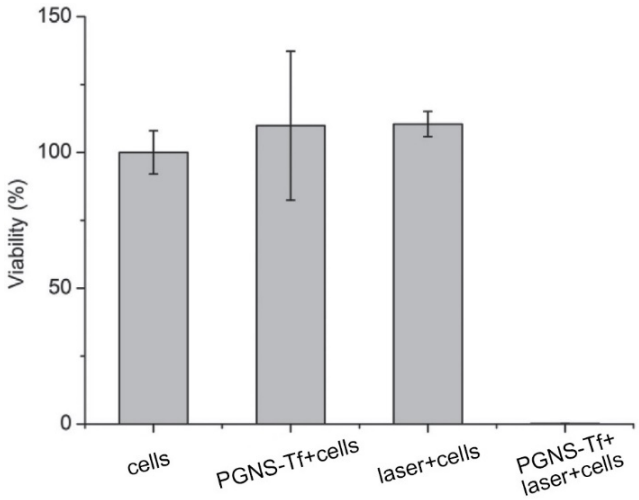

Figure 24. HeLa cells incubated with PGNS-Tf nanoparticles after laser ablation with 37 W/cm^2 intensity. The viability was estimated by luciferase assay with 24 h delay after 1 minute irradiation. The viability of cells treated with PGNS-Tf and laser was ≈0.15%. The viability of cells in controls without laser ablation or without PGNS-Tf stayed unchanged. *Adapted from Ref.*[106]

DNDs as a specific inhibitor of fibroblast growth factors[7]

Numerous observations in living systems indicate that the surface of nanoparticles interacts with a broad range of proteins thanks to a high surface to volume ratio and the possibility of polyvalent display of binding site. This feature can significantly affect their pharmacokinetic and pharmacodynamic behaviors and enable their application in targeted drug delivery systems. Even though the specificity of nanoparticle-protein interactions with regard to the composition of functional groups on the surface is still not well understood, research in this area holds great potential. The steric, thermodynamic, and kinetic similarity of certain nanoparticles to biomolecules such as globular proteins may allow binding, blocking, and mimicking of specific proteins in living organisms. This may have a dramatic effect on cell behavior, even at negligible nanoparticle concentrations.

In this study, we identified the strong interaction between NDs and members of fibroblast growth factors (FGF) already at sub-nanomolar concentrations. FGFs represent a large family of polypeptide growth factors. FGFs are involved in angiogenesis, embryonic development, and various signaling pathways. They also play an irreplaceable role in cell proliferation, migration, and differentiation. Some FGFs can also contribute to the pathogenesis of cancer.[136]

The hypothesis that NDs inhibit FGF signalizing in cells was tested on rat chondrosarcoma cells (RCS). These types of cells were chosen because of their well-characterized array of cell phenotype changes in response to the activation FGF receptors. Cells with a growth-arrest caused by preincubation with FGF2 were treated with five different types of NDs that varied in size, synthesis method, origin, and zeta-potential (**Fig. 25 A, B**). Activity was shown in the case of a DND sample with positive zeta-potential, which, unlike other NDs, rescued

[7] **Manuscript submitted as**: Balek, L.; Buchtova, M.; Foldynova-Trantirkova, S.; Havlik J.; Varecha, M.; Turner, S.; Vesela, I.; Klimaschewski, L.; Claus, P.; Trantirek, L.; Cigler, P.; Krejci, P.; *Nanodiamonds as artificial proteins: regulation of a cell signalling system using picomolar solutions of inorganic nanocrystals*

the growth-arrest caused by FGF2. It was anticipated that this interaction might be size dependent. Therefore, a fraction of DNDs with different sizes and size-distributions were separated using ultracentrifugation. The rescue of FGF-mediated RCS growth arrest was more effective as the size of DNDs particles decreased (**Fig. 25C**).

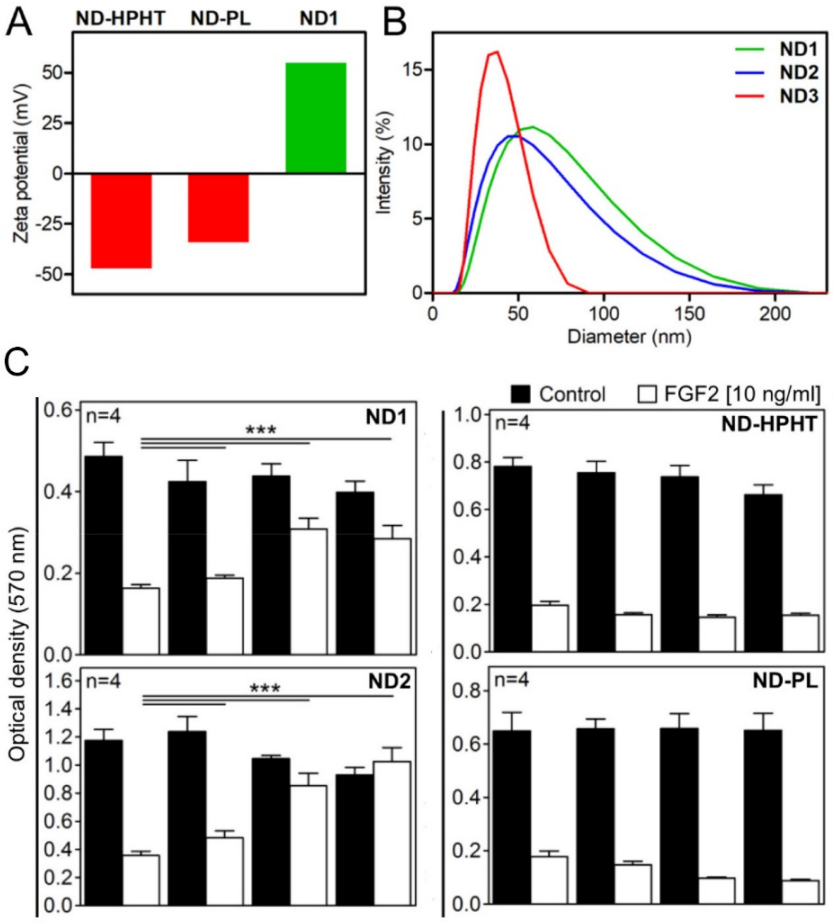

Figure 25. (**A**) Zeta-potential of NDs employed. **ND-HPHT** – smallest isolated fraction of HPHT NDs, **ND-PL** and **ND1** – DNDs with negative and positive zeta-potentials, respectively. (**B**) Size distribution of DND fractions separated from **ND1** by ultracentrifugation measured by DLS. **ND2** – supernatant after ND1 centrifugation at 15,000 rfc, 2 h. **ND3** – supernatant after subsequent ND2 centrifugation at 30,000 rfc, 2 h (**C**) ND inhibition of FGF2 signalizing in cells. RCS cells were treated in medium containing 10% FBS serum with FGF2 (10 ng/ml) alone or together with four types of fNDs differing in zeta-potential and particle size.

To exclude the influence of any other compound in the form of a minor impurity, DND colloidal solutions were dialyzed five times against DI water and

tested for activity. A second test was performed on a supernatant obtained from DNDs ultra-centrifuged at 200,000 g for 4 hours. While the washed DNDs retained their activities unchanged, their supernatant without detectable DNDs did not inhibit FGF2 signaling in RCS cells. These results indicate that positively charged DNDs are responsible for the observed effect.

To gain insight into the mechanisms of ND-mediated inhibition for FGF signaling, the effect of DNDs on activation of FGF receptors was analyzed. The absence of FGF2-mediated phosphorylation of signaling mediators indicates an inhibition of extracellular signal–regulated kinase (ERK) activation.

All the aforementioned experiments were successfully performed in tissue culture media containing 10% fetal bovine serum (FBS). The total concentration of proteins in the solution was 10^5-fold higher when compared to FGF, and the concentration of extremely diluted DNDs was ≤10 μg/ml. This corresponds to approximately ≤50 pM. These findings illustrate the remarkably strong nature of FGF2–DND interactions.

The specificity of DNDs was further investigated on other ligands belonging to the FGF family. Studies of RCS and MCF7 (human breast cancer) cells proved that ERK activation mediated by FGF2,9,18 and FGF7,10,22, respectively, could be rescued using DND treatments. It was also demonstrated that DNDs do not interfere with five FGF-unrelated ligand-receptor systems (TGF, IL6, IFN, EGF and NGF).

The mechanisms of DND actions were also studied with the hypothesis that DNDs inhibit FGF signaling by the sequestration of FGFs from receptors. To confirm the mechanism, human recombinant FGFs were incubated with DNDs in a DMEM (Dulbecco's modified Eagle's minimal essential medium) supplemented with fetal bovine serum. DNDs were collected afterward using ultracentrifugation and analyzed for the presence of FGF with FGF-specific antibodies. Efficient depletion of recombinant FGF 1,4,8,10,14, and 22 was found. However, clearance was less effective for FGF hormones (FGF 19,21, and 23) and insignificant for other cytokines (IL6, IFNγ and IL1β). The less efficient

depletion of FGF19,21, and 23 can be explained by their structure which contains impaired heparin binding site (HBS). This hypothesis was tested by substituting FGF23 with a chimeric FGF23 protein with inserted HBS from FGF2. The addition of HBS significantly improved the clearance of FGF23 from the culture media, demonstrating that HBS contributes to the specific interaction of FGFs with DNDs.

The effect of DNDs on FGF signaling obtained on RCS cells was further extended in a study of *in vitro* cultures of limb rudiments isolated from mouse CD1 embryos (**Fig. 26**). Continuous treatment with FGF2 without DNDs caused significant inhibition of limb rudiment growth accompanied by a reduction in hypertrophic cartilage evidenced by changes in growth plate anatomical appearance. This effect was suppressed by a treatment with DNDs, which partially rescued the FGF2 growth-inhibitory effect, including restoration of the hypertrophic cartilage. Moreover, the normal growth of limb rudiments with DNDs in the absence of FGF2 suggests a negligible influence of DNDs on FGF-unrelated signaling pathways.

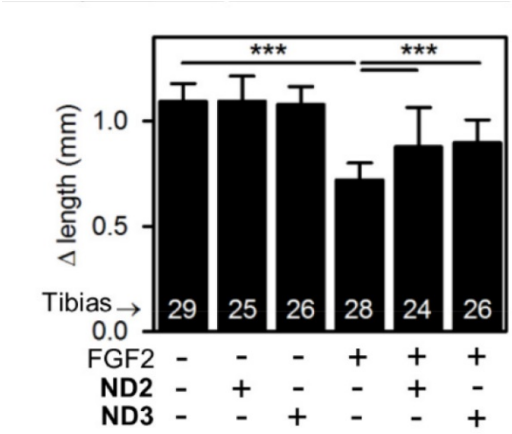

Figure 26. The length differences of tibias isolated from mice embryos after 8 days cultivation with FGF2 and two fractions of DNDs varying in mean particle size (ND2 and ND3). Statistically significant differences are highlighted (Student's t-test, ***p<0.001). The results are a compilation of six independent experiments; n is the number of tibias analyzed.

Up to now, an unexplored system for selective protein-protein regulation using purely inorganic nanoparticles in biological environment has not yet been

discovered. It was found that DNDs with a positive zeta-potential can interact with members of FGF growth factor family and sequester FGFs at their biologically relevant concentrations. DNDs compete by this interaction with FGFR which can mitigate their inhibitory effects on cell growth. This type of regulation was found to be highly selective, without any influence on other signaling systems unrelated to FGF. The ability of DNDs to mitigate pathologic FGF signaling was demonstrated using a restoration of cartilage growth in a mouse limb rudiment model. Moreover, no manifestation of DND toxicity was observed. These findings suggest the potential applicability of DNDs in the treatment of diseases and regulation of signal transduction in biological systems. The high selectivity and strength of interaction between DND and FGF could also be used in novel biotechnology applications.

6. Conclusions

This thesis was devoted to the research and development of surface-modified fluorescent nanodiamonds. In the theoretical introduction, the properties of NDs were summarized using relevant literature. Attention was devoted mainly to the question of fluorescence because this property makes NDs unique. In addition to highlighting the strong points and successful employments of NDs, the study also describes weaknesses preventing possible wider use do date.

These findings were used to formulate the aims of this work. In the first section of the practical part, new nanodiamond irradiation procedures were developed to produce NDs that have a tenfold higher fluorescence intensity and, compared to previously described materials, an increased fraction of fluorescent NDs within the material and lower surface damage caused by graphitization. The newly developed method of indirect neutron irradiation in the nuclear reactor also enabled shortening the required irradiation time to just minutes as well as opening the door to cheap and fast preparation of up to a hundredfold larger amount of FNDs. Findings were summarized in two papers in impact journals and one manuscript, currently under review.

The second section was focused on investigating influences on the size, shape, and surface chemistry of NDs. As a new approach to direct modification of the surface of NDs, a synthetic pathway utilizing selective substitutions of carboxyl groups with fluorine atoms was developed. The effect of this partial surface substitution on the stabilization of NV^- centers was also demonstrated. The published results constitute an experimental foundation for future studies utilizing the described effects in sensing. Further, a novel shaping process which combines treatment of NDs in molten KNO3 and subsequent size-sorting of the

nanoparticles by ultracentrifugation was developed. With this combined technique, the feasibility of obtaining rounded particles with narrow polydispersity was illustrated, providing one of the key assumptions for possible future *in vivo* applications. The article summarizing this research is currently being prepared for publication.

The last section of the experimental part focused on applications of NDs in the biosciences. This section consisted of two projects differing in approach. The first study built on the development of a plasmonic surface architecture on the NDs aimed at recognition and internalization of cancer cells and their subsequent destruction with laser irradiation. The synthesized material showed an ability to bind and internalize into SKBR3 cancer cells *in vitro* and kill them upon 750 nm pulse laser irradiation while leaving untreated cells untouched. The obtained results were summarized in a publication in an impact journal. The second project identified highly selective binding between DNDs with a positive zeta-potential and FGFs. The occurrence of DNDs in picomolar concentration in the cell medium effectively inhibited FGF-related signal pathways, while the function of other signal proteins remained unaffected. This ability was confirmed in both *in vitro* and *ex vivo* models. Moreover, no toxicity of DNDs was observed. The manuscript bringing the results of this study showing the great potential of NDs for the regulation of signal transduction was, at the time of writing this thesis, undergoing review.

The multifaceted, multidisciplinary nature of nanodiamond research which pervades this thesis demonstrates how scientific wealth often hides behind the boundaries of established disciplines. It is very difficult to make predictions about the future development of a rapidly growing field such as nanodiamond research or even nanotechnology in general. However, it is certain that the most fruitful research paths will be led primarily by intensive and close cooperation of scientists from diverse fields.

7. References

(1) Frondel, C.; Marvin, U. B. Lonsdaleite, a Hexagonal Polymorph of Diamond. *Nature* **1967**, *214*, 587–589.

(2) Shenderova, O. A.; Zhirnov, V. V.; Brenner, D. W. Carbon Nanostructures. *Crit. Rev. Solid State Mater. Sci.* **2002**, 27, 227–356

(3) Kroto, H. W.; Heath, J. R.; O'Brien, S. C.; Curl, R. F.; Smalley, R. E. C60: Buckminsterfullerene. *Nature* **1985**, *318*, 162–163.

(4) Iijima, S. Helical Microtubules of Graphitic Carbon. *Nature* **1991**, *354*, 56–58.

(5) Geim, A. K.; Novoselov, K. S. The Rise of Graphene. *Nat. Mater.* **2007**, *6*, 183–191.

(6) Wiberg, E.; Wiberg, N.; Holleman, A. F. *Inorganic Chemistry*; 1st English ed.; Academic Press; De Gruyter: San Diego : Berlin ; New York, **2001**, 778–791

(7) Koshino, M. Stacking-Dependent Optical Absorption in Multilayer Graphene. *New J. Phys.* **2013**, *15*, 015010.

(8) Bundy, F. P.; Bassett, W. A.; Weathers, M. S.; Hemley, R. J.; Mao, H. U.; Goncharov, A. F. The Pressure-Temperature Phase and Transformation Diagram for Carbon; Updated through 1994. *Carbon* **1996**, *34*, 141–153.

(9) Vohlidal, J.; Stulik, K.; Julak, A. *Chemické a analytické tabulky*; Grada: Praha, **1999**, 77.

(10) *CRC Handbook of Chemistry and Physics: A Ready-Reference Book of Chemical and Physical Data*; Chemical Rubber Company; Lide, D. R., Eds.; 83. ed., 2002-2003.; CRC Press: Boca Raton, Fla., **2002**.

(11) Robertson, R.; Fox, J. J.; Martin, A. E. Two Types of Diamond. *Philos. Trans. R. Soc. Math. Phys. Eng. Sci.* **1934**, *232*, 463–535.

(12) Kaiser, W.; Bond, W. L. Nitrogen, A Major Impurity in Common Type I Diamond. *Phys. Rev.* **1959**, *115*, 857–863.

(13) Dyer, H. B.; Raal, F. A.; Du Preez, L.; Loubser, J. H. N. Optical Absorption Features Associated with Paramagnetic Nitrogen in Diamond. *Philos. Mag.* **1965**, *11*, 763–774.

(14) *Properties, Growth and Applications of Diamond*; Nazaré, M. H.; Neves, A. J.; Institution of Electrical Engineers, Eds.; INSPEC: London, **2001**.

(15) Wentorf, R. H.; Bovenkerk, H. P. Preparation of Semiconducting Diamonds. *J. Chem. Phys.* **1962**, *36*, 1987.

(16) *Optical Engineering of Diamond*; Mildren, R. P.; Rabeau, J., Eds.; Wiley-VCH: Weinheim, **2013**, *5*, 146–150

(17) Fahy, S.; Louie, S. G.; Cohen, M. L. Pseudopotential Total-Energy Study of the Transition from Rhombohedral Graphite to Diamond. *Phys. Rev. B* **1986**, *34*, 1191–1199.
(18) Bundy, F. P.; Hall, H. T.; Strong, H. M.; Wentorf, R. H. Man-Made Diamonds. *Nature* **1955**, *176*, 51–55.
(19) Wentorf Jr, R. H. Diamond Growth Rates. *J. Phys. Chem.* **1971**, *75*, 1833–1837.
(20) Burns, R. C.; Cvetkovic, V.; Dodge, C. N.; Evans, D. J. F.; Rooney, M.-L. T.; Spear, P. M.; Welbourn, C. M. Growth-Sector Dependence of Optical Features in Large Synthetic Diamonds. *J. Cryst. Growth* **1990**, *104*, 257–279.
(21) Strong, H. M.; Chrenko, R. M. Diamond Growth Rates and Physical Properties of Laboratory-Made Diamond. *J. Phys. Chem.* **1971**, *75*, 1838–1843.
(22) *Physics and Applications of CVD Diamond*; Koizumi, S., Ed.; Wiley-VCH-Verl: Weinheim, **2008**.
(23) Butler, J. E.; Sumant, A. V. The CVD of Nanodiamond Materials. *Chem. Vap. Depos.* **2008**, *14*, 145–160.
(24) DeCarli, P. S.; Jamieson, J. C. Formation of Diamond by Explosive Shock. *Science* **1961**, *133*, 1821–1822.
(25) Danilenko, V. v. On the History of the Discovery of Nanodiamond Synthesis. *Phys. Solid State* **2004**, *46*, 595–599.
(26) Dolmatov, V. Y. Detonation-Synthesis Nanodiamonds: Synthesis, Structure, Properties and Applications. *Russ. Chem. Rev.* **2007**, *76*, 339–360.
(27) Mochalin, V. N.; Shenderova, O.; Ho, D.; Gogotsi, Y. The Properties and Applications of Nanodiamonds. *Nat. Nanotechnol.* **2012**, *7*, 11–23.
(28) Krüger, A.; Kataoka, F.; Ozawa, M.; Fujino, T.; Suzuki, Y.; Aleksenskii, A. E.; Vul', A. Y.; Ōsawa, E. Unusually Tight Aggregation in Detonation Nanodiamond: Identification and Disintegration. *Carbon* **2005**, *43*, 1722–1730.
(29) Yang, G.-W.; Wang, J.-B.; Liu, Q.-X. Preparation of Nano-Crystalline Diamonds Using Pulsed Laser Induced Reactive Quenching. *J. Phys. Condens. Matter* **1998**, *10*, 7923.
(30) Daulton, T. L.; Kirk, M. A.; Lewis, R. S.; Rehn, L. E. Production of Nanodiamonds by High-Energy Ion Irradiation of Graphite at Room Temperature. *Nucl. Instrum. Methods Phys. Res. Sect. B Beam Interact. Mater. At.* **2001**, *175–177*, 12–20.
(31) Welz, S.; Gogotsi, Y.; McNallan, M. J. Nucleation, Growth, and Graphitization of Diamond Nanocrystals during Chlorination of Carbides. *J. Appl. Phys.* **2003**, *93*, 4207.
(32) Wang, C. X.; Yang, G. W. Thermodynamics of Metastable Phase Nucleation at the Nanoscale. *Mater. Sci. Eng. R Rep.* **2005**, *49*, 157–202.
(33) Jiang, Q.; Chen, Z. P. Thermodynamic Phase Stabilities of Nanocarbon. *Carbon* **2006**, *44*, 79–83.

(34) Wang, C.; Chen, J.; Yang, G.; Xu, N. Thermodynamic Stability and Ultrasmall-Size Effect of Nanodiamonds. *Angew. Chem. Int. Ed.* **2005**, *44*, 7414–7418.
(35) Sun, X.; Wang, R.; Zhang, B.; Huang, R.; Huang, X.; Su, D. S.; Chen, T.; Miao, C.; Yang, W. Evolution and Reactivity of Active Oxygen Species on sp2@sp3 Core–Shell Carbon for the Oxidative Dehydrogenation Reaction. *ChemCatChem* **2014**, *6*, 2270–2275.
(36) Xie, F. Y.; Xie, W. G.; Gong, L.; Zhang, W. H.; Chen, S. H.; Zhang, Q. Z.; Chen, J. Surface Characterization on Graphitization of Nanodiamond Powder Annealed in Nitrogen Ambient. *Surf. Interface Anal.* **2010**, *42*, 1514–1518.
(37) Zaitsev, A. M. Vibronic Spectra of Impurity-Related Optical Centers in Diamond. *Phys. Rev. B* **2000**, *61*, 12909–12922.
(38) Walker, J. Optical Absorption and Luminescence in Diamond. *Rep. Prog. Phys.* **1979**, *42*, 1605–1659.
(39) Zaitsev, A. *Optical Properties of Diamond a Data Handbook*; Springer Berlin Heidelberg: Berlin, Heidelberg, **2001**.
(40) Collins, A. T. The Detection of Colour-Enhanced and Synthetic Gem Diamonds by Optical Spectroscopy. *Diam. Relat. Mater.* **2003**, *12*, 1976–1983.
(41) Breeding, C. M.; Shigley, J. E. The "Type" Classification System of Diamonds and Its Importance in Gemology. *Gems Gemol.* **2009**, *45*, 96–111.
(42) Greentree, A. D.; Olivero, P.; Draganski, M.; Trajkov, E.; Rabeau, J. R.; Reichart, P.; Gibson, B. C.; Rubanov, S.; Huntington, S. T.; Jamieson, D. N.; *et al.* Critical Components for Diamond-Based Quantum Coherent Devices. *J. Phys. Condens. Matter* **2006**, *18*, S825–S842.
(43) Wrachtrup, J.; Jelezko, F. Processing Quantum Information in Diamond. *J. Phys. Condens. Matter* **2006**, *18*, S807–S824.
(44) Aharonovich, I.; Greentree, A. D.; Prawer, S. Diamond Photonics. *Nat. Photonics* **2011**, *5*, 397–405.
(45) Hui, Y. Y.; Cheng, C. L.; Chang, H. C. Nanodiamonds for Optical Bioimaging. *J. Phys. Appl. Phys.* **2010**, *43*, 374021.
(46) Chang, Y.-R.; Lee, H.-Y.; Chen, K.; Chang, C.-C.; Tsai, D.-S.; Fu, C.-C.; Lim, T.-S.; Tzeng, Y.-K.; Fang, C.-Y.; Han, C.-C.; *et al.* Mass Production and Dynamic Imaging of Fluorescent Nanodiamonds. *Nat. Nanotechnol.* **2008**, *3*, 284–288.
(47) Mamin, H. J.; Kim, M.; Sherwood, M. H.; Rettner, C. T.; Ohno, K.; Awschalom, D. D.; Rugar, D. Nanoscale Nuclear Magnetic Resonance with a Nitrogen-Vacancy Spin Sensor. *Science* **2013**, *339*, 557–560.
(48) Maze, J. R.; Stanwix, P. L.; Hodges, J. S.; Hong, S.; Taylor, J. M.; Cappellaro, P.; Jiang, L.; Dutt, M. V. G.; Togan, E.; Zibrov, A. S.; *et al.* Nanoscale Magnetic Sensing with an Individual Electronic Spin in Diamond. *Nature* **2008**, *455*, 644–647.
(49) Davies, G.; Hamer, M. F. Optical Studies of the 1.945 eV Vibronic Band in Diamond. *Proc. R. Soc. Lond. Math. Phys. Eng. Sci.* **1976**, *348*, 285–298.

(50) Jelezko, F.; Tietz, C.; Gruber, A.; Popa, I.; Nizovtsev, A.; Kilin, S.; Wrachtrup, J. Spectroscopy of Single NV Centers in Diamond. *Single Mol.* **2001**, *2*, 255–260.
(51) Doherty, M. W.; Michl, J.; Dolde, F.; Jakobi, I.; Neumann, P.; Manson, N. B.; Wrachtrup, J. Measuring the Defect Structure Orientation of a Single NV $^-$ Centre in Diamond. *New J. Phys.* **2014**, *16*, 063067.
(52) *Properties and Growth of Diamond*; Davies, G.; Institution of Electrical Engineers, Eds.; INSPEC, the Institution of Electrical Engineers: London, 1994.
(53) Iakoubovskii, K.; Adriaenssens, G. J. Trapping of Vacancies by Defects in Diamond. *J. Phys. Condens. Matter* **2001**, *13*, 6015–6018.
(54) Waldermann, F. C.; Olivero, P.; Nunn, J.; Surmacz, K.; Wang, Z. Y.; Jaksch, D.; Taylor, R. A.; Walmsley, I. A.; Draganski, M.; Reichart, P.; *et al.* Creating Diamond Color Centers for Quantum Optical Applications. *Diam. Relat. Mater.* **2007**, *16*, 1887–1895.
(55) Davies, G.; Collins, A. T. Vacancy Complexes in Diamond. *Diam. Relat. Mater.* **1993**, *2*, 80–86.
(56) Petrakova, V.; Taylor, A.; Kratochvílová, I.; Fendrych, F.; Vacik, J.; Kučka, J.; Štursa, J.; Cígler, P.; Ledvina, M.; Fišerová, A.; *et al.* Luminescence of Nanodiamond Driven by Atomic Functionalization: Towards Novel Detection Principles. *Adv. Funct. Mater.* **2012**, *22*, 812–819.
(57) Doherty, M. W.; Manson, N. B.; Delaney, P.; Jelezko, F.; Wrachtrup, J.; Hollenberg, L. C. L. The Nitrogen-Vacancy Colour Centre in Diamond. *Phys. Rep.* **2013**, *528*, 1–45.
(58) Bradac, C.; Gaebel, T.; Naidoo, N.; Sellars, M. J.; Twamley, J.; Brown, L. J.; Barnard, A. S.; Plakhotnik, T.; Zvyagin, A. V.; Rabeau, J. R. Observation and Control of Blinking Nitrogen-Vacancy Centres in Discrete Nanodiamonds. *Nat. Nanotechnol.* **2010**, *5*, 345–349.
(59) Gruber, A.; Dräbenstedt, A.; Tietz, C.; Fleury, L.; Wrachtrup, J.; Borczyskowski, C. von. Scanning Confocal Optical Microscopy and Magnetic Resonance on Single Defect Centers. *Science* **1997**, *276*, 2012–2014.
(60) Fu, C.-C.; Lee, H.-Y.; Chen, K.; Lim, T.-S.; Wu, H.-Y.; Lin, P.-K.; Wei, P.-K.; Tsao, P.-H.; Chang, H.-C.; Fann, W. Characterization and Application of Single Fluorescent Nanodiamonds as Cellular Biomarkers. *Proc. Natl. Acad. Sci.* **2007**, *104*, 727–732.
(61) Ziem, F. C.; Götz, N. S.; Zappe, A.; Steinert, S.; Wrachtrup, J. Highly Sensitive Detection of Physiological Spins in a Microfluidic Device. *Nano Lett.* **2013**, *13*, 4093–4098.
(62) Dolde, F.; Fedder, H.; Doherty, M. W.; Nöbauer, T.; Rempp, F.; Balasubramanian, G.; Wolf, T.; Reinhard, F.; Hollenberg, L. C. L.; Jelezko, F.; *et al.* Electric-Field Sensing Using Single Diamond Spins. *Nat. Phys.* **2011**, *7*, 459–463.
(63) Shao, L.; Zhang, M.; Markham, M.; Edmonds, A. M.; Lončar, M. Diamond Radio Receiver: Nitrogen-Vacancy Centers as Fluorescent Transducers of Microwave Signals. *Phys. Rev. Appl.* **2016**, *6*.

(64) Zhang, B.; Fang, C.-Y.; Chang, C.-C.; Peterson, R.; Maswadi, S.; Glickman, R. D.; Chang, H.-C.; Ye, J. Y. Photoacoustic Emission from Fluorescent Nanodiamonds Enhanced with Gold Nanoparticles. *Biomed. Opt. Express* **2012**, *3*, 1662.
(65) Rogers, L. J.; Doherty, M. W.; Barson, M. S. J.; Onoda, S.; Ohshima, T.; Manson, N. B. Singlet Levels of the NV $^-$ Centre in Diamond. *New J. Phys.* **2015**, *17*, 013048.
(66) Loubser, J. H. N.; Wyk, J. A. van. Electron Spin Resonance in the Study of Diamond. *Rep. Prog. Phys.* **1978**, *41*, 1201–1248.
(67) Manson, N. B.; Harrison, J. P.; Sellars, M. J. Nitrogen-Vacancy Center in Diamond: Model of the Electronic Structure and Associated Dynamics. *Phys. Rev. B* **2006**, *74*.
(68) Balasubramanian, G.; Chan, I. Y.; Kolesov, R.; Al-Hmoud, M.; Tisler, J.; Shin, C.; Kim, C.; Wojcik, A.; Hemmer, P. R.; Krueger, A.; *et al.* Nanoscale Imaging Magnetometry with Diamond Spins under Ambient Conditions. *Nature* **2008**, *455*, 648–651.
(69) Fuchs, G. D.; Dobrovitski, V. V.; Hanson, R.; Batra, A.; Weis, C. D.; Schenkel, T.; Awschalom, D. D. Excited-State Spectroscopy Using Single Spin Manipulation in Diamond. *Phys. Rev. Lett.* **2008**, *101*, 117601.
(70) Tamarat, P.; Gaebel, T.; Rabeau, J. R.; Khan, M.; Greentree, A. D.; Wilson, H.; Hollenberg, L. C. L.; Prawer, S.; Hemmer, P.; Jelezko, F.; *et al.* Stark Shift Control of Single Optical Centers in Diamond. *Phys. Rev. Lett.* **2006**, *97*.
(71) Tamarat, P.; Manson, N. B.; Harrison, J. P.; McMurtrie, R. L.; Nizovtsev, A.; Santori, C.; Beausoleil, R. G.; Neumann, P.; Gaebel, T.; Jelezko, F.; *et al.* Spin-Flip and Spin-Conserving Optical Transitions of the Nitrogen-Vacancy Centre in Diamond. *New J. Phys.* **2008**, *10*, 045004.
(72) Batalov, A.; Zierl, C.; Gaebel, T.; Neumann, P.; Chan, I.-Y.; Balasubramanian, G.; Hemmer, P. R.; Jelezko, F.; Wrachtrup, J. Temporal Coherence of Photons Emitted by Single Nitrogen-Vacancy Defect Centers in Diamond Using Optical Rabi-Oscillations. *Phys. Rev. Lett.* **2008**, *100*.
(73) Jelezko, F.; Gaebel, T.; Popa, I.; Gruber, A.; Wrachtrup, J. Observation of Coherent Oscillations in a Single Electron Spin. *Phys. Rev. Lett.* **2004**, *92*, 076401.
(74) McGuinness, L. P.; Yan, Y.; Stacey, A.; Simpson, D. A.; Hall, L. T.; Maclaurin, D.; Prawer, S.; Mulvaney, P.; Wrachtrup, J.; Caruso, F.; *et al.* Quantum Measurement and Orientation Tracking of Fluorescent Nanodiamonds inside Living Cells. *Nat. Nanotechnol.* **2011**, *6*, 358–363.
(75) Wu, T.-J.; Tzeng, Y.-K.; Chang, W.-W.; Cheng, C.-A.; Kuo, Y.; Chien, C.-H.; Chang, H.-C.; Yu, J. Tracking the Engraftment and Regenerative Capabilities of Transplanted Lung Stem Cells Using Fluorescent Nanodiamonds. *Nat. Nanotechnol.* **2013**, *8*, 682–689.
(76) Weng, M.-F.; Chang, B.-J.; Chiang, S.-Y.; Wang, N.-S.; Niu, H. Cellular Uptake and Phototoxicity of Surface-Modified Fluorescent Nanodiamonds. *Diam. Relat. Mater.* **2012**, *22*, 96–104.

(77) Dantelle, G.; Slablab, A.; Rondin, L.; Lainé, F.; Carrel, F.; Bergonzo, P.; Perruchas, S.; Gacoin, T.; Treussart, F.; Roch, J.-F. Efficient Production of NV Colour Centres in Nanodiamonds Using High-Energy Electron Irradiation. *J. Lumin.* **2010**, *130*, 1655–1658.
(78) Boudou, J.-P.; Curmi, P. A.; Jelezko, F.; Wrachtrup, J.; Aubert, P.; Mohamed Sennour; Balasubramanian, G.; Reuter, R.; Thorel, A.; Gaffet, E. High Yield Fabrication of Fluorescent Nanodiamonds. *Nanotechnology* **2009**, *20*, 235602.
(79) Rabeau, J. R.; Reichart, P.; Tamanyan, G.; Jamieson, D. N.; Prawer, S.; Jelezko, F.; Gaebel, T.; Popa, I.; Domhan, M.; Wrachtrup, J. Implantation of Labelled Single Nitrogen Vacancy Centers in Diamond Using 15N. *Appl. Phys. Lett.* **2006**, *88*, 023113.
(80) Meijer, J.; Burchard, B.; Domhan, M.; Wittmann, C.; Gaebel, T.; Popa, I.; Jelezko, F.; Wrachtrup, J. Generation of Single Color Centers by Focused Nitrogen Implantation. *Appl. Phys. Lett.* **2005**, *87*, 261909.
(81) Loveland, W. D. *Modern Nuclear Chemistry*; Wiley-Interscience: Hoboken, N.J, 2006.
(82) Campbell, B.; Mainwood, A. Radiation Damage of Diamond by Electron and Gamma Irradiation. *Phys. Status Solidi A* **2000**, *181*, 99–107.
(83) Mainwood, A.; Cunningham, J.; Usher, D. Radiation Damage of Silicon and Diamond by High Energy Neutrons, Protons and α Particles. *Mater. Sci. Forum* **1997**, *258–263*, 787–792.
(84) Jagannadham, K.; Verghese, K.; Butler, J. E. Thermal Conductivity Changes upon Neutron Transmutation of 10B Doped Diamond. *J. Appl. Phys.* **2014**, *116*, 083706.
(85) Popovici, G.; Melnikov, A. A.; Varichenko, V. S.; Khasawinah, S.; Sung, T.; Prelas, M. A.; Denisenko, A. B.; Penina, N. M.; Martinovich, V. A.; Drozdova, E. N.; *et al.* Properties of Li Doped Diamond Films, Obtained by Transmutation of 10B into 7Li. *Diam. Relat. Mater.* **1996**, *5*, 761–765.
(86) Jeffrey Coderre. 22.55J Principles of Radiation Interactions. Fall 2004. Massachusetts Institute of Technology: MIT OpenCourseWare, https://ocw.mit.edu. License: Creative Commons BY-NC-SA.
(87) Choppin, G. R.; Choppin, G. R.; Liljenzin, J.-O.; Rydberg, J. *Radiochemistry and Nuclear Chemistry*; 3rd ed.; Butterworth-Heinemann: Woburn, MA, 2002.
(88) Terasawa, T.; Dvorak, T.; Ip, S.; Raman, G.; Lau, J.; Trikalinos, T. A. Systematic Review: Charged-Particle Radiation Therapy for Cancer. *Ann. Intern. Med.* **2009**, *151*, 556–565.
(89) Cepheiden. (File: Tiefendosiskurven.svg) [GFDL], Wikimedia Commons
(90) Wee, T.-L.; Mau, Y.-W.; Fang, C.-Y.; Hsu, H.-L.; Han, C.-C.; Chang, H.-C. Preparation and Characterization of Green Fluorescent Nanodiamonds for Biological Applications. *Diam. Relat. Mater.* **2009**, *18*, 567–573.
(91) Hsiao, W. W.-W.; Hui, Y. Y.; Tsai, P.-C.; Chang, H.-C. Fluorescent Nanodiamond: A Versatile Tool for Long-Term Cell Tracking, Super-Resolution Imaging, and Nanoscale Temperature Sensing. *Acc. Chem. Res.* **2016**, *49*, 400–407.

(92) Clogston, J. D.; Patri, A. K. Zeta Potential Measurement. In *Characterization of Nanoparticles Intended for Drug Delivery*; McNeil, S. E., Ed.; Humana Press: Totowa, NJ, 2011; Vol. 697, pp. 63–70.
(93) Ozawa, M.; Inaguma, M.; Takahashi, M.; Kataoka, F.; Krüger, A.; Ōsawa, E. Preparation and Behavior of Brownish, Clear Nanodiamond Colloids. *Adv. Mater.* **2007**, *19*, 1201–1206.
(94) Yongwei, Z. H.; SHEN, X.; FENG, Z.; XU, X.; WANG, B. On the Zeta-potential of Nanodiamond in Aqueous Systems. *J. Mater. Sci. Technol.* **2004**, *20*, 469.
(95) Xu, X.; Yu, Z.; Zhu, Y.; Wang, B. Effect of Sodium Oleate Adsorption on the Colloidal Stability and Zeta Potential of Detonation Synthesized Diamond Particles in Aqueous Solutions. *Diam. Relat. Mater.* **2005**, *14*, 206–212.
(96) Shenderova, O.; Koscheev, A.; Zaripov, N.; Petrov, I.; Skryabin, Y.; Detkov, P.; Turner, S.; Van Tendeloo, G. Surface Chemistry and Properties of Ozone-Purified Detonation Nanodiamonds. *J. Phys. Chem. C* **2011**, *115*, 9827–9837.
(97) Osswald, S.; Yushin, G.; Mochalin, V.; Kucheyev, S. O.; Gogotsi, Y. Control of sp^2 /sp^3 Carbon Ratio and Surface Chemistry of Nanodiamond Powders by Selective Oxidation in Air. *J. Am. Chem. Soc.* **2006**, *128*, 11635–11642.
(98) Krueger, A.; Lang, D. Functionality Is Key: Recent Progress in the Surface Modification of Nanodiamond. *Adv. Funct. Mater.* **2012**, *22*, 890–906.
(99) Paci, J. T.; Man, H. B.; Saha, B.; Ho, D.; Schatz, G. C. Understanding the Surfaces of Nanodiamonds. *J. Phys. Chem. C* **2013**, *117*, 17256–17267.
(100) Gibson, N.; Shenderova, O.; Luo, T. J. M.; Moseenkov, S.; Bondar, V.; Puzyr, A.; Purtov, K.; Fitzgerald, Z.; Brenner, D. W. Colloidal Stability of Modified Nanodiamond Particles. *Diam. Relat. Mater.* **2009**, *18*, 620–626.
(101) Boehm, H. Surface Oxides on Carbon and Their Analysis: A Critical Assessment. *Carbon* **2002**, *40*, 145–149.
(102) Wolcott, A.; Schiros, T.; Trusheim, M. E.; Chen, E. H.; Nordlund, D.; Diaz, R. E.; Gaathon, O.; Englund, D.; Owen, J. S. Surface Structure of Aerobically Oxidized Diamond Nanocrystals. *J. Phys. Chem. C* **2014**, *118*, 26695–26702.
(103) Li, C.-C.; Huang, C.-L. Preparation of Clear Colloidal Solutions of Detonation Nanodiamond in Organic Solvents. *Colloids Surf. A.* **2010**, *353*, 52–56.
(104) Dahoumane, S. A.; Nguyen, M. N.; Thorel, A.; Boudou, J.-P.; Chehimi, M. M.; Mangeney, C. Protein-Functionalized Hairy Diamond Nanoparticles. *Langmuir* **2009**, *25*, 9633–9638.
(105) Rehor, I.; Slegerova, J.; Kucka, J.; Proks, V.; Petrakova, V.; Adam, M.-P.; Treussart, F.; Turner, S.; Bals, S.; Sacha, P.; *et al.* Fluorescent Nanodiamonds Embedded in Biocompatible Translucent Shells. *Small* **2014**, *10*, 1106–1115.
(106) Rehor, I.; Lee, K. L.; Chen, K.; Hajek, M.; Havlik, J.; Lokajova, J.; Masat, M.; Slegerova, J.; Shukla, S.; Heidari, H.; *et al.* Plasmonic Nanodiamonds:

Targeted Core-Shell Type Nanoparticles for Cancer Cell Thermoablation. *Adv. Healthc. Mater.* **2015**, *4*, 460–468.
(107) Krueger, A. Nanodiamond. In *Carbon Materials and Nanotechnology*; Wiley-VCH Verlag GmbH & Co. KGaA, **2010**; 329–388.
(108) Krueger, A. The Structure and Reactivity of Nanoscale Diamond. *J. Mater. Chem.* **2008**, *18*, 1485–1492.
(109) Cheng, J.; He, J.; Li, C.; Yang, Y. Facile Approach to Functionalize Nanodiamond Particles with V-Shaped Polymer Brushes. *Chem. Mater.* **2008**, *20*, 4224–4230.
(110) Tisler, J.; Balasubramanian, G.; Naydenov, B.; Kolesov, R.; Grotz, B.; Reuter, R.; Boudou, J.-P.; Curmi, P. A.; Sennour, M.; Thorel, A.; *et al.* Fluorescence and Spin Properties of Defects in Single Digit Nanodiamonds. *ACS Nano* **2009**, *3*, 1959–1965.
(111) Rondin, L.; Dantelle, G.; Slablab, A.; Grosshans, F.; Treussart, F.; Bergonzo, P.; Perruchas, S.; Gacoin, T.; Chaigneau, M.; Chang, H.-C.; *et al.* Surface-Induced Charge State Conversion of Nitrogen-Vacancy Defects in Nanodiamonds. *Phys. Rev. B* **2010**, *82*, 115449.
(112) Zheng, W.-W.; Hsieh, Y.-H.; Chiu, Y.-C.; Cai, S.-J.; Cheng, C.-L.; Chen, C. Organic Functionalization of Ultradispersed Nanodiamond: Synthesis and Applications. *J. Mater. Chem.* **2009**, *19*, 8432.
(113) Krüger, A.; Liang, Y.; Jarre, G.; Stegk, J. Surface Functionalisation of Detonation Diamond Suitable for Biological Applications. *J. Mater. Chem.* **2006**, *16*, 2322–2328.
(114) Martín, R.; Heydorn, P. C.; Alvaro, M.; Garcia, H. General Strategy for High-Density Covalent Functionalization of Diamond Nanoparticles Using Fenton Chemistry. *Chem. Mater.* **2009**, *21*, 4505–4514.
(115) Ida, S.; Tsubota, T.; Hirabayashi, O.; Nagata, M.; Matsumoto, Y.; Fujishima, A. Chemical Reaction of Hydrogenated Diamond Surface with Peroxide Radical Initiators. *Diam. Relat. Mater.* **2003**, *12*, 601–605.
(116) Arnault, J.-C.; Petit, T.; Girard, H.; Chavanne, A.; Gesset, C.; Sennour, M.; Chaigneau, M. Surface Chemical Modifications and Surface Reactivity of Nanodiamonds Hydrogenated by CVD Plasma. *Phys. Chem. Chem. Phys.* **2011**, *13*, 11481–11487.
(117) Widmann, C. J.; Giese, C.; Wolfer, M.; Kono, S.; Nebel, C. E. F- and Cl-Terminations of (100)-Oriented Single Crystalline Diamond. *Phys. Status Solidi A* **2014**, *211*, 2328–2332.
(118) Liu, Y.; Gu, Z.; Margrave, J. L.; Khabashesku, V. N. Functionalization of Nanoscale Diamond Powder: Fluoro-, Alkyl-, Amino-, and Amino Acid-Nanodiamond Derivatives. *Chem. Mater.* **2004**, *16*, 3924–3930.
(119) Huang, H.; Wang, Y. H.; Zang, J. B.; Bian, L. Y. Improvement of Suspension Stability and Electrophoresis of Nanodiamond Powder by Fluorination. *Appl. Surf. Sci.* **2012**, *258*, 4079–4084.
(120) Freedman, A.; Stinespring, C. D. Fluorination of Diamond (100) by Atomic and Molecular Beams. *Appl. Phys. Lett.* **1990**, *57*, 1194.
(121) Kealey, C. P.; Klapötke, T. M.; McComb, D. W.; Robertson, M. I.; Winfield, J. M. Fluorination of Polycrystalline Diamond Films and Powders. An

Investigation Using FTIR Spectroscopy, SEM, Energy-Filtered TEM, XPS and Fluorine-18 Radiotracer Methods. *J. Mater. Chem.* **2001**, *11*, 879–886.
(122) Cui, S.; Hu, E. L. Increased Negatively Charged Nitrogen-Vacancy Centers in Fluorinated Diamond. *Appl. Phys. Lett.* **2013**, *103*, 051603.
(123) Shanley, T. W.; Martin, A. A.; Aharonovich, I.; Toth, M. Localized Chemical Switching of the Charge State of Nitrogen-Vacancy Luminescence Centers in Diamond. *Appl. Phys. Lett.* **2014**, *105*, 063103.
(124) Freedman, A. Halogenation of Diamond (100) and (111) Surfaces by Atomic Beams. *J. Appl. Phys.* **1994**, *75*, 3112.
(125) Steenackers, M.; Lud, S. Q.; Niedermeier, M.; Bruno, P.; Gruen, D. M.; Feulner, P.; Stutzmann, M.; Garrido, J. A.; Jordan, R. Structured Polymer Grafts on Diamond. *J. Am. Chem. Soc.* **2007**, *129*, 15655–15661.
(126) Mochalin, V. N.; Neitzel, I.; Etzold, B. J. M.; Peterson, A.; Palmese, G.; Gogotsi, Y. Covalent Incorporation of Aminated Nanodiamond into an Epoxy Polymer Network. *ACS Nano* **2011**, *5*, 7494–7502.
(127) Man, H. B.; Lam, R.; Chen, M.; Osawa, E.; Ho, D. Nanodiamond-Therapeutic Complexes Embedded within Poly(ethylene Glycol) Diacrylate Hydrogels Mediating Sequential Drug Elution. *Phys. Status Solidi A* **2012**, *209*, 1811–1818.
(128) Haartman, E. von; Jiang, H.; Khomich, A. A.; Zhang, J.; Burikov, S. A.; Dolenko, T. A.; Ruokolainen, J.; Gu, H.; Shenderova, O. A.; Vlasov, I. I.; *et al.* Core–shell Designs of Photoluminescent Nanodiamonds with Porous Silica Coatings for Bioimaging and Drug Delivery I: Fabrication. *J. Mater. Chem. B* **2013**, *1*, 2358–2366.
(129) Prabhakar, N.; Näreoja, T.; Haartman, E. von; Karaman, D. Ş.; Jiang, H.; Koho, S.; Dolenko, T. A.; Hänninen, P. E.; Vlasov, D. I.; Ralchenko, V. G.; *et al.* Core–shell Designs of Photoluminescent Nanodiamonds with Porous Silica Coatings for Bioimaging and Drug Delivery II: Application. *Nanoscale* **2013**, *5*, 3713–3722.
(130) Vial, S.; Mansuy, C.; Sagan, S.; Irinopoulou, T.; Burlina, F.; Boudou, J.-P.; Chassaing, G.; Lavielle, S. Peptide-Grafted Nanodiamonds: Preparation, Cytotoxicity and Uptake in Cells. *ChemBioChem* **2008**, *9*, 2113–2119.
(131) Nicolau, E.; Méndez, J.; Fonseca, J. J.; Griebenow, K.; Cabrera, C. R. Bioelectrochemistry of Non-Covalent Immobilized Alcohol Dehydrogenase on Oxidized Diamond Nanoparticles. *Bioelectrochemistry* **2012**, *85*, 1–6.
(132) Stursa, J.; Havlik, J.; Petrakova, V.; Gulka, M.; Ralis, J.; Zach, V.; Pulec, Z.; Stepan, V.; Zargaleh, S. A.; Ledvina, M.; *et al.* Mass Production of Fluorescent Nanodiamonds with a Narrow Emission Intensity Distribution. *Carbon* **2016**, *96*, 812–818.
(133) Ferrari, A. C. Raman Spectroscopy of Graphene and Graphite: Disorder, Electron–phonon Coupling, Doping and Nonadiabatic Effects. *Solid State Commun.* **2007**, *143*, 47–57.
(134) Havlik, J.; Petrakova, V.; Rehor, I.; Petrak, V.; Gulka, M.; Stursa, J.; Kucka, J.; Ralis, J.; Rendler, T.; Lee, S.-Y.; *et al.* Boosting Nanodiamond

Fluorescence: Towards Development of Brighter Probes. *Nanoscale* **2013**, *5*, 3208–3211.
(135) Havlik, J.; Raabova, H.; Gulka, M.; Petrakova, V.; Krecmarova, M.; Masek, V.; Lousa, P.; Stursa, J.; Boyen, H.-G.; Nesladek, M.; *et al.* Benchtop Fluorination of Fluorescent Nanodiamonds on a Preparative Scale: Toward Unusually Hydrophilic Bright Particles. *Adv. Funct. Mater.* **2016**, 26, 4134–4142.
(136) Ornitz, D. M.; Itoh, N. Fibroblast Growth Factors. *Genome Biol.* **2001**, *2*, Reviews3005.

8. List of publications

The contents of this thesis are based on the following publications:

A. **Havlik, J.**; Petrakova, V.; Rehor, I.; Petrak, V.; Gulka, M.; Stursa, J.; Kucka, J.; Ralis, J.; Rendler, T.; Lee, S.-Y.; Reuter, R.; Wrachtrup, J.; Ledvina, M.; Nesladek, M.; Cigler, P.; Boosting Nanodiamond Fluorescence: Towards Development of Brighter Probes. *Nanoscale* **2013**, *5*, 3208–3211. IF = 7.4

B. Rehor, I.; Lee, K. L.; Chen, K.; Hajek, M.; **Havlik, J.**; Lokajova, J.; Masat, M.; Slegerova, J.; Shukla, S.; Heidari, H.; Bals, S.; Steinmetz, N. F.; Cigler, P.; Plasmonic Nanodiamonds: Targeted Core-Shell Type Nanoparticles for Cancer Cell Thermoablation. *Adv. Healthcare Mater.* **2015**, *4*, 460–468. IF = 5.1

C. Stursa, J.; **Havlik, J.**; Petrakova, V.; Gulka, M.; Ralis, J.; Zach, V.; Pulec, Z.; Stepan, V.; Zargaleh, S. A.; Ledvina, M.; Nesladek, M.; Treussart, F.; Cigler, P.Mass Production of Fluorescent Nanodiamonds with a Narrow Emission Intensity Distribution. *Carbon* **2016**, *96*, 812–818. IF = 6.3

D. **Havlik, J.**; Raabova, H.; Gulka, M.; Petrakova, V.; Krecmarova, M.; Masek, V.; Lousa, P.; Stursa, J.; Boyen, H.-G.; Nesladek, M.; Cigler, P.; Benchtop Fluorination of Fluorescent Nanodiamonds on a Preparative Scale: Toward Unusually Hydrophilic Bright Particles. *Adv. Funct. Mater.* **2016**, 26, 4134–4142. IF = 12.1

E. **Havlik, J.**; Kucka, J.; Raabova, H.; Petrakova, V.; Stepan, V.; Zlamalova Cilova, Z.; Kucera, J.; Hruby, M.; Cigler, P.; Extremely rapid irradiation of nanoparticles with ions generated in situ by a nuclear reaction **manuscript submitted**

F. Balek, L.; Buchtova, M.; Foldynova-Trantirkova, S.; **Havlik J.**; Varecha, M.; Turner, S.; Vesela, I.; Klimaschewski, L.; Claus, P.; Trantirek, L.; Cigler, P.; Krejci, P.; Nanodiamonds as artificial proteins: regulation of a cell signalling system using picomolar solutions of inorganic nanocrystals
manuscript submitted

G. Rehor, I.; Raabova, H.; **Havlik, J.**; Fiserova, A.; Richter, J.; Turner, S.; Van Tendeloo, G.; Stursa, J.; Petrakova, V.; Dai, L.; Cigler, P.; Rounded monodisperse nanodiamonds: properties and mass production
manuscript in preparation

9. Other related publications

H. Slegerova J., Rehor I., **Havlik J.**, Raabova H., Muchova E., Cigler P. Nanodiamonds as Intracellular Probes for Imaging in Biology and Medicine.; *Intracellular Delivery II. Fundamental Biomedical Technologies*, Prokop, A., Iwasaki, Y., Harada, A. (Eds.), 2014, Vol. 7, Dordrecht: Springer Netherlands; 363-401.

I. Rehor, I., Slegerova, J., **Havlik, J.**, Raabova, H., Hyvl, J., Muchova, E., Cigler, P. Nanodiamonds: Behavior in Biological Systems and Emerging Bio-applications; *Carbon Nanomaterials for Biomedical Applications*, Zhang, M., Naik, R. R., Dai, L. (Eds.), Springer International Publishing, 2016, 319–361.

J. Neburkova, J., Vavra, J., Raabova, H., Pramanik G., **Havlik, J.**, Cigler, P. Nanodiamonds embedded in shells; *Nanodiamonds. Advanced Material Analysis, Properties and Applications*, Arnault, J.-C. (Ed.), Elsevier, 2017, 339–363.

10. The author's contributions to the publications

A. Jan Havlík manufactured the samples and performed the annealing and oxidation experiments. He also contributed to the design of experiments, interpretation of results and manuscript preparation.

B. Jan Havlík contributed to *in vitro* cell studies, colloidal stability experiments, flow cytometry measurements, confocal microscopy measurements, interpretation of results and manuscript preparation.

C. Jan Havlík manufactured the samples. He performed irradiation pretreatment, annealing and oxidation procedure. He wrote the manuscript in cooperation with Petr Cigler. He also contributed to the design of simulations and data interpretation.

D. Jan Havlík manufactured the samples, developed fluorination procedure and analysis, carried out colloidal characterization, performed the analytical calculations and wrote the manuscript in cooperation with Petr Cigler. He also contributed to particle distribution analysis.

E. Jan Havlík manufactured the majority of the samples, carried out pretreatment, washing, annealing and oxidation of NDs and wrote the manuscript in cooperation with Petr Cigler. He also contributed to SEM measurement and to the design of computer simulations.

F. Jan Havlík manufactured the DNDs samples, separated different size fractions by ultracentrifugation and carried out the colloidal characterization of samples. He also contributed to the design of *in vitro* experiments.

G. Jan Havlík carried out the centrifugal fractionation of NDs. He also contributed to the calculations of particle size distributions.

.....

Mgr. Petr Cígler, Ph.D.

Corresponding author

11. Appendices

Appendix A

Havlik, J.; Petrakova, V.; Rehor, I.; Petrak, V.; Gulka, M.; Stursa, J.; Kucka, J.; Ralis, J.; Rendler, T.; Lee, S.-Y.; Reuter, R.; Wrachtrup, J.; Ledvina, M.; Nesladek, M.; Cigler, P.; Boosting Nanodiamond Fluorescence: Towards Development of Brighter Probes. *Nanoscale* **2013**, *5*, 3208–3211.

Appendix A

Nanoscale

RSC Publishing

COMMUNICATION

View Article Online
View Journal | View Issue

Boosting nanodiamond fluorescence: towards development of brighter probes†

Cite this: *Nanoscale*, 2013, **5**, 3208

Received 16th September 2012
Accepted 9th December 2012

DOI: 10.1039/c2nr32778c

www.rsc.org/nanoscale

Jan Havlik,‡[ab] Vladimira Petrakova,‡[cd] Ivan Rehor,[a] Vaclav Petrak,[cd] Michal Gulka,[cd] Jan Stursa,[e] Jan Kucka,[e] Jan Ralis,[e] Torsten Rendler,[f] San-Yung Lee,[f] Rolf Reuter,[f] Joerg Wrachtrup,[f] Miroslav Ledvina,[a] Milos Nesladek[g] and Petr Cigler*[a]

A novel approach for preparation of ultra-bright fluorescent nanodiamonds (fNDs) was developed and the thermal and kinetic optimum of NV center formation was identified. Combined with a new oxidation method, this approach enabled preparation of particles that were roughly one order of magnitude brighter than particles prepared with commonly used procedures.

Diamond nanoparticles have recently been introduced as promising luminescent probes for various applications.[1–4] They possess exceptional biocompatibility, making them suitable for bioimaging.[5] Photoluminescence (PL) in nanodiamonds can be engineered by enrichment with nitrogen-vacancy (NV) color centers, which are localized defects of a diamond crystalline lattice. An NV center consists of a nearest-neighbor pair of a substitutional N atom and a lattice vacancy. It exists in two-charge states, neutral (NV^0) and negative (NV^-), with ZPL (zero phonon line) emissions of 575 nm and 637 nm, respectively.[6–8] The NV center is extremely photostable, showing no photobleaching or blinking unless incorporated into small diameter (<5 nm) nanocrystals. Its properties have enabled a variety of new experimental methods, ranging from quantum photonics[9] to single particle tracking in cells.[10]

For biological applications,[5,11] very bright fluorescent nanodiamonds (fNDs) are critically needed for fND probes to compete with the more commonly used quantum dots (QDs). PL brightness of fNDs, in contrast to that of QDs, can be scaled up linearly by increasing the NV concentration, which is an important advantage. At the same time, the NV charge state and fND size distribution have to be precisely controlled.

Although formation of NV centers has been investigated in single crystal diamonds,[12–16] to our knowledge, no systematic study has been performed on fNDs. We focused on systematic optimizing fluorescence of the fNDs in order to boost the particle brightness in a controlled manner. This is the first time the formation efficiency of NV centers in fNDs has been tuned and increased by about one order of magnitude, providing highly bright particles.

The most favorable method for preparation of fNDs is irradiation of a type Ib high pressure high temperature (HPHT) diamond with high-energy particles (p^+, He^+, or e^-)[10,17] followed by thermal annealing. The advantage of Ib diamonds is their natural content of isolated substitutional N. The subsequent irradiation generates lattice vacancies that are further recombined by annealing with N to produce NV centers (see Fig. 1). By irradiation of Ib diamonds, two types of vacancies are formed: negatively charged (ND1) and neutral vacancies (GR1). The number of ND1 vacancies created greatly exceeds the number of GR1 vacancies, because substitutional nitrogen acts as an electron donor to the vacancy.[18] At temperatures above 600 °C, single nitrogen remains still immobile, however, the vacancies in diamond lattices become mobile and can be trapped by the nitrogen, creating thermally stable NV centers. On the other hand, when a mobile vacancy reaches the surface, the formation of an NV center is entirely suppressed. The activation energy of vacancy migration in natural type I diamonds is 2.30 to 2.45 eV. In the nitrogen rich diamonds the migration of the vacancies is in general slower, because ND1 needs to be first converted to GR1 to become mobile. As a result, longer annealing times are required to form the maximum number of NV centers.[15,19]

[a]*Institute of Organic Chemistry and Biochemistry AS CR, v.v.i., Flemingovo nam. 2, 166 10, Prague 6, Czech Republic. E-mail: cigler@uochb.cas.cz*

[b]*Faculty of Science, Charles University, Hlavova 2030, 128 40, Prague 2, Czech Republic*

[c]*Faculty of Biomedical Engineering, Czech Technical University in Prague, Sitna sq. 3105, 272 01, Kladno, Czech Republic*

[d]*Institute of Physics, Academy of Sciences of the Czech Republic, v.v.i., Prague 8, Czech Republic*

[e]*Nuclear Physics Institute AS CR, v.v.i., 250 68, Rez near Prague, Czech Republic*

[f]*3. Physikalisches Institut and Research Center SCOPE, University of Stuttgart, Pfaffenwaldring 57, 70569, Stuttgart, Germany*

[g]*IMOMEC division, IMEC, Institute for Materials Research, University Hasselt, Wetenschapspark 1, B-3590, Diepenbeek, Belgium*

† Electronic supplementary information (ESI) available: Experimental details and further characterization of materials. See DOI: 10.1039/c2nr32778c

‡ These authors contributed equally.

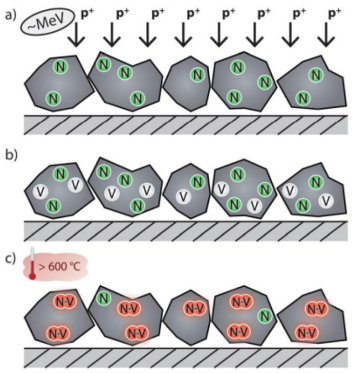

Fig. 1 Preparation of fNDs from type Ib NDs. (a) Irradiation by high-energy protons, (b) vacancies created by irradiation, and (c) formation of NV centers by thermal annealing. N – nitrogen atom, V – vacancy (either GR1 or ND1), N-V – nitrogen vacancy center.

Notably, NV centers in fNDs are, thanks to their high surface–volume ratio, much more sensitive to the surface chemistry than NV centers in single crystal diamonds.[6] Oxidation of particles causes an increase in NV^- PL,[6,20–23] while the presence of a disordered carbon and graphitic shell in fNDs quenches PL.[21] The subtle balance between the content of oxidized and sp^2 carbons can strongly influence particle brightness.

Commonly used annealing parameters for NDs are in the range of 700–800 °C for 1–2 hours.[10,24] In order to explore the annealing conditions of proton-irradiated NDs in detail, we extended the range to higher values (700–950 °C, 0.5–8 h) to perform 2D parameter mapping. As calculated by SRIM (Stopping and Range of Ions in Matter),[25] the maximal vacancy concentration of the atomic displacements created by irradiation was 10^{19} cm^{-3} (which corresponds to 100 ppm). Two sizes of type Ib NDs were used (45 and 140 nm in diameter). All samples were annealed in an argon atmosphere at normal pressure and subsequently oxidized in a mixture of H_2SO_4 and HNO_3 to remove sp^2 carbons.[26] PL normalized to the diamond Raman line at 1332 cm^{-1} was used for determination of relative NV^0 and NV^- center yields,[13] as well as for monitoring the amorphization of the particles (Fig. S3†).[14] To estimate the total number of NV centers in the particles, PL was compared to a reference sample with a known number of NV centers. This number was counted from single particle measurements using anti-bunching time-correlation spectroscopy[27] (see Fig. S4 and S5 in the ESI†).

After irradiation, the samples showed characteristic emission (ZPL around 741 nm) originating from GR1 centers (Fig. S1 in the ESI†) that diminish during annealing.[13] The PL behavior of 45 and 140 nm particles then clearly differed: the NV PL of smaller particles was approximately 10-fold lower. A longer annealing time and higher temperature led to a higher creation efficiency of NV centers in 140 nm fNDs (Fig. 2). In contrast, either annealing longer than 1–2 hours or increasing temperature did not lead to a further increase in the PL of 45 nm fNDs. For both particles, however, we observed an unexpected discrete maximum at 900 °C (see below). If we consider annealing times, the 140 nm particles behave similarly to single crystal diamonds, in which the loss in GR1 and ND1 absorption and increase in NV absorption can be monitored even after 20 hours of annealing.[15] The decrease in the intensity of NV PL after annealing above 900 °C can be explained by the formation of an NVN (H3) center. Its characteristic emission (503 nm) was observed in a small fraction (<15%) of fNDs annealed at temperatures 900 °C and higher, which is in agreement with studies performed on single crystal diamonds.[13]

We suppose that the increase in NV PL intensity for longer annealing times for 140 nm NDs is related to the diffusion and charge state of the vacancies. Our assumption is based on the fact that in Ib diamonds with high concentrations of nitrogen, mainly ND1 centers are formed, but the capture of vacancies only occurs through the motion of GR1 vacancies. During annealing, the ND1 needs to be first converted to GR1, which is then mobile.[15] Longer annealing times are thus more suitable for NV center formation in Ib diamonds. In the case of 45 nm NDs, the reason for the decrease in the NV PL intensity for longer annealing times and higher temperatures could be explained by the diffusion of the vacancies to the surface, which is reasonably higher for smaller NDs.

The most striking, as well as practically applicable, result of the study is the identification of a discrete maximum of NV PL in samples annealed at 900 °C for 1 hour. This result shows unprecedented conditions enabling generation of up to 3-fold brighter particles (compared with particles annealed in the commonly used range of 700–800 °C for 1–2 hours) by a subtle change in annealing temperature and time. The concentration of NVs per fND particle was calculated based on anti-bunching measurements. On average, ~1.7 NVs were produced in 45 nm particles (averaged NV distribution from 25 particles), while about 360 NV centers were present in 140 nm particles. To confirm the repeatability of this result and to rule out experimental error, the NV PL was measured on 20 additional samples (five replicates prepared at either 900 °C or 700 °C for 1 hour, for both 140 and 45 nm NDs), and similar results were obtained (see Table S1 in the ESI†). One could speculate that the notably lower sp^2 content observed in samples annealed at 900 °C for 1 hour (Fig. S2 in the ESI†) plays a role in this high PL intensity by decreasing the nonradiative quenching of PL and increasing the number of active NV centers. The evolution of sp^2 structures upon thermal annealing depends critically on the damage density created during irradiation. On the other hand, when the damage density is below the critical threshold, thermal annealing has the effect of converting the sp^2 structure back to the crystalline diamond phase with the residual point defect formed in the crystal.[28,29]

In order to further increase the particle brightness, we also studied the influence of different oxidation treatments (air, oxygen plasma, and melted potassium nitrate) on the samples with the highest PL. The PL of air-oxidized fNDs at 510 °C increases with time of exposure (Fig. 3). This dependence corresponds with previous findings[6,8,20–22] showing the rise of NV PL with higher degrees of surface oxidation. The treatment

Appendix A

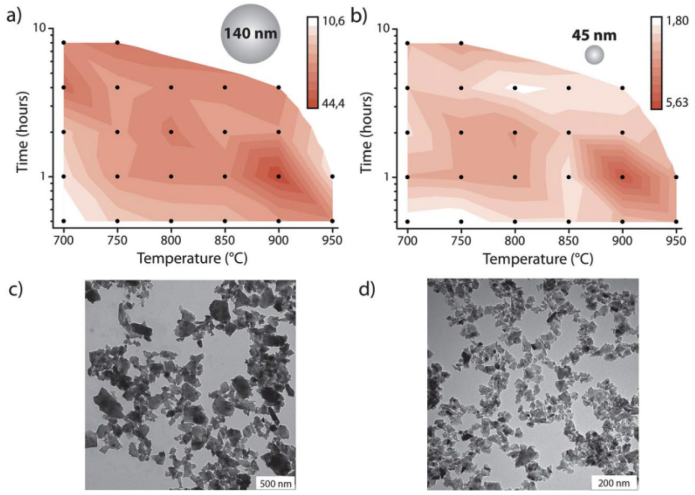

Fig. 2 Normalized total PL intensity of NV centers ($NV^- + NV^0$) from (a) 140 nm and (b) 45 nm ND particles as a function of annealing time and temperature. Black dots represent the individual points of the matrix of annealing conditions. Darker color represents brighter samples. Transmission electron microscopy (TEM) images of (c) 45 nm and (d) 140 nm particles before irradiation.

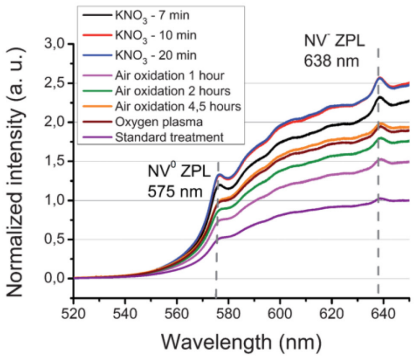

Fig. 3 Normalized relative PL spectra of fNDs oxidized under various conditions.

with oxygen plasma pronounced PL comparable to that obtained with the longest exposure to air. For deeper surface oxidation, we heated fNDs in melted KNO_3 (560 °C). We observed a substantial increase in fluorescence for samples treated for as little as 10 min. Compared with the standard treatment (heating in a mixture of H_2SO_4 and HNO_3 for 3 days),[30] this rapid procedure produced more than 2.5-fold brighter particles with excellent colloidal stability in aqueous solution (see Fig. S6 in the ESI†).

Conclusions

In summary, we have developed a novel approach for preparation of highly bright fND particles. This is the first time the thermal and kinetic optimum of NV center formation in fNDs was identified. Combined with a new oxidation method in melted potassium nitrate, this approach enabled preparation of particles that were roughly one order of magnitude brighter than particles prepared with commonly used procedures. The results presented here are significant from several additional perspectives: (1) the sharp maximum of NV center formation was identical for both 45 and 140 nm particles and can likely be applied to other particle sizes; (2) the overall procedure is rapid and can be performed without special laboratory equipment; (3) the particles show excellent colloidal stability in aqueous solutions. Advanced applications of highly bright fNDs as tools for bio-labeling and biosensing are a subject of ongoing research.

Acknowledgements

This work was supported by GACR project P108/12/0640 (to P.C. and J.S.), MSMT CR grant no. LH11027 (to P.C.), OP VK grant CZ.1.07/2.3.00/20.0306, AS CR grant KAN200100801, European R&D projects (FP7 ITN Grant nos 245122 DINAMO and COST LD11078), and CTU grant no. CTU 10/811700 (to V.P. and M.N.).

Notes and references

1 S. Pezzagna, B. Naydenov, F. Jelezko, J. Wrachtrup and J. Meijer, *New J. Phys.*, 2010, **12**, 065017.
2 V. N. Mochalin, O. Shenderova, D. Ho and Y. Gogotsi, *Nat. Nanotechnol.*, 2012, **7**, 11–23.
3 Y. Xing and L. Dai, *Nanomedicine*, 2009, **4**, 207–218.
4 A. Krueger and D. Lang, *Adv. Funct. Mater.*, 2012, **22**, 890–906.
5 A. M. Schrand, H. Huang, C. Carlson, J. J. Schlager, E. Omacr Sawa, S. M. Hussain and L. Dai, *J. Phys. Chem. B*, 2007, **111**, 2–7.

6 V. Petráková, A. Taylor, I. Kratochvílová, F. Fendrych, J. Vacík, J. Kučka, J. Šturs a, P. Cígler, M. Ledvina, A. Fišerová, P. Kneppo and M. Nesládek, *Adv. Funct. Mater.*, 2012, **22**, 812–819.
7 K. Iakoubovskii, G. J. Adriaenssens and M. Nesladek, *J. Phys.: Condens. Matter*, 2000, **12**, 189–199.
8 M. Hauf, B. Grotz, B. Naydenov, M. Dankerl, S. Pezzagna, J. Meijer, F. Jelezko, J. Wrachtrup, M. Stutzmann, F. Reinhard and J. Garrido, *Phys. Rev. B: Condens. Matter Mater. Phys.*, 2011, **83**, 081304.
9 I. Aharonovich, A. D. Greentree and S. Prawer, *Nat. Photonics*, 2011, **5**, 397–405.
10 Y.-R. Chang, H. Lee, K. Chen, C.-C. Chang, D. Tsai, C. Fu, T. Lim, Y. Tzeng, C. Fang, C. Han, H. Chang and W. Fann, *Nat. Nanotechnol.*, 2008, **3**, 284–288.
11 K.-K. Liu, C.-L. Cheng, C.-C. Chang and J.-I. Chao, *Nanotechnology*, 2007, **18**, 325102.
12 J. Botsoa, T. Sauvage, M.-P. Adam, P. Desgardin, E. Leoni, B. Courtois, F. Treussart and M.-F. Barthe, *Phys. Rev. B: Condens. Matter Mater. Phys.*, 2011, **84**, 1–5.
13 A. T. A. Collins, *New Diamond Front. Carbon Technol.*, 2007, **17**, 47–61.
14 W. Fortunato, A. J. Chiquito, J. C. Galzerani and J. R. Moro, *J. Mater. Sci.*, 2007, **42**, 7331–7336.
15 G. Davies and A. T. Collins, *Diamond Relat. Mater.*, 1993, **2**, 80–86.
16 T. Sharda, A. Sikder, D. Misra, A. Collins, S. Bhargava, H. D. Bist, P. Veluchamy, H. Minoura, D. Kabiraj, D. K. Awasthi and P. Selvam, *Diamond Relat. Mater.*, 1998, **7**, 250–254.
17 G. Dantelle, A. Slablab, L. Rondin, F. Lainé, F. Carrel, P. Bergonzo, S. Perruchas, T. Gacoin, F. Treussart and J.-F. Roch, *J. Lumin.*, 2010, **130**, 1655–1658.
18 S. C. Lawson, D. Fisher, D. C. Hunt and M. E. Newton, *J. Phys.: Condens. Matter*, 1998, **10**, 6171–6180.
19 G. Davies, S. Lawson, A. Collins, A. Mainwood and S. Sharp, *Phys. Rev. B: Condens. Matter Mater. Phys.*, 1992, **46**, 13157–13170.
20 K.-M. C. Fu, C. Santori, P. E. Barclay and R. G. Beausoleil, *Appl. Phys. Lett.*, 2010, **96**, 121907.
21 B. R. Smith, D. Gruber and T. Plakhotnik, *Diamond Relat. Mater.*, 2010, **19**, 314–318.
22 L. Rondin, G. Dantelle, A. Slablab, F. Grosshans, F. Treussart, P. Bergonzo, S. Perruchas, T. Gacoin, M. Chaigneau, H.-C. Chang, V. Jacques and J.-F. Roch, *Phys. Rev. B: Condens. Matter Mater. Phys.*, 2010, **82**, 1–5.
23 N. Mohan, Y.-K. Tzeng, L. Yang, Y.-Y. Chen, Y. Y. Hui, C.-Y. Fang and H.-C. Chang, *Adv. Mater.*, 2010, **22**, 843–847.
24 C.-C. Fu, H.-Y. Lee, K. Chen, T.-S. Lim, H.-Y. Wu, P.-K. Lin, P.-K. Wei, P.-H. Tsao, H.-C. Chang and W. Fann, *Proc. Natl. Acad. Sci. U. S. A.*, 2007, **104**, 727–732.
25 J. Zeigler, "SRIM-2008," can be found under http://srim.org.
26 S. Osswald, G. Yushin, V. Mochalin, S. O. Kucheyev and Y. Gogotsi, *J. Am. Chem. Soc.*, 2006, **128**, 11635–11642.
27 F. Jelezko, C. Tietz, A. Gruber, I. Popa, A. Nizovtsev, S. Kilin and J. Wrachtrup, *Single Mol.*, 2001, **2**, 255–260.
28 F. C. Waldermann, P. Olivero, J. Nunn, K. Surmacz, Z. Y. Wang, D. Jaksch, R. a. Taylor, I. a. Walmsley, M. Draganski, P. Reichart, A. D. Greentree, D. N. Jamieson and S. Prawer, *Diamond Relat. Mater.*, 2007, **16**, 1887–1895.
29 L. Allers, A. T. Collins and J. Hiscock, *Diamond Relat. Mater.*, 1998, **7**, 228–232.
30 L. C. L. Huang and H.-C. Chang, *Langmuir*, 2004, **20**, 5879–5884.

Electronic Supplementary Material (ESI) for Nanoscale

Electronic Supplementary Information

Boosting Nanodiamond Fluorescence: Towards Development of Brighter Probes

By *Jan Havlik*[†], *Vladimira Petrakova*[†], *Ivan Rehor, Vaclav Petrak, Michal Gulka, Jan Stursa, Jan Kucka, Jan Ralis, Torsten Rendler, San-Yung Lee, Rolf Reuter, Joerg Wrachtrup, Miroslav Ledvina, Milos Nesladek*, and *Petr Cigler**

[†] These authors contributed equally.

Experimental Section

Chemicals
Sodium hydroxide, nitric acid (65%), and sulfuric acid (96%) were purchased from Penta (Czech Republic). Potassium nitrate was purchased from Sigma-Aldrich (Prague, Czech Republic). All chemicals were *p.a.* quality and were used as received without further purification. Deionized water was prepared with a Millipore Synergy UV Ultrapure water system.
Two types of nanodiamonds were supplied by Microdiamant (Switzerland) (MSY 0-0.05 and MSY 0-0.25). The particles were oxidized by air in a Thermolyne 21100 tube furnace at 510 °C for 5 hours. The nanodiamonds were subsequently treated with a mixture of HNO_3 and H_2SO_4 (85 °C, 3 days).[1]

Irradiation and annealing
Purified nanodiamond powder (160 mg), containing approximately 100 ppm of natural nitrogen impurities, was pressed in an aluminum target holder and irradiated with a 15.5 MeV proton beam extracted from the isochronous cyclotron U-120M for 70 min (fluence 6 x 10^{16} cm^{-2}). The irradiated material was annealed at various conditions (for the individual annealing points of the 2D matrix, see Fig. S3). The annealing was performed at normal pressure under an argon atmosphere.

Oxidation of samples
All samples evaluated for the influence of annealing conditions on luminescence intensity were treated with a mixture of HNO_3 and H_2SO_4 (85 °C, 3 days) („standard treatment“).[1] The sample annealed at 900 °C for 1 hour was selected for further studies, including oxidative treatment by air, oxygen plasma, and heating in melted potassium nitrate. The air oxidation was performed at 510 °C for 1, 2, or 4.5 hours at normal pressure in a Thermolyne 21100 tube furnace calibrated with an external thermocouple (Testo AG 1009). The oxygen plasma treatment was performed for 2 min at 500 °C in an ASTeX AX 5010 series Microwave Plasma Enhanced Chemical Vapor Deposition (MPECVD) reactor. For oxidation in potassium nitrate, 2 mg of ND sample and 1 g of KNO_3 were powdered in an agate mortar. The homogeneous mixture was placed in a quartz boat and placed in a Thermolyne 21100 tube furnace pre-heated to 560 °C for 7, 10, or 20 min. The sample was then cooled down, dissolved in water, and centrifuged. The pellet was resuspended in 3 mL of water, sonicated for 10 seconds in an ultrasonic bath, and centrifuged again. This washing step was repeated five times to remove all salt residue.

Raman and photoluminescence measurements
Although absorption spectroscopy can be used to directly determine the concentrations of defect centers in natural and synthetic single crystal diamonds,[2] its use is rather limited in the

Electronic Supplementary Material (ESI) for Nanoscale

case of nanodiamond particles (due to high reflection, extreme scattering, and low signal intensity). Instead, we focused on evaluation of NV center formation resulting from annealing using Raman and photoluminescence spectroscopy.[3,4] If combined with anti-bunching time-correlation spectroscopy,[5] it does allow us to assess the number of defect centers, *i.e.* quantitative comparison of optically active NV center formation and the related brightness of particles. The photoluminescence normalized to the diamond Raman signal at 1332 cm^{-1} and compared to a reference sample with known number of NV centers enabled the determination of NV^0 and NV^- center yields. The normalization to the diamond Raman signal served also for the monitoring of particle amorphization (changes in sp^3 carbon content).[6]
It should be noted that effects other than the number of NV centers created can be involved in the total luminescent yield, for example, the quenching effect of the surface leading to the "dark state" of NV centers,[7,8] which is of importance especially for small particles.
Before measurement, all samples were lyophilized from water and diluted in DI water to the concentration of 10mg/ml by high-power ultrasonic horn (Hielscher UP400S, Sonotrode H3) using 400 W at a 1:1 (on/off) cycle for 30 minutes under liquid cooling. The samples we prepared by drop-casting of the aqueous dispersion of NDs on the polished silicon waffer. Raman and luminescence spectra were measured using a Renishaw InVia Raman Microscope; the excitation wavelength was 514 nm (luminescence measurements) and 325 nm (Raman measurements)[6] with 15 mW laser power, x20 objective, the exposure time was 10 seconds, acculumation 10x. 20 measurements were made on each sample. The Raman and luminescence spectra were taken at room temperature and, to make the luminescence quantitatively comparable, spectra were normalized to the diamond Raman peak. The standard deviance of the normalized luminescence spectra did not exceed 15%. The average of measurements performed on each sample was used for further calculations and comparisons. For results, see Figs. 2, S2, and S3. The NVN centers were examined with the Renishaw InVia Raman Microscope set at an excitation wavelength of 488 nm in combination with an AFM NTEGRA Prima NT MDT system equipped with a soft HA_NC etalon tip. The anti-bunching time-correlation spectroscopy was performed using setup described in reference[5].

Table S1 Results of repeated annealing experiments performed with 45 and 140 nm particles. The samples were annealed for 1 hour. The standard error (Std. error) was calculated from 5 sample replicates.

Nanodiamond size	Temperature	Average relative fluorescence intensity	Std. error
45 nm	700 °C	0.78	0.093
45 nm	900 °C	1.81	0.133
140 nm	700 °C	5.1	0.131
140 nm	900 °C	12.8	0.098

Electronic Supplementary Material (ESI) for Nanoscale

Figures

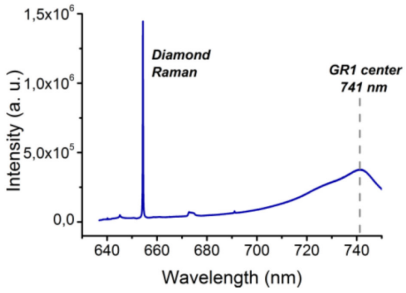

Figure S1 Raman spectrum of GR1 centers observed in samples after proton beam irradiation.

a)

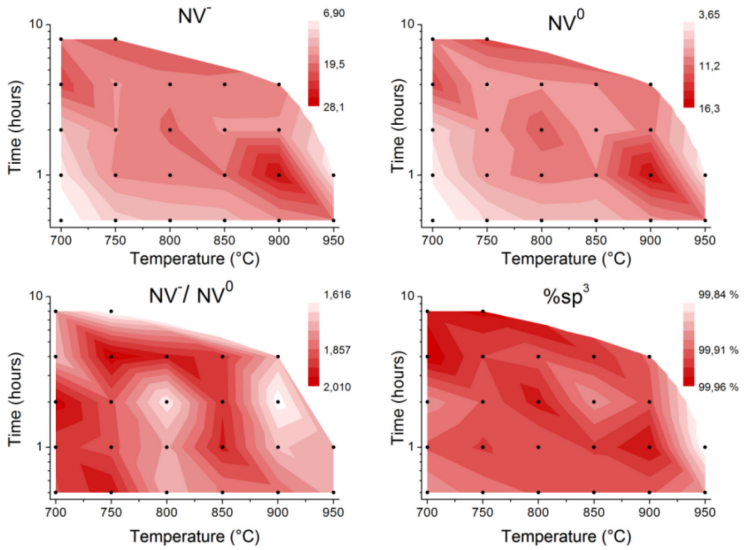

Electronic Supplementary Material (ESI) for Nanoscale

b)

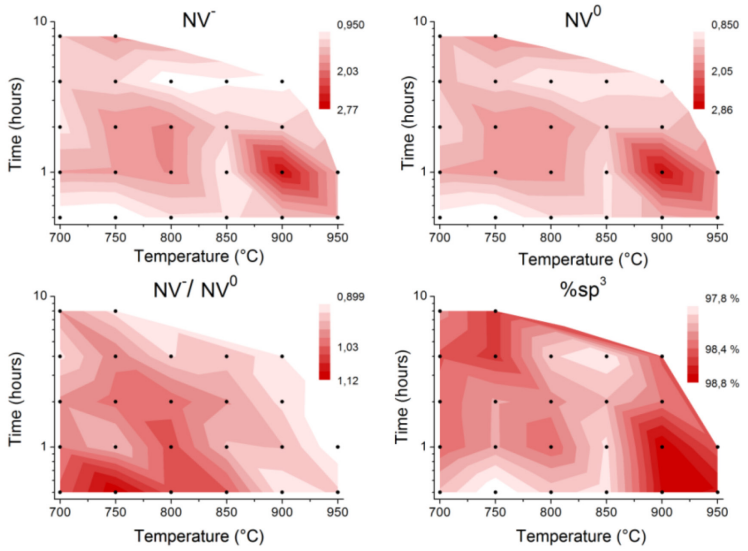

Figure S2 Normalized relative luminescence intensities of NV^- and NV^0, ratios of NV^-/NV^0 luminescence, and "%" of sp^3 carbons for a) 140 nm and b) 45 nm ND particles as a function of annealing time and temperature. Black dots represent the matrix of annealing conditions, darker color represents brighter samples. Interestingly, the NV^- in 45 nm fNDs are preferentially formed at lower temperatures and shorter times (compare the ratios of NV^-/NV^0 luminescence). This trend is not pronounced in 140 nm fNDs.

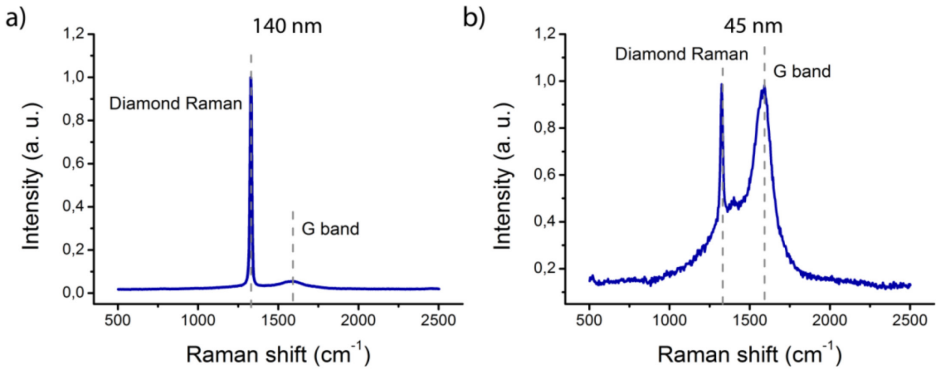

Figure S3 Raman spectra of a) 140 nm and b) 45 nm fND particles after annealing. The intensity is normalized to the diamond Raman band. The G band, corresponding to the amorphized sp^2 carbons, is markedly higher for smaller particles.

Appendix A

Electronic Supplementary Material (ESI) for Nanoscale

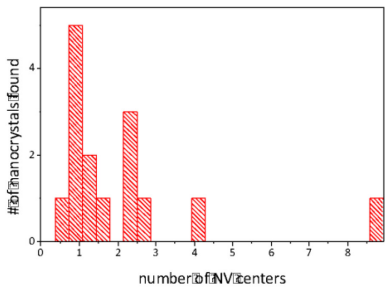

Figure S4 Statistic distribution of NV centers in fND measured using single particle detection fluorescence setup and determined from anti-bunching experiments after laser excitation 532 nm. The measurements were executed on 25 spots.

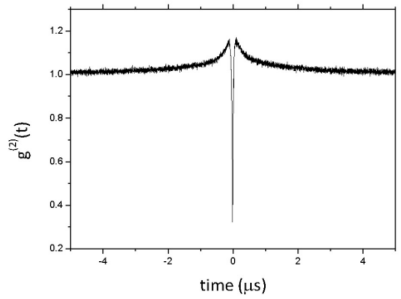

Figure S5 Typical anti-bunching behavior of few emitters as measured from fND used on our study as a reference.

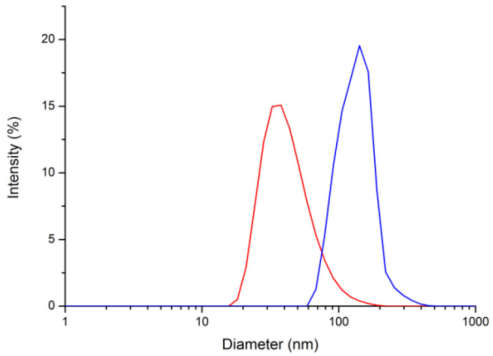

Figure S6 Size distributions by volume of 45 nm (red) and 140 nm (blue) particles in aqueous solution determined by dynamic light scattering.

Electronic Supplementary Material (ESI) for Nanoscale

References

[1] L. C. L. Huang, H.-C. Chang, *Langmuir* **2004**, *20*, 5879–84.
[2] A. T. A. Collins, *New Diam. Front. C. Tech.* **2007**, *17*, 47–61.
[3] S. Pezzagna, B. Naydenov, F. Jelezko, J. Wrachtrup, J. Meijer, *New J. Phys.* **2010**, *12*, 065017.
[4] C. Santori, P. Barclay, K.-M. Fu, R. Beausoleil, *Phys. Rev. B* **2009**, *79*, 125313.
[5] F. Jelezko, C. Tietz, A. Gruber, I. Popa, A. Nizovtsev, S. Kilin, J. Wrachtrup, *Single Mol.* **2001**, *2*, 255–260.
[6] W. Fortunato, a. J. Chiquito, J. C. Galzerani, J. R. Moro, *J. Mater. Sci.* **2007**, *42*, 7331–7336.
[7] V. Petráková, A. Taylor, I. Kratochvílová, F. Fendrych, J. Vacík, J. Kučka, J. Štursa, P. Cígler, M. Ledvina, A. Fišerová, P. Kneppo, M. Nesládek, *Adv. Funct. Mater.* **2012**, *22*, 812–819.
[8] M. Hauf, B. Grotz, B. Naydenov, M. Dankerl, S. Pezzagna, J. Meijer, F. Jelezko, J. Wrachtrup, M. Stutzmann, F. Reinhard, J. Garrido, *Phys. Rev. B* **2011**, *83*, 081304.

Appendix B

Rehor, I.; Lee, K. L.; Chen, K.; Hajek, M.; **Havlik, J.**; Lokajova, J.; Masat, M.; Slegerova, J.; Shukla, S.; Heidari, H.; Bals, S.; Steinmetz, N. F.; Cigler, P.; Plasmonic Nanodiamonds: Targeted Core-Shell Type Nanoparticles for Cancer Cell Thermoablation. Adv. Healthcare Mater. 2015, 4, 460–468.

FULL PAPER

ADVANCED HEALTHCARE MATERIALS
www.advhealthmat.de

Materials Views
www.MaterialsViews.com

Plasmonic Nanodiamonds: Targeted Core–Shell Type Nanoparticles for Cancer Cell Thermoablation

Ivan Rehor, Karin L. Lee, Kevin Chen, Miroslav Hajek, Jan Havlik, Jana Lokajova, Milan Masat, Jitka Slegerova, Sourabh Shukla, Hamed Heidari, Sara Bals, Nicole F. Steinmetz, and Petr Cigler**

Targeted biocompatible nanostructures with controlled plasmonic and morphological parameters are promising materials for cancer treatment based on selective thermal ablation of cells. Here, core–shell plasmonic nanodiamonds consisting of a silica-encapsulated diamond nanocrystal coated in a gold shell are designed and synthesized. The architecture of particles is analyzed and confirmed in detail using electron tomography. The particles are biocompatibilized using a PEG polymer terminated with bioorthogonally reactive alkyne groups. Azide-modified transferrin is attached to these particles, and their high colloidal stability and successful targeting to cancer cells overexpressing the transferrin receptor are demonstrated. The particles are nontoxic to the cells and they are readily internalized upon binding to the transferrin receptor. The high plasmonic cross section of the particles in the near-infrared region is utilized to quantitatively ablate the cancer cells with a short, one-minute irradiation by a pulse 750-nm laser.

1. Introduction

Plasmonic nanostructures (PNs) of various shapes and composition[1,2] have garnered scientific interest in recent years due to their unique optical properties, which allow their use for construction of therapeutic and theranostic nanoparticles, bioprobes, and sensors.[1,3] For a nanosized noble metal particle, the de Broglie wavelength of the valence electrons is of the same order of magnitude as the size of the particle, and quantum size effects may appear. The valence electrons then start to oscillate at a collective oscillation frequency, giving rise to characteristic plasmon resonance bands.[3,4] Because of these properties, PNs gained interest in the fields of biotechnology and biomedicine. Through nanostructure design, their plasmonic absorption wavelength can be finely tuned to fall in the near-infrared tissue imaging window (650–900 nm) where light can penetrate up to a few centimeters into the tissue. The huge absorption and scattering of PNs enables their use as a contrast agent for optical imaging of tissues, e.g., in optical coherence tomography[5,6] or photoacoustic[7] imaging. Furthermore, the absorbed light is transformed into heat, allowing for use of PNs in cancer therapy.[8–10] The heat may be used for thermal ablation of tumors or to control the release of therapeutics, which are usually but not exclusively,[11] attached to the PN surface.[12] Merging diagnostic imaging ability with a therapeutic function in one so-called "theranostic" agent is indeed promising, as evidenced by numerous recent publications addressing the topic.[13,14]

Dr. I. Rehor, Dr. M. Hajek, J. Havlik, Dr. J. Lokajova, Dr. M. Masat, J. Slegerova, Dr. P. Cigler
Institute of Organic Chemistry and Biochemistry, v.v.i
Academy of Sciences of the Czech Republic
Flemingovo nam. 2, 166 10 Prague 6, Czech Republic
E-mail: cigler@uochb.cas.cz

K. L. Lee, K. Chen, Dr. S. Shukla, Dr. N. F. Steinmetz
Department of Biomedical Engineering
Case Western Reserve University
Schools of Medicine and Engineering
10900 Euclid Avenue, Cleveland OH 44106, USA
E-mail: nicole.steinmetz@case.edu

Dr. N. F. Steinmetz
Department of Radiology
Department of Materials Science and Engineering
Department of Macromolecular Science and Engineering
Case Western Reserve University, Schools of Medicine and Engineering
10900 Euclid Avenue, Cleveland, OH 44106, USA

J. Havlik
Faculty of Science
Charles University, Hlavova 2030
128 40 Prague 2, Czech Republic

J. Slegerova
First Faculty of Medicine
Charles University, Katerinska 32
121 08, Prague 2, Czech Republic

Dr. H. Heidari, Dr. S. Bals
EMAT, University of Antwerp
Groenenborgerlaan 171, B-2020 Antwerp, Belgium

DOI: 10.1002/adhm.201400421

Materials Views
www.MaterialsViews.com

ADVANCED HEALTHCARE MATERIALS
www.advhealthmat.de

Here, we describe preparation of a plasmonic gold nanoshell (GNS) around silica-encapsulated diamond nanocrystals. Nanodiamonds (NDs) are highly biocompatible materials with applications in nanomedicine[15] and bioimaging.[16–19] Previous studies on gold plasmonic structures connected with diamonds were performed primarily on macroscopic substrates.[20–25] They have focused mainly on the photophysics of fluorescent nitrogen-vacancy centers embedded in a diamond crystal lattice. Creation of a well-defined plasmonic system on a single diamond nanoparticle in solution is limited by the colloidal instability of NDs in aqueous buffers.[26] To date, only direct covalent attachment of gold nanoparticles to NDs has been achieved,[27,28] and materials with unordered structural morphology[29,30] have been prepared.

We took advantage of our recently published methodology for silica coating of NDs,[31] which enables the creation of a well-defined plasmonic material based on a ND dielectric core coated with a GNS. We chose the core-shell design because it provides an extremely high plasmonic absorption cross section, as well as the possibility to tune the position of the absorption maximum within the near-infrared region, where light is minimally absorbed and scattered by the tissue. As a first step to demonstrate the utility of this newly constructed biomaterial in nanomedical applications, we show that it can be stabilized and rendered biocompatible by addition of PEG-containing ligands bearing bioorthogonally reactive alkyne groups, followed by decoration with synthetically modified transferrin (Tf). We use these particles to target cancer cells, which overexpress the Tf-receptor, and thermally ablate them by irradiation with a near-infrared pulse laser.

2. Results and Discussion

2.1. Preparation and Characterization of Particles

Creation of GNSs with a diamond core was achieved via multistep encapsulation, as depicted in **Figure 1**A. Commercially available ND particles (Figure 1B) are of irregular shape (circularity ~0.67) with sharp edges and often appear elongated in one dimension (needle–like). Their size distribution is broad, ranging from several nm to more than 50 nm in diameter. Therefore, before the GNS is generated on the ND surface, the particle shape needs to be normalized to spherical, and the size distribution should be narrowed. We achieved this through encapsulation of NDs in a silica shell, approximately 20 nm thick, using a method we described earlier.[31] The formation of the desired architecture was confirmed at each step by transmission electron microscopy (TEM), as shown in Figure 1B-E. After coating with silica (Figure 1C), the particles became more spherical (circularity ~0.87), and their diameter increased to 66 ± 10 nm. These pseudospherical silica-coated NDs (**ND@Sil**) are suitable for encapsulation with a GNS, according to a procedure introduced by Halas and collaborators.[32,33] First, small gold nanoparticles (2–3 nm in diameter) were electrostatically anchored onto the silica particle surface (Figure 1D). These assemblies were exposed to a reductive environment containing gold(III) ions, which served as nucleation centers for GNS growth (Figure 1E). The growth of shells ended after several tens of seconds, yielding a deep blue solution containing GNS-coated NDs (**ND@Au**).

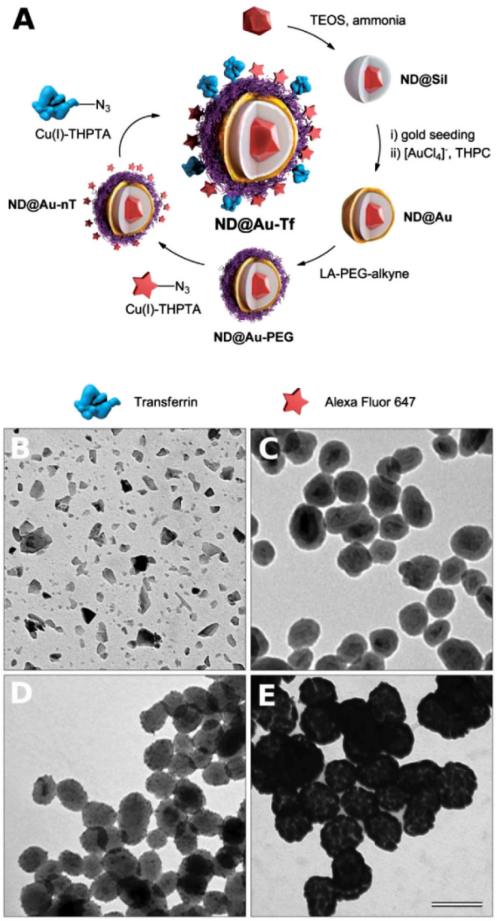

Figure 1. (A) Schematic representation of the preparation of GNSs with a diamond core. First, a silica shell is created on diamond particles, followed by formation of a GNS upon reduction of $[AuCl_4]^-$ promoted by adsorbed gold nanoparticle seeds. The GNS is modified with a lipoic acid-PEG conjugate, which is terminated with an alkyne. Using click chemistry, Alexa Fluor 647 dye and azide-modified transferrin (the targeting protein) are attached in consecutive steps. (B–D) TEM microphotographs of (B) diamond particles, (C) silica-coated diamond particles (**ND@Sil**), (D) silica-coated diamond particles with gold seeds, and (E) GNSs a with diamond core (**ND@Au**). The magnification is the same for all microphotographs, and the scale bar corresponds to 100 nm.

To investigate the structure and thickness of these GNSs in detail, we analyzed individual **ND@Au** particles using HAADF-STEM electron tomography. This technique yields images in which the intensity approximately scales with the square of the atomic number of the elements present in the region

ADVANCED HEALTHCARE MATERIALS
www.advhealthmat.de
www.MaterialsViews.com

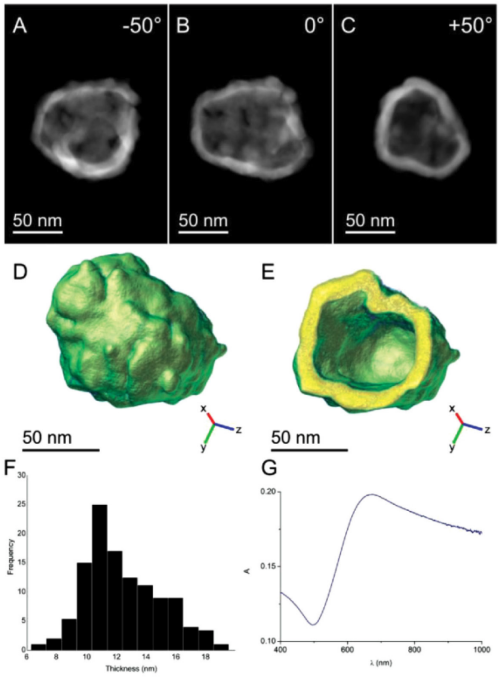

Figure 2. (A–C) 2D HAADF-STEM projections of a ND-silica particle coated with a GNS (**ND@Au**) obtained at different tilt angles. The diamond core and silica coating are not visible due to the limited dynamic range of the image detector. (D) A 3D representation of the reconstructed nanoshell. (E) A slice through the 3D reconstruction of the GNS demonstrating the homogeneity of shell thickness. (F) A histogram indicating the measured thicknesses of the shell based on electron tomography reconstruction. The average shell thickness was 12.6 ± 0.3 nm. (G) Absorption spectrum of **ND@Au** in water at 15 μg/mL concentration (which corresponds to a ND concentration of 0.5 μg/mL).

of interest. Due to the limited dynamic range of the HAADF detector, maintaining similar intensities for Au and silica in the projection images is not feasible because of the large differences in atomic number. We therefore focused on 3-dimensional reconstruction of GNSs. In **Figure 2** A–C, 2-dimensional projections of a GNS imaged at different angles are presented. The 3-dimensional reconstruction resulting from the electron tomography experiment is presented in Figure 2D and E. The shell thickness is mostly homogenous. We evaluated the average shell thickness as 12.6 ± 0.3 nm, and the total internal surface of the GNS was 32 600 nm^2. The intermittent presence of small holes is likely caused by incomplete filling of the spaces between individual seeds with gold.

The formation of the GNS is reflected in absorption spectra by a characteristic broad plasmonic band with an absorption maximum at 675 nm (Figure 2G). The position of the maximum corresponds to values published for silica particles coated with GNSs of similar sizes and thicknesses.[34]

2.2. Introduction of Protective and Bioorthogonally Reactive PEG Coating

The application of GNS-based materials in living systems requires their protection against ionic-strength-induced aggregation/precipitation in buffers and biological liquids, as well as against opsonization. Poly(ethylene oxide) (PEG) is an effective polymeric bio-nanointerface, shielding particles against these factors, rendering them "stealth" to the immune system, and prolonging their circulation in the body.[35] In addition to these attributes, PEG can serve as heterobifunctional linker to connect nanoparticles with attached moieties. For functionalization of **ND@Au**, we utilized mid-size PEG (5 kDa) terminated with lipoic acid at one end and an aliphatic alkyne at the other (**Figure 3**A). Lipoic acid serves as an instant anchoring group, possessing stronger and more stable interaction with gold than terminal aplihatic thiols.[36] Of the available bioconjugation techniques, we chose Cu(I)-catalyzed Huisgen alkyne-azide cycloaddition (click reaction) because of its high orthogonality with other reactive groups in biomolecules and excellent conjugation yields in aqueous solution even at very dilute concentrations.[37]

To analyze the effect of PEG protection on the colloidal stability of particles, we performed comparative stability tests of PEG-modified GNSs (**ND@Au-PEG**) and unmodified **ND@Au**. We exposed the particles to different aqueous solutions with high ionic strength and monitored the hydrodynamic radii over time by dynamic light scattering. While PEG-protected **ND@Au-PEG** exhibited unlimited colloidal stability in PBS, physiological solution (0.15 M NaCl) and cell growth media (RPMI media + serum) (Figure 3B), naked **ND@Au** particles immediately agglomerated and precipitated from the buffers (Figure 3C), with the exception of cell growth media. The particles remained stable in media, most likely due to formation of a protein corona by adsorption of proteins from serum.

2.3. Modification of Particles with Alexa Fluor 647 and Transferrin

For cancer cell targeting experiments, we selected human holotransferrin (Tf), a glycoprotein that is internalized into cells via clathrin-mediated endocytosis upon binding to Tf receptors (TfR). TfR are expressed in negligible numbers on non-dividing cells, but are highly upregulated on rapidly dividing cancer cells, reaching expression levels of up to 10^5 TfR per cell.[38] This makes Tf a suitable targeting ligand to direct nanomaterials, such as **ND@Au**, to cancer cells. This general approach has been successfully demonstrated for various nanoparticles,[39] such as virus-like particles,[40] liposomes[41] and nanodiamonds.[42,43] To ensure protein reactivity for the click bioconjugation strategy, we introduced azide groups to the protein. As previously described,[44] Tf offers a favorable pathway for selective derivatization: a reactive aldehyde can be produced by mild periodate cleavage of 1,2-diols on sialic acid (*N*-acetyl neuraminic acid) moieties present in the Tf glycosylation pattern. We derivatized the obtained aldehydes with aminooxypropylazide, a "clickable" heterobifunctional linker that forms a physiologically stable aldoxime (for structures, see Figure 3A). Compared to ligation via amino or thiol groups, this approach

Materials Views
www.MaterialsViews.com

ADVANCED HEALTHCARE MATERIALS
www.advhealthmat.de

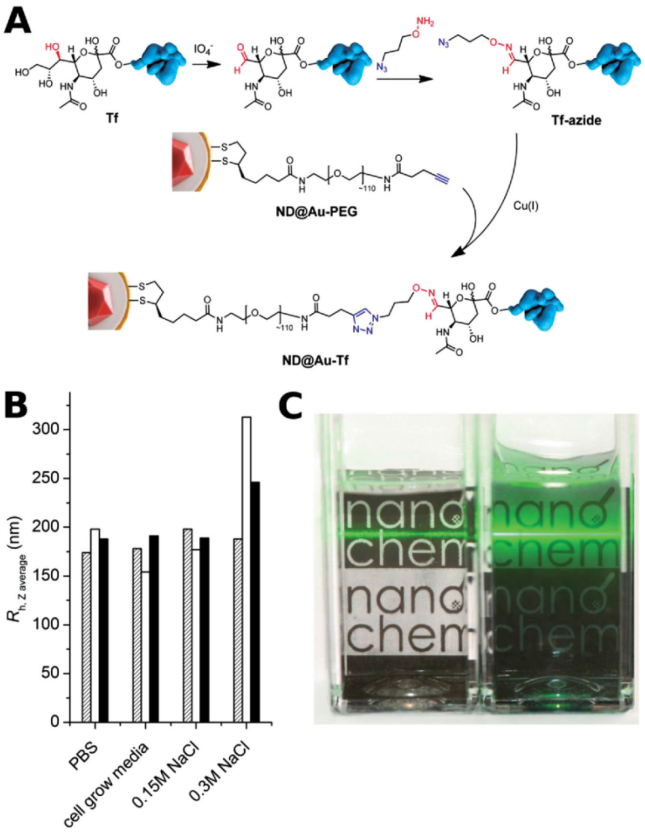

Figure 3. Structure of **ND@Au-PEG** conjugate and its colloidal stability in aqueous solutions with high ionic strength. A) Composition of the particle surface architecture after modification and attachment of Tf. B) Hydrodynamic radii of **ND@Au-PEG** in various solutions after 1 h (hatched), 1 week (white) and 1 month (black), showing no aggregation. C) Photograph of naked (**ND@Au**, left) and PEG-coated (**ND@Au-PEG**, right) particles dispersed in PBS (20 min after mixing; 0.2 mg/mL concentration). The precipitating **ND@Au** particles are already partially sedimented on the bottom of the vial, while the remaining large aggregates unevenly scatter the laser beam. The **ND@Au-PEG** particles form a stable colloidal solution, which evenly and strongly scatters the laser beam.

results in better control over protein attachment points, because one Tf molecule contains only four sialic acids residues at well-defined and sterically accessible positions.[44]

To obtain fluorescent particles, which enable quantification of targeting by flow cytometry and analysis of the particles' subcellular localization by confocal microscopy, we first reacted the alkyne-bearing **ND@Au-PEG** particles with Alexa Fluor 647-azide, yielding fluorescent **ND@Au-nT** conjugate. Although gold plasmonic systems can quench emission from fluorescent dyes,[45] the dye in this case remained fluorescent and was observable with both flow cytometry and confocal microscopy. Linear PEG with a molecular weight of 5000 Da has a Flory dimension of ≈6.0 nm in solution;[46] it is therefore anticipated that the PEG spacer placed between the plasmon surface and fluorophore will effectively shield the quenching effects. The number of Alexa Fluor 647 molecules per particle, however, was difficult to estimate because of the strong interference of particles' plasmonic properties and the extinction and emission fluorescence bands of the dye. As a next step, we attached azide-modified Tf to unreacted alkyne groups of **ND@Au-nT** under similar conditions, providing **ND@Au-Tf**.

2.4. Targeting of Cancer Cells

Target-specificity and cellular uptake of particles was evaluated in TfR-expressing SKBR3 cells (a human breast cancer cell line) using flow cytometry (quantitative) and confocal microscopy (qualitative). Flow cytometry indicated that both types of particles, **ND@Au-nT** and **ND@Au-Tf**, bound to the cells, with the Tf-targeted preparation **ND@Au-Tf** showing enhanced interactions. Our data indicate that 26% of the cell population was targeted by **ND@Au-Tf**, while non-specific uptake was attributed to 18% of the cells, as indicated by **ND@Au-nT**-cell interactions ($p < 0.05$, **Figure 4**). Cell targeting properties were found to be reproducible in other cell lines, such as HeLa cells (not shown).

Competition binding assays using free Tf ligand further confirmed the target-specificity of the **ND@Au-Tf** conjugate. Competition with a molar excess of 5:1 or 20:1 **Tf:ND@Au-Tf** particles resulted in reduced cell uptake, with levels comparable to those observed for non-targeted **ND@Au-nT**. This indicates that the **ND@Au-Tf** particles indeed target the cells, and binding can be attributed to specific interactions between TfR and **ND@Au-Tf** (Supporting Information Figure S2).

Next, we sought to investigate the cellular fates of **ND@Au-Tf** and **ND@Au-nT**, specifically addressing whether the ND formulations would be taken up into cells. Cell membranes and nuclei were stained, and Z-stacked (0.3 micrometer/steps) confocal images were recorded. Data indicate that after a 3-hour incubation period, both **ND@Au-Tf** and **ND@Au-nT** formulations were bound to cell membranes (data not shown). Interestingly, after a 16-hour incubation period, **ND@Au-Tf** appeared intracellularly, whereas **ND@Au-nT** particles co-registered with the cell membrane (**Figure 5**), indicating that although both formulations are able to bind to cellular membranes, only **ND@Au-Tf** are internalized. Because our cell binding studies showed that **ND@Au-Tf** particles specifically bind TfR, **ND@Au-Tf** internalization is

ADVANCED HEALTHCARE MATERIALS
www.advhealthmat.de

Materials Views
www.MaterialsViews.com

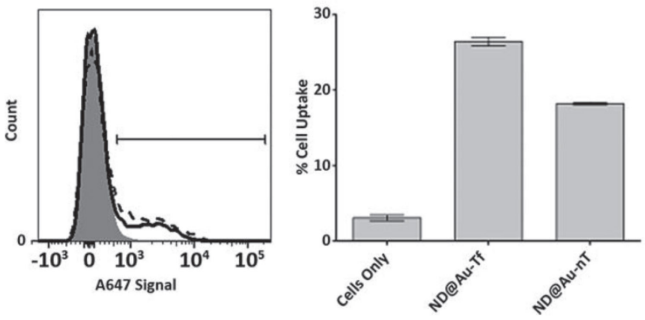

Figure 4. SKBR3 cell interactions with particles determined by flow cytometry. Left histogram: gray, cells only; dashed, **ND@Au-Tf**; solid, **ND@Au-nT**. Right graph: Statistical analysis showing percent cellular uptake (positive cells shown on histogram by gate) for each sample. Error bars indicate standard deviation. Experiments were conducted in triplicate, and 10 000 gated events were analyzed. Student's *t*-test indicates significant differences comparing targeted **ND@Au-Tf** and non-targeted **ND@Au-nT** formulations ($p < 0.05$).

likely mediated by TfR endocytosis. Co-localization studies were carried out, further indicating that non-targeted **ND@Au-nT** are co-localized with the cell membrane with Mander's coefficient M2 = 0.99. In stark contrast, only a fraction of the targeted **ND@Au-Tf** formulation remained bound to the cell membrane (M2 = 0.21), while the remainder translocated inside the cell. Our flow cytometry and confocal imaging results are in agreement, and the data support **ND@Au-Tf** targeting of TfR on cancer cells, leading to receptor-mediated internalization.

2.5. Toxicity Study

The toxicity of the **ND@Au-Tf** particles themselves was investigated in SKBR3 cells, using an XTT cell proliferation assay. After 3- or 24-hour incubation with **ND@Au-Tf** particles, we did not observe significant differences in cell viability compared to non-treated cells, indicating that **ND@Au-Tf** particles are not cytotoxic (Supporting Information Figure S3).

2.6. Laser Ablation

The ability of GNSs to kill cancer cells upon red laser irradiation was demonstrated in vitro. HeLa cells were incubated with **Nd@Au-Tf**, and after successive washing, irradiated with a Ti:Sapphire pulse laser. After a one-minute irradiation, cells were incubated for 24 hours, and their viability was estimated using luciferase assay (**Figure 6**). Exposing HeLa cells to **ND@Au-Tf** did not affect their viability, supporting the non-toxicity of these particles. Laser irradiation of cells also had no influence on their viability. Only cells exposed to both nanoparticles and laser were affected and—after only one minute of irradiation—completely killed. The laser power we used (37 W/cm^2) was of the same order of magnitude as values described in the literature for in vitro experiments.[9,10,47]

3. Conclusion

In summary, we synthesized a novel plasmonic nanomaterial consisting of a diamond core coated with a silica layer and encapsulated with a thin GNS. PEG chains were attached to the surface of GNSs using lipoic acid as an anchor. The other ends of the PEG chains were further functionalized with Alexa Fluor 647 and modified transferrin via click chemistry. Transferrin-labeled ND-based GNSs (**ND@Au-Tf**) target transferrin receptors, which are overexpressed on many cancer cell types. We found that **ND@Au-Tf** bind and are internalized into human SKBR3 breast cancer cells and HeLa cervical cancer cells. Cell viability assays were also conducted using XTT assay; toxic effects were not observed after 3- or 24-hour incubation periods. We also demonstrated the ability of the prepared GNSs to kill cancer cells upon red laser irradiation in vitro. HeLa cells were completely killed after a one-minute irradiation with a pulse 750-nm pulse laser (37 W/cm^2), while no harm was caused to cells by irradiation itself or by the presence of GNSs without irradiation.

This work lays the foundation for the multi-step synthetic route leading to ND core plasmonic nanoparticles and is the first stepping stone toward translational research. Future work will focus on targeted therapeutic studies of plasmonic NDs in vivo. Specifically, studies will set out to gain an understanding on the therapeutic efficacy in the context of biodistribution and overall biocompatibility of the materials. At the same time, studies will assess the photophysical interactions of the fluorescent nitrogen-vacancy (NV) centers in NDs with the gold plasmonic shell.

It is well recognized that cancer nanotechnology holds great promise in modern medicine, and several nanoparticles have advanced into clinical application.[48–50] While the development pipeline with new nanomaterial-based technologies is moving rapidly, the fundamenal understanding of the nanomaterial's in vivo fate; i.e., the biodistribution, clearance or persistence, pharmacokinetics and pharmacodynamics, is often lacking. However, detailed understanding of the biological behaviour, the interplay of tissue-targeting and immune surveillance in the context of imaging sensitivity and therapeutic efficacy, is imperative for rapid clinical viability and success of plasmonic nanostructures.[51] The combined knowledge of the biological properties and diagnostic/therapeutic potential will help identify a suitable nitch application harnessing the unique properties of the proposed material.

4. Experimental Section

Chemicals and Solvents: The NHS ester of lipoic acid was prepared according to a previously published procedure.[52] H_2N-PEG(5000)-alkyne was purchased from Iris Biotech. Alexa Fluor 647-azide was purchased from Invitrogen. Tetrakis(hydroxymethyl)phosphonium chloride (THPC)

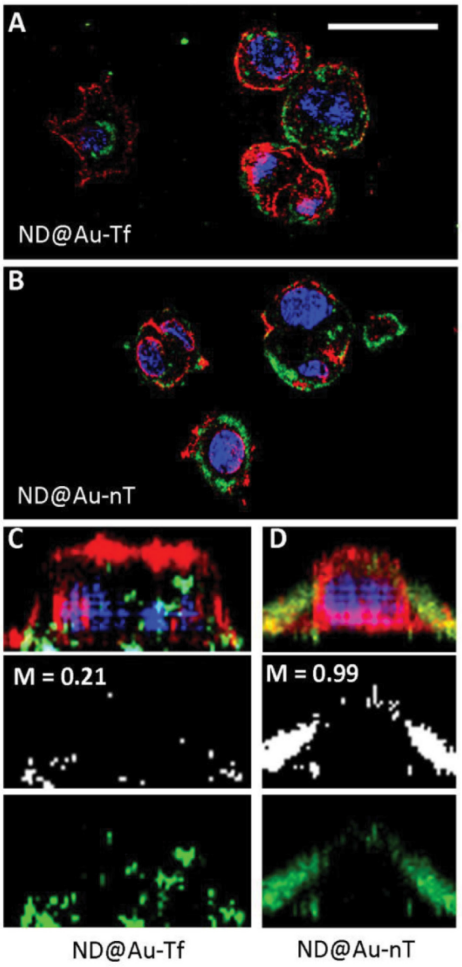

Figure 5. SKBR3 cell interactions with particles observed by confocal microscopy. The particles were incubated with SKBR3 cells for 16 h, fixed, stained, and imaged. **ND@Au-Tf** (A+C) and **ND@Au-nT** (B+D) are pseudo-colored in green (imaged based on the Alexa Fluor 647 label), nuclei are shown in blue (stained with DAPI), and cell membranes are shown in red (stained with WGA-A555); the scale bar is 30 μm. C+D shows 3D reconstruction of single cells: the top panel shows all channels, the middle panel depicts co-localization of the particles and WGA signals (M = Mander's coefficient of co-localization determined using ImageJ software), and the bottom panel shows ND signals.

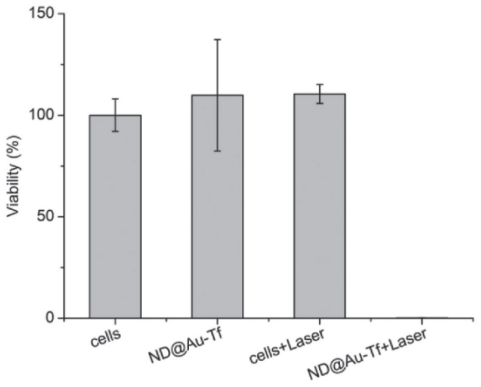

Figure 6. Laser ablation of HeLa cells incubated with **ND@Au-Tf** nanoparticles. Cell viability was estimated by luciferase assay with 24 h delay after 1 min irradiation with 37 W/cm^2 intensity. The viability of cells treated with **ND@Au-Tf** and laser was ≈0.15%.

and tetraethyl orthosilicate (TEOS) were purchased from Sigma-Aldrich. $HAuCl_4$ was purchased from Alfa Aesar.

UV–Vis Spectroscopy: The spectra were recorded with a Specord 210 (Analytik Jena) spectrometer in the 400–1000 nm range at room temperature with an optical path of 1 cm.

Dynamic Light Scattering: For stability studies in buffers, DLS was recorded with a Zetasizer Nano ZS system (Malvern Instruments) at 25 °C. The particle concentration was 0.3 mg/mL (10 μg ND/mL).

Electron Microscopy: Bright field TEM experiments were performed with a JEOL JEM-1011 electron microscope operated at 60 kV and equipped with a Veleta side-mounted camera. Carbon coated grids (Pyser) were used in all cases. Nanodiamond samples were prepared according to a previously published procedure.[53] Other samples were prepared as follows: a 3 μL droplet of particle dispersion (0.2 mg/mL) was placed on the grid and gently removed with a piece of tissue after 1 min incubation. Tilt series of 2-dimensional projection images for electron tomography were acquired using a FEI Tecnai G^2 transmission electron microscope operated at 200 kV in scanning transmission electron microscopy (STEM) mode. To prepare the samples, a drop of diluted colloidal solution was placed on a carbon-coated copper grid and left to dry. The high angle annular dark field (HAADF-STEM) image series was acquired using a single tilt tomography holder (Fischione 2020) over the angular range (–64°,+76°) with step increments of 2°. The alignment and 3D reconstruction were carried out with FEI Inspect3D software. Quantification of the 3D data was performed using MATLAB codes.

Synthesis of LA-PEG-alkyne: Synthesis was performed according to published procedures,[36,54] with some modifications. Briefly, H_2N-PEG(5000)-alkyne (50 mg, 10 μmol) was dissolved in DCM (1 mL) and mixed with LA-NHS (50 mg, 165 μmol). The reaction mixture was stirred overnight, then washed 3 times with 10 mL hot water. The combined aqueous fractions were purified using a Millipore Ultracel 3K separation tube (washed 3 times with 20 mL water). TLC: MeOH:triethylamine 100:5 (R_f = 0.5), visualized with $Co(NCS)_x$ and $KMnO_4$ (no reaction with ninhydrin). H_2N-PEG(5000)-alkyne R_f < 0.3, visualized with ninhydrin and $Co(NCS)_x$ (no reaction with $KMnO_4$). ^{1}H NMR (400 MHz, $CDCl_3$, δ): 1.6 (m, 2H), 1.7–1.9 (m, 3H), 2.0 (m, 1H), 2.1 (t, 1H, J = 3.6 Hz), 2.2–2.4 (m, 4H), 2.5 (t, 2H, J = 7.2 Hz), 2.6 (m, 3H), 3.2–3.3 (m, 2H), 3.5–3.9 (m, ~240H), 3.9 (t, 1H, J = 5.2).

4.1. Transferrin-Azide (Tf-Azide)

Preparation: (see Figure 3A) We used a procedure similar to that previously described for preparation of transferrin-alkyne.[44] $NaIO_4$ solution was slowly added to a cooled solution of human holo-transferrin (30 mg, 390 nmol; 2 mg/mL) in acetate buffer (0.1 M, pH 5.5) to a final $NaIO_4$ concentration of 1 mM. The mixture was incubated

Appendix B

on ice in the dark for 30 min. The solution containing Tf-aldehyde was concentrated six times in an ultrafiltration cell (from 70 mL to 5 mL). HEPES buffer (0.1 M, pH 7.2) was used to refill the volume. Tf-aldehyde was incubated with 3-aminooxypropyl-1-azide (16.2 mg, 140 µmol) in HEPES buffer with dimethyl sulfoxide (DMSO, 20%, total volume of 17 mL) for 5 h at room temperature with gentle mixing. Removal of excess 3-aminooxypropyl-1-azide was performed by ultrafiltration (70 mL to 5 mL, repeated six times) in HEPES buffer (0.1 M, pH 8). The solution was freeze-dried to obtain **Tf-azide**.

Characterization: The presence of a reactive azide group in **Tf-azide** was tested by reaction with fluorescein-alkyne. All solutions were aqueous except the fluorescein-alkyne stock, which was prepared in DMSO. The solutions were mixed to achieve the following final concentrations: 0.02 mM **Tf-azide**, 0.075 mM fluorescein-alkyne, 0.17 mM $CuSO_4{\cdot}5H_2O$, 0.33 mM tris(3-hydroxypropyltriazolylmethyl) amine (THPTA), and 5 mM sodium ascorbate. The solutions of $CuSO_4{\cdot}5H_2O$ and THPTA were premixed (in a 1:2 molar ratio) before adding to the reaction mixture. The reaction mixture was well-sealed after adding sodium ascorbate, mixed, and reacted for 2 h with no stirring. The reaction product (**Tf-Fl**) was analyzed by SDS-PAGE (for details, see ESI). All samples (**Tf**, **Tf-azide**, and **Tf-Fl**) were of the same molecular weight, and only **Tf-Fl** can be seen under UV-lamp (Supporting Information Figure S1).

4.2. Nanoshell Preparation

Silica Encapsulation: NDs were solubilized in a manner similar to that described in commonly used procedures.[16,55] Briefly, NDs were treated with a mixture of HNO_3 and H_2SO_4 (85 °C, 3 days), washed with 2 M NaOH and 2 M HCl, washed five times with water, and freeze-dried. Prior to use, the particles were dissolved in water (2 mg/mL) and sonicated with a probe (Cole-Parmer, 750 W) for 30 min. The resulting transparent colloid was filtered using a 0.2 µm PVDF microfilter to provide a colloidal solution of ND particles. A modified version[31] of previously described general procedure[56] was used to coat NDs with silica shells. Polyvinylpyrrolidone (96 mg, 9.6 µmol) was dissolved in water (204 mL) and sonicated for 10 min in an ultrasonic bath. ND colloid (6 mL, 2 mg/mL) was added, and the mixture was stirred for 24 h. The colloid was then concentrated via centrifugation in two steps. In the first step (40 000 rcf, 1 h), the volume was reduced to approximately 12 mL. The second centrifugation step (30 000 rcf, 30 min) was performed in microvials and reduced the solvent volume to approximately 0.4 mL. Sedimented NDs were resuspended in ethanol (12 mL) in a round bottom flask and sonicated in an ultrasonic bath for 2–4 min. TEOS (112 mg, 539 µmol) was added. After 2 min of vigorous stirring, ammonia solution (25%, 500 µL) was added, and the reaction mixture was stirred for 14 h, affording silica-coated particles **ND@Sil**. The product was purified by centrifugation (14 000 rcf, 5 min) with ethanol (12 mL, 4×) and MeCN (12 mL, 2×) and was dissolved in 6 mL MeCN. **ND@Sil** particles were stored in the freezer (–18 °C) as a stable colloid for several months without changes in particle characteristics (confirmed with TEM and DLS) or reactivity.

GNS Formation: GNSs were prepared according to modified published procedures.[32–34] First, seeding gold colloid was prepared. Water (45 mL) was mixed with NaOH (5 mL, 0.1 M). Tetrakis(hydroxymethyl) phosphonium chloride (THPC, 67.2 µmol in 1 mL water) was added. After exactly 5 min, $HAuCl_4$ solution (2 mL of a 1% w/w solution in water, 59 µmol) was added in one portion under vigorous stirring. The mixture was stirred for 10 min, and the resulting gold colloid was aged at 4 °C for 2 weeks without purification. **ND@Sil** particles (1 mL MeCN dispersion, 2 mg ND content, 8 mg total **ND@Sil** weight) were mixed with 2-week aged gold colloid (30 mL). The pH of the mixture was adjusted to 3. The mixture was gently stirred for 20 min and then kept at 4 °C for 16 h. **ND@Sil** particles coated with gold seeds were isolated by centrifugation (2500 rcf, 1 h) and washed twice with water (30 mL, isolated at 2500 rcf, 1 h). The volume of the dispersion was adjusted to 5 mL. K_2CO_3 (200 mg, 1.44 mmol) was dissolved in 800 mL water, and $HAuCl_4$ solution (12 mL of a 1% w/w solution in water, 3.5 µmol) was added. The solution was stirred for 24 h in the dark. Then, the pH of the solution was adjusted to 9.0. Gold-seeded **ND@Sil** dispersion (1.25 mL; 0.5 mg ND content) was added to 200 mL solution. A stream of CO was bubbled through the solution for 2 min under vigorous stirring. The color changed from transparent to red, purple, and then dark blue. Gold encapsulated **ND@Sil** (**ND@Au**) were separated by centrifugation at 20 rcf overnight and concentrated to 2.5 mL. The total mass of **ND@Au** particles obtained in one run was on average 15 mg, i.e., 30-fold the mass of ND and 7.5-fold the mass of **ND@Sil**.

PEGylation of **ND@Au**: LA-PEG-alkyne (10.3 mg, 2 µmol) was added to **ND@Au** dispersion (15 mg; corresponds to 0.5 mg ND) in 2.5 mL water. The mixture was sonicated in an ultrasonic bath for 20 min, then stirred overnight and sonicated for another 20 min. PEG-coated **ND@Au** particles were separated by centrifugation (5×, 500 rcf, 20 min), yielding **ND@Au-PEG**.

Modification with transferrin and Alexa Fluor 647: A solution of Cu-catalyst was prepared in a separate vial by mixing $CuSO_4{\cdot}5H_2O$ (20 µL of a 25 mM solution) and THPTA ligand (20 µL of a 50 mM solution).The click reactions were performed similarly to those described in the literature[57] by mixing reactants in a 0.6 mL vial. **ND@Au-PEG** solution (1.5 mg particles in 125 µL) was mixed with a DMSO solution of Alexa Fluor 647-azide (1.7 µL of a 5.88 mM solution). Other components were added in the following order and quantities: aminoguanidine hydrochloride (12 µL of a 100 mM solution) and Cu-catalyst solution (3.2 µL) (see above). Water was added to adjust the total reaction volume to 200 µL. Sodium ascorbate (12 µL of a 100 mM solution) was added. The vials were well-sealed and kept for 2 h without stirring or shaking. Modified nanoparticles were isolated in near-quantitative yield by centrifugation (500 rcf, 20 min) and washed with water (2×, 1 mL) and PBS (1×, 1 mL) to yield gold-coated NDs tagged with Alexa Fluor 647 (**ND@Au-nT**). **ND@Au-nT** was further modified with Tf-azide in a similar manner. Solid Tf-azide (0.2 mg) was added to nanoparticles, and other components were added in the same quantities and order as in the previous reaction step. After centrifugal separation, **ND@Au-Tf** was obtained.

Stability Experiments: A colloidal aqueous solution of **ND@Au-PEG** (1.5 mg/mL, 100 µL) was added to buffer (900 µL). The following buffers were used: PBS (pH = 7.5), 0.15 M NaCl, 0.3 M NaCl, and cell growth medium (RPMI-1640 + serum). The samples were stored at 25 °C, and the aggregation state was examined with DLS 2 h, 1 day, and 1 month after mixing. Ten minutes before each measurement, samples were sonicated in a bath for 20 s.

4.3. Cell Studies

Flow Cytometry: SKBR3 cells were cultured in McCoy's 5A media supplemented with 10% (v/v) fetal bovine serum (FBS), 1% (v/v) penicillin-streptomycin, and 1% (v/v) L-glutamine at 37 °C and 5% CO_2 (all reagents were obtained from Invitrogen). Cells (100 000 cells/500 µL media/well) were added to untreated 24-well plates and incubated overnight. The following day, triplicates of i) culture medium alone (negative control), ii) gold-coated NDs tagged with Alexa Fluor 647 (**ND@Au-nT**), and iii) gold-coated NDs tagged with Alexa Fluor 647 and transferrin (**ND@Au-Tf**) were added. Particle concentrations were approximately 1×10^{12} particles/mL (1.2 mg particles per 1 mL, 300 µL final volume; 3×10^6 particles/cell) in culture medium. Particles were incubated with cells for 3 h. (Competition binding assays were also carried out: **ND@Au-Tf** were incubated with free Tf added to the medium in a molar excess of 5:1 or 20:1, see Supporting Information). Following incubation, cells were washed three times with 0.09% (w/v) saline to remove non-bound particles remaining in solution. Cells were removed using 200 µL enzyme-free Hank's based cell dissociation buffer (Gibco), added to untreated 96-well v-bottom plates, and centrifuged at 500 g for 4 min. The supernatant was removed. Cells were then washed in FACS buffer (0.1 mL of 0.5 M EDTA, 0.5 mL FBS, and 1.25 mL of 1 M HEPES, pH 7.0, in 50 mL Ca^{2+}- and Mg^{2+}-free PBS). Washing was repeated twice.

Cells were fixed in 2% (v/v) paraformaldehyde in FACS buffer at room temperature for 10 min and washed twice. Samples were analyzed using a BD LSR II flow cytometer, with a total of 10,000 gated events collected per sample. FlowJo 10.0.00003 software was used for data analysis.

Confocal Microscopy: SKBR3 cells (25 000 cells/500 µL media/well) were added to coverslips, which were placed in untreated 24-well plates and incubated overnight. The following day, duplicates of i) no particles, ii) **ND@Au-nT**, and iii) **ND@Au-Tf** were added at concentrations of approximately 1×10^{12} particles/mL (1.2 mg particles per 1 mL, 300 µL final volume, 1.2×10^7 particles/cell) and incubated with the cells for 16 h. Following incubation, cells were washed three times with 0.09% (w/v) saline to remove excess particles. Samples were fixed in 5% (v/v) paraformaldehyde and 0.3% (v/v) gluteraldehyde in Dulbecco's PBS (Fisher) for 10 min at room temperature. Cells were blocked in 5% (v/v) goat serum (Invitrogen) for 90 min at room temperature. Cell membranes were stained using 1 µg/mL wheat germ agglutinin-A555 (Invitrogen) and 1% (v/v) goat serum in Dulbecco's PBS for 45 min at room temperature. Cell nuclei were stained using 4'6'-diamidino-2-phenylindole (DAPI) (MP Biomedicals) diluted 1:9,500 in Dulbecco's PBS for 15 min at room temperature. In between each step, cells were washed three times with Dulbecco's PBS. Slides were mounted using Permount mounting media (Fisher). Confocal analysis was performed using the Olympus FV1000 laser scanning confocal microscope and a 40x objective. Images were analyzed using ImageJ 1.43u software.

XTT Cell Proliferation Assay: SKBR3 cells (25,000 cells, 200 µL media per well) were added to 96-well plates and incubated at 37 °C under 5% CO_2 overnight. The following day, **ND@Au-Tf** particles were added at a concentration of approximately 1×10^{12} particles/mL (1.2 mg particles per 1 mL, 75 µL final volume, 3×10^6 particles/cell); control cells with no added particles were also set up. Following a 3 or 24 h incubation, wells were washed three times with 0.09% (w/v) saline to remove unbound NDs. Then, 200 µL fresh media was added, and cells were returned to incubate for an additional 24 h. An XTT cell proliferation assay (ATCC) was used to assess cellular viability; the protocol was performed according to the manufacturer's instructions. A Tecan Infinite 200 plate reader was used to measure the absorbance, and percent viability was determined by normalizing to the cell-only control.

Laser Ablation Experiments: Human cervical adenocarcinoma (HeLa) cells (ATCC® CCL-2™) were cultured in RPMI 1640, Dutch modification medium supplemented with 10% (v/v) heat-inactivated fetal bovine serum (FBS), antibiotics (200 µg/mL streptomycin and 100 U/mL penicillin G) and 2 mM glutamine (all purchased from Sigma-Aldrich) at 37 °C in a humidified atmosphere containing 5% CO_2. Cells were subcultured as needed (2–3 times a week in a subcultivation ratio of 1:5 to 1:8) and harvested from flasks using 0.25% (w/v) trypsin-EDTA. HeLa cells were seeded into a white wall clear bottom 384-well plate in 30 µL at a density of 3000 cells/well. Then, cells were grown for 48 h under standard conditions (37 °C and 5% CO_2) before adding **ND@Au-Tf** nanoparticles at a final amount of approximately 2×10^{11} (240 µg of particles per 1 mL) in tetraplicates. After 24 h of treatment with or without nanoparticles, the medium was removed, and the cells were thoroughly washed with fresh medium (three times). Then, the medium in each well was replaced with PBS, and selected wells were illuminated immediately (Ti:Sapphire laser – 75 MHz, 750 nm, pumped at 532 nm by ND:YAG, laser power of 2.1 W, spot diameter of 2.7 mm, irradiation time of 60 sec). After irradiation, PBS was replaced with a fresh complete growth medium (30 µL), and the plate was incubated for an additional 24 h before viability measurement. Cell viability was determined using the CellTiter-Glo Luminescent Cell Viability Assay (Promega, Madison, WI, USA), which is based on quantification of the ATP present in cell lysates, according to the manufacturer's protocol. Briefly, the 384-well plate and its contents were equilibrated at room temperature for 30 min. CellTiter-Glo reagent was prepared by reconstituting the lyophilized enzyme/substrate mixture with CellTiter-Glo buffer equilibrated to room temperature. After an equal volume of CellTiter-Glo reagent was added to the wells (30 µL), the plate was shaken for 2 min on an orbital shaker (500 RPM) to induce cell lysis. Luminescence was recorded after an additional 10 min incubation in the dark using the multimode microplate reader Tecan Infinite M1000 (Tecan Austria GmbH, Grödig, Austria). Blank wells (containing medium without cells) were measured for luminescence and deducted from the values obtained from experimental wells (background luminescence). The viability values of treated cells were expressed as percentages of the values obtained for the corresponding control cells. Values (of the luminescent signal) represent the mean ± S.D. of four replicates obtained from two independent experiments.

Supporting Information

Supporting Information is available from the Wiley Online Library or from the author.

Acknowledgements

I. Rehor and K. L. Lee contributed equally to this work. This work was supported by GACR project P108/12/0640, MSMT CR grant no. LH11027, the National Science Foundation, CMMI NM 333651 (to NFS), a NCI R25 CA148052 Cancer Pharmacology training grant (KLL), and NPU I project LO 1302 from Ministry of Education (MH). Part of this work was performed within OPPK project CZ.2.16/3.1.00/24016. S.B. acknowledges financial support from the European Research Council (ERC Starting Grant #335078-COLOURATOMS).

Received: July 19, 2014
Revised: September 3, 2014
Published online: October 21, 2014

[1] N. G. Khlebtsov, L. A. Dykman, *J. Quant. Spectrosc. Radiat. Transf.* **2010**, *111*, 1.
[2] M. R. Jones, K. D. Osberg, R. J. Macfarlane, M. R. Langille, C. A. Mirkin, *Chem. Rev.* **2011**, *111*, 3736.
[3] M. C. Daniel, D. Astruc, *Chem. Rev.* **2004**, *104*, 293.
[4] A.-I. Henry, J. M. Bingham, E. Ringe, L. D. Marks, G. C. Schatz, R. P. Van Duyne, *J. Phys. Chem. C* **2011**, *115*, 9291.
[5] A. Agrawal, S. Huang, A. Wei Haw Lin, J. K. Barton, R. A. Drezek, T. J. Pfefer, M.-H. Lee, *J. Biomed. Opt.* **2006**, *11*, 041121.
[6] J. C. Y. Kah, T. H. Chow, B. K. Ng, S. G. Razul, M. Olivo, C. J. R. Sheppard, *Appl. Opt.* **2009**, *48*, D96.
[7] Y.-S. Chen, W. Frey, S. Kim, P. Kruizinga, K. Homan, S. Emelianov, *Nano Lett.* **2011**, *11*, 348.
[8] J. M. Stern, J. Stanfield, W. Kabbani, J.-T. Hsieh, J. A. Cadeddu, *J. Urol.* **2008**, *179*, 748.
[9] W. Lu, C. Xiong, G. Zhang, Q. Huang, R. Zhang, J. Z. Zhang, C. Li, *Clin. Cancer Res.* **2009**, *15*, 876.
[10] X. Huang, I. H. El-Sayed, W. Qian, M. A. El-Sayed, *J. Am. Chem. Soc.* **2010**, *128*, 2115.
[11] G. Wu, A. Mikhailovsky, H. A. Khant, C. Fu, W. Chiu, J. A. Zasadzinski, *J. Am. Chem. Soc.* **2008**, *130*, 8175.
[12] R. Bardhan, S. Mukherjee, N. A. Mirin, S. D. Levit, P. Nordlander, N. J. Halas, *J. Phys. Chem. C* **2010**, *114*, 7378.
[13] R. Bardhan, S. Lal, A. Joshi, N. J. Halas, *Acc. Chem. Res.* **2011**, *44*, 936.
[14] A. M. Gobin, M. H. Lee, N. J. Halas, W. D. James, R. A. Drezek, J. L. West, *Nano Lett.* **2007**, *7*, 1929.
[15] E. K. Chow, X.-Q. Zhang, M. Chen, R. Lam, E. Robinson, H. Huang, D. Schaffer, E. Osawa, A. Goga, D. Ho, *Sci Transl Med* **2011**, *3*, 73ra21.
[16] V. Vaijayanthimala, P.-Y. Cheng, S.-H. Yeh, K.-K. Liu, C.-H. Hsiao, J.-I. Chao, H.-C. Chang, *Biomaterials* **2012**, *33*, 7794.

Appendix B

[17] Y. Y. Hui, C. L. Cheng, H. C. Chang, *J. Phys. Appl. Phys.* **2010**, *43*, 374021.
[18] J. Slegerova, M. Hajek, I. Rehor, F. Sedlak, J. Stursa, M. Hruby, P. Cigler, *Nanoscale* **2014**, DOI: 10.1039/C4NR02776K.
[19] J. Slegerova, I. Rehor, J. Havlik, H. Raabova, E. Muchova, P. Cigler, in *Intracellular Delivery II*, (Eds: A. Prokop, Y. Iwasaki, A. Harada), Dordrecht: Springer, Netherlands **2014**, 363.
[20] T.-S. Lim, C.-C. Fu, K.-C. Lee, H.-Y. Lee, K. Chen, W.-F. Cheng, W. W. Pai, H.-C. Chang, W. Fann, *Phys. Chem. Chem. Phys.* **2009**, *11*, 1508.
[21] S. Schietinger, M. Barth, T. Aichele, O. Benson, *Nano Lett.* **2009**, *9*, 1694.
[22] Y. Y. Hui, Y.-C. Lu, L.-J. Su, C.-Y. Fang, J.-H. Hsu, H.-C. Chang, *Appl. Phys. Lett.* **2013**, *102*, 013102.
[23] M. Barth, S. Schietinger, T. Schröder, T. Aichele, O. Benson, *J. Lumin.* **2010**, *130*, 1628.
[24] G. Chen, Y. Liu, M. Song, B. Wu, E. Wu, H. Zeng, *IEEE J. Sel. Top. Quantum Electron.* **2013**, *19*, 4602404.
[25] Y. Chi, G. Chen, F. Jelezko, E. Wu, H. Zeng, *IEEE Photonics Technol. Lett.* **2011**, *23*, 374.
[26] I. Rehor, H. Mackova, S. K. Filippov, J. Kucka, V. Proks, J. Slegerova, S. Turner, G. Van Tendeloo, M. Ledvina, M. Hruby, P. Cigler, *ChemPlusChem* **2014**, *79*, 21.
[27] B. Zhang, C.-Y. Fang, C.-C. Chang, R. Peterson, S. Maswadi, R. D. Glickman, H.-C. Chang, J. Y. Ye, *Biomed. Opt. Express* **2012**, *3*, 1662.
[28] H. Ismaili, M. S. Workentin, *Chem. Commun.* **2011**, *47*, 7788.
[29] L.-C. Cheng, H. M. Chen, T.-C. Lai, Y.-C. Chan, R.-S. Liu, J. C. Sung, M. Hsiao, C.-H. Chen, L.-J. Her, D. P. Tsai, *Nanoscale* **2008**, *5*, 3931.
[30] Y. L. Liu, K. W. Sun, *Appl. Phys. Lett.* **2011**, *98*, 153702.
[31] I. Rehor, J. Slegerova, J. Kucka, V. Proks, V. Petrakova, M.-P. Adam, F. Treussart, S. Turner, S. Bals, P. Sacha, M. Ledvina, A. M. Wen, N. F. Steinmetz, P. Cigler, *Small* **2014**, *10*, 1106.
[32] B. E. Brinson, J. B. Lassiter, C. S. Levin, R. Bardhan, N. Mirin, N. J. Halas, *Langmuir* **2008**, *24*, 14166.
[33] S. Oldenburg, R. Averitt, S. Westcott, N. Halas, *Chem. Phys. Lett.* **1998**, *288*, 243.
[34] M. R. Rasch, K. V. Sokolov, B. A. Korgel, *Langmuir* **2009**, *25*, 11777.
[35] A. Prokop, J. M. Davidson, *J. Pharm. Sci.* **2008**, *97*, 3518.
[36] B. C. Mei, K. Susumu, I. L. Medintz, J. B. Delehanty, T. J. Mountziaris, H. Mattoussi, *J. Mater. Chem.* **2008**, *18*, 4949.
[37] S. I. Presolski, V. P. Hong, M. G. Finn, *Curr. Protoc. Chem. Biol.* **2011**, *3*, 153.
[38] T. R. Daniels, T. Delgado, G. Helguera, M. L. Penichet, *Clin. Immunol.* **2006**, *121*, 159.
[39] T. R. Daniels, E. Bernabeu, J. A. Rodríguez, S. Patel, M. Kozman, D. A. Chiappetta, E. Holler, J. Y. Ljubimova, G. Helguera, M. L. Penichet, *Biochim. Biophys. Acta BBA – Gen. Subj.* **2012**, *1820*, 291.
[40] R. K. Huang, N. F. Steinmetz, C.-Y. Fu, M. Manchester, J. E. Johnson, *Nanomedicine* **2006**, *6*, 55.
[41] H. Iinuma, K. Maruyama, K. Okinaga, K. Sasaki, T. Sekine, O. Ishida, N. Ogiwara, K. Johkura, Y. Yonemura, *Int. J. Cancer* **2002**, *99*, 130.
[42] M.-F. Weng, B.-J. Chang, S.-Y. Chiang, N.-S. Wang, H. Niu, *Diam. Relat. Mater.* **2012**, *22*, 96.
[43] B.-M. Chang, H.-H. Lin, L-J. Su, W.-D. Lin, R.-J. Lin, Y.-K. Tzeng, R. T. Lee, Y. C. Lee, A. L. Yu, H.-C. Chang, *Adv. Funct. Mater.* **2013**, *23*, 5737.
[44] D. Banerjee, A. P. Liu, N. R. Voss, S. L. Schmid, M. G. Finn, *ChemBioChem* **2010**, *11*, 1273.
[45] K. A. Kang, J. Wang, J. B. Jasinski, S. Achilefu, *J. Nanobiotechnology* **2011**, *9*, 16.
[46] P. G. de Gennes, *Adv. Colloid Interface Sci.* **1987**, *27*, 189.
[47] R. J. Bernardi, A. R. Lowery, P. A. Thompson, S. M. Blaney, J. L. West, *J. Neurooncol.* **2008**, *86*, 165.
[48] O. C. Farokhzad, R. Langer, *ACS Nano* **2009**, *3*, 16.
[49] M. Ferrari, *Nat. Rev. Cancer* **2005**, *5*, 161.
[50] E. K.-H. Chow, D. Ho, *Sci. Transl. Med.* **2013**, *5*, 216rv4.
[51] J. A. Webb, R. Bardhan, *Nanoscale* **2014**, *6*, 2502.
[52] M. Howarth, W. Liu, S. Puthenveetil, Y. Zheng, L. F. Marshall, M. M. Schmidt, K. D. Wittrup, M. G. Bawendi, A. Y. Ting, *Nat. Methods* **2008**, *5*, 397.
[53] I. Rehor, P. Cigler, *Diam. Relat. Mater.* **2014**, *46*, 21.
[54] K. Susumu, B. C. Mei, H. Mattoussi, *Nat. Protoc.* **2009**, *4*, 424.
[55] N. Mohan, C.-S. Chen, H.-H. Hsieh, Y.-C. Wu, H.-C. Chang, *Nano Lett.* **2010**, *10*, 3692.
[56] C. Graf, D. L. J. Vossen, A. Imhof, A. van Blaaderen, *Langmuir* **2003**, *19*, 6693.
[57] V. Hong, S. I. Presolski, C. Ma, M. G. Finn, *Angew. Chem. Int. Ed.* **2009**, *48*, 9879.

WILEY-VCH

Supporting Information

Plasmonic Nanodiamonds – Targeted Core-shell Type Nanoparticles for Cancer Cell Thermoablation

Ivan Rehor, Karin L. Lee, Kevin Chen, Miroslav Hajek, Jan Havlik, Jana Lokajova, Milan Masat, Jitka Slegerova, Sourabh Shukla, Hamed Heidari, Sara Bals, Nicole F. Steinmetz, Petr Cigler**

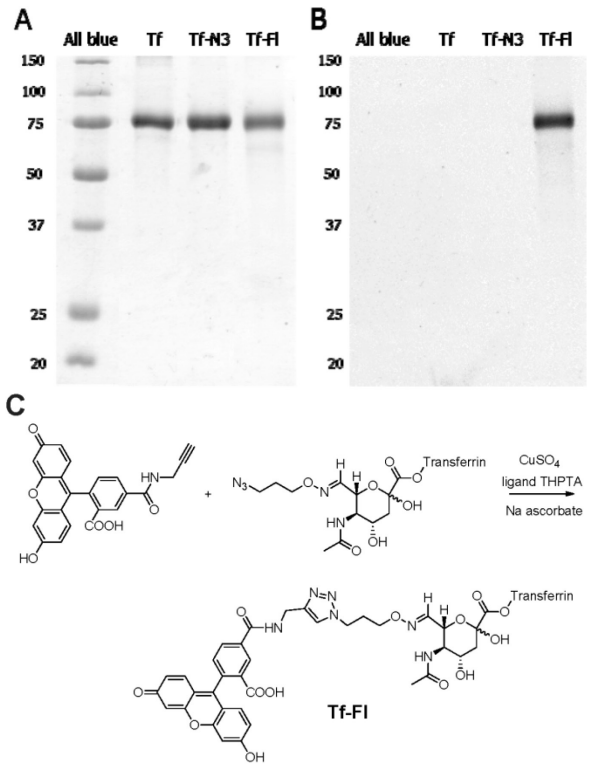

Figure S1. SDS-PAGE of Tf-Fl. (A) 14% SDS-PAGE gel stained with Coomassie Brilliant Blue. From left to right, the lanes contain 4 μL each of Precision Plus Protein All blue standards, **Tf**, **Tf-azide** (Tf-N3), and **Tf-Fl**. (B) Photograph of the gel under UV lamp (before staining). (C) Reaction scheme of **Tf-azide** with fluorescein-alkyne, yielding **Tf-Fl**.

Details of SDS-PAGE analysis: Aliquots (25 μl) of twice-diluted samples (Tf, Tf-azide, and Tf-Fl; 0.01 mM) were mixed with 5 μL sample buffer and boiled for 5 min. We loaded 4 μL portions of the mixtures to the gel.

Resolving gel (14%): 313 mM Tris-HCl, pH 8.8; 13.3% acrylamide; 0.37% N,N´-methylene-bisacrylamide; 0.1% sodium dodecylsulfate (SDS); 0.001% tetramethylethylendiamine; 0.1% ammonium persulfate
Stacking gel (6.6%): 250 mM Tris-HCl, pH 6.8; 6.42% acrylamide, 0.18% N,N´-methylene-bisacrylamide; 0.1% SDS; 0.005% tetramethylethylendiamine; 0.1% ammonium persulfate
Sample buffer: 50 mM Tris-HCl, pH 6.8; 30% glycerol; 10% SDS; 6% 2-mercaptoethanol; 0.012% bromphenol blue
Running buffer: 125 mM Tris-HCl, 1.25M glycine, 0.5% SDS, pH 8.8
Coomassie staining: 0.5% Coomassie Brilliant Blue; 50% methanol; 10% acetic acid
Destaining solution: 10% acetic acid
The gel was stained for 10 min with Coomassie Brilliant Blue and destained overnight. SDS-PAGE was run at 140 V. Figures were processed in Inkscape and the GNU Image Manipulation Program.

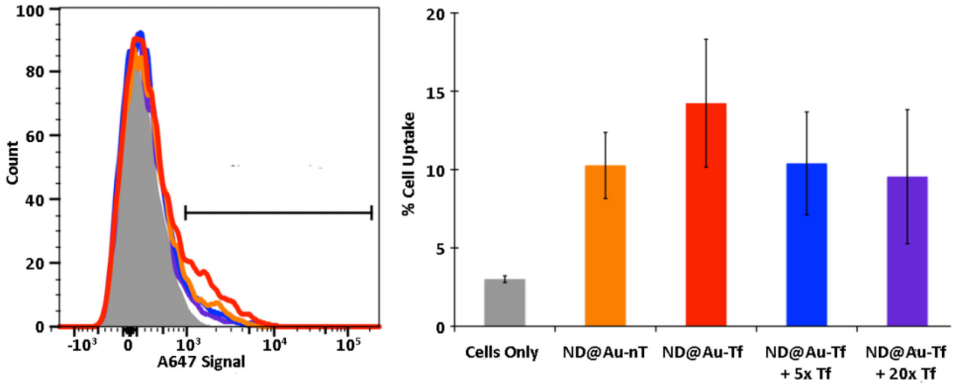

Figure S2. Nanodiamond-SKBR3 cell interactions determined by flow cytometry – competition binding assay. Left: Histograms: gray, cells only; red, **ND@Au-Tf**; orange, **ND@Au-nT**; blue, competition with 5-fold molar excess of free Tf; purple, competition with 20-fold molar excess of free Tf. Right: Statistical analysis showing percent cellular uptake (positive cells shown on histogram by gate) for each sample. Error bars indicate mean ± standard deviation. Experiments were conducted in triplicate, and 10,000 gated events were analyzed.

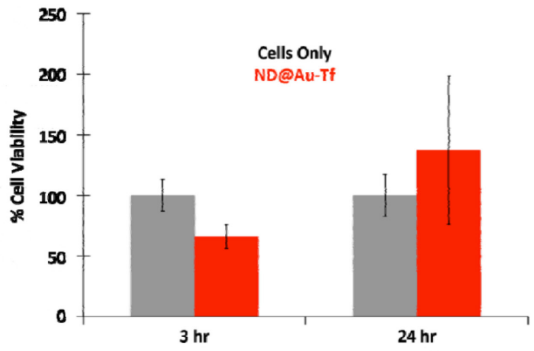

Figure S3. Viability of SKBR3 cells after exposure to ND@Au-Tf. **ND@Au-Tf** (red) were incubated with SKBR3 cells for 3 or 24 h. Cell viability (%) was evaluated using an XTT assay and compared to a cell-only control (gray). Toxicity is not indicated. Although reduced cell viability was indicated for cells exposed to **ND@Au-Tf** for a 3-h time frame, the toxic effects were not statistically significant, nor were toxic effects observed at longer exposure times (24 h).

Appendix B

Appendix C

Stursa, J.; **Havlik, J.**; Petrakova, V.; Gulka, M.; Ralis, J.; Zach, V.; Pulec, Z.; Stepan, V.; Zargaleh, S. A.; Ledvina, M.; Nesladek, M.; Treussart, F.; Cigler, P.Mass Production of Fluorescent Nanodiamonds with a Narrow Emission Intensity Distribution. Carbon 2016, 96, 812–818.

Appendix C

Carbon 96 (2016) 812–818

Contents lists available at ScienceDirect

Carbon

journal homepage: www.elsevier.com/locate/carbon

Mass production of fluorescent nanodiamonds with a narrow emission intensity distribution

Jan Stursa [a], Jan Havlik [b, c], Vladimira Petrakova [d, e], Michal Gulka [d, e], Jan Ralis [a], Vaclav Zach [a], Zdenek Pulec [a], Vaclav Stepan [a], Soroush Abbasi Zargaleh [f], Miroslav Ledvina [b], Milos Nesladek [d, g, h], François Treussart [f], Petr Cigler [b, *]

[a] Nuclear Physics Institute AS CR, v.v.i., 250 68 Rez near Prague, Czech Republic
[b] Institute of Organic Chemistry and Biochemistry AS CR, v.v.i. Flemingovo nam. 2, 166 10 Prague 6, Czech Republic
[c] Faculty of Science, Charles University, Hlavova 2030, 128 40 Prague 2, Czech Republic
[d] Faculty of Biomedical Engineering, Czech Technical University in Prague, Sítná sq. 3105, 272 01 Kladno, Czech Republic
[e] Institute of Physics AS CR, v.v.i., Na Slovance 2, Prague 8, 182 01, Czech Republic
[f] Laboratoire Aimé Cotton, CNRS, Université Paris Sud and ENS Cachan, Université Paris Saclay, F-91405, Orsay, France
[g] IMOMEC Division, IMEC, University Hasselt, Wetenschapspark 1, B-3590, Diepenbeek, Belgium
[h] Institute for Materials Research, University Hasselt, Wetenschapspark 1, B-3590, Diepenbeek, Belgium

ARTICLE INFO

Article history:
Received 25 May 2015
Received in revised form
27 September 2015
Accepted 30 September 2015
Available online 9 October 2015

ABSTRACT

Fluorescent diamond nanocrystals are attracting increasing interest for a broad range of applications, from biolabeling and single particle tracking to nanoscale magnetic field sensing. Their fluorescence stems from nitrogen-vacancy color centers created within synthetic diamond nanoparticles by high-temperature annealing, which results in the association of pre-existing nitrogen impurities and vacancies generated by high-energy particle (electron, proton, or helium ion) beam irradiation. Up to now, diamond nanocrystals have been irradiated as dry powder in a container or deposited as a thin layer on a flat substrate, depending on the type and energy of the irradiating particles. However, these techniques suffer from intrinsic inhomogeneities: the fluence of particles may vary over the whole sample area, as well as the thickness and density of the nanodiamond layer. Here, we present an approach based on direct large-scale irradiation of nanodiamonds in aqueous colloidal solution by high-energy protons. This approach results in a larger fraction of fluorescent particles, with a more homogenous distribution of nitrogen-vacancy centers per particle and less severe lattice damages compared to dry powder irradiation.

1. Introduction

Nanodiamond (ND) is a biocompatible carbon nanomaterial that has been recently introduced as a useful platform for construction of nanoprobes and quantum nanosensors for optical [1–4] and biomedical [5–11] applications. ND can accommodate lattice point defects, nitrogen-vacancy (NV^-) centers, which exhibit an electronic spin resonance between the triplet ground state sublevels that can be detected optically [3,12]. Because the energies of these sublevels are sensitive to external magnetic fields, the NV centers in ND have prospects for use as a nanoscale magnetic field sensor [13–15]. These remarkable properties, together with the perfect photostability of NV center fluorescence, the absence of photoblinking for nanocrystals with diameters larger than 5 nm [16–19] and an emission wavelength in the near-infrared region (low background in a biological environment) [20], have enabled use of NDs in high-impact applications, particularly in the biomedical domain [21–27]. Fluorescent NDs (fNDs) have been proposed as tools for real-time sensing of voltage-gated ion channels [28] and as chemosensors [29,30]. They have already been used, for example, as detectors of very low concentrations of paramagnetic ions [31–33], for tracing of neuronal processes [34], revealing the relations between particle shape and their intracellular fate [35,36], temperature nanosensing [37], in drug delivery systems [38–40] and for targeting of various cell types [41].

NV centers are found as rare defects in synthetic diamonds

* Corresponding author.
E-mail address: cigler@uochb.cas.cz (P. Cigler).

http://dx.doi.org/10.1016/j.carbon.2015.09.111
0008-6223/

owing to the presence of (i) nitrogen impurities at concentrations of 100–200 ppm and (ii) rare vacancies [42,43]. However, at nanometer sizes (<20 nm) the fraction of NDs naturally containing at least one NV center is less than 1% [44]. To increase this fraction and/or the concentration of NV centers, one needs to generate more vacancies, which may be done by irradiating the diamond with high-energy particles (i.e., alpha particles [23,45,46], protons [47–49] or electrons [18,50,51]). After irradiation, the ND is annealed in an inert atmosphere or in a vacuum [52]. In this process, crystal lattice vacancies created by irradiation thermally recombine with naturally occurring nitrogen impurities [53]. Despite the fact that demand for fNDs is rapidly growing, the available procedures for creating NV centers in large amount (mass of about 1 g) of nanodiamonds per run are limited to solid state techniques, which produce a characteristic non-homogeneous distribution of fluorescence centers in individual ND particles [54].

In this study, we present an approach to fND mass production based on direct irradiation of NDs in aqueous colloidal solution with high-energy (≈16 MeV) protons. We show that fNDs prepared this way contain a larger fraction of fluorescent particles, with a more homogenous distribution of NV centers per particle and fewer lattice damages, compared to NDs irradiated in the pellet state with the same proton beam.

2. Materials and methods

2.1. Sample preparation and irradiation procedures

2.1.1. Chemicals

Sodium hydroxide, nitric acid (65%) and sulfuric acid (96%) were purchased from Penta (Czech Republic). Potassium nitrate was purchased from Sigma–Aldrich (Prague, Czech Republic). All chemicals were p.a. quality and were used as received without further purification. Deionized water was prepared with a Millipore Synergy UV Ultrapure water system.

Synthetic NDs containing approximately 100 ppm of natural nitrogen impurities [53] and produced by high pressure high temperature method with size <50 nm (MSY 0–0.05, Microdiamant, Switzerland) were used [55]. The particles were oxidized by air at 510 °C for 5 h in a tube furnace (Thermolyne 21100) calibrated with an external thermocouple (Testo AG 1009). The NDs were subsequently treated with a mixture of HNO_3 and H_2SO_4 (85 °C, 3 days).

2.1.2. Pellet target irradiation procedure

The pellet target was prepared by pressing ND powder into a target back plate using a purpose-made press. The back plate is a duralumin disc with a hole in the middle. ND powder was molded in the hole with 5.88 MPa pressure. The ND layer thickness was chosen to optimally stop accelerated particles in the material. The average density of the material after molding was 2.0 g/cm^3. Targets were molded with a 150 mg portion for proton irradiation. Samples were irradiated with a 14.9 MeV proton beam extracted from the isochronous cyclotron U-120M for 125 min (fluence 5.0×10^{16} H^+/cm^2). The overall dose of protons for the pellet target was 2.52×10^{16}. After irradiation, radiograms of the pellet surface and target back plate (after removal of the ND layer) were recorded using the Cyclone Plus – Storage Phosphor System (Perkin Elmer) (Fig. S1 in the Supplementary material).

2.1.3. Liquid target irradiation procedure

For ND irradiation, the chamber was filled with 2.4 ml of 5% weight ND aqueous colloidal solution. Filling and processing of the irradiated solution was remote-controlled. The sample was irradiated with a 16.0 MeV proton beam extracted from the isochronous cyclotron U-120M for 270 min (fluence 6.6×10^{17} H^+/ml). The overall dose of protons recalculated for 5% of ND particles present in liquid target was 7.93×10^{16}. During irradiation, there was a pressure increase in the chamber. To avoid exceeding the maximal system operating pressure during lengthy irradiation with high currents, we degassed the solution before irradiation and filled the system with helium gas. After irradiation, the ND solution was pushed out of the chamber with helium gas.

2.1.4. Annealing procedure

Samples from both pellet and liquid target were annealed at 900 °C for 1 h under an argon atmosphere followed by air oxidation at 510 °C for 4 h at atmospheric pressure in a furnace tube (Thermolyne 21100) calibrated with an external thermocouple (Testo AG 1009).

2.1.5. Geant4 simulation

Energy deposition in irradiated targets was calculated using the Geant4 general particle transport simulation toolkit [56,57], version 10.2 beta. Simulations were performed for pure liquid water, colloidal solution of ND in liquid water and for a solid ND pellet. User application used for the application was based on the TestEm11 extended example, all calculations were performed with emstandard_opt3 physics list and production cut set to 10 μm.

Liquid target was modeled as a cube of liquid water, with density 1.0 g/cm^3 and 3.5 mm sides. Solid ND pellet was approximated by a cube of amorphous carbon, with 2.0 g/cm^3 density and 1.7 mm sides. Particles were emitted from a point in center of entrance cube surface, toward center of the cube. In both cases, 10^6 primary protons with energy 16 MeV were modeled.

In order to describe the colloidal solution of ND in liquid water, the NDs were approximated by carbon spheres with 35 nm diameter and 3.5 g/cm^3 density. Due to memory constraints, we used a nested replicated geometry: 636 ND spheres were randomly placed in a 1-μm side cube and this cube has then been reused to fill the target 3 × 2 × 3 mm volume. 16 MeV protons were shot from a 3 × 3 μm surface at entrance volume side, along the x-axis. Calculation was performed for 10^5 primary protons.

2.2. Fluorescence and size measurements

2.2.1. Raman and photoluminescence measurements

Before measurement, all samples were lyophilized from water and diluted in deionized water to a concentration of 10 mg/ml with a high-power ultrasonic horn (Hielscher UP400S, Sonotrode H3) using 400 W at a 1:1 (on/off) cycle for 30 min under liquid cooling. The samples were prepared by drop-casting of the aqueous dispersion of NDs on the polished silicon wafer. Raman and luminescence spectra were measured using a Renishaw InVia Raman Microscope; the excitation wavelength was 514 nm (luminescence measurements) and 325 nm (Raman measurements) with 15 mW laser power,×20 objective. The exposure time was 6 s, 10 accumulations. Twenty measurements were taken for each sample. The Raman and luminescence spectra were taken at room temperature.

2.2.2. Simultaneous AFM and fluorescence intensity measurements

The sizes of the spincoated NDs were estimated with an atomic force microscope (MFP – 3D-BIO, Asylum Research, USA) placed on top of a homemade fluorescence confocal microscope used to locate fNDs (more details in Ref. [58]). The AFM enabled us to measure the height (i.e., the vertical dimension) of the ND with a resolution of approximately 1 nm, but the lateral resolution was practically limited to about 80 nm due to the finite radius of the curvature of the AFM tip. The confocal inverted fluorescence microscope has a single NV color center sensitivity, and therefore

Appendix C

provides a means to determine whether each ND observed by AFM contains at least one NV center.

2.2.3. Automatic AFM and fluorescence scan analysis

The heights and fluorescence intensities of combined AFM-confocal scans (see Fig. S2 in the Supplementary material for examples of such scans) were determined with the following automatic data processing procedure: (i) NDs were identified in the AFM scan using the Spot Detector plugin of ICY image processing software [59] (Institut Pasteur, Paris, France), relying on a "à trou" wavelet decomposition of the image followed by a thresholding of non-significant coefficients, a strategy that is well-adapted to a low signal-over-background ratio [60]; (ii) AFM spot vertical sizes were extracted, and the size distributions were plotted for both types of targets (Fig. S3 in the Supplementary material); (iii) the fluorescence spots corresponding to each ND of the AFM scan were localized in the confocal scan; they have a full width at half maximum size limited by diffraction to about 250 nm, covering 19 pixels in each *X* and *Y* direction. The fluorescence intensity attached to each spot is defined as the maximum among the pixels forming each spot.

3. Results and discussion

The number of vacancies created in the diamond increases as the hadron particles slow down. Most of the damage is therefore caused at the end of the particle path (Bragg peak), contributing to a nonhomogeneous distribution of formed vacancies (and consequently of NV centers). Although for optimal production of NV centers relatively low particle energies (tens of keV) are needed [23,61], the particles' penetration depth is, in this case, very small and the created higher densities of NV centers in particles are at the expense of small fND quantities produced per batch. This problem can be partially compensated by depositing ND on a long metallic tape to form a thin film, exposing it to a beam and slowly winding [23]. However, direct mass production of fNDs in a pellet target (Fig. 1(a)) introduces further serious technological challenges related to i) target surface irradiation homogeneity and ii) the particle range uncertainty.

Problems with inhomogeneous surface irradiation dose are caused mainly by the shape of the irradiation beam spot. After acceleration and extraction from the cyclotron, the ions are directed to the target by ion-optical elements. To scale up the mass of irradiated NDs, uniform irradiation of an ND pellet with a diameter of 8–10 mm is needed. For that reason, the particle beam is defocused and consequently collimated just before hitting the target. Despite this beam adjustment, the particle density on the target surface may vary up to 20% due to beam distribution of particle density in the beam cross-section.

The uncertainty in the range of particles is mainly caused by inhomogeneous material density and by particle energy spread. The ND pellet to be irradiated is prepared by mechanical pressing of ND powder, which cannot ensure a strictly homogeneous layer density. Moreover, the cyclotron beam is not monoenergetic. For example, the energy spread of a typically used H^+ beam with mean energy 15 MeV is approximately ±0.25 MeV, which corresponds to a difference in particle ranges from 1.37 mm to 1.45 mm. Due to these uncertainties, the accelerated particles are not stopped at the same depth during penetration of the ND layer, and some of them even leave the ND layer and end up in the target back plate. We have identified these problems from radiograms of ND pellet and target back plate recorded after irradiation (Fig. S1 in the Supplementary material). Indeed, the inhomogeneities result in a complex spatial distribution of stopping powers and subsequently affect the number of vacancies created. Although it is possible to repeat irradiation procedures several times with homogenization and re-deposition steps on the target between every irradiation [23], this approach lengthens the preparation.

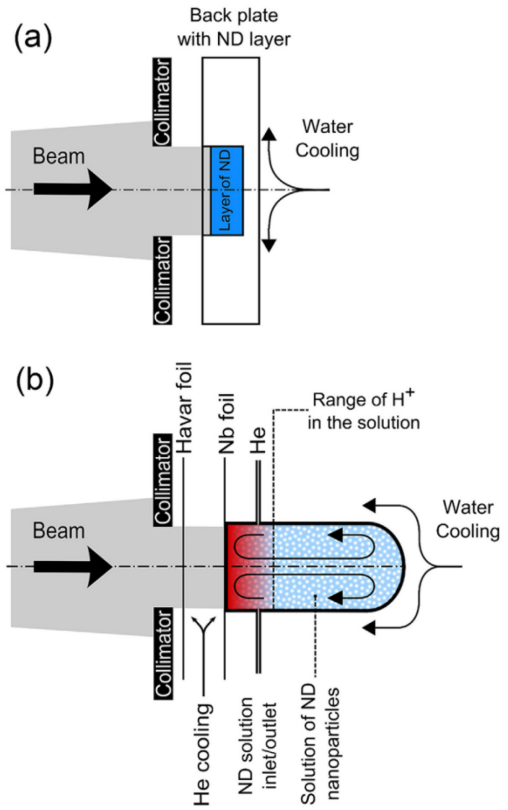

Fig. 1. ND pellet target (a) and liquid target (b) irradiation configurations. The pellet target contains a compressed solid ND pellet. The liquid target is filled with 5% ND aqueous solution. The "active stopping zone" for protons in liquid target is outlined by proton range. The arrows inside the liquid target indicate a vigorous agitation occurring upon penetration of the proton beam in the solution. (A color version of this figure can be viewed online.)

To limit the undesirable influences of inhomogeneous irradiation and sample preparations, we constructed a target enabling direct irradiation of an aqueous colloidal solution of NDs. The main component of the liquid target setup is a water-cooled niobium chamber with niobium entrance foil cooled with helium and an integrated collimator at the beam entrance (Fig. 1(b)). The target is separated from the ion-beam line by a thin Havar foil. The ion-beam penetrates through both foils and enters then directly the solution of NDs.

To compare the situations occurring in the liquid and pellet targets we calculated depth-dose curves of protons in 5% ND aqueous solution and a compressed solid ND pellet (Fig. 2). Note that for calculations we used exactly the same same proton energies (16 MeV) for both pellets, although the experimentally used energies were slightly different (see Materials and methods). Simulations using the same energies ensure direct comparability of the depth-dose distributions.

Although the maxima of energy deposition in both environments falls into the same order of magnitude (~1.5 and 2.7 mm,

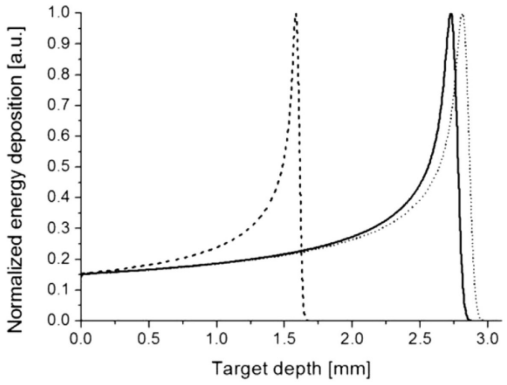

Fig. 2. Normalized depth-dose distribution of a 16 MeV proton beam in a compressed solid ND pellet (density of 2.0 g/cm^3; dashed line), 5% ND aqueous solution (solid line) and water (dotted line). The simulation was performed using Geant4 software [56,57].

respectively), the processes related to ion stopping are distinctly different. While the solid ND layer is "imprinted" by the beam to characteristic Bragg-distribution of vacancies, in the aqueous solution the inherent thermal convection caused by the beam contributes to a vigorous agitation. The ND particles are therefore continuously exchanged in the "active stopping zone" (up to approximately 2.8 mm behind the Nb foil), which is reflected in better irradiation homogeneity (see below). The presence of ND in solution has only a negligible effect on the position of Bragg peak in water (Fig. 2).

We irradiated the nanodiamonds either in a pellet or liquid target form (see Materials and methods for details) and analyzed their properties. First, we focused on analyzing the irradiation damage of the diamond lattice for both types of targets. We expected that the liquid setup can contribute to a decrease in the diamond lattice damage caused by local sample overheating, which is typically followed by strong surface graphitization. From the lower G band intensity observed in Raman spectra for the liquid target, we inferred that liquid target NDs are better protected from graphitization than pellet target NDs (Fig. 3). After high temperature annealing, which naturally causes graphitization of oxidized NDs till subsurface region, the content of sp^2 carbon in both samples is approximately the same. Finally, after air oxidation at 510 °C and 5 h (which we previously found as optimal for this type of particles [53]) the samples from both the target set-up had a comparable sp^3 purity. We note that an accurate control of annealing temperatures is a key parameter in reproducibility and comparability of the experiments, because the air oxidation can contribute, besides the surface removal of sp^2 carbon, also to decrease of particle size [62].

To prove the superiority of the liquid target over pellet target irradiation, we compared the fraction of fluorescent particles in the two types of irradiated samples. To that purpose, we measured both the size and fluorescence intensity of fNDs at the single particle level, after having spincoated ND suspensions on quartz coverslips with the appropriate dilution to achieve a surface density of approximately one ND per square micrometer. We then raster-scanned the samples and measured the ND heights with an atomic force microscope (AFM) installed on a homemade confocal microscope, allowing us to simultaneously record the fluorescence intensity of each ND. From these data, we inferred a fraction of 77% (135 fNDs among a total of 175 NDs detected by AFM) of fNDs in the liquid target sample, and only 24% (225 fNDs among a total of 950

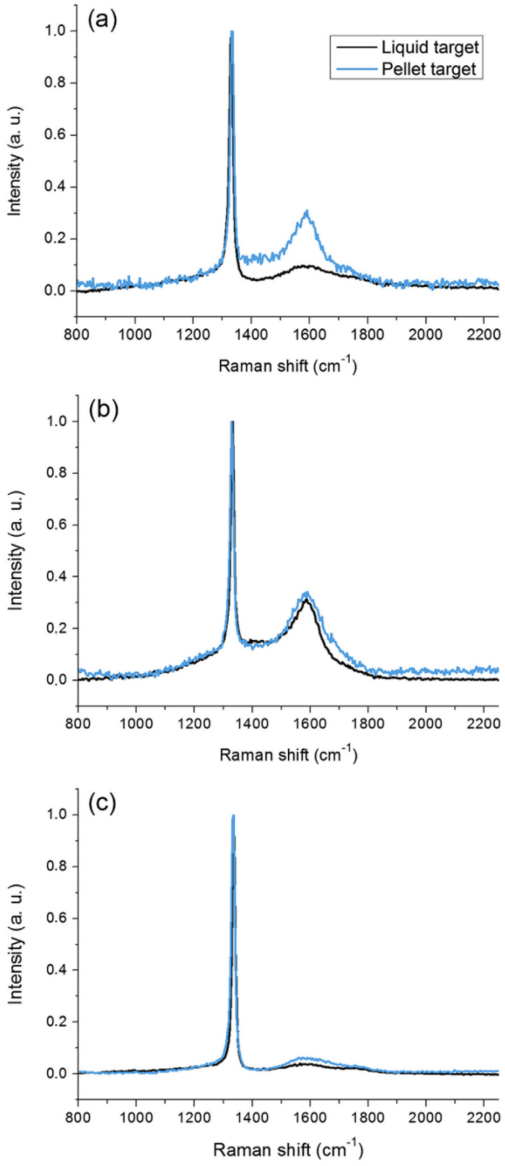

Fig. 3. Raman spectra of NDs from the pellet target and liquid target setups. Spectra were measured (a) after irradiation, (b) after annealing (900 °C, 1 h, argon) and (c) after air oxidation (510 °C, 4 h). The spectral intensities are normalized to the diamond Raman band (1332 cm^{-1}). The G-band (1583 cm^{-1}) originates from graphite-like inclusions consisting of sp^2-hybridized carbon atoms and indicates the presence of defective graphite structures [43]. (A color version of this figure can be viewed online.)

NDs detected by AFM) fluorescent particles in the pellet target (Table 1).

Fig. 4 shows the fluorescence intensity distributions of individual fNDs in both samples. The solid target has higher mean brightness compared to the liquid target (Table 1), as well as a larger standard deviation. This can be explained by the fact that some stationary particles in the pellet target experience a larger

Appendix C

Table 1
Single particle analysis of the fluorescence intensity for pellet and liquid target samples.

	Pellet target	Liquid target
Fraction of fNDs (%)	24	77
Mean fluorescence intensity (kcounts/s)	122 ± 8	66 ± 7
Median intensity (kcounts/s)	75	38
Standard deviation (kcounts/s)	123	80

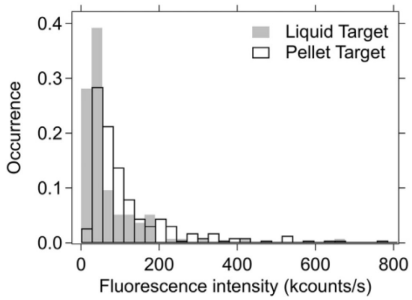

Fig. 4. Normalized distribution of single fND fluorescence intensity as measured by confocal fluorescence microscopy for pellet (open black bars) and liquid (solid grey bars) targets. Excitation laser wavelength: 532 nm, laser power: 200 μW.

radiation dose compared to non-stationary particles in solution, leading to the creation of a larger concentration of vacancies for some NDs. In contrast, in the liquid target case, the effective dose per particle for the same irradiation conditions is smaller but also more homogeneous, owing to the random thermal motion of particles in solution, leading to a smaller mean fluorescence intensity value together with a narrower distribution (see standard deviations in Table 1).

To confirm that the single particle fluorescence intensity distributions (Fig. 4) correspond to different fND populations and is not biased by a too small sample size, we performed a two-sample Wilcoxon-Mann-Whitney rank test, which tests the null hypothesis that two sets of data are from the same population against an alternative hypothesis. Such a test is well-adapted to compare non-normal distributions. The test yielded a very low two-tail probability of $P = 1.8 \times 10^{-15}$ (typically, two sets of data are considered with very high confidence to stem from different populations when $P < 0.001$). Therefore, the hypothesis that the two sets of fluorescence intensity data are from the same fND population can be rejected.

It is worth pointing out that liquid and pellet target irradiations yield identical ensemble photoluminescence spectra with the same ratio of the negatively charged NV^- over the neutral form NV^0 as identified from their zero-phonon lines (Fig. 5). As both sets of samples were treated with an identical post-annealing oxidative procedure, the effect of surface composition [29,52] should not influence the shape of spectra.

4. Conclusions

We showed mass production of fND by irradiating an aqueous suspension of diamond nanocrystals yields a more homogeneous distribution of NV color centers per particle than solid phase pellet irradiation with a three-fold larger fraction of fNDs, which is important for applications such as bioimaging. Moreover, we foresee that lower fluence irradiation in a liquid target followed by high-temperature annealing and air oxidation can also be used to

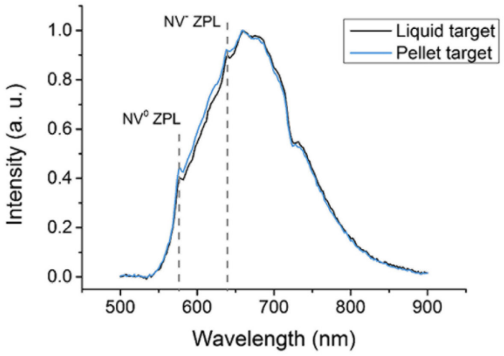

Fig. 5. Photoluminescence spectra of fNDs from liquid and pellet targets dropcasted on a silicon wafer. The spectra were normalized at their maximum. Vertical dash lines labeled ZPL denotes the Zero Phonon Line of either the NV^- (wavelength 637 nm) or NV^0 (wavelength 575 nm) color center with typical phonon side band structures [63]. (A color version of this figure can be viewed online.)

produce fNDs containing exactly one NV center in high yield, improving upon a recently reported approach based solely on annealing and air oxidation [64]. Such particles are essential for magnetic field sensing relying on the optical detection of electron spin resonances of NV^- color centers.

Acknowledgments

The work was supported by MZ-VES project Nr. 15–33094A. Irradiations of NDs were carried out at the CANAM infrastructure of the NPI ASCR Rez supported through MŠMT project No. LM2011019. MN, VP and MG would like to acknowledge the financial support from ESF – Grant No. CZ.1.07/2.3.00/20.0306 and CZ.1.05/4.1.00/11.0253. MN would like to acknowledge the project FWO (Flanders) G.0.943.11.N.10. Work of SAZ was supported by a public grant overseen by the French National Research Agency (ANR) as part of the "Investissement d'Avenir" program IDEX Paris-Saclay, ANR-11-IDEX-0003-02.

Appendix A. Supplementary data

Supplementary data related to this article can be found at http://dx.doi.org/10.1016/j.carbon.2015.09.111.

References

[1] I. Aharonovich, A.D. Greentree, S. Prawer, Diamond photonics, Nat. Photonics 5 (2011) 397–405, http://dx.doi.org/10.1038/nphoton.2011.54.
[2] J. Wrachtrup, F. Jelezko, B. Grotz, L. McGuinness, Nitrogen-vacancy centers close to surfaces, MRS Bull. 38 (2013) 149–154, http://dx.doi.org/10.1557/mrs.2013.22.
[3] F. Jelezko, J. Wrachtrup, Single defect centres in diamond: a review, Phys. Status Solidi A 203 (2006) 3207–3225, http://dx.doi.org/10.1002/pssa.200671403.
[4] Vlasov II, A.A. Shiryaev, T. Rendler, S. Steinert, S.-Y. Lee, D. Antonov, et al., Molecular-sized fluorescent nanodiamonds, Nat. Nanotechnol. 9 (2014) 54–58, http://dx.doi.org/10.1038/nnano.2013.255.
[5] I. Badea, R. Kaur, Nanodiamonds as novel nanomaterials for biomedical applications: drug delivery and imaging systems, Int. J. Nanomed. 8 (2013) 203–220, http://dx.doi.org/10.2147/IJN.S37348.
[6] V.N. Mochalin, O. Shenderova, D. Ho, Y. Gogotsi, The properties and applications of nanodiamonds, Nat. Nanotechnol. 7 (2011) 11–23, http://dx.doi.org/10.1038/nnano.2011.209.
[7] A. Krueger, New carbon materials: biological applications of functionalized nanodiamond materials, Chem. Eur. J. 14 (2008) 1382–1390, http://dx.doi.org/10.1002/chem.200700987.
[8] V. Vaijayanthimala, H.-C. Chang, Functionalized fluorescent nanodiamonds for biomedical applications, Nanomedicine 4 (2009) 47–55, http://dx.doi.org/

Appendix C

10.2217/17435889.4.1.47.
[9] O. Faklaris, V. Joshi, T. Irinopoulou, P. Tauc, M. Sennour, H. Girard, et al., Photoluminescent diamond nanoparticles for cell labeling: study of the uptake mechanism in mammalian cells, ACS Nano 3 (2009) 3955–3962, http://dx.doi.org/10.1021/nn901014j.
[10] J. Slegerova, M. Hajek, I. Rehor, F. Sedlak, J. Stursa, M. Hruby, et al., Designing the nanobiointerface of fluorescent nanodiamonds: highly selective targeting of glioma cancer cells, Nanoscale 7 (2015) 415–420, http://dx.doi.org/10.1039/C4NR02776K.
[11] L. Zhao, Y.-H. Xu, H. Qin, S. Abe, T. Akasaka, T. Chano, et al., Platinum on nanodiamond: a promising prodrug conjugated with stealth polyglycerol, targeting peptide and acid-responsive antitumor drug, Adv. Funct. Mater. 24 (2014) 5348–5357, http://dx.doi.org/10.1002/adfm.201304298.
[12] N.B. Manson, J.P. Harrison, M.J. Sellars, Nitrogen-vacancy center in diamond: model of the electronic structure and associated dynamics, Phys. Rev. B 74 (2006), http://dx.doi.org/10.1103/PhysRevB.74.104303.
[13] J.R. Maze, P.L. Stanwix, J.S. Hodges, S. Hong, J.M. Taylor, P. Cappellaro, et al., Nanoscale magnetic sensing with an individual electronic spin in diamond, Nature 455 (2008) 644–647, http://dx.doi.org/10.1038/nature07279.
[14] M.S. Grinolds, S. Hong, P. Maletinsky, L. Luan, M.D. Lukin, R.L. Walsworth, et al., Nanoscale magnetic imaging of a single electron spin under ambient conditions, Nat. Phys. 9 (2013) 215–219, http://dx.doi.org/10.1038/nphys2543.
[15] F. Dolde, H. Fedder, M.W. Doherty, T. Nöbauer, F. Rempp, G. Balasubramanian, et al., Electric-field sensing using single diamond spins, Nat. Phys. 7 (2011) 459–463, http://dx.doi.org/10.1038/nphys1969.
[16] C. Bradac, T. Gaebel, N. Naidoo, M.J. Sellars, J. Twamley, L.J. Brown, et al., Observation and control of blinking nitrogen-vacancy centres in discrete nanodiamonds, Nat. Nanotechnol. 5 (2010) 345–349, http://dx.doi.org/10.1038/nnano.2010.56.
[17] J.-P. Boudou, J. Tisler, R. Reuter, A. Thorel, P.A. Curmi, F. Jelezko, et al., Fluorescent nanodiamonds derived from HPHT with a size of less than 10 nm, Diam. Relat. Mater. 37 (2013) 80–86, http://dx.doi.org/10.1016/j.diamond.2013.05.006.
[18] A. Gruber, A. Dräbenstedt, C. Tietz, L. Fleury, J. Wrachtrup, C. von Borczyskowski, Scanning confocal optical microscopy and magnetic resonance on single defect centers, Science 276 (1997) 2012–2014, http://dx.doi.org/10.1126/science.276.5321.2012.
[19] J. Tisler, R. Reuter, A. Lämmle, F. Jelezko, G. Balasubramanian, P.R. Hemmer, et al., Highly efficient FRET from a single nitrogen-vacancy center in nanodiamonds to a single organic molecule, ACS Nano 5 (2011) 7893–7898, http://dx.doi.org/10.1021/nn2021259.
[20] R. Weissleder, V. Ntziachristos, Shedding light onto live molecular targets, Nat. Med. 9 (2003) 123–128, http://dx.doi.org/10.1038/nm0103-123.
[21] N. Mohan, C.-S. Chen, H.-H. Hsieh, Y.-C. Wu, H.-C. Chang, In vivo imaging and toxicity assessments of fluorescent nanodiamonds in caenorhabditis elegans, Nano Lett. 10 (2010) 3692–3699, http://dx.doi.org/10.1021/nl1021909.
[22] V. Vaijayanthimala, P.-Y. Cheng, S.-H. Yeh, K.-K. Liu, C.-H. Hsiao, J.-I. Chao, et al., The long-term stability and biocompatibility of fluorescent nanodiamond as an in vivo contrast agent, Biomaterials 33 (2012) 7794–7802, http://dx.doi.org/10.1016/j.biomaterials.2012.06.084.
[23] Y.-R. Chang, H.-Y. Lee, K. Chen, C.-C. Chang, D.-S. Tsai, C.-C. Fu, et al., Mass production and dynamic imaging of fluorescent nanodiamonds, Nat. Nanotechnol. 3 (2008) 284–288, http://dx.doi.org/10.1038/nnano.2008.99.
[24] C.-Y. Fang, V. Vaijayanthimala, C.-A. Cheng, S.-H. Yeh, C.-F. Chang, C.-L. Li, et al., The exocytosis of fluorescent nanodiamond and its use as a long-term cell tracker, Small 7 (2011) 3363–3370, http://dx.doi.org/10.1002/smll.201101233.
[25] A. Alhaddad, M.-P. Adam, J. Botsoa, G. Dantelle, S. Perruchas, T. Gacoin, et al., Nanodiamond as a vector for siRNA delivery to Ewing sarcoma cells, Small 7 (2011) 3087–3095, http://dx.doi.org/10.1002/smll.201101193.
[26] I. Rehor, J. Slegerova, J. Kucka, V. Proks, V. Petrakova, M.-P. Adam, et al., Fluorescent nanodiamonds embedded in biocompatible translucent shells, Small 10 (2014) 1106–1115, http://dx.doi.org/10.1002/smll.201302336.
[27] I. Rehor, H. Mackova, S.K. Filippov, J. Kucka, V. Proks, J. Slegerova, et al., Fluorescent nanodiamonds with bioorthogonally reactive protein-resistant polymeric coatings, ChemPlusChem 79 (2014) 21–24, http://dx.doi.org/10.1002/cplu.201300339.
[28] L.T. Hall, C.D. Hill, J.H. Cole, B. Stadler, F. Caruso, P. Mulvaney, et al., Monitoring ion-channel function in real time through quantum decoherence, Proc. Natl. Acad. Sci. 107 (2010) 18777–18782, http://dx.doi.org/10.1073/pnas.1002562107.
[29] V. Petrakova, A. Taylor, I. Kratochvilova, F. Fendrych, J. Vacik, J. Kucka, et al., Luminescence of nanodiamond driven by atomic functionalization: towards novel detection principles, Adv. Funct. Mater. 22 (2012) 812–819, http://dx.doi.org/10.1002/adfm.201101936.
[30] V. Petrakova, I. Rehor, J. Stursa, M. Ledvina, M. Nesladek, P. Cigler, Charge-sensitive fluorescent nanosensors created from nanodiamonds, Nanoscale 7 (2015) 12307–12311, http://dx.doi.org/10.1039/C5NR00712G.
[31] S. Kaufmann, D.A. Simpson, L.T. Hall, V. Perunicic, P. Senn, S. Steinert, et al., Detection of atomic spin labels in a lipid bilayer using a single-spin nanodiamond probe, Proc. Natl. Acad. Sci. U. S. A. 110 (2013) 10894–10898, http://dx.doi.org/10.1073/pnas.1300640110.
[32] L.P. McGuinness, L.T. Hall, A. Stacey, D.A. Simpson, C.D. Hill, J.H. Cole, et al., Ambient nanoscale sensing with single spins using quantum decoherence, New J. Phys. 15 (2013) 073042, http://dx.doi.org/10.1088/1367-2630/15/7/073042.
[33] A. Ermakova, G. Pramanik, J.-M. Cai, G. Algara-Siller, U. Kaiser, T. Weil, et al., Detection of a few metallo-protein molecules using color centers in nanodiamonds, Nano Lett. 13 (2013) 3305–3309, http://dx.doi.org/10.1021/nl4015233.
[34] T.-C. Hsu, K.-K. Liu, H.-C. Chang, E. Hwang, J.-I. Chao, Labeling of neuronal differentiation and neuron cells with biocompatible fluorescent nanodiamonds, Sci. Rep. 4 (2014) 5004, http://dx.doi.org/10.1038/srep05004.
[35] Z. Chu, S. Zhang, B. Zhang, C. Zhang, C.-Y. Fang, I. Rehor, et al., Unambiguous observation of shape effects on cellular fate of nanoparticles, Sci. Rep. 4 (2014) 4495, http://dx.doi.org/10.1038/srep04495.
[36] Z. Chu, K. Miu, P. Lung, S. Zhang, S. Zhao, H.-C. Chang, et al., Rapid endosomal escape of prickly nanodiamonds: implications for gene delivery, Sci. Rep. 5 (2015) 11661, http://dx.doi.org/10.1038/srep11661.
[37] Y.-K. Tzeng, P.-C. Tsai, H.-Y. Liu, O.Y. Chen, H. Hsu, F.-G. Yee, et al., Time-resolved luminescence nanothermometry with nitrogen-vacancy centers in nanodiamonds, Nano Lett. 15 (2015) 3945–3952, http://dx.doi.org/10.1021/acs.nanolett.5b00836.
[38] H. Huang, E. Pierstorff, E. Osawa, D. Ho, Active nanodiamond hydrogels for chemotherapeutic delivery, Nano Lett. 7 (2007) 3305–3314, http://dx.doi.org/10.1021/nl071521o.
[39] M. Chen, E.D. Pierstorff, R. Lam, S.-Y. Li, H. Huang, E. Osawa, et al., Nanodiamond-mediated delivery of water-insoluble therapeutics, ACS Nano 3 (2009) 2016–2022, http://dx.doi.org/10.1021/nn900480m.
[40] M. Chen, X.-Q. Zhang, H.B. Man, R. Lam, E.K. Chow, D. Ho, Nanodiamond vectors functionalized with polyethylenimine for siRNA delivery, J. Phys. Chem. Lett. 1 (2010) 3167–3171, http://dx.doi.org/10.1021/jz1013278.
[41] J. Slegerova, I. Rehor, J. Havlik, H. Raabova, E. Muchova, P. Cigler, Nanodiamonds as intracellular probes for imaging in biology and medicine, in: A. Prokop, Y. Iwasaki, A. Harada (Eds.), Intracellular Delivery IISpringer Netherlands, Dordrecht, 2014, pp. 363–401.
[42] A.M. Zaitsev, Vibronic spectra of impurity-related optical centers in diamond, Phys. Rev. B 61 (2000) 12909–12922, http://dx.doi.org/10.1103/PhysRevB.61.12909.
[43] A. Zaitsev, Optical Properties of Diamond a Data Handbook, Springer Berlin Heidelberg, Berlin, Heidelberg, 2001.
[44] R. Schirhagl, K. Chang, M. Loretz, C.L. Degen, Nitrogen-vacancy centers in diamond: nanoscale sensors for physics and biology, Annu. Rev. Phys. Chem. 65 (2014) 83–105, http://dx.doi.org/10.1146/annurev-physchem-040513-103659.
[45] F.C. Waldermann, P. Olivero, J. Nunn, K. Surmacz, Z.Y. Wang, D. Jaksch, et al., Creating diamond color centers for quantum optical applications, Diam. Relat. Mater. 16 (2007) 1887–1895, http://dx.doi.org/10.1016/j.diamond.2007.09.009.
[46] T.-J. Wu, Y.-K. Tzeng, W.-W. Chang, C.-A. Cheng, Y. Kuo, C.-H. Chien, et al., Tracking the engraftment and regenerative capabilities of transplanted lung stem cells using fluorescent nanodiamonds, Nat. Nanotechnol. 8 (2013) 682–689, http://dx.doi.org/10.1038/nnano.2013.147.
[47] S.-J. Yu, M.-W. Kang, H.-C. Chang, K.-M. Chen, Y.-C. Yu, Bright fluorescent nanodiamonds: no photobleaching and low cytotoxicity, J. Am. Chem. Soc. 127 (2005) 17604–17605, http://dx.doi.org/10.1021/ja0567081.
[48] C.C. Fu, H.Y. Lee, K. Chen, T.S. Lim, H.Y. Wu, P.K. Lin, et al., Characterization and application of single fluorescent nanodiamonds as cellular biomarkers, Proc. Natl. Acad. Sci. 104 (2007) 727–732.
[49] M.-F. Weng, B.-J. Chang, S.-Y. Chiang, N.-S. Wang, H. Niu, Cellular uptake and phototoxicity of surface-modified fluorescent nanodiamonds, Diam. Relat. Mater. 22 (2012) 96–104, http://dx.doi.org/10.1016/j.diamond.2011.12.035.
[50] J.-P. Boudou, P.A. Curmi, F. Jelezko, J. Wrachtrup, P. Aubert, M. Sennour, et al., High yield fabrication of fluorescent nanodiamonds, Nanotechnology 20 (2009) 235602, http://dx.doi.org/10.1088/0957-4484/20/23/235602.
[51] G. Dantelle, A. Slablab, L. Rondin, F. Lainé, F. Carrel, P. Bergonzo, et al., Efficient production of NV colour centres in nanodiamonds using high-energy electron irradiation, J. Lumin. 130 (2010) 1655–1658, http://dx.doi.org/10.1016/j.jlumin.2009.12.003.
[52] L. Rondin, G. Dantelle, A. Slablab, F. Grosshans, F. Treussart, P. Bergonzo, et al., Surface-induced charge state conversion of nitrogen-vacancy defects in nanodiamonds, Phys. Rev. B 82 (2010) 115449, http://dx.doi.org/10.1103/PhysRevB.82.115449, 1 – 5.
[53] J. Havlik, V. Petrakova, I. Rehor, V. Petrak, M. Gulka, J. Stursa, et al., Boosting nanodiamond fluorescence: towards development of brighter probes, Nanoscale 5 (2013) 3208–3211, http://dx.doi.org/10.1039/c2nr32778c.
[54] O. Faklaris, J. Botsoa, T. Sauvage, J.-F. Roch, F. Treussart, Photoluminescent nanodiamonds: comparison of the photoluminescence saturation properties of the NV color center and a cyanine dye at the single emitter level, and study of the color center concentration under different preparation conditions, Diam. Relat. Mater. 19 (2010) 988–995, http://dx.doi.org/10.1016/j.diamond.2010.03.002.
[55] I. Rehor, P. Cigler, Precise estimation of HPHT nanodiamond size distribution based on transmission electron microscopy image analysis, Diam. Relat. Mater. 46 (2014) 21–24, http://dx.doi.org/10.1016/j.diamond.2014.04.002.
[56] S. Agostinelli, J. Allison, K. Amako, J. Apostolakis, H. Araujo, P. Arce, et al., Geant4—a simulation toolkit, Nucl. Instrum. Methods Phys. Res. Sect. Accel. Spectrom. Detect. Assoc. Equip. 506 (2003) 250–303, http://dx.doi.org/10.1016/S0168-9002(03)01368-8.

Appendix C

Appendix D

Havlik, J.; Raabova, H.; Gulka, M.; Petrakova, V.; Krecmarova, M.; Masek, V.; Lousa, P.; Stursa, J.; Boyen, H.-G.; Nesladek, M.; Cigler, P.; Benchtop Fluorination of Fluorescent Nanodiamonds on a Preparative Scale: Toward Unusually Hydrophilic Bright Particles. *Adv. Funct. Mater.* **2016**, 26, 4134–4142.

FULL PAPER

ADVANCED FUNCTIONAL MATERIALS
www.afm-journal.de

Materials Views
www.MaterialsViews.com

Benchtop Fluorination of Fluorescent Nanodiamonds on a Preparative Scale: Toward Unusually Hydrophilic Bright Particles

*Jan Havlik, Helena Raabova, Michal Gulka, Vladimira Petrakova, Marie Krecmarova, Vlastimil Masek, Petr Lousa, Jan Stursa, Hans-Gerd Boyen, Milos Nesladek, and Petr Cigler**

Fluorination of diamonds modulates their optical and electromagnetic properties and creates surfaces with increased hydrophobicity. In addition, fluorination of diamonds and nanodiamonds has been recently shown to stabilize fluorescent nitrogen-vacancy centers, which can serve as extremely sensitive single atomic defects in a vast range of sensing applications from quantum physics to high-resolution biological imaging. Traditionally, fluorination of carbon nanomaterials has been achieved using harsh and complex experimental conditions, creating hydrophobic interfaces with difficult dispersibility in aqueous environments. Here, a mild benchtop approach to nanodiamond fluorination is described using selective Ag^+-catalyzed radical substitution of surface carboxyls for fluorine. In contrast to other approaches, this high-yielding procedure does not etch diamond carbons and produces a highly hydrophilic interface with mixed C–F and C–OH termination. This dual functionalization of nanodiamonds suppresses detrimental hydrophobic interactions that would lead to colloidal destabilization of nanodiamonds. It is also demonstrated that even a relatively low surface density of fluorine contributes to stabilization of negatively charged nitrogen-vacancy centers and boosts their fluorescence. The simultaneous control of the surface hydrophilicity and the fluorescence of nitrogen-vacancy centers is an important issue enabling direct application of fluorescent nanodiamonds as nanosensors for quantum optical and magnetometry measurements operated in biological environment.

1. Introduction

In the past two decades, fluorinated carbon nanomaterials (CNMs) have attracted considerable interest because of their potential applications in electronic and optical devices. Introduction of a C—F bond confers a new quality to CNMs by changing and shifting their optical, electromagnetic, and mechanical properties,[1] specifically by opening of a bandgap.[2,3] Moreover, a fluorine-terminated surface can serve as an intermediate for subsequent modification by other reagents[4,5] and for structural control during synthesis, such as cutting of nanotubes.[6]

Fluorination of graphene,[5,7] carbon nanotubes,[8] and nano-onions[9] has been achieved using elemental fluorine. Alternative techniques, such as CF_4 plasma treatment and reaction with XeF_2, have been used to fluorinate carbon nanotubes[10] and graphene,[1] respectively. However, fluorination of nanodiamonds (NDs) is a special chemical challenge because of the fundamentally different

J. Havlik, H. Raabova, P. Lousa, Dr. P. Cigler
Institute of Organic Chemistry and Biochemistry ASCR
v.v.i. Flemingovo nam. 2, CZ-166 10 Prague 6, Czech Republic
E-mail: petr.cigler@uochb.cas.cz
J. Havlik
Faculty of Science
Charles University
Hlavova 2030, Prague 2, 128 40, Czech Republic
H. Raabova
Department of Inorganic Chemistry
University of Chemistry and Technology Prague
Technicka 5, 166 28 Prague 6, Czech Republic
M. Gulka, Dr. V. Petrakova, M. Krecmarova, Prof. M. Nesladek
Faculty of Biomedical Engineering
Czech Technical University in Prague
Sitna sq. 3105, Kladno 272 01, Czech Republic
M. Gulka, Dr. V. Petrakova
Institute of Physics, ASCR
v.v.i., Na Slovance 2, 182 01 Prague 8, Czech Republic

DOI: 10.1002/adfm.201504857

M. Krecmarova, Prof. H.-G. Boyen, Prof. M. Nesladek
Institute for Materials Research (IMO)
Hasselt University
Wetenschapspark 1, B-3590 Diepenbeek, Belgium
Dr. V. Masek
Institute of Molecular and Translational Medicine
Faculty of Medicine and Dentistry
Palacky University Olomouc
Hnevotinska 5, Olomouc 779 00, Czech Republic
Dr. V. Masek
Department of Pharmacology
Faculty of Medicine and Dentistry
Palacky University Olomouc
Hnevotinska 3, Olomouc 775 15, Czech Republic
Dr. J. Stursa
Nuclear Physics Institute AS CR
v.v.i., Rez near, Prague 250 68, Czech Republic
Prof. M. Nesladek
IMEC Division IMOMEC
Hasselt University
Wetenschapspark 1, B-3590 Diepenbeek, Belgium

Materials Views
www.MaterialsViews.com

ADVANCED FUNCTIONAL MATERIALS
www.afm-journal.de

chemical nature of NDs and the low reactivity of the sp^3-diamond surface compared to sp^2-based CNM relatives.

Here, we describe a preparative and high-yielding method for one-step fluorination of NDs that can be performed on a benchtop using modest synthetic equipment. Our interest in fluorination of NDs arose from recent studies[11–17] showing that fluorination of the diamond surface can be used to stabilize negatively charged nitrogen-vacancy (NV^-) centers located close to the surface. These atomic defects in the diamond lattice have been thoroughly studied in the past two decades due to their unique applications as single photon emitters,[18] ultrasensitive magnetic,[19–21] and electric[22] field sensors, chemical probes,[23] and qubits.[24] NV center fluorescence depends on the electron spin state, which enables coherent manipulation of single NVs[25] and measurement of optically[26] or photoelectrically[27] detected magnetic resonance of single spins.

The NV^- state is the actual "sensing species" and stabilization and boosting of its photoemission thus represent a critical milestone in all the above-mentioned applications. Covalent attachment of highly electronegative fluorine can serve as a pathway to bend the conduction and valence bands in the diamond downward,[13] changing the position of the ground state of NV centers relative to the Fermi level. This leads to stabilization of the NV^- charge state and in turn boosts the brightness of diamond nanoparticles. Highly bright and stable NDs are indeed essential for high-resolution biomedical imaging applications.[28,29]

The current fluorination approaches for sp^3-diamond surfaces typically involve handling of highly corrosive gases (atomic or molecular fluorine, HF, ClF_3) under harsh treatment conditions[30,31] and utilize technically demanding and potentially hazardous setups, such as a fluorine line,[31] fluorine-containing plasmas (e.g., CF_4, SF_6),[13,15,32–35] ultrahigh-vacuum fluorine atomic beams,[36] and X-ray irradiation.[37] In addition to the sp^3-diamond-directed procedures, the sp^2-structures on so-called detonation NDs have been fluorinated similarly—using molecular[38–40] or plasma-generated fluorine.[41–43]

Our approach is based on a mild fluorination procedure that can be performed on a multigram scale at a benchtop without special equipment and safety requirements. The procedure involves Ag^+-catalyzed selective substitution of diamond carboxyls for fluorine using Selectfluor reagent.[46] Here, we describe fluorination of oxidized carboxylated fluorescent NDs (FNDs) and present a detailed characterization of the fluorinated FNDs. Moreover, we demonstrate that this type of fluorinated ND surface manipulates the electronic structure of the surface of diamond nanocrystals, which results in changes to the fluorescence of nitrogen-vacancy centers present in NDs.

2. Results and Discussion

2.1. Fluorination Procedure

Fluorination causes significant changes in solvation of the diamond interface.[43,44] Fluorine bound to diamond carbon atoms acts as a poor hydrogen-bond acceptor (in contrast to fluoride anions in solution) and weakens the overall hydrogen bonding network formed at the solid–liquid interface.[45] Hydrophobicity caused by a high level of surface diamond coverage with fluorine can be even higher than for hydrogenated surfaces (as quantified by contact angle measurements)[44] and typically results in increased solubility of fluorinated NDs in organic solvents.[43]

For biological applications, hydrophobicity and poor solvation in water are unwanted; the nanobiointerface should ideally be hydrophilic. For example, cells cannot adhere either to hydrogenated or highly fluorinated diamond surfaces, whereas oxidized diamond surfaces promote their adhesion.[46]

To circumvent these drawbacks of fluorine chemistry, we focused on preparing a diamond surface with dual functionality involving both fluorine and hydrophilic oxygen-containing groups. Oxidized bulk diamond single crystals and NDs prepared by high-pressure high temperature (HPHT) or by the chemical vapor deposition approach predominantly bear hydroxy or ether moieties,[47] while carbonyl-containing groups (including carboxyls) are much less frequent. In a recent study,[48] the range of molar fraction of surface carboxyls obtained by air oxidation of these materials was estimated to be ≈2%–3%. Although treatment with mineral acids can further increase the fraction of carboxyls, the highest reported values are 4.7% and 7%.[49,50]

For partial fluorination of the oxidized diamond surface, we took advantage of a recently described selective substitution of carboxyls for fluorine.[46] We expected to reach maximally ≈7% coverage of surface carbons with fluorine, while the rest of the surface would remain predominantly covered with hydroxy or ether moieties. We hypothesized that this controlled amount of introduced fluorine can affect the electronic behavior of the nanocrystal and influence the population of NV^- centers. The hydroxy groups and unreacted carboxyls would keep the fluorinated NDs hydrophilic and colloidally stable in an aqueous environment.

The silver-catalyzed decarboxylative fluorination procedure uses the electrophilic fluorinating reagent 1-chloromethyl-4-fluoro-1,4-diazoniabicyclo[2.2.2]octane *bis*(tetrafluoroborate) (F-TEDA$^+$ BF_4^- or Selectfluor).[51] Compared to other fluorodecarboxylative approaches, this procedure is unique in its ease, mild reaction conditions, chemoselectivity, and extensive substrate scope (including extremely sterically hindered structures). According to the recently described reaction mechanism,[52] Ag(I) is oxidized to Ag(II) by F-TEDA$^+$ to generate TEDA$^{+\bullet}$ radical cation (**Scheme 1**). The resulting Ag(II) intermediate oxidizes the carboxyl ligand to produce a tertiary alkyl radical on the diamond. Fluorine abstraction from another F-TEDA$^+$ cation yields the product.

To ascertain factors influencing decarboxylative fluorination in a deaerated aqueous dispersion of NDs, we performed the reaction at different temperatures for various reaction times (**Table 1**).

2.2. Chemical Particle Analysis

To analyze the fluorination yields, we combusted the samples in an oxygen atmosphere and analyzed them for fluoride anion content using ion exchange chromatography with suppressed conductivity detection (for an example of a chromatogram, see

ADVANCED FUNCTIONAL MATERIALS
www.afm-journal.de

Materials Views
www.MaterialsViews.com

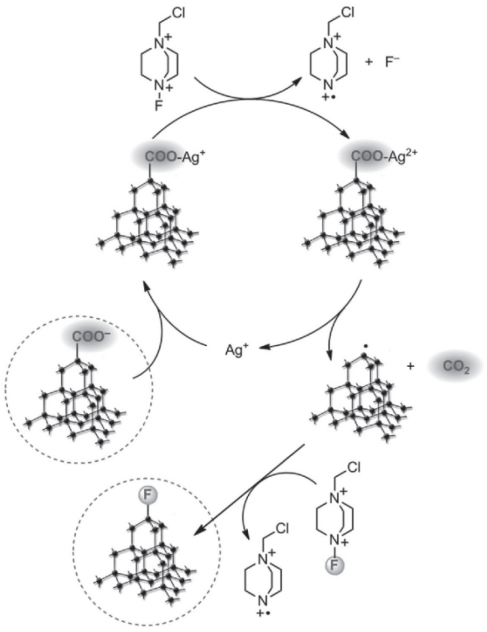

Scheme 1. A simplified scheme of the catalytic cycle for decarboxylative fluorination of NDs. The ND is represented by a fragment of the diamond lattice. The mechanism was adapted from results of a recent kinetic study performed with other substrates.[52]

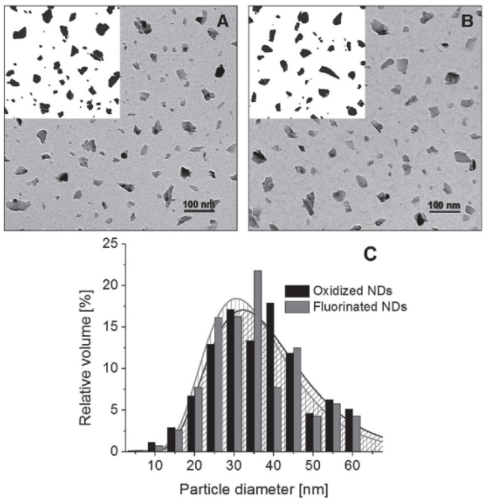

Figure 1. A) TEM images of HPHT NDs on carbon coated grids with oxidized surfaces and B) after fluorination treatment. For illustration, the upper left corner of each image is shown in the binary mode used for image analysis. C) Volume-weighted distribution histograms of ND sizes. The histograms are fitted with lognormal distribution functions. The estimated modes are at 32 and 31 nm for oxidized and fluorinated NDs, respectively.

Figure S1 in the Supporting Information). Within the range of conditions tested, we observed that fluorination is best accomplished after 2 d at 95 °C (Table 1).

Extrapolation of the weight percent of fluorine in the material to surface coverage can be based on various models, taking into account the different shapes of particles, their size distribution, and the original surface coverage with carboxyls. For estimation of the maximal theoretical load of fluorine on a perfluorinated surface, we assumed that the [111] diamond surface and every terminal carbon atom occupied by a carboxylic group are available for fluorination. The total number of available carbon atoms can be calculated from the size distribution obtained by precise image analysis of transmission electron microscopy (TEM) images of NDs, a method that we have recently developed.[53] From volume-weighted histograms of a polydisperse mixture of particles (see **Figure 1**), we obtained 3.7 mmol g^{-1} surface carbon atoms or theoretically exchangeable carboxyls. For comparison, a similar calculation using a simple spherical model and hydrodynamic radius of 38 nm obtained from dynamic light scattering (DLS) measurements provides a value of 2.7 mmol g^{-1}, which underestimates the value obtained from TEM by 27%.

Considering the experimentally determined coverage of NDs with carboxyls as 2% of all [111] surface functionalities[48] and the findings from the TEM image analysis, we obtained a maximal total theoretical fluorine content of ≈0.14 wt%. The best reaction conversion achieved (calculated for a fluorine content of 0.13 wt%) is therefore 94% (Table 1). Although this calculated yield is indeed affected by the accuracy of the input value of carboxyl content, it nevertheless shows that the fluorination proceeds with a high conversion.

For chemical analysis of the near-surface region of the most fluorinated sample (reacted for 2 d at 95 °C), we performed X-ray photoelectron spectroscopy (XPS). In addition to estimating the efficiency of the surface functionalization route, XPS provides information about the chemical environment of the atomic species by establishing binding energy shifts of appropriate core levels ("chemical shifts"). **Figure 2**A presents the F1s core level spectrum (open symbols) as acquired on fluorinated NDs. Based on a line shape analysis using a least-squares fitting routine,[54] a single line centered at 687.3 eV is

Table 1. Reaction conditions, results of elemental analysis of NDs, and calculated reaction conversions of fluorination.

Reaction temperature [°C]	Fluorine content [wt%]		Reaction conversion [%][a)]	
	1 d	2 d	1 d	2 d
55	0.09	0.11	65	80
95	0.11	0.13	80	94

[a)]The conversions are relative to the values of carboxyl coverage of the [111] surface of HPHT NDs obtained from the same supplier as in this work.[48] The total surface area used for calculation was obtained from volume-weighted histograms based on precise TEM image analysis.[53]

Materials Views
www.MaterialsViews.com

ADVANCED FUNCTIONAL MATERIALS
www.afm-journal.de

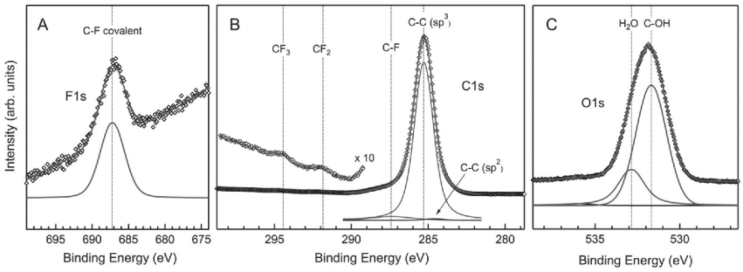

Figure 2. A) F1s, B) C1s, and C) O1s core level spectra (open symbols) of diamond nanoparticles fluorinated according to Scheme 1. Solid lines are the result of a line shape analysis following a previously described procedure.[54]

sufficient to describe the experimental data (solid curve). This value agrees well with the position observed earlier for covalent C—F bonds (687.5 eV),[55] thus providing evidence for the stable attachment of fluorine atoms to the nanoparticle surface.

In order to derive a more quantitative picture of the successful fluorination, we analyzed the C1s core level region in more detail (Figure 2B). The main peak observed at a binding energy of 285.3 eV can be assigned to photoemission from carbon atoms localized within the diamond lattice. On the high binding energy side, an additional component (shoulder) can be detected at 287.4 eV, representing 4.3% of the total C1s line intensity in the near-surface region. This is followed by very weak components at 291.8 and 294.5 eV, each contributing ≈0.1% to the C1s photoelectron intensity. While the latter two components can be assigned to the presence of negligible amounts of CF_2 and CF_3 at the sample surface, the contribution at 287.4 eV can be attributed to carbon atoms forming C—F covalent bonds (287.2 eV),[55] thus giving additional support for a successful fluorination procedure. On the low binding energy side of the main photoemission line, an additional component at 284.6 eV is required to achieve a reasonable fit, thereby contributing 0.8% to the total C1s line intensity. This weak signal arises from a small amount of sp^2-bound species at the sample surface.

After establishing the spectral weight of the different carbon species present in the near surface region, the surface coverage of C—F moieties can be estimated using a very simplified model. Assuming the particles to be spherical, the intensity ratio between the main line (representing diamond) and the shoulder at 287.4 eV (representing carbon atoms within C—F bonds) can serve as input for a core/shell model simulation. Briefly, the nanoparticle is divided into a large number of identical cells, each contributing to the photoelectron current an intensity that is affected by the attenuation in cells closer to the surface according to the mean free path within these cells. Taking a mean free path value of 1.9 nm for C1s photoelectrons travelling through both the bulk diamond[56] and the layer of surface carbon atoms covalently bound to fluorine atoms, an effective shell thickness of the affected carbon atoms can be estimated. This yields an effective thickness of 0.05 nm, which considering the size of carbon atoms in the diamond (0.18 nm), results in the formation of C—F bonds by about 28% of all terminal carbon atoms on the diamond surface. This finally translates into fluorine surface coverage of 9% of the monolayer (assuming each C—F moiety is attached to three C atoms, as shown in Scheme 1) thereby confirming that only part of the surface was functionalized with fluorine as has been aimed for.

To finally prove the nature of dual functionality induced by our procedure (fluorine & hydrophilic oxygen-containing groups), the O1s core level region has been characterized as well (Figure 2C). Here, a line-shape analysis of the experimental spectrum reveals the presence of 2 major components, one positioned at 532.8 eV which can be assigned to adsorbed water and one located at 531.7 eV. This line clearly represents C—OH functionalities.[57] Signals of other types of oxygen-containing groups were not found in the spectra, indicating a predominant fraction of hydroxy groups.

Both elemental and XPS analyses provide an evidence for the successful dual functionalization of the ND surface. We found that decarboxylative fluorination performed under mild conditions proceeds efficiently on a highly sterically hindered substrate, such as ND surface. The achieved fluorine surface coverage corresponds fairly well to the experimentally determined content of carboxylic moieties in starting material (oxidized HPHT NDs),[48] indicating a high conversion of the reaction. The surface termination consists of a smaller fraction of C—F groups, while the rest is covered by C—OH moieties.

2.3. Colloidal Characterization

The fluorodecarboxylation proceeds solely on carboxyls,[51,52] and we can therefore assume that the hydroxy groups remain intact during the reaction. Because hydroxy groups are the predominant oxygen-containing moieties on our surfaces (see above), we tested whether they can ensure the overall hydrophilicity of the partially fluorinated surface and compensate for the hydrophobicity of the terminal C—F groups. We investigated the colloidal behavior of oxidized and fluorinated particles in water using DLS and zeta potential measurements (**Figure 3**). Both samples had an average particle diameter of 38 nm with a size distribution characteristic of HPHT NDs.[58] Because DLS is extremely sensitive to signs of association and/or aggregation of the scattering particles, and we found both samples indistinguishable with DLS, we believe that the colloidal stability of the oxidized ND is not affected by the fluorination.

ADVANCED FUNCTIONAL MATERIALS
www.afm-journal.de

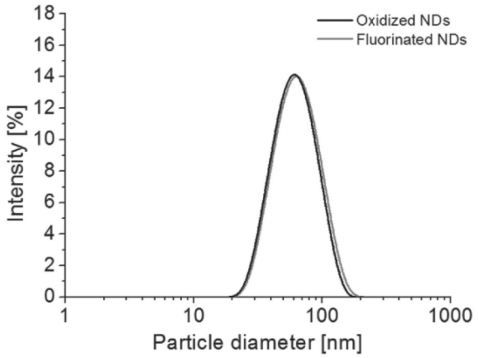

Figure 3. The intensity-weighted size distribution of NDs obtained from DLS.

The zeta potential of fluorinated NDs was −46 mV and showed a strong coulombic stabilization of the fluorinated surface by the remaining unreacted carboxyls. Interestingly, the value measured for oxidized NDs (−48 mV) is very similar, showing that a relatively low surface coverage with negatively charged groups in a fluorinated sample can still lead to highly charged surfaces (note that we are considering only a few percent of remaining unreacted carboxyls).

2.4. Structural and Morphological Analysis Using TEM

Chemical modifications of diamonds under harsh conditions, such as oxidative gas treatments at high temperatures (e.g., O_2, F_2, H_2O),[59] plasma treatment, mineral acid digestion, and treatment in molten KNO_3, lead to a significant surface etching.[60,61] This results in changes in particle size distributions[62,63] and in some cases particle shape as well.[64] During such treatments, the surface carbon atomic layers are typically converted into gases (e.g., CO_2, CO, CF_4) that escape from the surface, consecutively removing the diamond lattice. The decarboxylative fluorination introduced in this work is based on a localized and selective radical mechanism, which is fundamentally different from nonspecific etching. The substitution of carboxyl with fluorine is fixed on the reaction site and stops immediately after the carboxyl has been reacted. We therefore expected that the particles would not change their original size and shape distribution upon fluorination.

For comparison of the particles' size and shape distribution before and after fluorination, we used image analysis of TEM images (Figure 1).[53,65] For each sample, we analyzed nearly 1300 particles, acquired their equivalent circular diameters (see the Experimental Section), and recalculated them to volume-weighted histograms (Figure 1C). To compare the samples' size distributions, we used the Wilcoxon–Mann–Whitney rank test nonnormal distributions, which test the null hypothesis that two sets of data are from the same population against an alternative hypothesis. The resulting two-tailed probability was $P = 0.84$, which does not indicate different distribution of the particle volumes.

We characterized the shape of particles in each sample by particle circularity (see the Experimental Section). The average circularities were 0.71 ± 0.15 and 0.73 ± 0.13 for oxidized and fluorinated NDs, respectively. Comparison of the samples' circularities was performed using two sample t-test with unequal variances; this test showed that the circularities are equal at a significance level of $\alpha = 0.0001$.

Based on both size distribution and shape analysis, we conclude that the fluorination procedure has no significant impact on particle morphology. This finding is also an indirect confirmation that the radical fluorination proceeds on the terminal surface layer of carbons and that loss of particle mass observed typically under harsh etching conditions[59–64] does not take place.

2.5. Fluorescence Properties of NV Centers

Surface engineering of diamond is crucial for achieving high quantum yield of NV centers and for suppressing nonradiative recombination channels. The surface termination has also an influence on the spectral shape of fluorescent NV centers, as shown in studies comparing hydrogenated, oxidized,[14,66–70] fluorinated,[11–17] and nitrogen-terminated surfaces.[71] NV centers exist in two electronic states: Neutral (NV^0) and negatively charged (NV^-). The NV^0 state emits orange luminescence with zero phonon line (ZPL) around 575 nm; the NV^- state emits in the red region with ZPL at 637 nm. Both ZPLs are followed by broad phonon replica side band luminescence (Figure 4).[26] In general, highly electronegative atoms (O, F)[72] covalently attached to the surface shift the Fermi level at the surface and make the NV^- charge state predominant, while hydrogenation contributes to its depletion. In addition to direct atomic modification, noncovalent surface interactions can also modulate the NV emission.[23,73] Nevertheless, C—F termination is currently considered the most powerful surface termination for stabilization and precise control of the NV^- charge state,[11] which is essential for most measurements and applications of

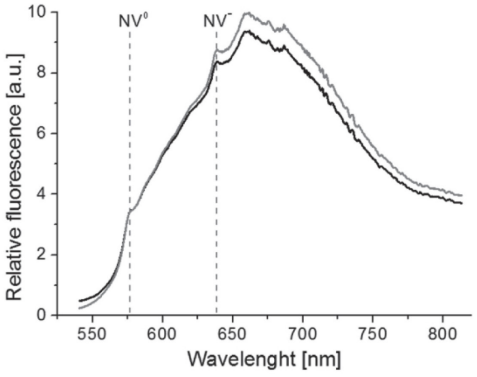

Figure 4. Fluorescence spectra of oxidized (black) and fluorinated (gray) NDs measured in acqueous colloidal solutions and normalized to NV^0 intensity. ZPL of the NV^0 and NV^- states are shown by dashed lines.

Materials Views
www.MaterialsViews.com

ADVANCED FUNCTIONAL MATERIALS
www.afm-journal.de

NDs related to detection of chemical, electrical, and magnetic changes occurring within the ND nanoenvironment.

To ascertain the influence of decarboxylative fluorination on the behavior of NV centers in fluorescent NDs, we compared quantitatively their fluorescence spectra measured in colloidal aqueous solution[74,75] before and after fluorination. We observed an ≈5% increase in emission intensity of the NV^- state upon fluorination of oxidized NDs (Figure 4). This change is important, considering that the starting oxygen termination already causes strong inversion of polarity of the surface dipole and the respective band-bending. Despite its low surface coverage the fluorine can contribute distinctly to the downward band-bending.[76]

For evaluation of the effects of fluorination on emission at single particle level, we measured photoluminescence of ND particles dispersed on quartz cover slip surface after drying up 1 µL ND colloidal solution (see Figure S2 in the Supporting Information for 3D maps of NV photoluminescence). By analyzing the NV center distribution in 20 photoluminescence intensity maps (10 for oxidized and 10 for fluorinated particles), we determined local extrema points of the photoluminescence and analyzed them statistically (see Figure S3 in the Supporting Information). To exclude influence of singularities of the noise we counted only the points with NV luminescence >8 kilocounts per second (kcps), i.e. 5 kcps above the background (which was ≈3 kcps for 2.5 mW laser power). The cover slips prepared from suspension of oxidized diamond showed higher agglomeration for ND crystals, displayed as local maxima with high number of counts. In contrast, the fluorination significantly promoted luminescence in ND particles with weakest fluorescence (see Figure S3 in the Supporting Information), presumably the smallest particles in the ensemble. Due to this effect, the total counts for particles or particle clusters containing 1–10 NV centers was 29% higher for fluorinated than for oxidized NDs.

The smaller NDs containing NV centers have been shown as more sensitive to the surface-related effects.[63,70,77,78] We anticipate that the fluorine-induced stabilization of NV^- state applies preferably to the shallow NV centers present in smaller particles, similarly as observed in oxidized NDs.[79] Nevertheless, the fraction of such particles in the whole ensemble is relatively low (Figure 1) and the corresponding increase in NV^- emission intensity from bulk colloidal solutions upon fluorination is therefore only modest (≈5%; see above).

Our data show that fluorination further boosts the fluorescence intensity of NV^-centers and can potentially awake some of the NV centers present in optically inactive states.[80] The possible reasons for NV awaking are the shift of the Fermi level at the surface induced by presence of electronegative fluorine atoms[11–17] and the compensation of the charge traps that are providing nonradiative recombination channels.[79,81,82] Our findings correspond fairly well to results from a fluorination study of the oxidized [100] surface, where changes in $NV^-/(NV^0 + NV^-)$ were also small (<0.04).[15] A very different situation occurs during comparison of hydrogenated and fluorinated surfaces.[11–13,15] In these cases, the detrimental upward band-bending caused by C—H termination is completely inverted and the change in $NV^-/(NV^0 + NV^-)$ ratio is extensive, causing robust changes in spectral shape.

3. Conclusion

We developed a synthetic pathway leading to selective Ag^+-catalyzed substitution of ND surface carboxyls with fluorine using selective sp^3-based radical chemistry. We focused on NDs because fluorination of this carbon nanomaterial leads to surface band-bending that stabilizes shallow fluorescent NV centers. In addition, we aimed to prepare a mixed oxygen-fluorine termination preserving the hydrophilic behavior of oxygen-containing groups and introducing the electronic properties of fluorine. In contrast to the harsh fluorination procedures used for diamonds (for example, treatments using molecular fluorine in a fluorine line, fluorine-containing plasmas, and X-ray irradiation), our one-step approach proceeds at mild conditions in an aqueous dispersion of NDs and can be easily performed on the benchtop without special safety precautions. The procedure is robust enough to proceed with high yields on extremely sterically demanding substrates such as NDs and results in the mixed C—F and C—OH termination. Thanks to the overall hydrophilic surface, the particles form a stable colloid in an aqueous environment, as we demonstrated by DLS. Moreover, using precise TEM image analysis, we found that the particles retain their size and shape, which supports our assumptions regarding the unique, nonetching nature of the decarboxylative fluorination. We characterized the resulting surface using XPS and elemental analysis and spectrally analyzed the effect of fluorination on stabilization of negatively charged fluorescent NV centers in NDs. Consistent with recent fluorination approaches achieved under harsh conditions,[11–17] we found that decarboxylative fluorination also positively influences the NV centers, boosting their overall fluorescent intensity. In our opinion, this finding significantly extends the current approaches to diamond surface engineering,[83–85] which has major implications for important quantum physical and bioimaging applications that require bright and stable NV centers.

Finally, we expect that decarboxylative fluorination of a diamond surface bearing a higher number of carboxyls may lead to correspondingly higher surface coverage with fluorine. This can be used for controlled high-yield fluorination of diamonds, which is essential for applications such as a recently described quantum simulator[86] and represents one possible pathway to stabilized ultrabright single-digit-sized ND probes relevant for bioimaging and quantum sensing. Substantially exceeding the current highest surface coverage of carboxyls (≈7%)[50] using de novo chemical approaches is therefore an important goal for further development of sp^3 chemistry on diamonds, not only from a fluorination perspective. We are currently working in this direction.

4. Experimental Section

Chemicals and Reagents: Sodium hydroxide, sodium chloride, sodium hydrogen carbonate, sodium carbonate, potassium thiocyanate, ammonia solution (24%), nitric acid (65%), sulfuric acid (96%), hydrogen peroxide (30%), and D–(+) glucose (p. a.) were purchased from Penta (Czech Republic). Hydrofluoric acid (48%), silver nitrate (>99%), potassium cyanide (>97%), and Selectfluor (>95%) were purchased from Sigma–Aldrich (Prague, Czech Republic). Poly(ethyleneimine) (M_W 2.5 kDa) was purchased from Polysciences, Inc. All chemicals were used

ADVANCED FUNCTIONAL MATERIALS
www.afm-journal.de

Materials Views
www.MaterialsViews.com

as received without further purification. Deionized water was prepared with a Millipore Synergy UV Ultrapure water system.

Nanodiamond Pretreatment: NDs containing ≈100–200 ppm of natural nitrogen impurities were supplied by Microdiamant Switzerland (MSY 0–0.05). NDs were oxidized by air in a Thermolyne 21100 tube furnace at 510 °C for 5 h[58] and subsequently treated with a mixture of HNO_3 and H_2SO_4 (90 °C, 3 d), 1 M NaOH (80 °C, 1 h), and 1 M HCl (80 °C, 1 h).[87] Between treatments, NDs were separated by centrifugation at 5000 rcf for 20 min. After HCl treatment, diamonds were centrifuged four times (5000 rcf, 20 min; 7000 rcf, 30 min; 20 000 rcf, 30 min; 30 000 rcf 30 min) with deionized water to obtain a stable colloid and freeze-dried.

Engineering NV Centers in NDs: Purified ND powder (160 mg) was pressed in an aluminum target holder and irradiated with a 14.8 MeV proton beam extracted from the isochronous cyclotron U-120M for 125 min (fluence 5.02×10^{16} cm^{-2}), as previously described.[58,88]

Surface Oxidation after Irradiation: The irradiated material was annealed at 900 °C for 1 h in argon atmosphere and subsequently oxidized in air for 5 h at 510 °C. The NDs were then treated with a mixture of HNO_3 and HF in a Teflon beaker on a hotplate (160 °C, 2 d), washed with water, 1 M NaOH, water again, and 1 M HCl. The precipitate was washed five times with water and freeze-dried.[89]

Nanodiamond Particle Fluorination: Oxidized FND particles (250 mg) were dissolved in water (250 mL) and sonicated with a probe (Cole-Parmer, 750 W) for 30 min. The colloidal solution was placed in a 500 mL flask with a septum. The flask was evacuated and blown through with argon for 30 min. $AgNO_3$ (425 mg) and Selectfluor (8.85 g) were placed in 500 mL flask with a septum and evacuated and refilled with argon three times. A deaerated FND solution (250 mL) was then added under inert atmosphere via cannula, and the reaction mixture was stirred in various conditions (see Table 1) under an argon atmosphere. The resulting mixture was cooled to room temperature and separated by centrifugation (4000 g, 20 min) and washed with water. The sediment was dispersed in aqueous KCN (1%, 500 mL) slowly stirred overnight. The suspension was separated by centrifugation. The KCN-containing supernatant was disposed of by adding it to an H_2O_2 solution (30%, 500 mL). Sedimented FNDs were dispersed in ammonia solution (24%, 500 mL) and precipitated by addition of brine (25 mL). The precipitate was washed once with 1 M HCl and five times with water and freeze-dried, providing 216 mg of the fluorinated FND.

X-Ray Photoelectron Spectroscopy: XPS was performed by drop-casting aqueous FND solutions onto Si wafers and loading them immediately after drying into a commercial electron spectrometer (PHI 5600LS). Core-level spectra were acquired using Al-k_a photons (1486.6 eV) as provided by a small-spot monochromator system (1 mm spot-size). High-resolution spectra were measured by setting the total energy resolution of the spectrometer (photons and electrons) to 0.36 eV full-width at half maximum. The binding energy scale of the spectrometer was calibrated using an independent Au bulk reference sample ($Au4f_{7/2}$: 84.0 eV).

TEM: Samples for TEM were prepared similarly as described elsewhere.[53] Carbon-coated copper grids (Pyser) were placed into a UV-ozonizing chamber (UV/Ozone Pro Cleaner Plus, Bioforce Nanosciences) for 15 min. Then, a droplet of poly(ethyleneimine) solution (M_W = 2.5 kDa, 0.1 mg mL^{-1}) was placed on the grid. After 10 min incubation, it was removed with a piece of tissue. Then, a droplet of deionized water was placed on the grid and removed after 1 min incubation with a piece of tissue. Finally, the aqueous ND solution (0.1 mg mL^{-1}) was placed on the grid and removed after 3 min incubation with a piece of tissue.

TEM Image Analysis: Analysis of particle size distributions was performed with ImageJ software using a previously described procedure.[53] Particle size was expressed by equivalent circular diameter (d_{eq}) defined as the diameter of a circular particle with the same area as the particle of interest (S)

$$d_{eq} = \sqrt{4S/\pi}$$

Equivalent diameters were used for calculation of the particle volume (PV)

$$PV = \frac{4}{3}\pi\left(\frac{d_{eq}}{2}\right)^3$$

and consequently for creation of the volume-weighted histogram. To confirm that the fluorination procedure does not influence the particle shape, the particle circularity (C) was analyzed, which is a dimensionless shape factor defined as

$$C = \frac{4\pi S}{P^2}$$

where P is particle perimeter (total length of the particle boundary).

Ion-Exchange Chromatography: The content of fluorine was determined by ion-exchange chromatography. A mixture of fluorinated NDs with glucose (1:1, 15 mg) was combusted in an oxygen atmosphere. The resulting mixture of gasses was absorbed in 25 mL of buffer solution (1.7×10^{-3} M $NaHCO_3$, 1.8×10^{-3} M Na_2CO_3, 0.1×10^{-3} M KSCN in water), which was filtered through a 0.2 µm PVDF syringe filter into polypropylene vials. The analyses of F^- content were carried out by Watrex Prague Ltd. with a purpose-built system consisting of a dual piston HPLC pump (P-102, WATREX), conductivity detector (Conducto Monitor III, range 0.1 µS, Thermo Separation Products), and SAMS standard conductivity suppressor (SeQuant). Anion separation was achieved with a Watrex IC Anion I column (150 × 4 mm; 7 µm) using a solution of 1.7×10^{-3} M Na_2CO_3, 1.8×10^{-3} M $NaHCO_3$, and 0.1×10^{-3} M NaSCN as a mobile phase. The flow rate was 1.0 mL min^{-1}. Samples were injected using a 20 µL loop injector (RHEODYNE 7125). The data were evaluated with CSW32 (Dataapex) chromatography software. The calibration range for F^- was 0.1–10 mg L^{-1} with a detection limit of 0.03 mg L^{-1}.

Dynamic Light Scattering (DLS) and Zeta Potentials: DLS and zeta potentials were recorded with a Zetasizer Nano ZS system (Malvern instrument) at room temperature. Sample concentrations were 1 mg mL^{-1} in deionized water.

Raman Spectroscopy: The ensemble fluorescence spectra of NDs were measured using Raman iHR320 imaging spectrometer (HORIBA JOBIN YVON) with 600 gr mm^{-1} grating and paired with liquid nitrogen-cooled 2048 × 512 pixel CCD detector Symphony (HORIBA JOBIN YVON). Verdi V5 (Coherent) 532 nm DPSS laser served as the source of excitation radiation. The radiant power on the sample was 50 mW. Solutions of NDs diluted in deionized water were sonicated using high-power ultrasonic horn (Hielscher UP400S, Sonotrode H3) set to 400 W and 1:1 (on/off) cycle for 30 min under liquid cooling. Stable colloidal solutions (1 mg mL^{-1}) were sonicated in a bath for 1 min before each measurement and measured in a Quartz SUPRASIL cell with 3 mm optical path length, type 101.015-QS (Hellma). The cell was precisely mounted in a fixed holder in laser focus which enables perfect reproducibility of spectra. The whole spectral interval of interest, ≈540–810 nm, consists of three overlapping spectral windows (100 pixels overlap) stitched together. For each spectral window 16 accumulations with 200 ms integration time were acquired. For each sample three independent measurements were done and averaged. Finally, Raman signal of water was subtracted in GRAMS/AI 7.2 software (Thermo Galactic) using the "dewiggle" auto subtraction algorithm.[90,91] This iterative algorithm calculates the subtraction factor by minimizing the complexity of the residual spectrum.

The photoluminescence maps were measured on luminescence-free quartz cover slips cleaned in ethanol before the use. Droplet of colloidal solutions of oxidized and fluorinated nanodiamond particles (1 µL, 0.1 mg mL^{-1}) was applied using micropipette to a cover slip and dried under infrared lamp. The ND particles were dispersed rather homogenously over the spot after drying the microdroplet with accumulation of particles at the edges of the microdroplet dried-up spot. Luminescence measurements were performed in the centre of the dried microdroplet spot. 20 microdroplets from suspension of each oxidized ND and fluorinated ND were produced. To measure photoluminescence (PL), a home-made confocal setup designed specifically for studying NV color centres in diamond was made. The PL was excited with 500 mW Gem laser form Laser Quantum producing 532 nm CW excitation, directed by Gaussian beam optics to Olympus 40× UPLSAPO 40×2 air

Materials Views
www.MaterialsViews.com

ADVANCED FUNCTIONAL MATERIALS
www.afm-journal.de

objective with N.A. 0.95 and working distance of 180 micrometers. The lateral resolution of the confocal setup was 350 nm. The laser power was adjusted to 2.5 mW. The PL counts were detected using Excelitas single photon counter. The number of counts corresponding to a single NV centre under laser power saturation was determined using single NV centres in quantum grade single crystal diamond (Element Six) located 15 micrometer from the surface of diamond and located in the crystal bulk. The number of PL counts corresponding to a single NV centre in ND on the quartz surface was recalculated using the geometry of the objective and the index of refraction of diamond. This ratio was 7.8. The PL was detected after dichroic mirror and 650 nm long pass filter, filtering out green laser. The PL spectra from selected spots were recorded, confirming a typical PL spectrum of NV color centre with ZPL at 578 nm (NV^0) and 636 nm (NV^-). For selected spots an optically detected magnetic resonance (ODMR) signal with resonance at 2.867 GHz was recorded. All detected spots showed no photobleaching. The maps were recorded by scanning the stage on the area of 10 × 10 µm. From the detected intensity, it was established that the PL counts corresponding to ND particles exhibited counts corresponding digital multiples of single NV centre count, matching also to the correction factor for NV counts in the bulk of single crystal diamond and ND on a surface of quartz. The intensity extrema maps were obtained by searching through columns, rows, and diagonals in each matrix element using Matlab software.

Supporting Information

Supporting Information is available from the Wiley Online Library or from the author.

Acknowledgements

The authors are grateful to Dr. Vladimir Pribyl for the development of software for spectra processing. The work was supported by the Grant Agency of the Czech Republic Project No. 16-16336S and the Ministry of Health of the Czech Republic, Grant No. 15-33094A (all rights reserved). Irradiations of NDs were carried out at the CANAM infrastructure of the NPI ASCR Rez supported through MŠMT Project No. LM2011019. H.R. acknowledges financial support from specific university research (MSMT No. 20/2015). M.N. would like to thank EU–FP7 Research Grant DIADEMS, Grant Agreement No. 611143, for the financial support. V.M. acknowledges to MSM project LO1304.

Received: November 12, 2015
Revised: March 14, 2016
Published online: May 2, 2016

[1] J. T. Robinson, J. S. Burgess, C. E. Junkermeier, S. C. Badescu, T. L. Reinecke, F. K. Perkins, M. K. Zalalutdniov, J. W. Baldwin, J. C. Culbertson, P. E. Sheehan, E. S. Snow, *Nano Lett.* **2010**, *10*, 3001.
[2] S.-H. Cheng, K. Zou, F. Okino, H. R. Gutierrez, A. Gupta, N. Shen, P. C. Eklund, J. O. Sofo, J. Zhu, *Phys. Rev. B* **2010**, *81*, 205435.
[3] T. Szilvási, A. Gali, *J. Phys. Chem. C* **2014**, *118*, 4410.
[4] V. N. Khabashesku, W. E. Billups, J. L. Margrave, *Acc. Chem. Res.* **2002**, *35*, 1087.
[5] R. Zbořil, F. Karlický, A. B. Bourlinos, T. A. Steriotis, A. K. Stubos, V. Georgakilas, K. Šafářová, D. Jančík, C. Trapalis, M. Otyepka, *Small* **2010**, *6*, 2885.
[6] Z. Gu, H. Peng, R. H. Hauge, R. E. Smalley, J. L. Margrave, *Nano Lett.* **2002**, *2*, 1009.
[7] R. R. Nair, W. Ren, R. Jalil, I. Riaz, V. G. Kravets, L. Britnell, P. Blake, F. Schedin, A. S. Mayorov, S. Yuan, M. I. Katsnelson, H.-M. Cheng, W. Strupinski, L. G. Bulusheva, A. V. Okotrub, I. V. Grigorieva, A. N. Grigorenko, K. S. Novoselov, A. K. Geim, *Small* **2010**, *6*, 2877.
[8] E. T. Mickelson, C. B. Huffman, A. G. Rinzler, R. E. Smalley, R. H. Hauge, J. L. Margrave, *Chem. Phys. Lett.* **1998**, *296*, 188.
[9] Y. Liu, R. L. Vander Wal, V. N. Khabashesku, *Chem. Mater.* **2007**, *19*, 778.
[10] N. O. V. Plank, L. Jiang, R. Cheung, *Appl. Phys. Lett.* **2003**, *83*, 2426.
[11] C. Osterkamp, J. Lang, J. Scharpf, C. Müller, L. P. McGuinness, T. Diemant, R. J. Behm, B. Naydenov, F. Jelezko, *Appl. Phys. Lett.* **2015**, *106*, 113109.
[12] C. Osterkamp, J. Scharpf, S. Pezzagna, J. Meijer, T. Diemant, R. J. Behm, B. Naydenov, F. Jelezko, *Appl. Phys. Lett.* **2013**, *103*, 193118.
[13] T. W. Shanley, A. A. Martin, I. Aharonovich, M. Toth, *Appl. Phys. Lett.* **2014**, *105*, 063103.
[14] M. Kaviani, P. Deák, B. Aradi, T. Frauenheim, J.-P. Chou, A. Gali, *Nano Lett.* **2014**, *14*, 4772.
[15] S. Cui, E. L. Hu, *Appl. Phys. Lett.* **2013**, *103*, 051603.
[16] H. Pinto, D. W. Palmer, R. Jones, J. P. Goss, P. R. Briddon, S. Öberg, *J. Nanosci. Nanotechnol.* **2012**, *12*, 8589.
[17] K. Ohashi, T. Rosskopf, H. Watanabe, M. Loretz, Y. Tao, R. Hauert, S. Tomizawa, T. Ishikawa, J. Ishi-Hayase, S. Shikata, C. L. Degen, K. M. Itoh, *Nano Lett.* **2013**, *13*, 4733.
[18] I. Aharonovich, A. D. Greentree, S. Prawer, *Nat. Photonics* **2011**, *5*, 397.
[19] G. Balasubramanian, I. Y. Chan, R. Kolesov, M. Al-Hmoud, J. Tisler, C. Shin, C. Kim, A. Wojcik, P. R. Hemmer, A. Krueger, T. Hanke, A. Leitenstorfer, R. Bratschitsch, F. Jelezko, J. Wrachtrup, *Nature* **2008**, *455*, 648.
[20] J. R. Maze, P. L. Stanwix, J. S. Hodges, S. Hong, J. M. Taylor, P. Cappellaro, L. Jiang, M. V. G. Dutt, E. Togan, A. S. Zibrov, A. Yacoby, R. L. Walsworth, M. D. Lukin, *Nature* **2008**, *455*, 644.
[21] A. Laraoui, J. S. Hodges, C. A. Meriles, *Nano Lett.* **2012**, *12*, 3477.
[22] F. Dolde, H. Fedder, M. W. Doherty, T. Nöbauer, F. Rempp, G. Balasubramanian, T. Wolf, F. Reinhard, L. C. L. Hollenberg, F. Jelezko, J. Wrachtrup, *Nat. Phys.* **2011**, *7*, 459.
[23] V. Petrakova, I. Rehor, J. Stursa, M. Ledvina, M. Nesladek, P. Cigler, *Nanoscale* **2015**, *7*, 12307.
[24] W. Pfaff, B. J. Hensen, H. Bernien, S. B. van Dam, M. S. Blok, T. H. Taminiau, M. J. Tiggelman, R. N. Schouten, M. Markham, D. J. Twitchen, R. Hanson, *Science* **2014**, *345*, 532.
[25] J. M. Taylor, P. Cappellaro, L. Childress, L. Jiang, D. Budker, P. R. Hemmer, A. Yacoby, R. Walsworth, M. D. Lukin, *Nat. Phys.* **2008**, *4*, 810.
[26] A. Gruber, A. Dräbenstedt, C. Tietz, L. Fleury, J. Wrachtrup, C. von Borczyskowski, *Science* **1997**, *276*, 2012.
[27] E. Bourgeois, A. Jarmola, P. Siyushev, M. Gulka, J. Hruby, F. Jelezko, D. Budker, M. Nesladek, *Nat. Commun.* **2015**, *6*, 8577.
[28] J. Slegerova, I. Rehor, J. Havlik, H. Raabova, E. Muchova, P. Cigler, In *Intracellular Delivery II: Fundamental Biomedical Technologies* (Eds: A. Prokop, Y. Iwasaki, A. Harada), Vol. *7*, Springer, Dordrecht, Netherlands **2014**, pp. 363.
[29] I. Rehor, J. Slegerova, J. Havlik, H. Raabova, J. Hyvl, E. Muchova, P. Cigler, In *Carbon Nanomaterials for Biomedical Applications* (Eds: M. Zhang, R. R. Naik, L. Dai), Vol. *5*, Springer International Publishing, Cham, Switzerland, **2016**, pp. 319.
[30] A. Freedman, C. D. Stinespring, *Appl. Phys. Lett.* **1990**, *57*, 1194.
[31] C. P. Kealey, T. M. Klapötke, D. W. McComb, M. I. Robertson, J. M. Winfield, *J. Mater. Chem.* **2001**, *11*, 879.
[32] C. J. Widmann, C. Giese, M. Wolfer, S. Kono, C. E. Nebel, *Phys. Status Solidi A* **2014**, *211*, 2328.
[33] M. A. Ray, T. Tyler, B. Hook, A. Martin, G. Cunningham, O. Shenderova, J. L. Davidson, M. Howell, W. P. Kang, G. McGuire, *Diamond Relat. Mater.* **2007**, *16*, 2087.
[34] S. Ferro, A. De Battisti, *J. Phys. Chem. B* **2003**, *107*, 7567.

Appendix D

[35] S. Q. Lud, M. Niedermeier, P. S. Koch, P. Bruno, D. M. Gruen, M. Stutzmann, J. A. Garrido, *Appl. Phys. Lett.* **2010**, *96*, 092109.
[36] A. Freedman, *J. Appl. Phys.* **1994**, *75*, 3112.
[37] V. S. Smentkowski, J. T. Yates, *Science* **1996**, *271*, 193.
[38] H. Huang, Y. H. Wang, J. B. Zang, L. Y. Bian, *Appl. Surf. Sci.* **2012**, *258*, 4079.
[39] Y. Wang, H. Huang, J. Zang, F. Meng, L. Dong, J. Su, *Int. J. Electrochem. Sci.* **2012**, *7*, 6807.
[40] A. M. Panich, H.-M. Vieth, A. I. Shames, N. Froumin, E. Ōsawa, A. Yao, *J. Phys. Chem. C* **2010**, *114*, 774.
[41] G. V. Lisichkin, I. I. Kulakova, Y. A. Gerasimov, A. V. Karpukhin, R. Y. Yakovlev, *Mendeleev Commun.* **2009**, *19*, 309.
[42] M. A. Ray, O. Shenderova, W. Hook, A. Martin, V. Grishko, T. Tyler, G. B. Cunningham, G. McGuire, *Diamond Relat. Mater.* **2006**, *15*, 1809.
[43] Y. Liu, Z. Gu, J. L. Margrave, V. N. Khabashesku, *Chem. Mater.* **2004**, *16*, 3924.
[44] M. C. Salvadori, W. W. R. Araújo, F. S. Teixeira, M. Cattani, A. Pasquarelli, E. M. Oks, I. G. Brown, *Diamond Relat. Mater.* **2010**, *19*, 324.
[45] T. A. Dolenko, S. A. Burikov, J. M. Rosenholm, O. A. Shenderova, I. I. Vlasov, *J. Phys. Chem. C* **2012**, *116*, 24314.
[46] F. Klauser, M. Hermann, D. Steinmüller-Nethl, O. Eiter, A. Pasquarelli, E. Bertel, T. Seppi, P. Lukas, T. Lechleitner, *Chem. Vap. Deposition* **2010**, *16*, 42.
[47] F. K. de Theije, M. F. Reedijk, J. Arsic, W. J. P. van Enckevort, E. Vlieg, *Phys. Rev. B* **2001**, *64*, 085403.
[48] A. Wolcott, T. Schiros, M. E. Trusheim, E. H. Chen, D. Nordlund, R. E. Diaz, O. Gaathon, D. Englund, J. S. Owen, *J. Phys. Chem. C* **2014**, *118*, 26695.
[49] X. Wang, A. R. Ruslinda, Y. Ishiyama, Y. Ishii, H. Kawarada, *Diamond Relat. Mater.* **2011**, *20*, 1319.
[50] T.-T.-B. Nguyen, H.-C. Chang, V. W.-K. Wu, *Diamond Relat. Mater.* **2007**, *16*, 872.
[51] F. Yin, Z. Wang, Z. Li, C. Li, *J. Am. Chem. Soc.* **2012**, *134*, 10401.
[52] N. R. Patel, R. A. Flowers, *J. Org. Chem.* **2015**, *80*, 5834.
[53] I. Rehor, P. Cigler, *Diamond Relat. Mater.* **2014**, *46*, 21.
[54] G. K. Wertheim, S. B. Dicenzo, *J. Electron Spectrosc. Relat. Phenom.* **1985**, *37*, 57.
[55] S. Hoste, D. F. Van De Vondel, G. P. Van Der Kelen, *J. Electron Spectrosc. Relat. Phenom.* **1979**, *17*, 191.
[56] S. Tanuma, C. J. Powell, D. R. Penn, *Surf. Interface Anal.* **2011**, *43*, 689.
[57] B. Folkesson, P. Sundberg, *Spectrosc. Lett.* **1987**, *20*, 193.
[58] J. Havlik, V. Petrakova, I. Rehor, V. Petrak, M. Gulka, J. Stursa, J. Kucka, J. Ralis, T. Rendler, S.-Y. Lee, R. Reuter, J. Wrachtrup, M. Ledvina, M. Nesladek, P. Cigler, *Nanoscale* **2013**, *5*, 3208.
[59] C. J. Chu, C. Pan, J. L. Margrave, R. H. Hauge, *Diamond Relat. Mater.* **1995**, *4*, 1317.
[60] N. Mohan, Y.-K. Tzeng, L. Yang, Y.-Y. Chen, Y. Y. Hui, C.-Y. Fang, H.-C. Chang, *Adv. Mater.* **2010**, *22*, 843.
[61] J. M. Say, C. Bradac, T. Gaebel, J. R. Rabeau, L. J. Brown, *Aust. J. Chem.* **2012**, *65*, 496.
[62] T. Gaebel, C. Bradac, J. Chen, J. M. Say, L. Brown, P. Hemmer, J. R. Rabeau, *Diamond Relat. Mater.* **2012**, *21*, 28.
[63] F. A. Inam, M. J. Steel, S. Castelletto, *Diamond Relat. Mater.* **2014**, *45*, 64.
[64] Z. Chu, S. Zhang, B. Zhang, C. Zhang, C.-Y. Fang, I. Rehor, P. Cigler, H.-C. Chang, G. Lin, R. Liu, Q. Li, *Sci. Rep.* **2014**, *4*, 4495.
[65] I. Rehor, J. Slegerova, J. Kucka, V. Proks, V. Petrakova, M.-P. Adam, F. Treussart, S. Turner, S. Bals, P. Sacha, M. Ledvina, A. M. Wen, N. F. Steinmetz, P. Cigler, *Small* **2014**, *10*, 1106.
[66] V. Petrakova, A. Taylor, I. Kratochvilova, F. Fendrych, J. Vacik, J. Kucka, J. Stursa, P. Cigler, M. Ledvina, A. Fiserova, P. Kneppo, M. Nesladek, *Adv. Funct. Mater.* **2012**, *22*, 812.
[67] V. Petrakova, M. Nesladek, A. Taylor, F. Fendrych, P. Cigler, M. Ledvina, J. Vacik, J. Stursa, J. Kucka, *Phys. Status Solidi A* **2011**, *208*, 2051.
[68] L. Rondin, G. Dantelle, A. Slablab, F. Grosshans, F. Treussart, P. Bergonzo, S. Perruchas, T. Gacoin, M. Chaigneau, H.-C. Chang, V. Jacques, J.-F. Roch, *Phys. Rev. B* **2010**, *82*, 115449.
[69] M. V. Hauf, B. Grotz, B. Naydenov, M. Dankerl, S. Pezzagna, J. Meijer, F. Jelezko, J. Wrachtrup, M. Stutzmann, F. Reinhard, J. A. Garrido, *Phys. Rev. B* **2011**, *83*, 081304.
[70] C. Bradac, T. Gaebel, C. I. Pakes, J. M. Say, A. V. Zvyagin, J. R. Rabeau, *Small* **2013**, *9*, 132.
[71] A. Stacey, K. M. O'Donnell, J.-P. Chou, A. Schenk, A. Tadich, N. Dontschuk, J. Cervenka, C. Pakes, A. Gali, A. Hoffman, S. Prawer, *Adv. Mater. Interfaces* **2015**, *2*, DOI: 10.1002/admi.201500079.
[72] A. K. Tiwari, J. P. Goss, P. R. Briddon, N. G. Wright, A. B. Horsfall, R. Jones, H. Pinto, M. J. Rayson, *Phys. Rev. B* **2011**, *84*, 245305.
[73] C. Bradac, T. Gaebel, N. Naidoo, M. J. Sellars, J. Twamley, L. J. Brown, A. S. Barnard, T. Plakhotnik, A. V. Zvyagin, J. R. Rabeau, *Nat. Nanotechnol.* **2010**, *5*, 345.
[74] Y.-R. Chang, H.-Y. Lee, K. Chen, C.-C. Chang, D.-S. Tsai, C.-C. Fu, T.-S. Lim, Y.-K. Tzeng, C.-Y. Fang, C.-C. Han, H.-C. Chang, W. Fann, *Nat. Nanotechnol.* **2008**, *3*, 284.
[75] L.-J. Su, C.-Y. Fang, Y.-T. Chang, K.-M. Chen, Y.-C. Yu, J.-H. Hsu, H.-C. Chang, *Nanotechnology* **2013**, *24*, 315702.
[76] K. J. Rietwyk, S. L. Wong, L. Cao, K. M. O'Donnell, L. Ley, A. T. S. Wee, C. I. Pakes, *Appl. Phys. Lett.* **2013**, *102*, 091604.
[77] S. Sotoma, K. Akagi, S. Hosokawa, R. Igarashi, H. Tochio, Y. Harada, M. Shirakawa, *RSC Adv.* **2015**, *5*, 13818.
[78] J. Tisler, G. Balasubramanian, B. Naydenov, R. Kolesov, B. Grotz, R. Reuter, J.-P. Boudou, P. A. Curmi, M. Sennour, A. Thorel, M. Börsch, K. Aulenbacher, R. Erdmann, P. R. Hemmer, F. Jelezko, J. Wrachtrup, *ACS Nano* **2009**, *3*, 1959.
[79] L. Rondin, G. Dantelle, A. Slablab, F. Grosshans, F. Treussart, P. Bergonzo, S. Perruchas, T. Gacoin, M. Chaigneau, H.-C. Chang, V. Jacques, J.-F. Roch, *Phys. Rev. B* **2010**, *82*, 115449.
[80] G. Waldherr, J. Beck, M. Steiner, P. Neumann, A. Gali, T. Frauenheim, F. Jelezko, J. Wrachtrup, *Phys. Rev. Lett.* **2011**, *106*, 157601.
[81] M. I. Landstrass, K. V. Ravi, *Appl. Phys. Lett.* **1989**, *55*, 975.
[82] M. Cannaerts, M. Nesladek, K. Haenen, L. De Schepper, L. M. Stals, C. Van Haesendonck, *Diamond Relat. Mater.* **2002**, *11*, 212.
[83] A. Krueger, *J. Mater. Chem.* **2008**, *18*, 1485.
[84] J. C. Arnault, In *Novel Aspects of Diamond* (Ed: N. Yang), Vol. *121*, Springer International Publishing, Cham, Switzerland **2015**, pp. 85–122.
[85] V. N. Mochalin, O. Shenderova, D. Ho, Y. Gogotsi, *Nat. Nanotechnol.* **2012**, *7*, 11.
[86] J. Cai, A. Retzker, F. Jelezko, M. B. Plenio, *Nat. Phys.* **2013**, *9*, 168.
[87] L.-C. L. Huang, H.-C. Chang, *Langmuir* **2004**, *20*, 5879.
[88] I. Rehor, H. Mackova, S. K. Filippov, J. Kucka, V. Proks, J. Slegerova, S. Turner, G. Van Tendeloo, M. Ledvina, M. Hruby, P. Cigler, *ChemPlusChem* **2014**, *79*, 21.
[89] J. Stursa, J. Havlik, V. Petrakova, M. Gulka, J. Ralis, V. Zach, Z. Pulec, V. Stepan, S. A. Zargaleh, M. Ledvina, M. Nesladek, F. Treussart, P. Cigler, *Carbon* **2016**, *96*, 812.
[90] S. Banerjee, D. Li, *Appl. Spectrosc.* **1991**, *45*, 1047.
[91] M. A. Friese, S. Banerjee, *Appl. Spectrosc.* **1992**, *46*, 246.

Supporting Information

Benchtop Fluorination of Fluorescent Nanodiamonds on a Preparative Scale: Towards Unusually Hydrophilic Bright Particles

*Jan Havlik, Helena Raabova, Michal Gulka, Vladimira Petrakova, Marie Jakl Krecmarova, Vlastimil Masek, Petr Lousa, Jan Stursa, Hans-Gerd Boyen, Milos Nesladek, Petr Cigler**

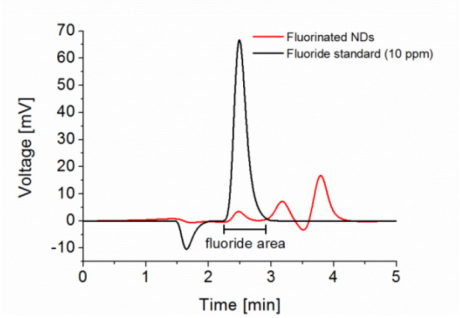

Figure S1: Ion-exchange chromatogram showing a typical analyzed sample (red) and fluoride concentration standard (black). Peaks at times >3 min correspond to other halogenide anions present as impurities and are well-separated from the fluoride peak.

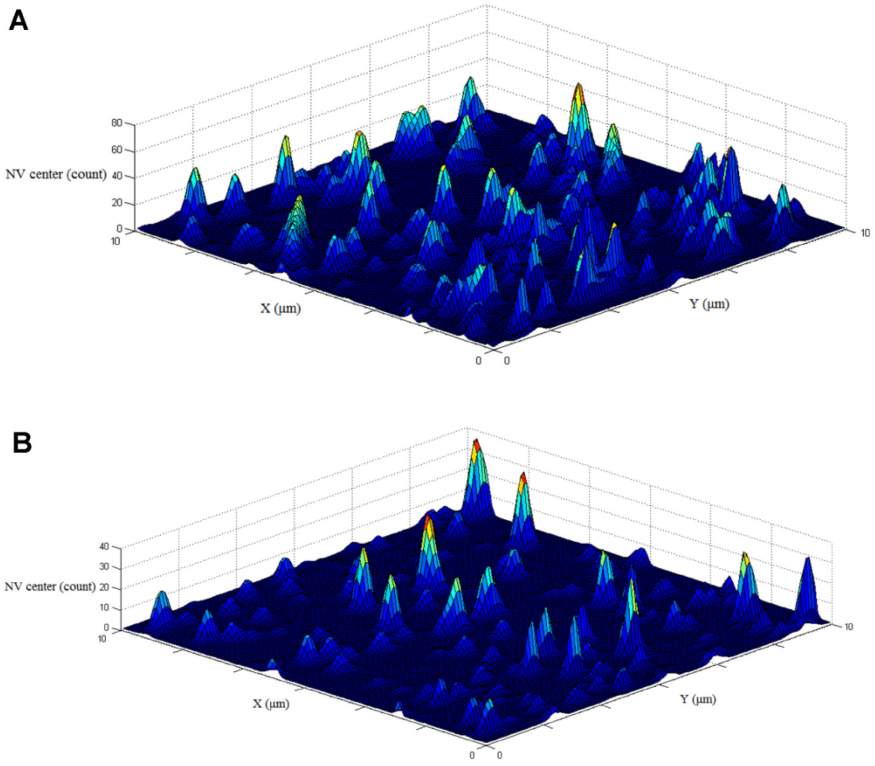

Figure S2: Representative 3D maps of NV luminescence, measured on ND particles dispersed on quartz cover slip surface after drying up 1 µl ND colloidal solution of (A) oxidised and (B) fluorinated ND. In the 3D plot one can easily identify spots corresponding to the ND particles as photoluminescence maxima protruding above the background. The NV emission intensities related to luminescent spots were calculated from the number of detected counts. The number of the NV centres at each ensured spot is shown on the z-axis. 3D maps for oxidized NDs show higher proportion of clustered particles with higher number of counts as compared to fluorinated NDs.

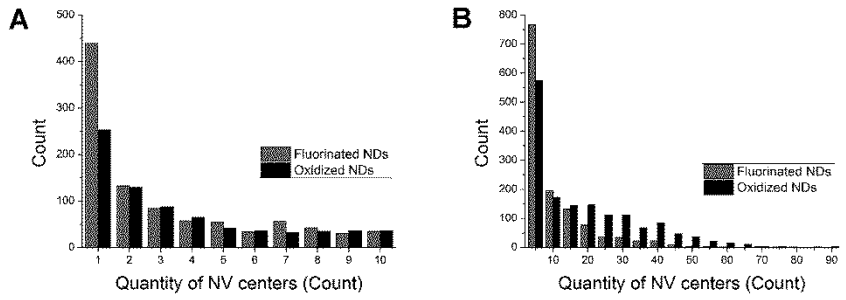

Figure S3: Statistic distribution of concentration of NV centres per luminescent spot as detected from confocal photoluminescence mapping and averaged from 20 experimental maps. (A) Spots with lower and (B) higher NV centers' counts. The fraction of nanodiamond particles containing just 1 NV center is significantly higher for fluorinated compared to oxidized NDs (A). The number of NV centres per luminescence spot is decreasing with increasing number of NV centres per spot. In micro-droplets created from colloidal solution of oxidized ND formation of larger cluster occured, which was partially supressed by fluorination (B).

Appendix D

Appendix E

Havlik, J.; Kucka, J.; Raabova, H.; Petrakova, V.; Stepan, V.; Zlamalova Cilova, Z.; Kucera, J.; Hruby, M.; Cigler, P.; Extremely rapid irradiation of nanoparticles with ions generated in situ by a nuclear reaction – **manuscript submitted**.

Appendix E

Extremely rapid isotropic irradiation of nanoparticles with ions generated *in situ* by a nuclear reaction

Jan Havlik[1,2], Jan Kucka[3], Helena Raabova[1,4], Vladimira Petrakova[5], Vaclav Stepan[6], Zuzana Zlamalova Cilova[4], Jan Stursa[6], Jan Kucera[6], Martin Hruby[3]* and Petr Cigler[1]*

[1]Institute of Organic Chemistry and Biochemistry of the CAS, v.v.i., Flemingovo nam. 2, 166 10 Prague 6, Czech Republic.

[2]Faculty of Science, Charles University, Hlavova 2030, 128 40 Prague 2, Czech Republic.

[3]Institute of Macromolecular Chemistry, v.v.i., The Czech Academy of Sciences, Heyrovskeho nam. 2, 162 06 Prague 6, Czech Republic.

[4]University of Chemistry and Technology, Prague, Technicka 5, 166 28 Prague 6, Czech Republic.

[5]Faculty of Biomedical Engineering, Czech Technical University in Prague, nam. Sitna 3105, 272 01 Kladno, Czech Republic.

[6]Nuclear Physics Institute of the CAS, v.v.i., Na Truhlářce 39/64, 180 00 Praha 8, Czech Republic.

*corresponding authors, e-mails: mhruby@centrum.cz, cigler@uochb.cas.cz

Abstract:

Energetic ions represent an important tool for creation of functional nanostructured materials. Although the potential applications of ion-irradiated nanomaterials span an impressive range from electronics to biomedicine, mass preparation remains a major challenge, largely due to the physical and technical limitations of irradiation techniques. Here, we describe an approach based on isotropic irradiation of nanomaterials by light ions formed homogeneously *in situ* by a nuclear reaction. The target nanoparticles are embedded in ^{10}B-isotopically enriched boron(III) oxide and placed in a neutron flux. Neutrons captured by ^{10}B generate an isotropic flux of energetic α particles and $^{7}Li^{+}$ that uniformly irradiate the surrounding nanoparticles. We applied this technique for production of fluorescent nanodiamonds, which we achieved with irradiation times as short as 3 minutes. Furthermore, our method increases current preparative yields by a factor of ~1,000, allowing production of hundreds of grams of nanoparticles in one day. We envision that our easily scalable technique will increase the world production of ion-irradiated nanoparticles, facilitating their use in various applications.

Over the past two decades, nanomaterials research has generated a wealth of experimental and theoretical data showing that the atomic structure and morphology of nanomaterials can be changed in a controllable manner[1,2]. While a chemical approach enables a plethora of synthetic modifications to the nanomaterial surface, currently available tools for post-preparative tailoring of the inner atomic structure of nanoparticles are based mostly on use of ionizing radiation and thermal annealing.

Among ionizing particles, energetic ions are attractive for materials science because they are very efficient in causing controlled structural defects in solid materials. Modification with energetic ions thus represents a key approach to the creation of a variety of functional nanostructured materials, which has enabled advances in numerous research fields. In optics, this approach is used to create lattice point defects, including vacancies, color centers,[3–5] and single-photon emitters.[6] In nanoscience, researchers have used modification with energetic ions to fabricate and tailor new types of materials[1,2,7–9], including magnetic[10], semiconductor[11], and carbon[12] nanomaterials. Irradiation with energetic ions also provides a means to radiolabel nanoparticles for biological tracing[13,14].

Most nanoparticles can be engineered using so-called light ions [$^{1}H^{+}$, $^{2}H^{+}$, $^{3}He^{+}$, $^{4}He^{+}$, α particles ($^{4}He^{2+}$), and $^{7}Li^{+}$]. Compared to heavier ions, their range in materials is much higher[2] and they cause less damage[15]. For example, irradiation with α particles or He^{+} ions has been used for tuning of the optical, electric, and magnetic properties of various nanomaterials—including graphene[16], carbon[17,18], and boron nitride[15] nanotubes; semiconductors[19]; magnetic nanoparticles[20–22]; silica[4]; metallic clusters[23]; and polymers[24].

Although there is an impressive range of suggested applications for ion-irradiated nanoparticles, a major challenge remains in well-controlled mass preparation of these particles. To achieve uniform irradiation of a sufficient amount of material in accelerator sources, the ion beam is defocused and collimated just before entry to the target. However, the ion density may vary up to 20% due to distribution of ion density in the beam cross section. Due to energetic inhomogeneity, the ion ranges in the target also may differ significantly[25]. For energetic ions, penetration depth is typically millimeters to centimeters in the case of p^{+}, but only micrometers to hundreds of micrometers for heavier ions, depending on ion energy and target density. The energetic ions lose energy along their path and end their way with the Bragg peak, beyond which there is negligible influence on the matter. Moreover, nanoparticle powders exhibit poor thermal conductivity and may overheat under irradiation, necessitating the use of thin nanoparticle layers in the target to prevent thermally induced alterations of the nanoparticles[26]. These reasons make scale-up of production extremely challenging, because only very thin layers of nanoparticles can be efficiently and homogeneously irradiated.[3,27]

Here, we describe an approach for mass production of ion-irradiated nanoparticles using light ions (α particles and $^{7}Li^{+}$ ions) generated *in situ*. The target nanoparticles are dispersed in ^{10}B-isotopically enriched boron(III) oxide and placed in an isotropic neutron flux, where a neutron-induced reaction on

^{10}B occurs homogeneously. Our approach utilizes the advantages of neutrons, including their long penetration depth into the target determined mainly by their absorption cross-sections, the absence of threshold energy for a nuclear reaction, and the availability of scale-up of irradiated material to tens of grams. The all-directional local flux of light ions formed *in situ* from ^{10}B uniformly irradiates the surrounding nanoparticles (see Figure 1). Moreover, using high neutron fluence rates (10^{12} – 10^{14} cm^{-2} s^{-1}), which are routinely available in experimental nuclear reactors, we also achieve unusually high fluxes of energetic ions. Therefore, we gain comparable effects to hours of irradiation in accelerator devices in a few minutes.

We demonstrate the benefits of our method on the mass production of diamond nanocrystals bearing fluorescent nitrogen-vacancy (NV) color centers in the crystal lattice (FNDs). These extremely photostable atomic defects have been thoroughly studied for their unique applications as ultrasensitive magnetic[28–30] and electric[31–33] field sensors, single photon emitters[34], chemical probes[35–37], and qubits[38]. The fluorescence of NV centers is spin-dependent, which enables coherent manipulation of single NVs[39] and measurement of optically detected magnetic resonance of single spins in ambient conditions[40]. FNDs show low toxicity, and their use as bright near-infrared fluorescent probes in high-resolution biomedical imaging[41–43] and nanomedicine[44–47] recently has been demonstrated. Despite recent achievements in the preparation procedures, wider use of FNDs remains limited by the need for time-consuming and expensive irradiation with energetic ions[3,25,27,48–51] or electrons[52,50,53] which allows production of only a small amount of material (up to hundreds of milligrams) at once. The irradiation approaches are summarized in recent reviews[54,55].

The formation of NV centers in NDs is technically a two-step process and typically involves i) generation of vacancies in the diamond lattice using irradiation with energetic particles followed by ii) recombination of vacancies with atomic nitrogen impurities upon high temperature annealing[3,25,48–50]. To efficiently produce energetic light ions (α particles and $^{7}Li^{+}$ ions) creating the vacancies, we used capture of neutrons by ^{10}B (Figure 1)[56]. Two reaction channels exist, described by equations (1) and (2), with different probabilities (*P*)

$$^{10}_{5}\mathrm{B} + {}^{1}_{0}n = {}^{4}_{2}\mathrm{He} + {}^{7}_{3}\mathrm{Li} + \gamma(0.48\ \mathrm{MeV}) + 2.31\ \mathrm{MeV} \qquad P = 94\% \qquad (1)$$

$$^{10}_{5}\mathrm{B} + {}^{1}_{0}n = {}^{4}_{2}\mathrm{He} + {}^{7}_{3}\mathrm{Li} + 2.79\ \mathrm{MeV} \qquad P = 6\% \qquad (2)$$

with a total absorption cross section of approximately 3,800 barns for thermal neutrons[57]. We utilized these nuclear reactions for isotropic irradiation of a bulk sample containing homogeneously distributed nanoparticles, instead of exposing a thin layer of nanoparticles to an energetic ion beam, the range of which is low and results in a characteristic non-homogeneous distribution of defects in material (Bragg peak). We generated energetic ions homogeneously in the entire sample volume by reaction of ^{10}B with thermal neutrons (Figure 1).

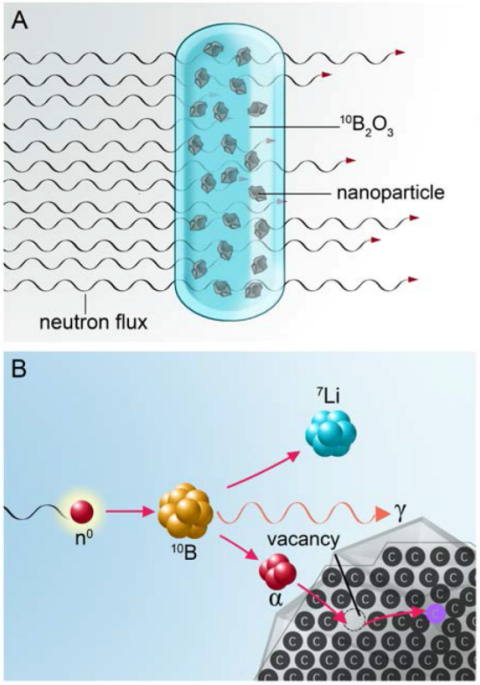

Figure 1. General scheme of the implantation of energetic ions into nanoparticles generated *in situ* by ^{10}B neutron capture. **(A)** A capsule containing nanoparticles embedded in a glassy melt of $^{10}B_2O_3$ exposed to a neutron flux. **(B)** Detail of *in situ*-formed α particles and $^7Li^+$ ions entering a nanodiamond particle and creating vacancies inside.

To understand the behavior of α particles and $^7Li^+$ ions in a glassy melt, we first simulated their trajectories for a composite containing 33 weight % NDs (approximated with 35-nm diamond spheres) and 67% $^{10}B_2O_3$ (volume fraction of nanoparticles is 22.6%). We randomly distributed the NDs in the melt and using the Geant4 toolkit analyzed the trajectories of α particles and $^7Li^+$ ions emitted from random surface points (for details, see Supporting Information). From 2.5×10^6 particle trajectories, we calculated the projected range (Figure S1 in Supporting Information) and the average number of ND particles hit by one α particle or $^7Li^+$ ion (Figure 2A). Clearly, either an α particle or $^7Li^+$ ion can penetrate far enough to create vacancies in dozens of individual NDs embedded in the $^{10}B_2O_3$ melt.

The vacancies are created with an efficiency that approximately corresponds to the amount of deposited energy from the ions. Figure 2B shows these energy deposition curves in the $^{10}B_2O_3$ melt for an α particle and $^7Li^+$ ion as a function of distance from a single ^{10}B nucleus. Merging both depositions provides a region where we can anticipate active creation of vacancies, subsequently leading to formation of NV centers upon annealing. Note that in the case of less probable reaction (2), this region

is slightly larger thanks to higher energy of both created ions (not shown). Because the nuclear reaction generating the α particles and $^{7}Li^{+}$ ions occurs randomly in the entire volume of the melt, we expected the irradiation of nanoparticles to be very homogeneous and effective.

The known composition and geometry of our sample, neutron fluence rates (see Methods) and involvement of self-shielding of thermal neutrons by ^{10}B enabled us to calculate the effective thermal neutron fluence rate inside the melt[58] and the corresponding yields of charged particles. The irradiation of our sample yielded 5.34×10^{13} s^{-1} of either α particles or $^{7}Li^{+}$ ions, i.e. 1.07×10^{14} s^{-1} of charged particles in total. Based on these values, we calculated the number of created vacancies in NDs for each type of energetic ion using SRIM simulation package[59]. The obtained values 2.50×10^{15} and 6.36×10^{15} s^{-1} for α particles and $^{7}Li^{+}$ ions, respectively, indicate effective and rapid formation of vacancies in the NDs present in the neutron irradiated melt. The known composition of the sample enabled us to calculate the overall damage rate 1.53×10^{-5} dpa s^{-1} for NDs [which is used for recalculation of irradiation times to doses in Figure 3A and 3C].

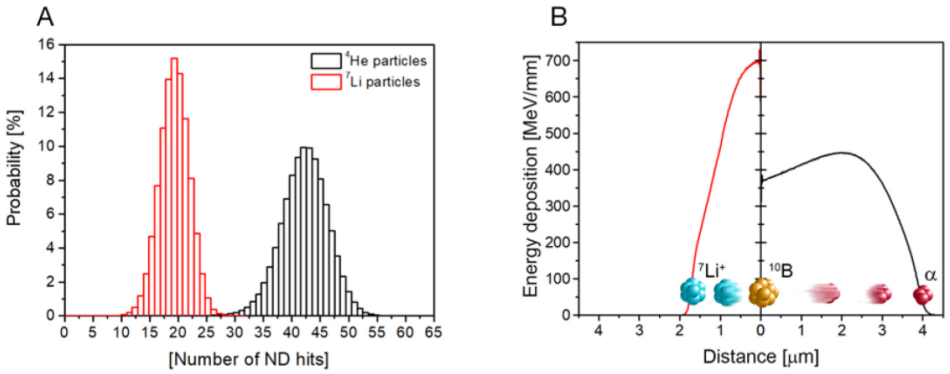

Figure 2. Compared to $^{7}Li^{+}$ particles, α particles can interact with higher number of ND particles and deposit lower energy over larger distance in 33 weight % dispersion of 35-nm spherical NDs in $^{10}B_2O_3$. **(A)** The number of ND hits per one α particle and $^{7}Li^{+}$ ion generated using reaction (1) and **(B)** energy deposition of these α particles (black) and $^{7}Li^{+}$ ions (red) along their trajectory. On average, a single α particle with an energy of 1.47 MeV interacts along its ~3.9 μm trajectory with 42 nanoparticles before losing its kinetic energy. Similarly, a 0.84 MeV $^{7}Li^{+}$ ion interacts along its ~1.7 μm trajectory with another 19 nanoparticles. The histograms and energy depositions were calculated from simulation of trajectories performed with the Geant4 toolkit.

To reach the highest efficacy of the irradiation procedure, it is essential to keep the nanoparticles in a close contact with the ^{10}B-rich environment. We met this condition by creating a dispersion of the nanoparticles in molten $^{10}B_2O_3$, which is formed by thermal dehydration of boric acid ($H_3{}^{10}BO_3$). As a primary source of ^{10}B, we used isotopically enriched boric acid (99.5 mole % ^{10}B), because boric acid with natural isotopic abundance contains only 20 mole % ^{10}B and 80 mole % inert nuclide ^{11}B. Notably, $H_3{}^{10}BO_3$ is generally available and inexpensive because large amounts are produced for the nuclear industry.

We prepared two glass melts containing a 33% dispersion of 35-nm and 150-nm NDs in $^{10}B_2O_3$. Their SEM micrographs indicated homogeneously dispersed nanoparticles without signs of major aggregation or separation of both components (Figure S2 in Supporting Information). The size of the visible granules roughly corresponds to the size of the nanoparticles.

To generate all-directional local flux of α particles and $^7Li^+$ ions creating vacancies in ND crystals, we loaded both glass melts in quartz tubes and irradiated them in a nuclear reactor for various times ranging from 3 to 100 min (see Supporting Information). After irradiation, we dissolved the $^{10}B_2O_3$ matrix in NaOH solution and further processed the NDs in a similar manner as previously established for cyclotron-irradiated samples (annealing to form fluorescent NV centers and oxidation by air followed by treatment with a mixture of mineral acids)[25,43,60]. Isolation from the $^{10}B_2O_3$ melt was almost quantitative in yield and provided NDs with the characteristic size distribution (Figure S3 in Supporting Information) and colloidal stability in aqueous solutions (Figure S4 in Supporting Information). Zeta potentials were -46.7 mV for 35-nm NDs and -41.0 mV for 150-nm NDs, suggesting strong Coulombic stabilization by negative charge of deprotonated carboxylates created by oxidation on the surface of the nanoparticles.

Using Raman spectroscopy, we analyzed the diamond lattice irradiation damage for both types of NDs. In general, we observed a slight decrease in sp^3 and increase in sp^2 carbon content caused by crystal lattice damage with increasing irradiation time (Figure 3A and B). The higher amount of sp^2 carbons for smaller NDs can be explained by their higher surface/volume ratio, which is consistent with the observation that the formation of sp^2 phases in NDs occurs preferentially in the surface region[61]. Consistently, we observed the highest fluorescence intensity for NDs irradiated for less than 20 min (Figure 3C). With longer irradiation times, the yield of NV centers after annealing gradually drops, which correlates with the observed progressive crystal lattice degradation into sp^2 and amorphous structures (Figure 3A).

To optimize the irradiation time, we next aimed to estimate the minimum required dose for obtaining highly bright NDs. To our surprise, we found that it was possible to reduce the dose to 2.75×10^{-3} (corresponds to 3 min – the shortest time for which irradiation is reproducible, due to loading-unloading lags into the water-cooled channels of LVR-15 nuclear reactor we used), while

maintaining the quality and the intensity of ND fluorescence (Figure 3C). In contrast, the control samples of NDs irradiated with neutrons only (without the presence of $^{10}B_2O_3$) show more than one order of magnitude lower fluorescence intensity (Figure S5 in Supporting Information). This indicates that the structural effects on NDs originate predominantly from interaction with α particles and $^{7}Li^{+}$ ions, but not directly from interaction with neutrons.

We were interested, whether this optimized irradiation causes some structural changes to our NDs. Besides the G-band intensity (~1600 cm^{-1}), we monitored also the appearance of the peak at ~1230 cm^{-1} (Figure 3B), which is typically observed in the Raman spectra of ND powders[62]. This peak increases with decreasing size of the diamond crystalline core[62] and it is an intrinsic feature of NDs prepared by HPHT synthesis with subsequent milling. Notably, the intensities of the ~1230 cm^{-1} peak as well as the G-band were undistinguishable for the non-irradiated NDs and the low irradiation times (≤12 min, which corresponds to ≤0.011 dpa; Figure S8B in Supporting Information). This result documents that our optimized irradiation procedure did not cause structural changes of diamond crystalline core of our NDs. Correspondingly, the progressive crystal lattice degradation occurring at longer irradiation times (≥15 min, ≥0.014 dpa; Figure 3A) is clearly reflected in the correlation between intensities of the G-band and the ~1230 cm^{-1} peak (Figure S8A in Supporting Information).

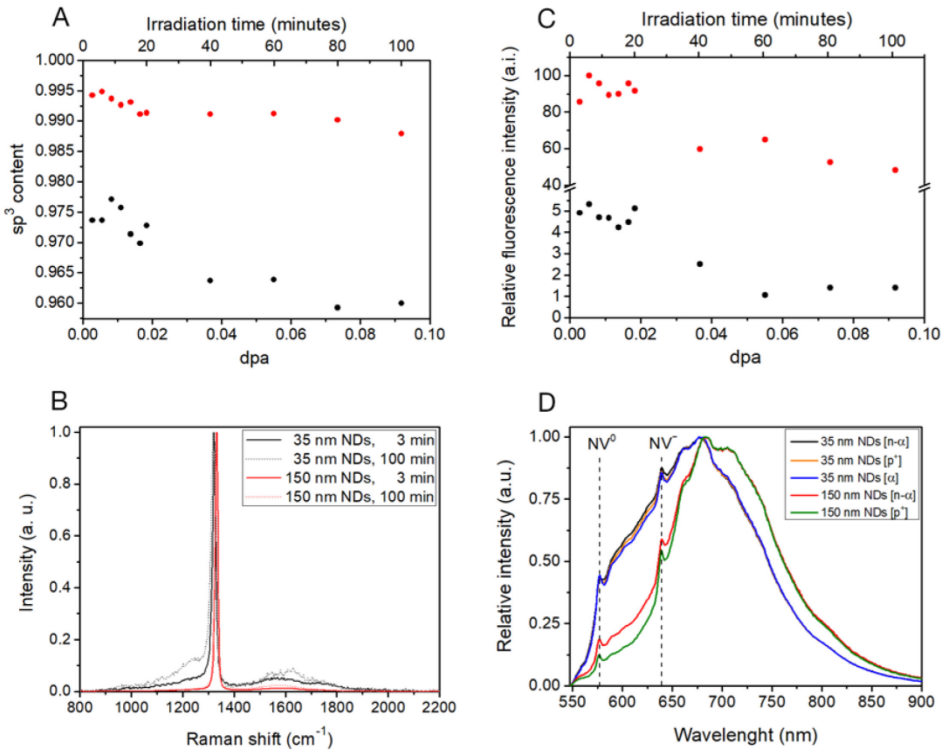

Figure 3. Spectral characterization of irradiated 35-nm and 150-nm NDs reveals how increased radiation damage **(A**, **B)** lowers relative fluorescence intensities (**C**) with increasing irradiation time in nuclear reactor: **(A)** Content of sp^3 carbon, **(B)** Raman spectra (for complete set of Raman spectra for all irradiation times, see Figure S6 in Supporting Information), **(C)** Relative fluorescence intensity. **(D)** Comparison of photoluminescence spectra of samples irradiated in a nuclear reactor (n-α) with samples irradiated in a cyclotron with protons (p^+) or α particles. For spectral measurements, the NDs were drop casted on a silicon wafer. The values of x-axes in **(A, C)** are expressed as either irradiation time or the overall radiation damage expressed as displacements per carbon atom (dpa) which corresponds to the number of vacancies formed in NDs obtained from SRIM simulation (see Methods). The intensities in **(C)** are normalized to the diamond Raman band (the values are quantitatively comparable). The spectra in **(D)** are normalized at their maxima. Vertical dash lines labeled ZPL denotes the zero phonon line of the NV^- (wavelength 637 nm) and NV^0 (wavelength 575 nm) color center with typical phonon side band structures[63].

Next, we compared our results with data on the creation of NV centers in bulk diamond crystals irradiated only by fast neutrons (without the presence of $^{10}B_2O_3$)[64]. In these cases, the number of created NV centers grew linearly with neutron dose, reaching an optimum at 7×10^{17} cm^{-2} and dropping rapidly above this value. Notably, under the conditions used in our setup, the estimated optimum dose would correspond to ~27 h of fast neutron irradiation, which is three orders of magnitude longer than the 3 min achieved with our novel approach. Correspondingly, 50 h of neutron irradiation[65] with a fluence of 5×10^{17} cm^{-2} and tens of hours[66] with neutron fluencies ~10^{17} were necessary for effective creation of NV centers in bulk diamond crystals. Inelastic fast neutron scattering causes the vacancy formation in samples without the presence of $^{10}B_2O_3$, while thermal neutron capture by ^{10}B leads to creation of vacancies upon interactions of the formed α particle and $^{7}Li^{+}$ ions with carbon atoms. To ascertain the dominant process contributing to NV center formation in our sample, we compared the cross sections of inelastic neutron scattering (for fast neutrons it is ~4.0 barns, for thermal neutrons 4.75 barns)[56] and thermal neutron capture by ^{10}B (3,800 barns)[57], and found a difference of approximately three orders of magnitude. Although these cross sections relate to different processes (direct vs. indirect interaction of neutrons with carbon atoms), the vast difference between them corresponds well with the observed predominance of neutron capture by ^{10}B in vacancy formation (Figure S5 in Supporting Information).

Importantly, the short irradiation time and space capacity of irradiation channels in the nuclear reactor presents the possibility of semi-continuous production of hundreds of grams of FNDs per day. In comparison to irradiation with electrons[52] or energetic ions in accelerators[3,25,49,50] in which the yield typically reaches hundreds of milligrams per day, using the very short irradiation times (3 min) we increased the daily output of FNDs by a factor of approximately 10^3. This allows for enormously high preparative yields and an economically feasible production of irradiated nanoparticles (the price per hour irradiation is roughly similar for nuclear reactors as well as accelerators).

FNDs produced in this way show spectral features consistent with results obtained previously in an accelerator[49]. Specifically, the 150-nm NDs had much higher fluorescence intensity than the smaller 35-nm NDs (Figure 3C). Because the maximum vacancy concentration is an increasing function of the particle size[67], the vacancy capture efficiency strongly rises with increasing size of the diamond crystal. The migration path of the vacancies to the surface of nanoparticles during annealing is shorter for smaller particles, and their recombination with nitrogen atoms is less effective[68].

The NV^{-}/NV^{0} zero phonon line (ZPL) intensity ratios and the width of the ZPL and phonon replicas were similar for neutron-irradiated NDs in $^{10}B_2O_3$ glass and for FNDs we prepared using direct cyclotron irradiation with either p^{+} or α particles (Figure 3D). Because these spectral parameters are related to the crystal properties (formed irregularities, other defect centers) and surface properties[69,70], the

similarities in the observed spectra indicate that the samples prepared by the different types of irradiation have comparable damage to the crystal lattice.

Although the spectral shapes and overall fluorescence of our FNDs were very similar to those of FNDs irradiated in an accelerator, we were interested in whether our procedure increases the homogeneity of irradiation, i. e., whether the material contains a higher fraction of FNDs. To distinguish the fluorescent and non-fluorescent NDs present in a large ensemble at the single-particle level[25,71], we utilized simultaneous measurement of fluorescence-lifetime imaging microscopy (FLIM) and atomic force microscopy (AFM) (Figure S7 in Supporting Information). We found that the fraction of FNDs in material irradiated in a nuclear reactor increased by a factor of 2.6 compared to optimally[49] p^+-irradiated pellet target with NDs in an accelerator (49% vs. 19%). Moreover, the particles irradiated in nuclear reactor were brighter on average, contained significantly higher fraction of very bright particles (fluorescence intensity corresponding to approximately 5 NV centers and higher). However, the largest fraction of particles exhibited lower fluorescence (corresponding to <3 NV centers), see histograms in Figure S9 in Supporting information.

	Irradiated in reactor	Proton irradiated
Fraction of fluorescent particles	49 %	19 %
Average fluorescence intensity per particle (normalized/a. u.)	3.2	1.7
Median fluorescence intensity per particle (normalized/a. u.)	2.1	1.4

Table 1: Isotropic irradiation with energetic light ions leads to higher fraction of fluorescent particles and to higher fluorescence intensities. The table compares fluorescent ND prepared by neutron irradiation in the reactor and by proton irradiation in cyclotron using optimized pellet target. Fluorescence intensity is normalized to average intensity of one NV center in ND particle. Parameters were calculated from more than 400 particles.

This increase in fraction of fluorescent particles is close to the enhancement factor of 3.2 achieved for a homogeneous liquid target containing a colloidal aqueous solution of NDs compared to an optimized pellet target[25]. Note that both types of accelerator irradiations took 4.5 h (compared to 3 min in a reactor).

In conclusion, we describe an easily scalable method for production of light ion-irradiated nanoparticles utilizing α particle and $^7Li^+$ ions generated *in situ*. The target nanoparticles embedded in

^{10}B-isotopically enriched boric oxide are placed in a neutron flux, where neutron-induced nuclear reaction on ^{10}B occurs homogeneously, producing an isotropic light ion flux. Our method thus combines the advantages of the neutron and ion irradiation approaches. We demonstrated its usefulness for large-scale production of fluorescent nanodiamonds bearing nitrogen-vacancy color centers. The irradiation was highly homogeneous, producing material with a high fraction of bright fluorescent particles. Because of the favorably high cross section of ^{10}B for neutron capture, our method can operate with extremely rapid irradiation times of only a few minutes. This provides access to yields of hundreds of grams of nanoparticles per day, accelerating the current production rates by a factor of nearly 10^3.

We envision that our technique, combined with general accessibility to nuclear reactors (currently, 59 research nuclear reactors with public access are operating worldwide)[72], can facilitate production of well-defined light ion-irradiated nanoparticles that can be widely used in diverse applications, such as in semiconductor, magnetic, quantum sensing, optical, and bioimaging devices.

Methods

Chemicals

Sodium hydroxide, hydrochloric acid (35%), nitric acid (65%), and sulfuric acid (96%) were purchased from Penta (Czech Republic). Potassium nitrate and hydrofluoric acid (40%) were purchased from Sigma Aldrich (Prague, Czech Republic). All chemicals were p.a. quality and were used as received without further purification. Boric acid enriched to 99.5% ^{10}B was supplied by Katchem Ltd., Czech Republic. Deionized water used for all washing steps and preparation of solutions was prepared with a Millipore Synergy UV Ultrapure water system.

ND Pretreatment

NDs were supplied by Microdiamant Switzerland (MSY 0-0.05 and MSY 0-0.25). The NDs were oxidized by air in a furnace (Thermolyne 21100 tube) at 510 °C for 5 h. Subsequently, the NDs were treated with a mixture of H_2SO_4 and HNO_3 (9:1) at 90 °C for 3 days and washed with water, 1 M NaOH, and 1 M HCl. They were washed an additional 5 times with water and then freeze-dried. Purified ND powder (500 mg), containing approximately 100–200 ppm of natural nitrogen impurities, was mixed with 2.0 g $H_3{}^{10}BO_3$ ground in a mortar and transferred into a synthetic corundum crucible. The mixture was placed in a vertical furnace (Thermolyne 21100 tube) and heated to 600 °C for 5 min (until the development of water vapor ceased). The temperature was then increased to 700 °C, and the melt was homogenized by mixing and left to cool to RT. The final glassy composite was first ground in a mortar and then pulverized in a small ball mill.

The typical weight loss within such melting was 39% due to dehydration of boric acid to boron(III) oxide. The final melt used for irradiations contained 33 weight % NDs and 22% ^{10}B.

The nanoparticles were carefully purified to remove trace amounts of elements (e.g., iron) that may activate in neutron flux, producing undesirable radioactive contamination of the product. The product had negligible radioactivity after the purification was successfully implemented.

Irradiation and Washing

The powderized melts of ND and $^{10}B_2O_3$ were sealed in quartz, sodium-free capillaries (inner diameter 1.5 mm; height of the melt 11 mm), inserted in an aluminum capsule, and irradiated in a vertical water-cooled (~45 °C) channel H8 positioned in the Be reflector of the LVR-15 nuclear reactor in Rez near Prague at neutron fluence rates of 2×10^{13} cm^{-2} s^{-1}, 1×10^{13} cm^{-2} s^{-1}, and 7×10^{12} cm^{-2} s^{-1} for thermal, epithermal, and fast neutrons, respectively, for various periods of time (3–100 min). Neither NDs nor quartz should contain traces of sodium, because natural monoisotope ^{23}Na is readily neutron-activated into ^{24}Na, which is beta and gamma emitter with half-life 14.95 h. If there are traces of sodium in starting materials, there is an easy option to let ^{24}Na extinct for 10 half-lives (i.e., ca one week, or even shorter time if less contaminated) after irradiation. The sample can be handled then as non-radioactive.

After irradiation, the capillaries were opened and left overnight in a vial with 6 M NaOH at 60 °C to dissolve boron(III) oxide. The residue adhering to quartz glass was released in an ultrasonic bath. Supernatant was washed gradually with 6 M NaOH, H_2O, 1 M HCl, and 5 times with H_2O. Possible quartz glass splinters were separated by sedimentation. The supernatant was treated with concentrated HF for 12 h; washed with H_2O, 1 M HCl, and 5 times with H_2O; and lyophilized.

Annealing and oxidation

All samples were annealed at 900 °C for 1 h in an argon atmosphere followed by air oxidation at 510 °C for 4 h at normal pressure in a Thermolyne 21100 tube furnace calibrated with an external thermocouple (Testo AG 1009). According to the TEM image analysis[73], the obtained particles were 35 nm in diameter.

TEM measurement

For particle size distribution evaluation, we used image analysis of TEM micrographs (Figure S2A, B). For each sample, we analyzed approximately 1000 particles, acquired their equivalent circular diameters, and recalculated them to volume-weighted histograms (Figure S2C).

Samples for TEM were prepared similarly as described in our previous work[73]. Carbon-coated copper grids (Pyser) were oxidized in a UV-ozonizing chamber (UV/Ozone Pro Cleaner Plus, Bioforce Nanosciences) for 15 min, then incubated in poly(ethyleneimine) solution (MW = 2.5 kDa, 0.1 mg/ml) for 10 min, washed with water, and incubated in an aqueous solution of NDs (0.1 mg/ml) for 3 mins. Micrographs were taken at with a JEOL JEM 1011 microscope at 80 kV acceleration voltage.

Analysis of particle size distributions was performed with ImageJ software using a previously described procedure[73]. Particle size was expressed as equivalent circular diameter (d_{eq}), defined as the diameter of a circular particle with the same area as the particle of interest (S).

$$d_{\mathrm{eq}} = \sqrt{4S/\pi}$$

Equivalent diameters were used to calculate particle volume (PV).

$$PV = \frac{4}{3}\pi\left(\frac{d_{\mathrm{eq}}}{2}\right)^3$$

and subsequently for creation of volume-weighted histogram.

SEM measurement

A silicon wafer (10×3 mm) with a small fragment of boron oxide-ND composite sample put on its surface was placed in a quartz tube. The sample was melted at 700 °C for 15 min under an argon atmosphere in a Thermolyne 21100 tube furnace and left to cool down to RT. Immediately after preparation, the silicon wafer with melted sample was fixed to a holder with double-sided tape and coated with a thin layer of gold. The morphologies of samples were observed by using a Hitachi S-4700 field emission scanning electron microscope (FE-SEM) at 15 kV.

Geant4 and SRIM simulations

Geant4 v10.2 general particle transport toolkit[74,75] was used to calculate the projected range and average number of ND particles hit by one α particle or $^{7}Li^{+}$ ion in a dispersion of NDs in $^{10}B_2O_3$. The user application was developed using the TestEm11 extended electromagnetic example as a template. ND particles were approximated by carbon spheres with radius 35 nm and density 3.5 g/cm^3. ND particles were then randomly distributed into $^{10}B_2O_3$ material, with density 1.82 g/cm^3, forming a homogeneous dispersion. Due to memory constraints, the nested replicated approach was applied to build the whole sample volume. The volume of the sample was filled by replicating a single building

block with base 0.3×0.3 µm and height set to match the sample height. The sample volume was set to 2.7×2.7×6 µm for α particles and to 2.7×2.7×2.4 µm for $^{7}Li^{+}$ ions. Primary particles generated by nuclear reaction (1) (1.47 MeV α particle and 0.84 MeV $^{7}Li^{+}$ ion) were emitted perpendicular to the building block base plane, from a random point in a square with 100 nm sides placed in the center of the entry surface of the middle building block.

250 different ND distributions inside the building block were generated, and for each of those configurations, calculations were run for 10^4 primaries. Results are presented for the resulting 2.5×10^6 primary particles for each type.

For simulation of damage of NDs upon irradiation, SRIM-2013 code (www.srim.org) was used. The damage rate (expressed as the number of vacancies created in the overall sample) was estimated using the known atomic composition (see ND Pretreatment) and the yield $5.34\times10^{13}\ s^{-1}$ for each the α particles (1.47 MeV) and $^{7}Li^{+}$ ions (0.84 MeV) generated upon neutron irradiation in the overall sample. Because the range of the energetic ions in the material (a few µm) is negligible compared to dimension of the sample (a cylinder of diameter 1.5 mm and height 11 mm), we consider all created ions to be captured in the sample. The displacement per atom (dpa) values were recalculated for the fraction of carbon atoms in the material.

Raman and fluorescence measurements

The samples were prepared by drop-casting of the aqueous dispersion of NDs on the polished silicon wafer. Raman and luminescence spectra were measured using a Renishaw InVia Raman Microscope; the excitation wavelength was 514 nm (luminescence measurements) and 325 nm (Raman measurements) with 15 mW laser power, x20 objective. The exposure time was 6 seconds, accumulation 10 times; 20 measurements were made on each sample. The Raman and luminescence spectra were taken at room temperature and normalized to the diamond Raman peak. The changes in sp3 carbon content) was measured and evaluated according the literature procedure[76]. Raman spectra were analyzed using Peak-o-mat program.

FLIM/AFM measurements

The nanoparticles were deposited on an oxygen-plasma-cleaned glass cover slip by dip coating for 5 min and rinsed using DI water (MilliQ). The concentration of the stock solution of nanoparticles was 0.001 mg/ml.

For FLIM, fluorescence images were taken using a time-resolved fluorescence confocal microscope (MicroTime200 – PicoQuant), with excitation wavelength 532 nm, 1.2 mW laser power, using a 60x water immersion objective (Olympus) and a 650 long pass filter (Edmund Optics, OD4). Data were processed using Matlab (R2014b, Mathworks). Selection of NDs was performed using calculated fast

fluorescence lifetime (FLIM) (>6 ns) and counts/pixel (>10 cts) thresholds. To obtain normalized PL intensity per particle, the measured fluorescence intensities were normalized to calculated average fluorescence intensity of single NV center (based on correlation measurements). The normalized intensity therefore represents approximately the number of NV centers in the particle.

AFM images were taken on a JPK Nanowizard® AFM combined on the FLIM Microtime setup. Scans were performed using AC mode measurements using silicon probes (ACTA, with aluminium coating of the reflex side, ACTA300 – TL).

References

1. Dhara, S. Formation, Dynamics, and Characterization of Nanostructures by Ion Beam Irradiation. *Crit. Rev. Solid State Mater. Sci.* **32,** 1–50 (2007).
2. Krasheninnikov, A. V. & Nordlund, K. Ion and electron irradiation-induced effects in nanostructured materials. *J. Appl. Phys.* **107,** 71301 (2010).
3. Chang, Y.-R. *et al.* Mass production and dynamic imaging of fluorescent nanodiamonds. *Nat. Nanotechnol.* **3,** 284–288 (2008).
4. Alessi, A. *et al.* Alpha and deuteron irradiation effects on silica nanoparticles. *J. Mater. Sci.* **49,** 6475–6484 (2014).
5. Pezzagna, S., Naydenov, B., Jelezko, F., Wrachtrup, J. & Meijer, J. Creation efficiency of nitrogen-vacancy centres in diamond. *New J. Phys.* **12,** 65017 (2010).
6. Aharonovich, I., Englund, D. & Toth, M. Solid-state single-photon emitters. *Nat. Photonics* **10,** 631–641 (2016).
7. Andrievskii, R. A. Effect of irradiation on the properties of nanomaterials. *Phys. Met. Metallogr.* **110,** 229–240 (2010).
8. Giulian, R. *et al.* Shape transformation of Pt nanoparticles induced by swift heavy-ion irradiation. *Phys. Rev. B* **78,** (2008).
9. Roorda, S. *et al.* Aligned Gold Nanorods in Silica Made by Ion Irradiation of Core–Shell Colloidal Particles. *Adv. Mater.* **16,** 235–237 (2004).
10. Fassbender, J., Ravelosona, D. & Samson, Y. Tailoring magnetism by light-ion irradiation. *J. Phys. Appl. Phys.* **37,** R179–R196 (2004).
11. Kozlov, V. A. & Kozlovski, V. V. Doping of semiconductors using radiation defects produced by irradiation with protons and alpha particles. *Semiconductors* **35,** 735–761 (2001).
12. Krasheninnikov, A. V. & Banhart, F. Engineering of nanostructured carbon materials with electron or ion beams. *Nat. Mater.* **6,** 723–733 (2007).
13. Perez-Campana, C. *et al.* Tracing nanoparticles in vivo: a new general synthesis of positron emitting metal oxide nanoparticles by proton beam activation. *Analyst* **137,** 4902–4906 (2012).
14. Gibson, N. *et al.* Radiolabelling of engineered nanoparticles for in vitro and in vivo tracing applications using cyclotron accelerators. *Arch. Toxicol.* **85,** 751–773 (2011).
15. Lehtinen, O. *et al.* Ion irradiation of multi-walled boron nitride nanotubes. *Phys. Status Solidi C* NA-NA (2010). doi:10.1002/pssc.200982956
16. Lehtinen, O., Kotakoski, J., Krasheninnikov, A. V. & Keinonen, J. Cutting and controlled modification of graphene with ion beams. *Nanotechnology* **22,** 175306 (2011).
17. Lehtinen, O. *et al.* Characterization of ion-irradiation-induced defects in multi-walled carbon nanotubes. *New J. Phys.* **13,** 73004 (2011).
18. Aitkaliyeva, A. & Shao, L. The production of amorphous regions in carbon nanotubes by 140keV He ion irradiation. *Carbon* **50,** 4680–4684 (2012).
19. Tongay, S. *et al.* Defects activated photoluminescence in two-dimensional semiconductors: interplay between bound, charged, and free excitons. *Sci. Rep.* **3,** (2013).

20. Dmitrieva, O., Rellinghaus, B., Kästner, J., Liedke, M. O. & Fassbender, J. Ion beam induced destabilization of icosahedral structures in gas phase prepared FePt nanoparticles. *J. Appl. Phys.* **97,** 10N112 (2005).
21. Järvi, T. T. *et al.* From multiply twinned to fcc nanoparticles via irradiation-induced transient amorphization. *EPL Europhys. Lett.* **85,** 26001 (2009).
22. Wiedwald, U. *et al.* Lowering of the L1 0 ordering temperature of FePt nanoparticles by He+ ion irradiation. *Appl. Phys. Lett.* **90,** 62508 (2007).
23. Manikandan, D., Mohan, S. & Nair, K. G. . Optical absorption of copper nanocluster composite soda-lime glass synthesized by binary ion-exchange and ion irradiation. *Mater. Lett.* **58,** 907–910 (2004).
24. El-Badry, B. A., Zaki, M. F., Abdul-Kader, A. M., Hegazy, T. M. & Morsy, A. A. Ion bombardment of Poly-Allyl-Diglycol-Carbonate (CR-39). *Vacuum* **83,** 1138–1142 (2009).
25. Stursa, J. *et al.* Mass production of fluorescent nanodiamonds with a narrow emission intensity distribution. *Carbon* **96,** 812–818 (2016).
26. Holzwarth, U. *et al.* Radiolabelling of nanoparticles by proton irradiation: temperature control in nanoparticulate powder targets. *J. Nanoparticle Res.* **14,** 880 (2012).
27. Mahfouz, R. *et al.* Size-controlled fluorescent nanodiamonds: a facile method of fabrication and color-center counting. *Nanoscale* **5,** 11776–11782 (2013).
28. Balasubramanian, G. *et al.* Nanoscale imaging magnetometry with diamond spins under ambient conditions. *Nature* **455,** 648–651 (2008).
29. Maze, J. R. *et al.* Nanoscale magnetic sensing with an individual electronic spin in diamond. *Nature* **455,** 644–647 (2008).
30. Laraoui, A., Hodges, J. S. & Meriles, C. A. Nitrogen-Vacancy-Assisted Magnetometry of Paramagnetic Centers in an Individual Diamond Nanocrystal. *Nano Lett.* **12,** 3477–3482 (2012).
31. Dolde, F. *et al.* Electric-field sensing using single diamond spins. *Nat. Phys.* **7,** 459–463 (2011).
32. Karaveli, S. *et al.* Modulation of nitrogen vacancy charge state and fluorescence in nanodiamonds using electrochemical potential. *Proc. Natl. Acad. Sci.* **113,** 3938–3943 (2016).
33. Bourgeois, E. *et al.* Photoelectric detection of electron spin resonance of nitrogen-vacancy centres in diamond. *Nat. Commun.* **6,** 8577 (2015).
34. Aharonovich, I., Greentree, A. D. & Prawer, S. Diamond photonics. *Nat. Photonics* **5,** 397–405 (2011).
35. Petrakova, V. *et al.* Charge-sensitive fluorescent nanosensors created from nanodiamonds. *Nanoscale* **7,** 12307–12311 (2015).
36. Petrakova, V. *et al.* Imaging of transfection and intracellular release of intact, non-labeled DNA using fluorescent nanodiamonds. *Nanoscale* **8,** 12002–12012 (2016).
37. Rendler, T. *et al.* Optical imaging of localized chemical events using programmable diamond quantum nanosensors. *Nat. Commun.* **8,** (2017).
38. Pfaff, W. *et al.* Unconditional quantum teleportation between distant solid-state quantum bits. *Science* **345,** 532–535 (2014).
39. Taylor, J. M. *et al.* High-sensitivity diamond magnetometer with nanoscale resolution. *Nat. Phys.* **4,** 810–816 (2008).
40. Gruber, A. *et al.* Scanning Confocal Optical Microscopy and Magnetic Resonance on Single Defect Centers. *Science* **276,** 2012–2014 (1997).
41. Wu, T.-J. *et al.* Tracking the engraftment and regenerative capabilities of transplanted lung stem cells using fluorescent nanodiamonds. *Nat. Nanotechnol.* **8,** 682–689 (2013).
42. Mohan, N., Chen, C.-S., Hsieh, H.-H., Wu, Y.-C. & Chang, H.-C. In Vivo Imaging and Toxicity Assessments of Fluorescent Nanodiamonds in Caenorhabditis elegans. *Nano Lett.* **10,** 3692–3699 (2010).
43. Slegerova, J. *et al.* Designing the nanobiointerface of fluorescent nanodiamonds: highly selective targeting of glioma cancer cells. *Nanoscale* **7,** 415–420 (2015).
44. Chow, E. K. *et al.* Nanodiamond therapeutic delivery agents mediate enhanced chemoresistant tumor treatment. *Sci Transl Med* **3,** 73ra21 (2011).

45. Alhaddad, A. *et al.* Nanodiamond as a Vector for siRNA Delivery to Ewing Sarcoma Cells. *Small* **7,** 3087–3095 (2011).
46. Zhao, L. *et al.* Platinum on Nanodiamond: A Promising Prodrug Conjugated with Stealth Polyglycerol, Targeting Peptide and Acid-Responsive Antitumor Drug. *Adv. Funct. Mater.* **24,** 5348–5357 (2014).
47. Rehor, I. *et al.* Plasmonic Nanodiamonds: Targeted Core–Shell Type Nanoparticles for Cancer Cell Thermoablation. *Adv. Healthc. Mater.* n/a-n/a (2014). doi:10.1002/adhm.201400421
48. Sotoma, S. *et al.* Effective production of fluorescent nanodiamonds containing negatively-charged nitrogen-vacancy centers by ion irradiation. *Diam. Relat. Mater.* **49,** 33–38 (2014).
49. Havlik, J. *et al.* Boosting nanodiamond fluorescence: towards development of brighter probes. *Nanoscale* **5,** 3208–3211 (2013).
50. Boudou, J.-P. *et al.* High yield fabrication of fluorescent nanodiamonds. *Nanotechnology* **20,** 235602 (2009).
51. Kozák, O. *et al.* Photoluminescent Carbon Nanostructures. *Chem. Mater.* **28,** 4085–4128 (2016).
52. Dantelle, G. *et al.* Efficient production of NV colour centres in nanodiamonds using high-energy electron irradiation. *J. Lumin.* **130,** 1655–1658 (2010).
53. Remes, Z. *et al.* N-V-related fluorescence of the monoenergetic high-energy electron-irradiated diamond nanoparticles: N-V-related fluorescence of electron-irradiated diamond nanoparticles. *Phys. Status Solidi A* n/a-n/a (2015). doi:10.1002/pssa.201532180
54. Nagl, A., Hemelaar, S. R. & Schirhagl, R. Improving surface and defect center chemistry of fluorescent nanodiamonds for imaging purposes—a review. *Anal. Bioanal. Chem.* **407,** 7521–7536 (2015).
55. Hsiao, W. W.-W., Hui, Y. Y., Tsai, P.-C. & Chang, H.-C. Fluorescent Nanodiamond: A Versatile Tool for Long-Term Cell Tracking, Super-Resolution Imaging, and Nanoscale Temperature Sensing. *Acc. Chem. Res.* **49,** 400–407 (2016).
56. Jagannadham, K., Verghese, K. & Butler, J. E. Thermal conductivity changes upon neutron transmutation of 10B doped diamond. *J. Appl. Phys.* **116,** 83706 (2014).
57. Walker, S. J. Boron neutron capture therapy: principles and prospects. *Radiography* **4,** 211–219 (1998).
58. Chilian, C., St-Pierre, J. & Kennedy, G. Complete thermal and epithermal neutron self-shielding corrections for NAA using a spreadsheet. *J. Radioanal. Nucl. Chem.* **278,** 745–749 (2008).
59. Ziegler, J. F., Ziegler, M. D. & Biersack, J. P. SRIM – The stopping and range of ions in matter (2010). *Nucl. Instrum. Methods Phys. Res. Sect. B Beam Interact. Mater. At.* **268,** 1818–1823 (2010).
60. Rehor, I. *et al.* Fluorescent Nanodiamonds with Bioorthogonally Reactive Protein-Resistant Polymeric Coatings. *ChemPlusChem* **79,** 21–24 (2014).
61. De Vita, A., Galli, G., Canning, A. & Car, R. A microscopic model for surface-induced diamond-to-graphite transitions. *Nature* **379,** 523–526 (1996).
62. Osswald, S., Mochalin, V. N., Havel, M., Yushin, G. & Gogotsi, Y. Phonon confinement effects in the Raman spectrum of nanodiamond. *Phys. Rev. B* **80,** (2009).
63. Iakoubovskii, K., Adriaenssens, G. J. & Nesladek, M. Photochromism of vacancy-related centres in diamond. *J. Phys.-Condens. Matter* **12,** 189–199 (2000).
64. Mita, Y. Change of absorption spectra in type-Ib diamond with heavy neutron irradiation. *Phys. Rev. B* **53,** 11360–11364 (1996).
65. Putz, S. *et al.* Protecting a spin ensemble against decoherence in the strong-coupling regime of cavity QED. *Nat. Phys.* (2014). doi:10.1038/nphys3050
66. Nöbauer, T. *et al.* Creation of ensembles of nitrogen-vacancy centers in diamond by neutron and electron irradiation. *ArXiv Prepr. ArXiv13090453* (2013).
67. Järvi, T. T., Kuronen, A., Nordlund, K. & Albe, K. Damage production in nanoparticles under light ion irradiation. *Phys. Rev. B* **80,** (2009).
68. Boudou, J.-P. *et al.* Fluorescent nanodiamonds derived from HPHT with a size of less than 10 nm. *Diam. Relat. Mater.* **37,** 80–86 (2013).

69. Petrakova, V. *et al.* Luminescence of Nanodiamond Driven by Atomic Functionalization: Towards Novel Detection Principles. *Adv. Funct. Mater.* **22,** 812–819 (2012).
70. Petrakova, V. *et al.* Luminescence properties of engineered nitrogen vacancy centers in a close surface proximity. *Phys. Status Solidi A* **208,** 2051–2056 (2011).
71. Havlik, J. *et al.* Benchtop Fluorination of Fluorescent Nanodiamonds on a Preparative Scale: Toward Unusually Hydrophilic Bright Particles. *Adv. Funct. Mater.* DOI: 10.1002/adfm.201504857 (2016). doi:10.1002/adfm.201504857
72. International Atomic Energy Agency (IAEA) database of nuclear reactors. https://nucleus.iaea.org/RRDB/RR/ReactorSearch.aspx. Accessed June 17, 2017.
73. Rehor, I. & Cigler, P. Precise estimation of HPHT nanodiamond size distribution based on transmission electron microscopy image analysis. *Diam. Relat. Mater.* **46,** 21–24 (2014).
74. Agostinelli, S. *et al.* Geant4—a simulation toolkit. *Nucl. Instrum. Methods Phys. Res. Sect. Accel. Spectrometers Detect. Assoc. Equip.* **506,** 250–303 (2003).
75. Allison, J. *et al.* Geant4 developments and applications. *IEEE Trans. Nucl. Sci.* **53,** 270–278 (2006).
76. Fortunato, W., Chiquito, A. J., Galzerani, J. C. & Moro, J. R. Crystalline quality and phase purity of CVD diamond films studied by Raman spectroscopy. *J. Mater. Sci.* **42,** 7331–7336 (2007).

Acknowledgements

This work was supported by the Czech Science Foundation project Nr. 16-16336S and Ministry of Health of the Czech Republic, grants Nr. 15-33094A (to J.H., H.R. and P.C.) and Nr. 15-25781A (to M.H.) (all rights reserved). Irradiations were carried out at the CANAM infrastructure of the NPI CAS Rez supported through MŠMT project No. LM2011019. Access to computing and storage facilities owned by parties and projects contributing to the National Grid Infrastructure MetaCentrum, provided under the program "Projects of Large Infrastructure for Research, Development and Innovations" (LM2010005), is greatly appreciated.

Author contributions

J.H., P.C., J. Kucka, and H.R. prepared and analyzed the ND samples. H.R. measured PL spectra. V.P. performed brightness analysis, Raman spectroscopy and single particle analysis. V.S. performed Geant4 simulations. Z.Z.C. and H.R. characterized the samples with electron microscopy. J. Kucera performed the irradiations in nuclear reactor. M.H., J. Kucka, and P.C. invented the method and designed the experiments. P.C. and M.H. supervised the project. All the authors were involved in the analyses and interpretation of data. P.C., M.H., and J.H. wrote the paper with the help of the co-authors.

Additional information

Supplementary information is available in the online version of the paper. Correspondence and requests for materials should be addressed to P.C. and M.H.

Competing financial interests

The authors declare no competing financial interests.

Appendix E

Supplementary information

Extremely rapid isotropic irradiation of nanoparticles with ions generated *in situ* by a nuclear reaction

Jan Havlik[1,2], Jan Kucka[3], Helena Raabova[1,4], Vladimira Petrakova[5], Vaclav Stepan[6], Zuzana Zlamalova Cilova[4], Jan Stursa[6], Jan Kucera[6], Martin Hruby[3]* and Petr Cigler[1]*

[1]Institute of Organic Chemistry and Biochemistry CAS, v.v.i. Flemingovo nam. 2, 166 10 Prague 6, Czech Republic.[2]Faculty of Science, Charles University, Hlavova 2030, 128 40 Prague 2, Czech Republic.
[3]Institute of Macromolecular Chemistry, v.v.i., The Czech Academy of Sciences, Heyrovskeho nam. 2, 162 06 Prague 6, Czech Republic.
[4]University of Chemistry and Technology, Prague, Technická 5, 166 28 Prague 6, Czech Republic.
[5]Faculty of Biomedical Engineering, Czech Technical University in Prague, nam. Sitna 3105, 272 01 Kladno, Czech Republic.
[6]Nuclear Physics Institute AS CR, v.v.i., 250 68 Rez near Prague, Czech Republic.

*corresponding authors, e-mails: mhruby@centrum.cz, cigler@uochb.cas.cz

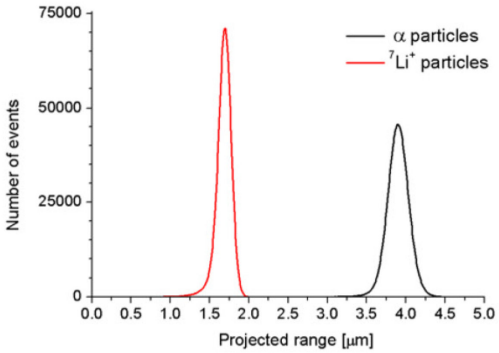

Figure S1. Projected ranges for 1.47 MeV α particles and 0.84 MeV $^{7}Li^{+}$ particles in a 33% dispersion of 35-nm NDs in $^{10}B_2O_3$ simulated with Geant4 toolkit.

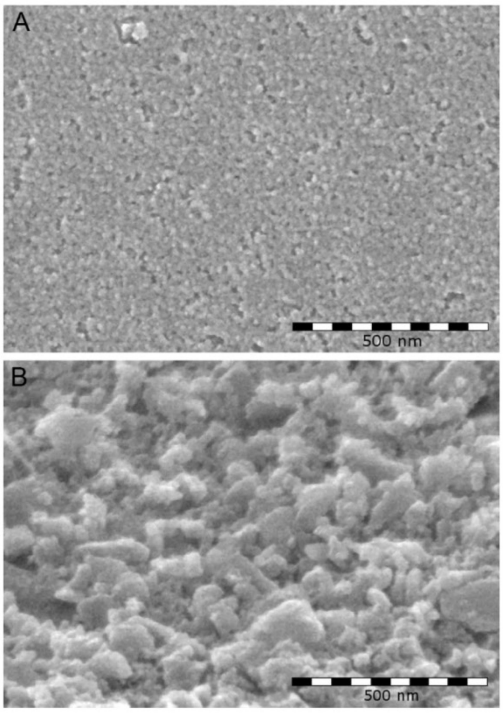

Figure S2. SEM micrographs of $^{10}B_2O_3$ melts containing **(A)** 35-nm and **(B)** 150-nm NDs.

2

Appendix E

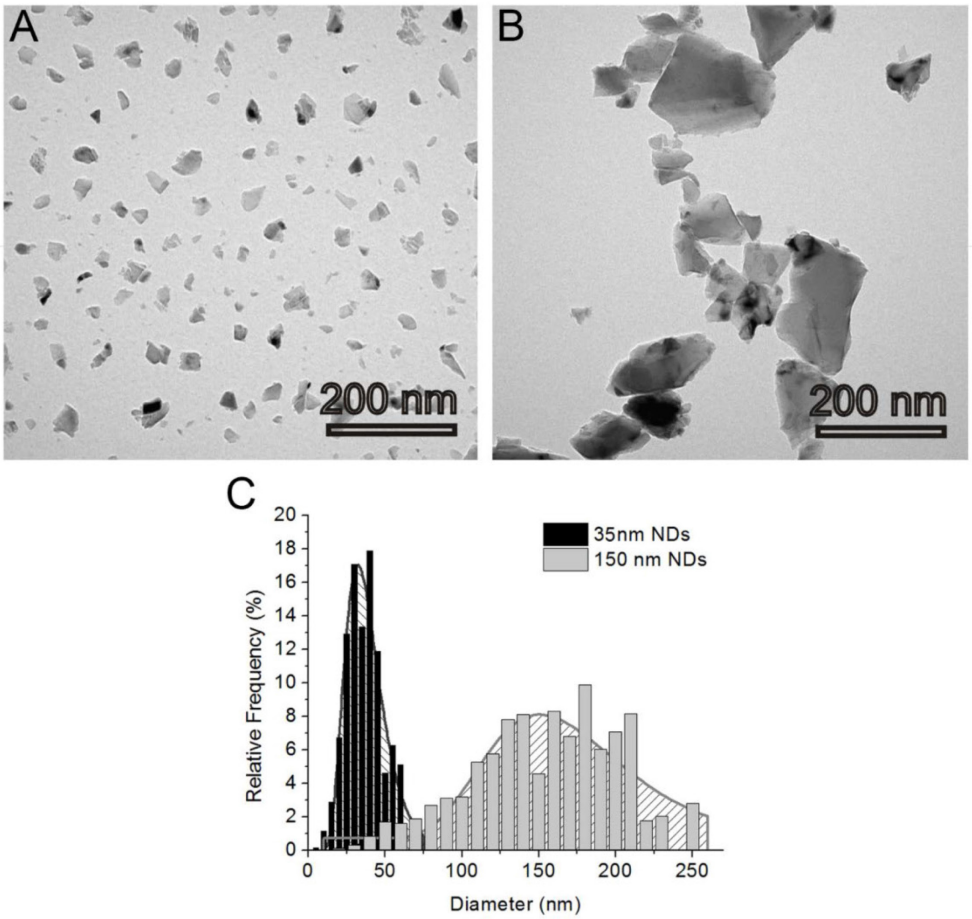

Figure S3. TEM images of **(A)** 35-nm and **(B)** 150-nm fluorescent nanodiamonds obtained after isolation and purification from the $^{10}B_2O_3$ melt. **(C)** Size distributions are based on analysis of approximately 1000 particles from each TEM micrograph. Particle size is expressed by equivalent circular diameters recalculated to volume-weighted histograms. Obtained histograms are fitted with a log-normal distribution.

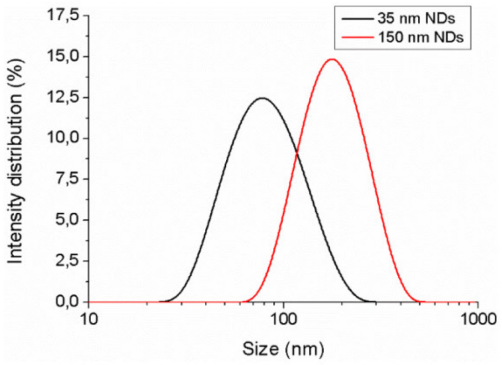

Figure S4. Dynamic light scattering (DLS) size distribution of 35-nm (black) and 150-nm (red) FNDs. Concentration of the colloids was 0.5 mg/ml. Measured zeta potentials were –46.7 mV for 35-nm particles and –41.0 mV for 150-nm particles.

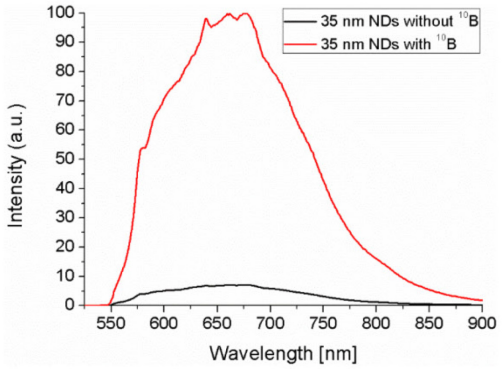

Figure S5. Comparison of fluorescence intensity of 35-nm NDs irradiated by neutrons only (control sample without presence of $^{10}B_2O_3$) and by neutrons in a melt of $^{10}B_2O_3$. The fluorescence intensity of the sample irradiated with $^{10}B_2O_3$ is 14× higher than that of the sample irradiated without $^{10}B_2O_3$.

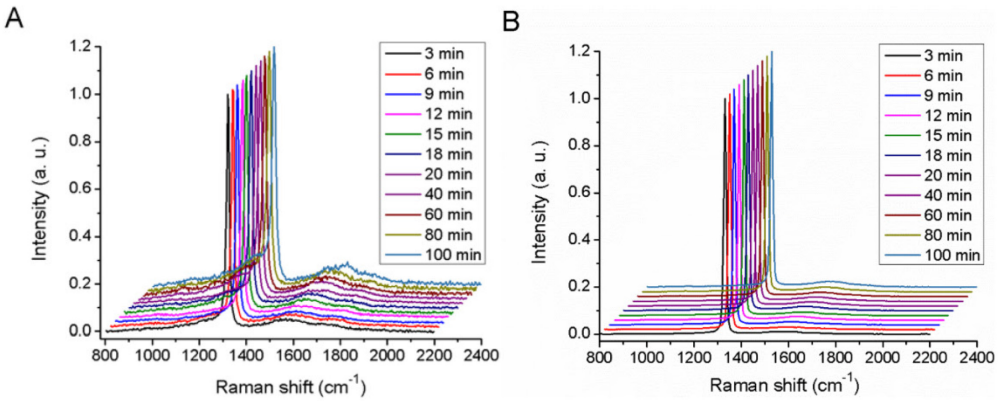

Figure S6. Raman spectra for **(A)** 35-nm and **(B)** 150-nm NDs irradiated in a nuclear reactor in melt with $^{10}B_2O_3$ as a function of irradiation time.

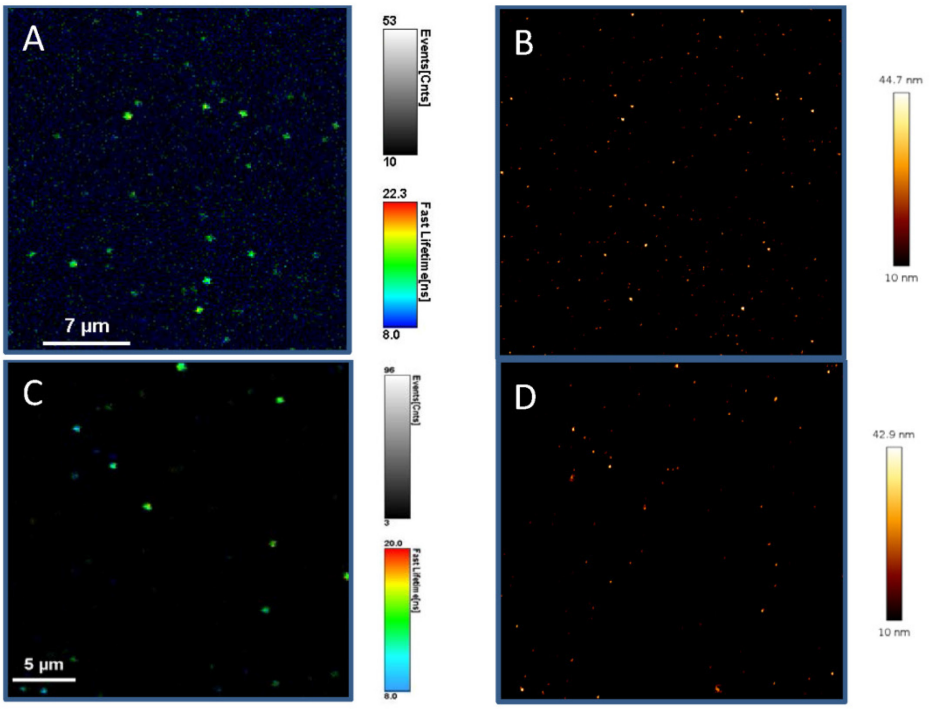

Figure S7. Representative examples of **(A, C)** FLIM and **(B, D)** AFM analysis of FNDs irradiated **(A, B)** by p^+ in a cyclotron and **(C, D)** by neutrons in a nuclear reactor in melt with $^{10}B_2O_3$. The FNDs were deposited on a glass cover slip, and AFM and FLIM were taken simultaneously. Nanoparticles with diameter below 10 nm and clusters of sized larger than 50 nm were not counted in the overall statistics.

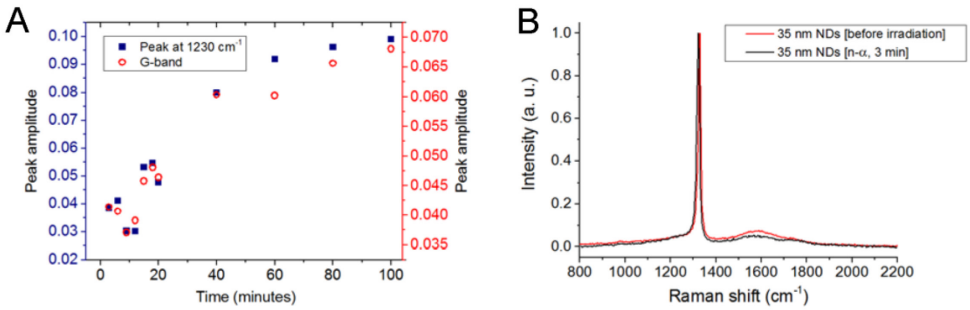

Figure S8. (**A**) Correlation of peak amplitudes in Raman spectra of 35nm NDs irradiated in nuclear reactor by neutrons in melt of $^{10}B_2O_3$. The increase of peak at ~1230 cm^{-1} corresponds with an increase in the G-band at ~1600 cm^{-1}. (**B**) Both peaks, related to the size and/or structural changes of diamond crystalline core, are present also in Raman spectra of NDs before irradiation and show comparable intensities.

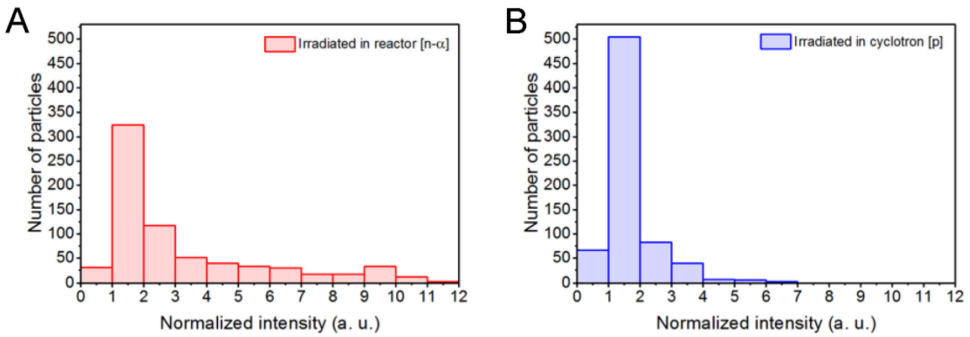

Figure S9. Histograms of fluorescence intensity distributions of 35 nm NDs (**A**) irradiated in nuclear reactor by neutrons in melt of $^{10}B_2O_3$, (**B**) irradiated in cyclotron by protons using optimized pellet target. Fluorescence intensity is normalized to average intensity of one NV center in ND particle. Total number of particles is normalized to 1000.

Appendix E

Appendix F

Balek, L.; Buchtova, M.; Foldynova-Trantirkova, S.; **Havlik J.**; Varecha, M.; Turner, S.; Vesela, I.; Klimaschewski, L.; Claus, P.; Trantirek, L.; Cigler, P.; Krejci, P.; Nanodiamonds as artificial proteins: regulation of a cell signalling system using picomolar solutions of inorganic nanocrystals – **manuscript submitted**.

Appendix F

Nanodiamonds as artificial proteins: regulation of a cell signalling system using picomolar solutions of inorganic nanocrystals

Lukas Balek[1], Marcela Buchtova[2,3], Silvie Foldynova-Trantirkova[4,5], Jan Havlik[6,7], Miroslav Varecha[1,8], Stuart Turner[9], Iva Vesela[2], Lars Klimaschewski[10], Peter Claus[11], Lukas Trantirek[4], Petr Cigler[6*], Pavel Krejci[1,8*]

[1]Department of Biology, Faculty of Medicine, [2]Institute of Experimental Biology, Faculty of Sciences, [4]Central European Institute of Technology, Masaryk University, 62500 Brno, Czech Republic

[3]Institute of Animal Physiology and Genetics of the CAS, 60200 Brno, Czech Republic

[5]Institute of Biophysics of the CAS, 61265 Brno, Czech Republic

[6]Institute of Organic Chemistry and Biochemistry of the CAS, 16610 Prague, Czech Republic

[7]Faculty of Science, Charles University, 12840 Prague, Czech Republic

[8]International Clinical Research Center, St. Anne's University Hospital, 65691 Brno, Czech Republic

[9]EMAT, University of Antwerp, Groenenborgerlaan 171, B-2020, Antwerp, Belgium

[10]Division of Neuroanatomy, Medical University of Innsbruck, A-6020 Innsbruck, Austria

[11]Institute of Neuroanatomy and Cell Biology, Hannover Medical School, 30625 Hannover, Germany

[*]Correspondence: cigler@uochb.cas.cz, krejcip@med.muni.cz

Abstract

The blocking of specific protein-protein interactions using nanoparticles is an emerging alternative to small molecule-based therapeutic interventions. However, the nanoparticles designed as "artificial proteins" generally require modification of their surface with (bio)organic molecules and/or polymers to ensure their selectivity and specificity of action. Here, we show that nanosized diamond crystals (nanodiamonds, NDs) without any synthetically installed (bio)organic interface enable the specific and efficient targeting of the family of extracellular signalling molecules known as fibroblast growth factors (FGFs). We found that picomolar solutions of detonation NDs with positive ζ-potential strongly associate with multiple FGF ligands present at sub-nanomolar concentrations and effectively neutralize the effects of FGF signalling in cells without interfering with other growth factor systems and serum proteins unrelated to FGFs. We identified an evolutionarily conserved FGF recognition motif, ~17 amino acids long, that contributes to the selectivity of the ND-FGF interaction. In addition, we inserted this motif into a *de novo* constructed chimeric protein, which significantly improved its interaction with NDs. We demonstrated that the interaction of NDs, as purely inorganic nanoparticles, with proteins can mitigate pathological FGF signalling and promote the restoration of cartilage growth in a mouse limb explant model. Based on our observations, we foresee that NDs may potentially be applied as nanotherapeutics to neutralize disease-related activities of FGFs *in vivo* and to purify/isolate proteins bearing the FGF recognition motif.

Keywords: nanodiamonds; cell signalling; FGF; fibroblast growth factor; nanotherapeutics**.**

Introduction

Since the upswing of nanomedicine in the early 1990s, the use of nanoparticles has strongly influenced the quality of treatment of various diseases and pathogens. The low toxicity of some nanoparticles, their high surface to volume ratio and the possibility of polyvalent binding sites on their surface have enabled the application of nanoparticles in targeted drug delivery systems, of theranostic nanoparticles that perform simultaneous therapeutic intervention and monitoring of the treatment, and of stimulus-responsive systems based on hybrid nanoparticles with a broad structural range[1,2]. Overcoming some of the current barriers in cancer treatment, such as poor circulation times, drug resistance and off-target toxicity, using nanotechnology-based systems catalysed the development of a number of drug delivery nanosystems that have already passed the translation phases and are currently marketed as drugs[3]. More recently, promising new directions utilizing nanoparticles for the selective binding or sequestration of biologically active and regulatory compounds have also been investigated. These "artificial proteins"[4] take advantage of the remarkable similarity of some nanoparticles to biomolecules, particularly to globular proteins. This analogy involves not only their comparable overall dimensions and surface charge but in general the analogous steric, thermodynamic and kinetic behaviour of nanoscale structures in an aqueous environment[5].

Similar to biomolecules, nanoparticles can thus bind, mimic, or block specific proteins in living organisms[6]. The use of nanoparticles therefore offers attractive alternative opportunities to small molecule-based therapeutic interventions. For example, the selective binding of one component and consequent blocking of a specific protein-protein recognition using non-toxic nanoparticles can have a strong impact on the control of key disease-related processes. However, owing to issues such as the lack of well-defined binding pockets, developing nanoparticles that selectively modulate protein-protein interactions remains highly challenging.

In the past decade, advanced experiments exploring the potential of artificial proteins have demonstrated that a molecularly designed nanoparticle interface can inhibit or regulate protein-protein interaction in structurally diverse systems. The seminal works in this field include the selective inhibition of cytochrome c peroxidase and cytochrome c interaction using gold nanoparticles of appropriate size coated with simple ligands terminated only with carboxyl groups[7,8] and the selective disaggregation of prion aggregates using dendrimeric nanoparticles,

leading to the elimination of prion molecules from neuroblastoma cells[9]. The high surface-to-volume ratio of nanoparticles has been later advantageously used also for sequestration of target molecules using long affinity DNA polymers attached to the nanoparticle surface[10], and for the capture of a broad range of pathogens and toxins related to sepsis from the blood using opsonin-modified magnetic nanobeads[11,12]. Very recently, an *in vivo* study on mice revealed the high potential of nanoparticles for preventing receptor phosphorylation and downstream endothelial growth factor-dependent cell migration and invasion into the extracellular matrix[13]. These and other examples[14] constitute strong evidence that the regulation of protein-protein interactions using nanoparticles can be used to control key biological processes.

The nanoparticles used for the selective control of protein-protein interactions have always been decorated with a bionanointerface consisting of (bio)organic molecules and/or polymers. The organic functional groups presented on nanoparticles and their flexible arrangement, however, can cause unwanted interactions with immune cells[15], which are observed even for the commonly used PEG coatings[16]. Here, we address a key task: is it possible to achieve direct control of the crystalline nanoparticle surface (without further organic modification) to obtain highly selective protein binding that can effectively compete with natural protein-protein interactions and mitigate their biological effects? In practice, this task requires identifying pairs of proteins and inorganic interfaces that show much stronger mutual interactions than the formation of the protein corona, which occurs immediately upon the exposure of a nanoparticle to a biological environment[17].

In our screening, we identified such a specifically interacting pair. We show here that one type of nanosized diamond crystals (nanodiamonds, NDs)[18] without any synthetically installed organic or bioorganic interface already display, at picomolar concentration, extremely strong interactions with members of the FGF family of growth factors and morphogens. Moreover, NDs selectively neutralize FGF signalling without interference using serum proteins and other tested FGF-unrelated growth factor systems, including EGF (epidermal growth factor), NGF (nerve growth factor), TGFβ1 (transforming growth factor β1), IL6 (interleukin 6) and IFNγ (γ-interferon) (Fig. 1A). We identify the evolutionarily conserved FGF region responsible for the selectivity of interaction with ND and discover the molecular principles responsible for the unprecedented strength of the FGF-ND interaction. Finally, we demonstrate that these purely

protein-inorganic nanoparticle interactions are strong enough to mitigate pathological FGF signalling and promote the restoration of cartilage growth in a mouse limb explant model.

Results and discussion

NDs with positive ζ-potential inhibit FGF signalling in cells

To test the nanoparticle-based inhibition of FGF signalling in cells, we used NDs, which form a diverse group of carbon nanomaterials based on the diamond core[19,20]. NDs can be classified into three basic types: detonation, high-pressure high-temperature (HPHT), and chemical vapour deposition NDs. The detonation NDs mostly used in this study are very small (<5 nm) nanoparticles that can easily be excreted from the body by glomerular filtration[21]. They are tolerated long term and are non-toxic even if applied at multiple clinically relevant doses as drug delivery nanosystems in rats and primates[22]. Because of the presence of both sp^3 and sp^2 hybridized carbon atoms at the surface[23], detonation NDs provide a wide range of anisotropic surface atomic arrangements consisting only of C, O and H atoms[24,25]. The resulting surface charges at facets[26] and uniquely organized interfacial water layers[27,28] can lead to interfaces with opposite ζ-potentials ranging approximately from –50 to +50 mV[29–32]. This disparity between ζ-potentials results in different affinities of particular proteins to NDs and in their diverse adsorption dynamics, attachments and conformations on the ND surface[33,34].

Based on these assumptions, we first focused on distinguishing the dominant charge effects on the ND surface that contribute to the inhibition of FGF signalling in cells. We selected three representative types of ND: detonation NDs with either positive or negative ζ-potentials (**ND1** and **ND-PL**, respectively) and oxidized **HPHT NDs** with negative ζ-potential (Fig. 1B). We used rat chondrosarcoma (RCS) cells, which expressed the cell surface FGF-receptors FGFR2 and FGFR3[35]. RCS cells respond to the activation of FGFR signalling via the addition of the prototypical FGF ligand FGF2, with a well-characterized array of phenotypic changes. These changes include potent growth arrest, loss of the extracellular matrix and the induction of premature senescence[36]. RCS cells offer a particular advantage for inhibitor evaluation because only specific targeting of the FGF pathway can restore cell growth, and thus inhibitor interference with other, pro-growth pathways will not generate a positive response in the growth arrest assay. We hypothesized that the addition of NDs, which can potentially interact with FGF2

(a ligand) or with FGFR2 and FGFR3 (receptors), would cause a concentration-dependent reversal of the RCS growth arrest phenotype induced by 72 hours of FGF2 treatment. While NDs with negative ζ-potential (**ND-PL** or **ND-HPHT**) did not show any influence on FGF2 signalling, **ND1,** which had positive ζ-potential, effectively reversed the cell growth arrest in a concentration-dependent manner (Fig. 2A, B). Thus, **ND1** restored RCS growth specifically, i.e., without simultaneous interference with serum-borne pro-growth signalling pathways, such as PDGF (platelet-derived growth factor) and insulin signalling.

The **ND1** particles show structural features characteristic of detonation NDs, as documented by transmission electron microscopy (Fig. 1D, E). The diameter of the primary particles is on average within a few nanometres; however, the NDs gently associate in solution, resulting in a slightly larger size measured by quasielastic light scattering (QELS). Because the observed effect of **ND1** on FGF2 signalling was most likely caused by the interaction of proteins with the diamond surface, we anticipated that this phenomenon might be size-dependent. We therefore separated fractions of smaller NDs from **ND1**, obtaining samples **ND2** and **ND3** with decreased sizes and a narrower size distribution of particles (Fig. 1C, F). The rescue of FGF-mediated RCS growth arrest by **ND2** was more effective than that by **ND1**, while a further decrease in size (**ND3**) did not show additional improvement (Fig. 2A). We therefore decided to use **ND2** in most of the following experiments.

To exclude the potential influence of some impurities that might be present in the starting colloidal solution of **ND1** (for example, traces of residual reagents used by the producer to purify the NDs after detonation synthesis), we prepared two control samples. First, we dialysed **ND1** 5x against water to remove any potential small-molecule contaminants, obtaining **ND4**. Second, we quantitatively removed all ND particles from **ND1** using high-speed ultracentrifugation, obtaining the supernatant **ND5**. **ND4** showed comparable colloidal properties to those of **ND1** and rescued FGF2-mediated RCS growth arrest to a similar extent. No NDs were detectable by QELS in **ND5** solution, which correspondingly produced no activity in the growth arrest assay (Figs. 1F, 2C). These results indicate that the positively charged detonation ND present in **ND1** is responsible for the observed effect.

To compare the efficacy of **ND1-4** with an established approach to the inhibition of FGF signalling, we performed the FGF2 growth arrest assay with a small-molecule inhibitor of FGFR

catalytic activity, BGJ398[37], which is currently being evaluated in clinical trials for FGFR-driven cancer[38]. BGJ398 rescued the FGF2-mediated growth arrest phenotype to a similar extent to that of **ND1-4** (Fig. 2D). Thus, the NDs inhibit FGFR signalling in RCS cells by interaction with FGF2 or with its receptors FGFR2/FGFR3.

Similar to the growth arrest, the FGF2-mediated induction of premature senescence in RCS chondrocytes, manifested as the upregulation of the senescence markers lamin A/C and caveolin and the downregulation of ID2[39], was rescued by **ND2** and by dialysis-purified **ND4** (Fig. 3A). To gain further insight into the mechanisms of the ND-mediated inhibition of FGF signalling, we analysed the effect of ND on the activation of FGFR signal transduction in RCS cells. Treatment with FGF2 induced potent phosphorylation of well-established mediators of FGF signalling, including ERK MAP kinase, the adapter protein FRS2 involved in ERK pathway activation, and the WNT pathway co-receptor LRP6, which is known to be phosphorylated by FGFR signalling during its interaction with WNT/β-catenin signalling[40,41]. Figure 3B shows that the FGF2-mediated phosphorylation of ERK, FRS2 and LRP6 was inhibited by **ND4**. As activation of the ERK pathway mediates both growth arrest and premature senescence in RCS cells[42], the inhibition of ERK activation thus explains the ND-mediated rescue of the FGF2 phenotypes in these cells.

Altogether, we demonstrate that ND particles with positive ζ-potential (**ND1-4**), but not those with negative ζ-potential (**ND-PL**, **ND-HPHT**), effectively inhibit FGF signalling in cells *via* protein-nanoparticle interactions. Notably, all experiments were successfully performed in tissue culture medium containing 10% foetal bovine serum (containing approximately 6 mg/ml proteins), while the concentration of FGF was typically $6x10^5$-fold lower (10 ng/ml; 0.32 nM) and the NDs were extremely diluted (≤10 μg/ml, which corresponds approximately to ≤50 pM ND concentration). The exposure of inorganic nanoparticles [17] and particularly of nanodiamonds[33,34,43–45] to this protein-rich environment typically leads to the rapid formation of a strongly bound protein corona. Thus, the observed interference with FGFR signalling had to be mediated by unusually strong protein-ND interactions to overcome the concomitant ND interactions with serum proteins. In the next set of experiments, we focused on the selectivity and structural nature of these interactions.

NDs inhibit signalling of multiple FGFs but not TGFβ1, IL6, IFNγ, EGF and NGF

Having determined that NDs inhibit the FGF2-mediated activation of FGFR signalling, we asked whether a similar effect might be achieved for other ligands belonging to the FGF family. Among the 18 existing FGF ligands, FGF1/2/4/5/6/8/9/16/17/18 can activate ERK and cause growth arrest in RCS cells. However, only FGF2, FGF9 and FGF18 can achieve this effect alone, while all other FGFs require stabilization with heparin due to their low intrinsic stability[46]. Because the addition of heparin could interfere with the ND-FGF interaction, we tested the effect of NDs only on FGF9 and FGF18. Similar to FGF2, the activation of ERK mediated by treatment with FGF9 and FGF18 was rescued by **ND2** (Fig. 4A). As shown before, RCS cells cannot respond to FGF ligands belonging to the FGF7 family (FGF7/10/22) due to the lack of the appropriate FGFR variants[46]. Thus, human breast carcinoma MCF7 cells were used to test the effect of ND on FGF7/10/22 signalling. Figure 4B demonstrates ERK activation mediated by FGF7, FGF10 and FGF22 treatment in MCF7 cells, which was rescued by **ND2**. Altogether, we demonstrate that the signalling of at least six different FGF ligands (FGF2/7/9/10/18/22) can be inhibited by NDs.

Next, we asked whether NDs inhibit other signalling systems unrelated to FGF. The tested systems were selected based on the diversity of their mechanisms of ligand-receptor interactions and on the diversity of their action *in vivo*. We thus determined the effect of ND on the signalling of a morphogene (TGFβ1), two unrelated cytokines (IL6, IFNγ), and two unrelated growth factors (EGF, NGF). In RCS cells, we found no effect of ND on the phosphorylation of SMAD2 transcriptional regulator in response to cell treatment with TGFβ1[47], on the phosphorylation of STAT3 transcriptional regulator in response to IL6 treatment[48], or on the phosphorylation of STAT1 in response to cell treatment with IFNγ[49] (Fig. 4C). These data indicate that NDs do not interfere with TGFβ1, IL6 and IFNγ signalling. Similarly, in 293T cells, no effect of **ND2** was observed on the activation of EGF signalling via cell treatment with EGF or on the activation of NGF signalling triggered by the NGF treatment of cells transiently expressing the NGF-receptor TRKA (Fig. 4D). Together, we have demonstrated that NDs do not interfere with the signalling of five different ligand-receptor systems not related to FGFs.

Mechanism of action: NDs sequester multiple FGF ligands

In FGF signal transduction, the tyrosine phosphorylation of FRS2 is caused directly by active

FGFRs[50]. Thus, the lack of FRS2 tyrosine phosphorylation in RCS cells treated with FGF2 and NDs demonstrates that NDs inhibit the FGF signalling cascade at the level of FGFR activation (Fig. 3B). We hypothesized that NDs inhibit FGF signalling by the sequestration of FGFs. To ascertain this mechanism, we incubated various human recombinant FGFs with NDs in DMEM supplemented with 10% foetal bovine serum (FBS) for 8 hours, collected the NDs by ultracentrifugation and analysed them for the presence of FGF by western blotting with FGF-specific antibodies (Fig. 5A). First, we found the effective depletion of medium FGF2 after incubation with **ND4** (a dialyzed version of **ND2**; Fig. 5B), which was confirmed by the lack of growth arrest in RCS cells grown in the FGF2-depleted media (Fig. 5C). Similar experiments carried out with other FGFs demonstrated an efficient ND-mediated depletion of recombinant FGF1/4/8/10/17/22, while less effective clearance was found in the case of the FGF hormones FGF19, FGF21 and FGF23 (Fig. 5D). No significant ND-mediated depletion of the recombinant signalling proteins IL6 and IFNγ was found (Fig. 5E). Because interleukin 1β (IL1β) shares evolutionary origins with FGFs[51], we tested IL1β in the depletion studies. No ND-mediated depletion of IL1β was found (Fig. 5E), demonstrating that sequence context is more important than secondary structure in the FGF-ND interaction.

Although we verified NDs as tight-binders of FGF1/2/4/8/10/17/22, the expected non-covalent nature of the binding can lead to reversibility of the ND-FGF interactions. Since all experiments were performed in the presence of 10% serum, we were interested in whether the absence of a serum protein corona might cause stronger sequestration of FGF by NDs. We emphasized the extreme mass ratio between serum proteins and FGFs: in pull-down experiments, we used approximately 6 mg/ml serum proteins (corresponding to 10% FBS) and 100 ng/ml FGF, which resulted in a mass excess of serum proteins by a factor of ~$6x10^4$. This excess was even higher in cell experiments (~$6x10^5$), but the FGF sequestration efficacy of the NDs was still very strong, as demonstrated by the almost complete ND-mediated rescue of the growth arrest (Fig. 2). We thus compared the FGF1- and FGF2-**ND2** interactions in DMEM/FBS, DMEM and phosphate buffered saline (PBS). In these experiments, the time dependence of the binding process was also analysed by adding the FGFs to the solution containing **ND2** and analysing the FGF content in the sample (solution and ND) after a given time (0-30') (Fig. 6A). While both FGF1 and FGF2 were detectable in the presence of FBS (i.e., could be washed off the **ND2** by

Laemmli sample buffer containing 4% SDS and 5% mercaptoethanol), incubation in either PBS or DMEM led to very strong sequestration by **ND2** and the virtual absence of both FGFs in the samples. This observation confirms a competition between serum proteins and FGF for binding on the ND surface. We also did not observe differences between the points in the 0-30' time scale (time point 0' is the sample taken immediately after mixing the FGFs with **ND2**), which implies the very rapid adsorption of both FGFs on the NDs (Fig. 6A).

Interestingly, we observed even tighter binding for FGF22. We found a complete lack of detectable FGF22 in all tested fractions, i.e., input, medium after incubation, supernatant and pellet after centrifugation (Fig. 5D). FGF22 was not released from pelleted NDs even after incubation with SDS-containing Laemmli sample buffer or incubation in lysis buffers containing up to 10% Triton X-100 or Igepal CA-630, combined with sonication. No FGF22 signal was detected even when FGF22 was added directly to an **ND2**-containing solution of DMEM/FBS mixed with Laemmli buffer (1:1) (data not shown). These data suggest a very strong association of FGF22 with NDs, even in the presence of a protein corona derived from FBS. To rule out the possibility that NDs somehow degrade FGFs, thus destroying the epitope needed for detection by western blot, we incubated **ND2** with FGF2 labelled with Cy5.5 dye (FGF2-Cy5.5) and analysed the resulting complexes by confocal microscopy. Figure 6B shows the association of FGF2-Cy5.5 with **ND2**, whereas no Cy5.5 signal was detected in **ND2** incubated with free Cy5.5 or with unlabelled FGF2. Because the putative ND-mediated degradation of FGF2 would release the Cy5.5, our data suggest an association of intact FGF2 with **ND2**.

<u>The heparin binding site (HBS) is involved in FGF interaction with NDs</u>

Figure 5 demonstrates the efficient ND-mediated depletion of FGFs belonging to the paracrine FGF subfamily (FGF1/2/4/8/10/17/22), while less effective depletion was found for endocrine FGFs (FGF19/21/23). Because the selectivity of ND for a specific group of proteins can be caused by the presence of a common type of binding domain, we focus here on its identification. FGF19/21/23 act as metabolic hormones regulating phosphate waste, the metabolic adaptation to starvation, and glucose homeostasis[52]. The slow metabolic action of endocrine FGFs dictates their persistence in circulation for prolonged periods, without association with proteoglycans at the endothelial cell surface. Although both paracrine and endocrine FGFs share a central

conserved core of ~120 amino acids, all endocrine FGFs lack the consensus motif required for heparin binding (heparin binding site, HBS), which is typical of paracrine FGFs (Fig. 7A)[53]. The less effective ND-mediated depletion of FGF19, FGF21 and especially FGF23 (Fig. 5D), therefore, indicates that the strong FGF-ND interaction observed for paracrine FGFs might be partially mediated by the HBS.

To address the role of the HBS in paracrine FGF-ND interaction, we generated a chimeric FGF23 protein, herein referred to as FGF23-HBS, in which the FGF2 HBS was inserted into the corresponding location in the FGF23 sequence (Fig. 7B). We transfected 293T cells with vectors expressing wt FGF23 and FGF23-HBS, released the expressed FGF23 and FGF23-HBS into the culture medium by snap freezing, and compared the ND-mediated clearance of both proteins. The addition of HBS significantly improved the sequestration of FGF23 on **ND2**, demonstrating that HBS contributes to the specific interaction between FGFs and NDs (Fig. 7C, D).

NDs inhibit FGFR signalling in mouse limb explant cultures

The structural selectivity and tight binding of certain FGFs to NDs suggest their potential use as therapeutics for FGF-related diseases. To test the efficacy of NDs in intervening with FGF-related pathological processes in complex biological systems, we utilized an established model based on limb explants isolated from E18 mouse CD1 embryos[35]. When isolated from the embryos, the limb explants continue their growth programme for several days in culture, driven by the intrinsic signalling of several pathways such as TGF/BMP, WNT and hedgehog, which act in concert to ensure proper chondrocyte proliferation and differentiation[54]. The limb explant model thus allows evaluation of the specificity and efficacy of the ND-mediated inhibition of FGF signalling in a complex tissue environment where many protein interactions must remain intact to allow normal growth. Similar to RCS chondrocytes, the activation of FGFR3 in limb explants inhibits their growth *via* impairing both proliferation and differentiation of the limb chondrocytes[35,55]. This effect stems from the physiological role of FGFR3 as a negative regulator of skeletal growth[56].

Continuous treatment with FGF2 for 8 days resulted in significant inhibition of the limb explant growth accompanied by a reduction in hypertrophic cartilage, as evidenced by changes in the microanatomical appearance of the growth plates and the diminished expression of the

hypertrophic chondrocyte marker collagen 10 (Fig. 8A, B). These effects were reversed by treatment with **ND2** or **ND3** (0.5 nM solution, 0.1 mg/ml). NDs partially rescued the FGF2 growth-inhibitory effect, including restoration of the hypertrophic cartilage (Fig. 8C). Importantly, normal growth and tissue microanatomy were found in limb explants cultured with **ND2** and **ND3** alone for 8 days, suggesting minimal influence of the NDs on non-FGF-related signalling pathways regulating limb growth.

Conclusions

Here, we have reported a hitherto unexplored approach to selectively regulating protein-protein interaction using purely inorganic nanoparticles in a biological environment. In contrast to previous studies utilizing nanoparticles modified with an organic interface, we focused on the identification of strong and selective interactions between the inorganic interface and proteins. We found that detonation NDs with positive ζ-potential can uniquely interact with members of the FGF growth factor family, which represents one of the major signalling systems regulating cell functions during development, life and disease. We observed that ND colloids diluted to picomolar concentrations could sequester FGFs at their biologically relevant concentrations (~10 ng/ml; 0.32 nM), compete with their interaction with FGFR and mitigate their inhibitory effects on cell growth in concentration-dependent manner. This regulation of protein-protein interaction was effective in a biological environment containing other proteins (at concentrations higher by a factor of ~$6x10^5$) that form a protein corona on the ND. The regulation was also highly selective: we did not observe any influence on other signalling systems unrelated to FGF, such as TGFβ, IL6, IFNγ, EGF and NGF. This quality of this interaction is similar to that of the highly potent biomolecular interactions evolved in nature. We further investigated the nature of the interactions between FGF and ND, identifying the involvement of the heparin binding site in the selective recognition of paracrine FGFs by ND. We confirmed this hypothesis by generating a chimeric FGF23-HBS protein, in which we artificially inserted the FGF2 heparin binding site into the corresponding location in the FGF23 sequence. FGF23-HBS showed much stronger affinity to ND than did the wild-type FGF23. Finally, thanks to the extremely tight FGF-ND binding, we were able to demonstrate that highly diluted 0.5 nM ND colloids are able to mitigate pathological FGF signalling and promote the restoration of cartilage growth in the mouse limb

explant model.

Notably, we observed no manifestations of ND toxicity, which is consistent with previous studies utilizing NDs as delivery agents for a broad range of therapies[57], including clinical trials that are currently under way[58]. We are optimistic regarding the potential use of NDs in the treatment of diseases, as their enormous potential for improving patient care and personalized medicine has already been demonstrated by Prof Ho and co-workers[59–63] as well as by other teams[64–71]. Our findings expand the spectrum of medicinal applications of NDs and suggest an unprecedented pathway for the control of signal transduction in biological systems using NDs as artificial regulatory proteins.

In addition to these potential nanotherapeutic applications of NDs, the high selectivity and unusual strength of the interaction between the NDs and FGFs can be exploited in a number of biotechnological applications. NDs at picomolar concentrations can readily sequester proteins that already bear the heparin FGF recognition segment in their sub-nanomolar concentrations. We thus foresee the potential of NDs for the pull-down/sequestration of molecules that naturally bear this segment from (biological) fluids and, conversely, the non-covalent attachment of (bio)organic molecules or polymers artificially tagged with this segment to the ND surface.

Material and methods

Chemicals, solvents, ND characterization and preparation of ND colloids

Sodium hydroxide, nitric acid and sulfuric acid were purchased from Penta (Czech Republic) in p.a. quality. Deionized water was used for the preparation of all colloids and particle treatments. The dispersion of detonation NDs in water (NanoAmando) was supplied by the Nanocarbon Research Institute (Japan). HPHT ND (MSY 0-0.05) was supplied by Microdiamant (Switzerland). A sample of oxidized detonation NDs (PL-D-G01) was obtained from Plasmachem, Germany. For sonication, a Cole Parmer 750 W probe sonicator was used. Samples **ND2**, **ND3** and **ND5** were prepared using centrifugation in a Beckman Coulter Le80K ultracentrifuge with an SW 41 Ti swinging bucket rotor. For other preparations, an Eppendorf Microcentrifuge 5430 was used. Gravimetric determination of ND concentration: The analysed sample (1000 μl) was evaporated in a pre-weighted 1.5 ml Eppendorf tube using a Labconco Centrivap system. The concentrations of the solutions were calculated from the weight of the

solid residues.

HPHT NDs were oxidized by air in a Thermolyne 21100 tube furnace at 510°C for 5 hours. The NDs were subsequently treated with a mixture of HNO_3 and H_2SO_4 (90°C, 3 days), with 1 M NaOH (80°C, 1 h) and finally with 1 M HCl (80°C, 1 h). Between treatments, the NDs were separated by centrifugation at 5000 rcf (20 min). After HCl treatment, the diamonds were 3x centrifuged (5000 rcf, 20 min; 7000 rcf, 30 min; 20,000 rcf, 30 min) and redispersed using a tip sonicator. The brown colloid remaining after the last centrifugation was diluted with water to yield a solution of **ND-HPHT** (1 mg/ml). **ND-PL**: Plasmachem detonation diamond powder (3 mg) was mixed with 3 ml of water in a plastic tube and sonicated for 60 min using a probe sonicator in an ice bath. The obtained colloid was filtered using a 0.45 μm glass microfibre syringe filter. **ND1**: The dispersion of detonation ND NanoAmando (10 ml, 5.0%) was diluted with water to a concentration of 10 mg/ml, sonicated for 10 min and filtered using a 0.2 μm PVDF syringe filter. **ND2**: **ND1** colloidal solution (40 ml, 10.3 mg/ml) was centrifuged in an ultracentrifuge (15,000 rfc, 2 h). The supernatant was isolated and filtered using a 0.2 μm PVDF syringe filter, yielding **ND2** colloid (26 ml, 7.8 mg/ml). The **ND3***:* **ND2** colloidal solution (13.2 ml, 7.8 mg/ml) was centrifuged in an ultracentrifuge (30,000 rfc, 2 h). The top 2/3 of the supernatant was isolated and filtered using a 0.2 μm PVDF syringe filter, yielding **ND3** colloid (7 ml, 4.0 mg/ml). **ND4***:* **ND1** colloidal solution (1 ml, 10 mg/ml) was dialysed 5x against water in 6-8 kDa dialysis tubing (Spectra/Por), filtered using a 0.2 μm PVDF syringe filter and diluted, yielding **ND4** colloid (9 ml, 1.0 mg/ml). **ND5***:* **ND1** colloidal solution (13.2 ml, 1 mg/ml) was centrifuged in an ultracentrifuge (200,000 rcf, 2 h). The top 2/3 of the supernatant was isolated, diluted by adding the same amount of water and centrifuged once more (200,000 rfc, 2 h). The top 1/3 of the supernatant was isolated and filtered using a 0.2 μm PVDF syringe filter, yielding a colourless **ND5** solution. The ultracentrifugation of FGF and ND tissue culture media solutions (100,000 rcf, 2 h) was conducted with 5 ml media from each condition using a SW55 Ti rotor and Optima XPN 90K Ultracentrifuge (Beckman Coulter, Brea, CA).

QELS and ζ-potential measurements were performed with 1 mg/ml NDs water using the Zetasizer Nano ZS system (Malvern) at room temperature. An aberration-corrected FEI titan "cubed" microscope operated at 80 kV was used for high-resolution TEM imaging and for diffraction work. For high-resolution TEM measurements, the **ND4** sample (1 mg/ml) was used.

Cell culture, transfection and western blot (WB)

RCS, 293T and MCF7 cells were cultivated in DMEM (Sigma-Aldrich, St. Louis, MO) supplemented with 10% FBS and antibiotics. For growth assays, 2.5 x 10^2 RCS cells per well were seeded in 96-well plates and grown for 5 days. Cell numbers were determined by crystal violet staining as described previously[72]. FGF1, FGF2, FGF4, FGF7, FGF8, FGF9, FGF10, FGF17, FGF18, FGF19, FGF21, FGF22, FGF23, EGF, NGF, TGFβ1, IL1β, IL6, and IFNγ were obtained from RnD Systems (Minneapolis, MN); BGJ398 was obtained from Selleckchem (Houston, TX). For WB, cells were extracted into Laemmli sample buffer (0.125 M Tris-Cl pH 6.8, 20% glycerol, 4% SDS, 0.005% bromophenol blue). Extracts were resolved by SDS-PAGE, transferred onto a PVDF membrane and visualized by chemiluminescence (Thermo Scientific, Rockford, IL). Antibodies against the following were used: lamin A/C, ID2, caveolin, LRP6, phospho-FRS2, ERK1/2, phospho-ERK1/2, actin, pSTAT1, STAT1, pSTAT3, STAT3, SMAD2, and pSMAD2 (Cell Signaling, Beverly, MA); FRS2 (Santa Cruz Biotechnology, Santa Cruz, CA); pLRP6 (Millipore, Billerica, MA); V5 (Invitrogen); FGF2 (Sigma-Aldrich); and FGF1, FGF4, FGF8, FGF10, FGF17, FGF19, FGF21, FGF22, FGF23, IL1β, IL6, and IFNγ (RnD Systems). Media with FGF2 and/or ND were preincubated for 8 hours at 37°C and 5% CO_2. Cells were transfected with vector expressing full-length V5-tagged human TRKA[73] using the FuGENE6 transfection reagent according to the manufacturer's protocol (Promega).

Cy5.5-FGF2 labelling and confocal microscopy

The 18 kDa isoform of His-tagged rat FGF2 was expressed in *E. coli* BL21 (DE3-trx) after IPTG induction and growth at 30°C. Recombinant 18 kDa FGF2 was purified as previously described[74] with the following modification: after the first purification of the His-tagged protein on Ni-beads, the protein was eluted and an additional purification step performed on heparin sepharose. After high-salt elution with 1.5 M NaCl, the protein was dialysed against phosphate buffered saline at 4°C overnight. Subsequently, recombinant FGF2 was fluorescently labelled with Cy5.5 maleimide mono-reactive dye (Amersham) according to the manufacturer´s protocol. Microscopic images were acquired using a Carl Zeiss LSM 700 confocal microscope with a 63x oil objective (Fig. 6B) or a 20x air objective (Fig. 2B).

Preparation of the FGF23-WT and FGF23-HBS

The synthetic genes for human FGF23-WT and FGF23-HBS (Fig. 7B) inserted into the pcDNA3.1 (+) vector were purchased from Thermo Fisher Scientific. The resulting plasmid DNAs were purified from transformed bacteria, and the final constructs were verified by sequencing. The 293T cells were transfected with FGF23-WT or FGF23-HBS for 24 hours. Proteins were released from the cells into the medium by freezing (-80°C/4 hours), and cell debris was removed by centrifugation (15,000 *g* for 30 minutes). Samples were incubated at 37°C in a 5% CO_2 incubator for 8 hours and then centrifuged at 100,000 *g* for 2 hours. The top 0.5 ml fractions were prepared as supernatant samples, and the bottoms of centrifugation tubes with or without ND were washed with Laemmli buffer and analysed as pellets. All samples were analysed for FGF23 by WB.

Limb explant culture, histology and collagen 10 *in situ* hybridization

Tibias obtained from E18 mouse embryos were grown for 8 days at 37°C in DMEM supplemented with **ND2** or **ND3** (100 μg/ml) and FGF2 (50 ng/ml). The medium was changed daily. The length of the tibias was measured at the beginning of the experiment (day 0) and at the end of cultivation (day 8) in Axio Vision (Zeiss, Germany). Tibia histology and collagen 10 *in situ* hybridization were performed as described previously[35].

Acknowledgements

We thank Miriam Minarikova and Hella Brinkmann for their excellent technical assistance. This work was supported by the Ministry of Education, Youth and Sports of the Czech Republic (KONTAKT II LH15231); project SYMBIT (CZ.02.1.01/0.0/0.0/15_003/0000477), financed by ERFD; the Agency for Healthcare Research of the Czech Republic (15-33232A, 15-34405A); the Czech Science Foundation (GA17-09525S); and the National Program of Sustainability II (MEYS CR: LQ1605 and CEITEC 2020 (LQ1601)). PC was supported by the Ministry of Health of the Czech Republic, grant Nr. 15e33094A.

References

(1) Scheinberg, D. A.; Villa, C. H.; Escorcia, F. E.; McDevitt, M. R. Conscripts of the Infinite Armada: Systemic Cancer Therapy Using Nanomaterials. *Nat. Rev. Clin. Oncol.* **2010**, *7*, 266–276.

(2) Chow, E. K.-H.; Ho, D. Cancer Nanomedicine: From Drug Delivery to Imaging. *Sci. Transl. Med.* **2013**, *5*, 216rv4.

(3) Jain, R. K.; Stylianopoulos, T. Delivering Nanomedicine to Solid Tumors. *Nat. Rev. Clin. Oncol.* **2010**, *7*, 653–664.

(4) Moyano, D. F.; Rotello, V. M. Nano Meets Biology: Structure and Function at the Nanoparticle Interface. *Langmuir* **2011**, *27*, 10376–10385.

(5) Kotov, N. A. Inorganic Nanoparticles as Protein Mimics. *Science* **2010**, *330*, 188–189.

(6) Lynch, I.; Dawson, K. A. Protein-Nanoparticle Interactions. *Nano Today* **2008,** *3*, 40–47.

(7) Bayraktar, H.; Ghosh, P. S.; Rotello, V. M.; Knapp, M. J. Disruption of Protein–protein Interactions Using Nanoparticles: Inhibition of Cytochrome c Peroxidase. *Chem. Commun.* **2006**, 1390–1392.

(8) Bayraktar, H.; You, C.-C. C.; Rotello, V. M. M.; Knapp, M. J. J. Facial Control of Nanoparticle Binding to Cytochrome c. *J. Am. Chem. Soc.* **2007**, *129*, 2732–2733.

(9) Heegaard, P. M. H.; Boas, U.; Otzen, D. E. Dendrimer Effects on Peptide and Protein Fibrillation. *Macromolecular Bioscience* **2007**, *7*, 1047–1059.

(10) Chen, N.; Huang, Y.; Wang, Y. Bioinspired Affinity DNA Polymers on Nanoparticles for Drug Sequestration and Detoxification. *Biomaterials* **2014**, *35*, 9709–9718.

(11) Herrmann, I. K.; Urner, M.; Graf, S.; Schumacher, C. M.; Roth-Z'graggen, B.; Hasler, M.; Stark, W. J.; Beck-Schimmer, B. Endotoxin Removal by Magnetic Separation-Based Blood Purification. *Adv. Healthc. Mater.* **2013**, *2*, 829–835.

(12) Kang, J. H.; Super, M.; Yung, C. W.; Cooper, R. M.; Domansky, K.; Graveline, A. R.; Mammoto, T.; Berthet, J. B.; Tobin, H.; Cartwright, M. J.; *et al.* An Extracorporeal Blood-Cleansing Device for Sepsis Therapy. *Nat. Med.* **2014**, *20*, 1211–1216.

(13) Koide, H.; Yoshimatsu, K.; Hoshino, Y.; Lee, S.-H.; Okajima, A.; Ariizumi, S.; Narita, Y.; Yonamine, Y.; Weisman, A. C.; Nishimura, Y.; *et al.* A Polymer Nanoparticle with Engineered Affinity for a Vascular Endothelial Growth Factor (VEGF165). *Nat. Chem.*

2017, *9*, 715–722.

(14) van Rijt, S.; Habibovic, P. Enhancing Regenerative Approaches with Nanoparticles. *J. R. Soc. Interface* **2017**, *14*, 20170093.

(15) Dobrovolskaia, M. A.; Aggarwal, P.; Hall, J. B.; McNeil, S. E. Preclinical Studies to Understand Nanoparticle Interaction with the Immune System and Its Potential Effects on Nanoparticle Biodistribution. *Molecular Pharmaceutics* **2008**, *5*, 487–495.

(16) Hatakeyama, H.; Akita, H.; Harashima, H. A Multifunctional Envelope Type Nano Device (MEND) for Gene Delivery to Tumours Based on the EPR Effect: A Strategy for Overcoming the PEG Dilemma. *Advanced Drug Delivery Reviews* **2011**, *63*, 152–160.

(17) Cedervall, T.; Lynch, I.; Lindman, S.; Berggård, T.; Thulin, E.; Nilsson, H.; Dawson, K. A. A.; Linse, S.; Berggard, T.; Thulin, E.; *et al.* Understanding the Nanoparticle-Protein Corona Using Methods to Quantify Exchange Rates and Affinities of Proteins for Nanoparticles. *Proc. Natl. Acad. Sci.* **2007**, *104*, 2050–2055.

(18) Mochalin, V. N.; Shenderova, O.; Ho, D.; Gogotsi, Y. The Properties and Applications of Nanodiamonds. *Nat. Nanotechnol.* **2011**, *7*, 11–23.

(19) Rehor, I.; Slegerova, J.; Havlik, J.; Raabova, H.; Hyvl, J.; Muchova, E.; Cigler, P. Nanodiamonds: Behavior in Biological Systems and Emerging Bioapplications. *Carbon Nanomaterials for Biomedical Applications* **2016**, *5*, 319–361.

(20) Turcheniuk, K.; Mochalin, V. N. Biomedical Applications of Nanodiamond (Review). *Nanotechnology* **2017**, *28*, 252001.

(21) Chow, E. K. K.; Zhang, X.-Q. X.-Q.; Chen, M.; Lam, R.; Robinson, E.; Huang, H.; Schaffer, D.; Osawa, E.; Goga, A.; Ho, D. Nanodiamond Therapeutic Delivery Agents Mediate Enhanced Chemoresistant Tumor Treatment. *Sci Transl Med* **2011**, *3*, 73ra21.

(22) Moore, L.; Yang, J.; Lan, T. T. H.; Osawa, E.; Lee, D.-K.; Johnson, W. D.; Xi, J.; Chow, E. K.-H.; Ho, D. Biocompatibility Assessment of Detonation Nanodiamond in Non-Human Primates and Rats Using Histological, Hematologic, and Urine Analysis. *ACS Nano* **2016**, *10*, 7385–7400.

(23) Dideikin, A. T.; Aleksenskii, A. E.; Baidakova, M. V.; Brunkov, P. N.; Brzhezinskaya, M.; Davydov, V. Y.; Levitskii, V. S.; Kidalov, S. V.; Kukushkina, Y. A.; Kirilenko, D. A.; *et al.* Rehybridization of Carbon on Facets of Detonation Diamond Nanocrystals and

Forming Hydrosols of Individual Particles. *Carbon* **2017**, *122*, 737–745.

(24) Lai, L.; Barnard, A. S. Anisotropic Adsorption and Distribution of Immobilized Carboxyl on Nanodiamond. *Nanoscale* **2014**, *6*, 14185–14189.

(25) Paci, J. T.; Man, H. B.; Saha, B.; Ho, D.; Schatz, G. C. Understanding the Surfaces of Nanodiamonds. *J. Phys. Chem. C* **2013**, *117*, 17256–17267.

(26) Barnard, A. S.; Sternberg, M. Crystallinity and Surface Electrostatics of Diamond Nanocrystals. *J. Mater. Chem.* **2007**, *17*, 4811.

(27) Petit, T.; Yuzawa, H.; Nagasaka, M.; Yamanoi, R.; Osawa, E.; Kosugi, N.; Aziz, E. F. Probing Interfacial Water on Nanodiamonds in Colloidal Dispersion. *J. Phys. Chem. Lett.* **2015**, *6*, 2909–2912.

(28) Stehlik, S.; Glatzel, T.; Pichot, V.; Pawlak, R.; Meyer, E.; Spitzer, D.; Rezek, B. Water Interaction with Hydrogenated and Oxidized Detonation Nanodiamonds — Microscopic and Spectroscopic Analyses. *Diam. Relat. Mater.* **2016**, *63*, 97–102.

(29) Williams, O. A.; Hees, J.; Dieker, C.; Jäger, W.; Kirste, L.; Nebel, C. E. Size-Dependent Reactivity of Diamond Nanoparticles. *ACS Nano* **2010**, *4*, 4824–4830.

(30) Petit, T.; Arnault, J.-C.; Girard, H. A.; Sennour, M.; Kang, T.-Y.; Cheng, C.-L.; Bergonzo, P. Oxygen Hole Doping of Nanodiamond. *Nanoscale* **2012**, *4*, 6792.

(31) Mchedlov-Petrossyan, N. O.; Kamneva, N. N.; Marynin, A. I.; Kryshtal, A. P.; Ōsawa, E. Colloidal Properties and Behaviors of 3 Nm Primary Particles of Detonation Nanodiamonds in Aqueous Media. *Phys. Chem. Chem. Phys.* **2015**, *17*, 16186–16203.

(32) Ginés, L.; Mandal, S.; Ashek-I-Ahmed; Cheng, C.-L.; Sow, M.; Williams, O. A. Positive Zeta Potential of Nanodiamonds. *Nanoscale* **2017**, *9*, 12549–12555.

(33) Aramesh, M.; Shimoni, O.; Ostrikov, K.; Prawer, S.; Cervenka, J. Surface Charge Effects in Protein Adsorption on Nanodiamonds. *Nanoscale* **2015**, *7*, 5726–5736.

(34) Tian, Y.; Larsson, K. Protein-Functionalized Diamond Surfaces in a Water Solvent: A Theoretical Approach. *J. Phys. Chem. C* **2015**, *119*, 8608–8618.

(35) Gudernova, I.; Vesela, I.; Balek, L.; Buchtova, M.; Dosedelova, H.; Kunova, M.; Pivnicka, J.; Jelinkova, I.; Roubalova, L.; Kozubik, A.; *et al.* Multikinase Activity of Fibroblast Growth Factor Receptor (FGFR) Inhibitors SU5402, PD173074, AZD1480, AZD4547 and BGJ398 Compromises the Use of Small Chemicals Targeting FGFR Catalytic Activity for

Therapy of Short-Stature Syndromes. *Hum. Mol. Genet.* **2016**, *25*, 9–23.

(36) Krejci, P.; Murakami, S.; Prochazkova, J.; Trantirek, L.; Chlebova, K.; Ouyang, Z.; Aklian, A.; Smutny, J.; Bryja, V.; Kozubik, A.; *et al.* NF449 Is a Novel Inhibitor of Fibroblast Growth Factor Receptor 3 (FGFR3) Signaling Active in Chondrocytes and Multiple Myeloma Cells. *J. Biol. Chem.* **2010**, *285*, 20644–20653.

(37) Guagnano, V.; Furet, P.; Spanka, C.; Bordas, V.; Le Douget, M.; Stamm, C.; Brueggen, J.; Jensen, M. R.; Schnell, C.; Schmid, H.; *et al.* Discovery of 3-(2,6-Dichloro-3,5-Dimethoxy-Phenyl)-1-{6-[4-(4-Ethyl-Piperazin-1-Yl)-Phenylamino]-Pyrimidin-4-Yl}-1-Methyl-Urea (NVP-BGJ398), a Potent and Selective Inhibitor of the Fibroblast Growth Factor Receptor Family of Receptor Tyrosine Kinase. *J. Med. Chem.* **2011**, *54*, 7066–7083.

(38) Tanner, Y.; Grose, R. P. Dysregulated FGF Signalling in Neoplastic Disorders. *Semin. Cell Dev. Biol.* **2016**, *53*, 126–135.

(39) Krejci, P.; Prochazkova, J.; Smutny, J.; Chlebova, K.; Lin, P.; Aklian, A.; Bryja, V.; Kozubik, A.; Wilcox, W. R. FGFR3 Signaling Induces a Reversible Senescence Phenotype in Chondrocytes Similar to Oncogene-Induced Premature Senescence. *Bone* **2010**, *47*, 102–110.

(40) Hadari, Y. R.; Gotoh, N.; Kouhara, H.; Lax, I.; Schlessinger, J. Critical Role for the Docking-Protein FRS2 Alpha in FGF Receptor-Mediated Signal Transduction Pathways. *Proc. Natl. Acad. Sci. U. S. A.* **2001**, *98*, 8578–8583.

(41) Buchtova, M.; Oralova, V.; Aklian, A.; Masek, J.; Vesela, I.; Ouyang, Z.; Obadalova, T.; Konecna, Z.; Spoustova, T.; Pospisilova, T.; *et al.* Fibroblast Growth Factor and Canonical WNT/β-Catenin Signaling Cooperate in Suppression of Chondrocyte Differentiation in Experimental Models of FGFR Signaling in Cartilage. *Biochim. Biophys. Acta - Mol. Basis Dis.* **2015**, *1852*, 839–850.

(42) Krejci, P.; Salazar, L.; Kashiwada, T. A.; Chlebova, K.; Salasova, A.; Thompson, L. M.; Bryja, V.; Kozubik, A.; Wilcox, W. R. Analysis of STAT1 Activation by Six FGFR3 Mutants Associated with Skeletal Dysplasia Undermines Dominant Role of STAT1 in FGFR3 Signaling in Cartilage. *PLoS One* **2008**, *3*, e3961.

(43) Hemelaar, S. R.; Nagl, A.; Bigot, F.; Rodríguez-García, M. M.; de Vries, M. P.; Chipaux,

M.; Schirhagl, R. The Interaction of Fluorescent Nanodiamond Probes with Cellular Media. *Mikrochim. Acta* **2017**, *184*, 1001–1009.

(44) Wang, H.-D.; Niu, C. H.; Yang, Q.; Badea, I. Study on Protein Conformation and Adsorption Behaviors in Nanodiamond Particle-Protein Complexes. *Nanotechnology* **2011**, *22*, 145703.

(45) Huang, L. C. L.; Chang, H.-C. Adsorption and Immobilization of Cytochrome c on Nanodiamonds. *Langmuir* **2004**, *20*, 5879–5884.

(46) Buchtova, M.; Chaloupkova, R.; Zakrzewska, M.; Vesela, I.; Cela, P.; Barathova, J.; Gudernova, I.; Zajickova, R.; Trantirek, L.; Martin, J.; *et al.* Instability Restricts Signaling of Multiple Fibroblast Growth Factors. *Cell. Mol. Life Sci.* **2015**, *72*, 2445–2459.

(47) Nakao, A.; Imamura, T.; Souchelnytskyi, S.; Kawabata, M.; Ishisaki, A.; Oeda, E.; Tamaki, K.; Hanai, J.; Heldin, C. H.; Miyazono, K.; *et al.* TGF-Beta Receptor-Mediated Signalling through Smad2, Smad3 and Smad4. *EMBO J.* **1997**, *16*, 5353–5362.

(48) Horvath, C. M. The Jak-STAT Pathway Stimulated by Interleukin 6. *Sci. STKE* **2004**, *2004*, tr9.

(49) Darnell, J. E.; Kerr, I. M.; Stark, G. R. Jak-STAT Pathways and Transcriptional Activation in Response to IFNs and Other Extracellular Signaling Proteins. *Science* **1994**, *264*, 1415–1421.

(50) Kouhara, H.; Hadari, Y. R.; Spivak-Kroizman, T.; Schilling, J.; Bar-Sagi, D.; Lax, I.; Schlessinger, J. A Lipid-Anchored Grb2-Binding Protein That Links FGF-Receptor Activation to the Ras/MAPK Signaling Pathway. *Cell* **1997**, *89*, 693–702.

(51) Murzin, A. G.; Lesk, A. M.; Chothia, C. Beta-Trefoil Fold. Patterns of Structure and Sequence in the Kunitz Inhibitors Interleukins-1 Beta and 1 Alpha and Fibroblast Growth Factors. *J. Mol. Biol.* **1992**, *223*, 531–543.

(52) Degirolamo, C.; Sabbà, C.; Moschetta, A. Therapeutic Potential of the Endocrine Fibroblast Growth Factors FGF19, FGF21 and FGF23. *Nat. Rev. Drug Discov.* **2015**, *15*, 51–69.

(53) Itoh, N.; Ornitz, D. M. Fibroblast Growth Factors: From Molecular Evolution to Roles in Development, Metabolism and Disease. *J. Biochem.* **2011**, *149*, 121–130.

(54) Provot, S.; Schipani, E. Molecular Mechanisms of Endochondral Bone Development.

Biochem. Biophys. Res. Commun. **2005**, *328*, 658–665.

(55) Zhou, S.; Xie, Y.; Tang, J.; Huang, J.; Huang, Q.; Xu, W.; Wang, Z.; Luo, F.; Wang, Q.; Chen, H.; *et al.* FGFR3 Deficiency Causes Multiple Chondroma-like Lesions by Upregulating Hedgehog Signaling. *PLoS Genet.* **2015**, *11*, e1005214.

(56) Deng, C.; Wynshaw-Boris, A.; Zhou, F.; Kuo, A.; Leder, P. Fibroblast Growth Factor Receptor 3 Is a Negative Regulator of Bone Growth. *Cell* **1996**, *84*, 911–921.

(57) Ho, D.; Wang, C.-H. K.; Chow, E. K.-H. Nanodiamonds: The Intersection of Nanotechnology, Drug Development, and Personalized Medicine. *Sci. Adv.* **2015**, *1*, e1500439.

(58) Nanodiamond Modified Gutta Percha (NDGP) Composite for Non-surgical Root Canal Therapy (RCT) Filler Material https://clinicaltrials.gov/ct2/show/NCT02698163.

(59) Hong, C.; Song, D.; Lee, D.-K.; Lin, L.; Pan, H. C.; Lee, D.; Deng, P.; Liu, Z.; Hadaya, D.; Lee, H.-L.; *et al.* Reducing Posttreatment Relapse in Cleft Lip Palatal Expansion Using an Injectable Estrogen–nanodiamond Hydrogel. *Proc. Natl. Acad. Sci.* **2017**, *114*, E7218–E7225.

(60) Wang, H.; Lee, D.-K.; Chen, K.-Y.; Chen, J.-Y.; Zhang, K.; Silva, A.; Ho, C.-M.; Ho, D. Mechanism-Independent Optimization of Combinatorial Nanodiamond and Unmodified Drug Delivery Using a Phenotypically Driven Platform Technology. *ACS Nano* **2015**, *9*, 3332–3344.

(61) Wang, X.; Low, X. C.; Hou, W.; Abdullah, L. N.; Toh, T. B.; Mohd Abdul Rashid, M.; Ho, D.; Chow, E. K.-H. Epirubicin-Adsorbed Nanodiamonds Kill Chemoresistant Hepatic Cancer Stem Cells. *ACS Nano* **2014**, *8*, 12151–12166.

(62) Zhang, X.-Q.; Lam, R.; Xu, X.; Chow, E. K.; Kim, H.-J.; Ho, D. Multimodal Nanodiamond Drug Delivery Carriers for Selective Targeting, Imaging, and Enhanced Chemotherapeutic Efficacy. *Adv. Mater.* **2011**, *23*, 4770–4775.

(63) Moore, L. K.; Chow, E. K.; Osawa, E.; Bishop, J. M.; Ho, D. Diamond-Lipid Hybrids Enhance Chemotherapeutic Tolerance and Mediate Tumor Regression. *Adv. Mater.* **2013**, *25*, 3532–3541.

(64) Mochalin, V. N.; Pentecost, A.; Li, X.-M.; Neitzel, I.; Nelson, M.; Wei, C.; He, T.; Guo, F.; Gogotsi, Y. Adsorption of Drugs on Nanodiamond: Toward Development of a Drug

Delivery Platform. *Mol. Pharm.* **2013**, *10*, 3728–3735.

(65) Setyawati, M. I.; Mochalin, V. N.; Leong, D. T. Tuning Endothelial Permeability with Functionalized Nanodiamonds. *ACS Nano* **2016**, *10*, 1170–1181.

(66) Grall, R.; Girard, H.; Saad, L.; Petit, T.; Gesset, C.; Combis-Schlumberger, M.; Paget, V.; Delic, J.; Arnault, J.-C.; Chevillard, S. Impairing the Radioresistance of Cancer Cells by Hydrogenated Nanodiamonds. *Biomaterials* **2015**, *61*, 290–298.

(67) Alhaddad, A.; Adam, M.-P.; Botsoa, J.; Dantelle, G.; Perruchas, S.; Gacoin, T.; Mansuy, C.; Lavielle, S.; Malvy, C.; Treussart, F.; *et al.* Nanodiamond as a Vector for siRNA Delivery to Ewing Sarcoma Cells. *Small* **2011**, *7*, 3087–3095.

(68) Zhao, L.; Xu, Y.-H.; Akasaka, T.; Abe, S.; Komatsu, N.; Watari, F.; Chen, X. Polyglycerol-Coated Nanodiamond as a Macrophage-Evading Platform for Selective Drug Delivery in Cancer Cells. *Biomaterials* **2014**, *35*, 5393–5406.

(69) Zhao, L.; Xu, Y.-H.; Qin, H.; Abe, S.; Akasaka, T.; Chano, T.; Watari, F.; Kimura, T.; Komatsu, N.; Chen, X. Platinum on Nanodiamond: A Promising Prodrug Conjugated with Stealth Polyglycerol, Targeting Peptide and Acid-Responsive Antitumor Drug. *Adv. Funct. Mater.* **2014**, *24*, 5348–5357.

(70) Steinmüller-Nethl, D.; Kloss, F. R.; Najam-Ul-Haq, M.; Rainer, M.; Larsson, K.; Linsmeier, C.; Köhler, G.; Fehrer, C.; Lepperdinger, G.; Liu, X.; *et al.* Strong Binding of Bioactive BMP-2 to Nanocrystalline Diamond by Physisorption. *Biomaterials* **2006**, *27*, 4547–4556.

(71) Kloss, F. R.; Gassner, R.; Preiner, J.; Ebner, A.; Larsson, K.; Hächl, O.; Tuli, T.; Rasse, M.; Moser, D.; Laimer, K.; *et al.* The Role of Oxygen Termination of Nanocrystalline Diamond on Immobilisation of BMP-2 and Subsequent Bone Formation. *Biomaterials* **2008**, *29*, 2433–2442.

(72) Krejci, P.; Pejchalova, K.; Wilcox, W. R. Simple, Mammalian Cell-Based Assay for Identification of Inhibitors of the Erk MAP Kinase Pathway. *Invest. New Drugs* **2007**, *25*, 391–395.

(73) Gudernova, I.; Foldynova-Trantirkova, S.; Ghannamova, B. E. El; Fafilek, B.; Varecha, M.; Balek, L.; Hruba, E.; Jonatova, L.; Jelinkova, I.; Kunova Bosakova, M.; *et al.* One Reporter for in-Cell Activity Profiling of Majority of Protein Kinase Oncogenes. *Elife*

2017, *6*, 117–120.

(74) Müller-Ostermeyer, F.; Claus, P.; Grothe, C. Distinctive Effects of Rat Fibroblast Growth Factor-2 Isoforms on PC12 and Schwann Cells. *Growth Factors* **2001**, *19*, 175–191.

(75) Raman, R.; Venkataraman, G.; Ernst, S.; Sasisekharan, V.; Sasisekharan, R. Structural Specificity of Heparin Binding in the Fibroblast Growth Factor Family of Proteins. *Proc. Natl. Acad. Sci. U. S. A.* **2003**, *100*, 2357–2362.

Figure 1

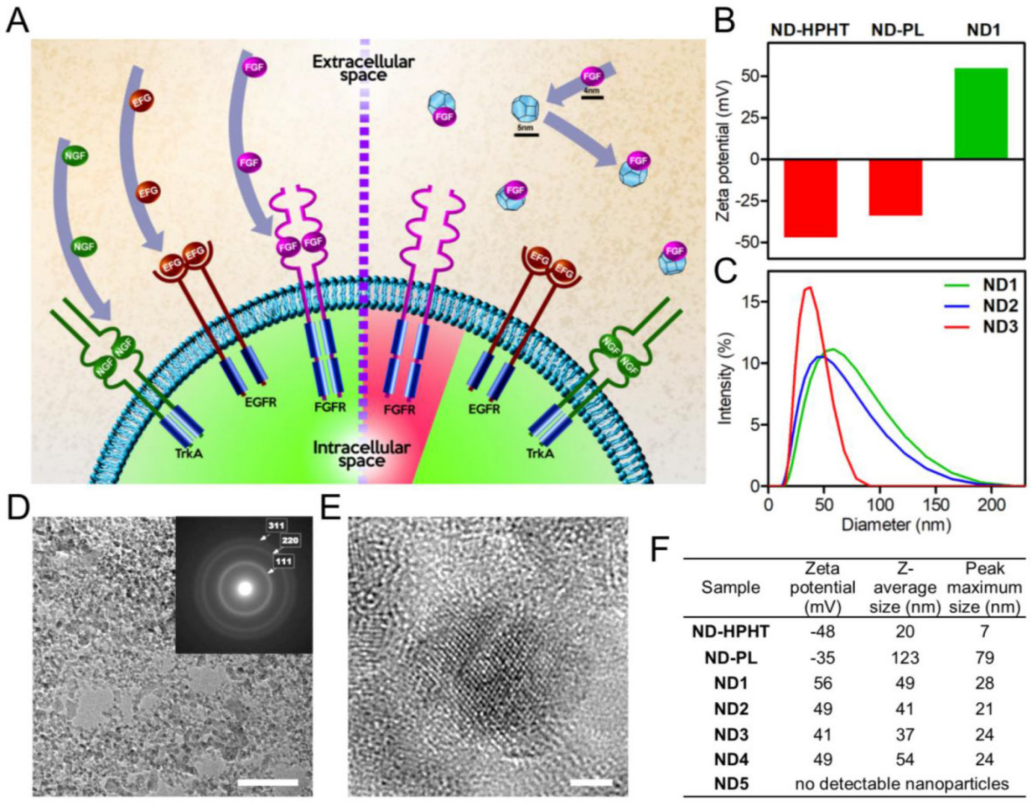

F

Sample	Zeta potential (mV)	Z-average size (nm)	Peak maximum size (nm)
ND-HPHT	-48	20	7
ND-PL	-35	123	79
ND1	56	49	28
ND2	49	41	21
ND3	41	37	24
ND4	49	54	24
ND5	no detectable nanoparticles		

Figure 1 General scheme of ND action in cell signalling and physico-chemical characteristics of ND particles

(A) The cartoon depicting the selective inhibition of FGF signalling by ND particles described in this study. NDs bind FGF ligands preventing their association with transmembrane receptors (FGFR) and activation of signalling. Signalling of other ligand-receptor systems exemplified in this cartoon by NGF-TrkA and EGF-EGFR is not affected by NDs. (B) The ζ-potentials of the ND particles used. **ND-HPHT**, high-pressure, high-temperature NDs (smallest isolated fraction); **ND-PL** and **ND1**, detonation NDs with negative and positive ζ-potentials, respectively. (C) Size distributions of detonation NDs (positive ζ-potential) with decreasing mean size measured by QELS. **ND1**-**ND3** originate from the same starting sample; their sizes gradually decreased from

ND1 to **ND3** by ultracentrifugation (see Materials and Methods for details). (D) TEM micrograph of **ND1**. The diffraction ring pattern displays only diamond rings, showing the structure. The scalebar corresponds to 100 nm. (E) High-resolution TEM micrograph depicting a detail of the **ND1** particle. Scalebar corresponds to 2 nm. (F) Characterization of NDs using ζ-potential and QELS measurements. While the ζ-potentials for **ND-HPHT** and **ND-PL** are negative, all other particles tested in the study show positive values. The decrease in the peak maximum for **ND1**-**ND3** corresponds to the data shown for (C). The **ND4** sample was prepared by the dialysis of **ND1** against water, but no significant change in ζ-potential or size was observed. **ND5** is the supernatant from a control sample in which all particles were quantitatively removed from **ND1** by high-speed ultracentrifugation.

Figure 2

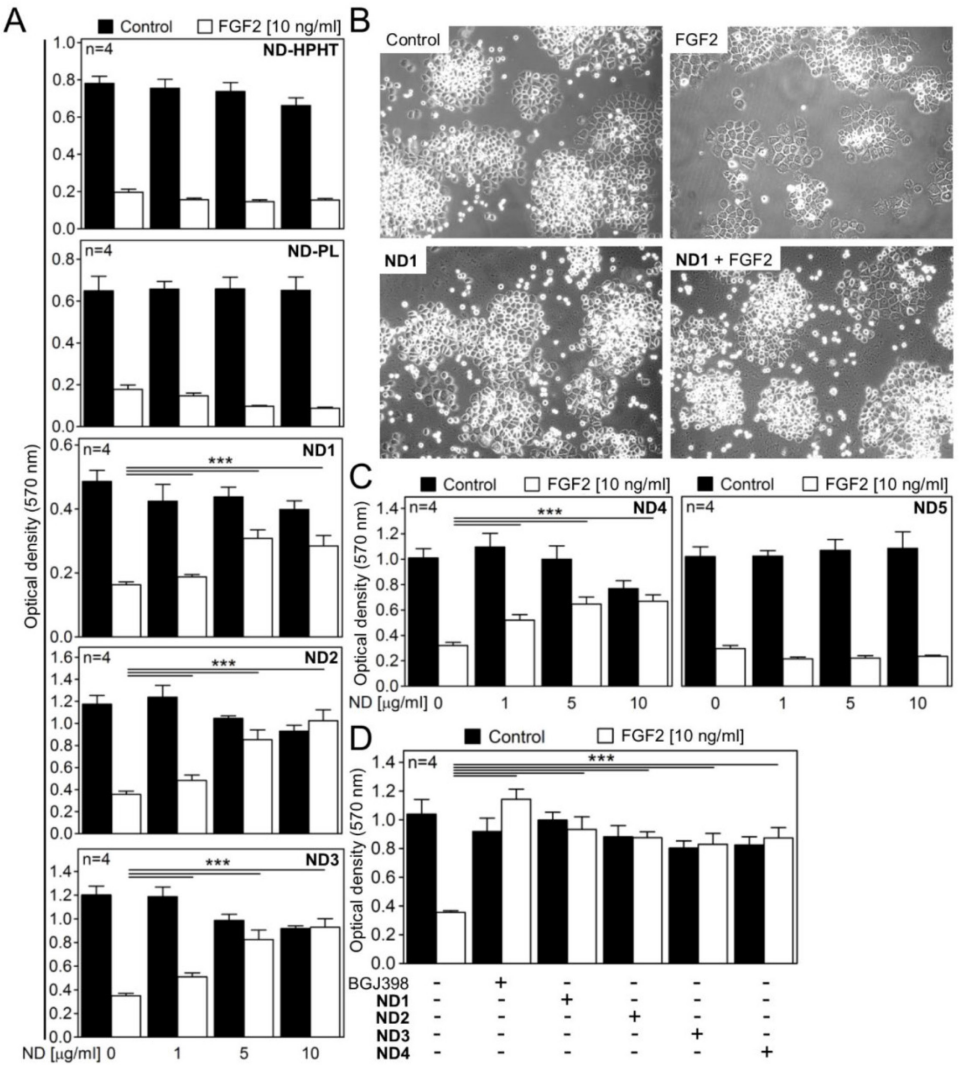

Figure 2 NDs inhibit FGF2 signalling in cells

(A) RCS cells were treated in medium containing 10% FBS with FGF2 (10 ng/ml) alone or with five types of NDs differing in ζ-potential and particle size for 72 hours, and the FGF2-mediated growth arrest was quantified by crystal violet staining. Note the rescue of the FGF2-mediated growth arrest phenotype in cells treated with **ND1-3**. Data represent averages of eight biological

replicates with the indicated SD (***p<0.001, Student's t-test). The results represent four (n) independent experiments. (B) Microscopic appearance (phase contrast, 200x) of RCS cells treated with FGF2 and **ND1** for 72 hours. Note the smaller colonies with enlarged cells in culture treated with FGF2 (10 ng/ml); this phenotype is rescued by **ND1** (10 μg/ml). (C) The effect of **ND4** (i.e., repeatedly dialysed **ND1** solution) and the supernatant obtained by quantitative removal of the NDs from **ND1** by ultracentrifugation (**ND5**) on the FGF2-mediated RCS growth arrest, demonstrating that only ND but not any possible soluble impurity in their solution inhibits FGF2 signalling. (D) The effect of **ND1-4** (10 μg/ml) on FGF2-mediated RCS growth arrest compared to a chemical inhibitor of FGFR kinase activity BGJ398 (10 nM).

Figure 3

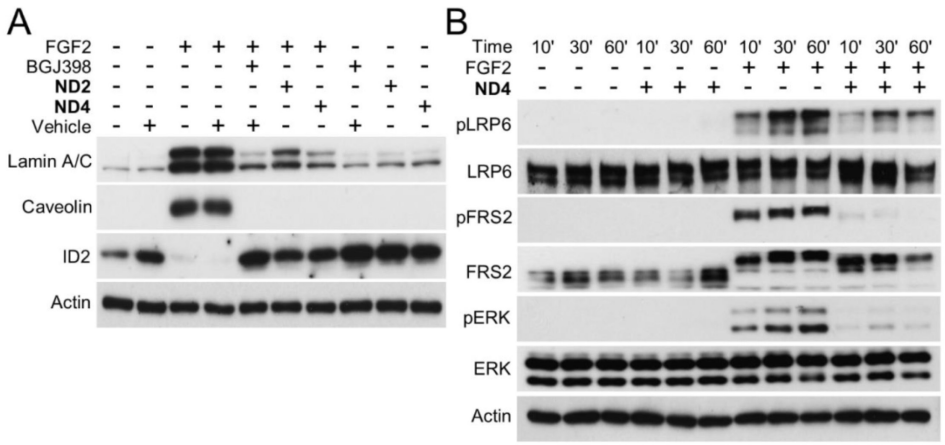

Figure 3 NDs inhibit the FGF2-mediated activation of FGFR signalling and the induction of senescence.

(A) RCS cells were treated in medium containing 10% FBS with 20 ng/ml FGF2, 10 μg/ml **ND2** or **ND4**, and 10 nM BGJ398. The effects of inhibitors on the FGF2-mediated induction of the senescence markers lamin A/C and caveolin was determined by western blot 72 hours later. The reduction in ID2 expression, which correlates with premature senescence in RCS cells, is also shown[39]. Actin served as a loading control. (B) Cells were treated with FGF2 and **ND4** for the indicated times, and the ND effect on the FGF2-mediated phosphorylation (p) of LRP6, FRS2 and ERK members of FGFR downstream signalling pathways was determined by western blot. The total levels of each molecule and actin serve as loading controls.

Figure 4

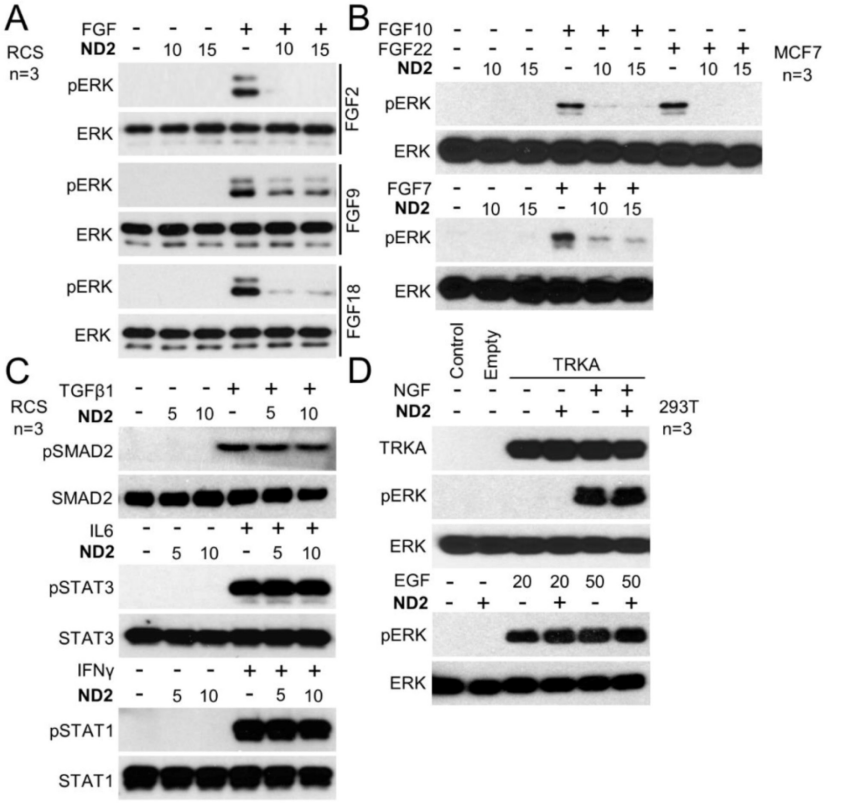

Figure 4 NDs inhibit FGF signalling but not TGFβ1, IL6, IFNγ, EGF or NGF signalling.
(A) RCS or (B) MCF7 cells were treated in medium containing 10% FBS with 20 ng/ml FGF2, FGF7, FGF9, FGF18 and with 10 ng/ml FGF10 or FGF22 either alone or together with 10 or 15 μg/ml **ND2** for 1 hours, and ERK phosphorylation (p) was analysed by western blot. The total ERK levels serve as a loading control; n, number of independent experiments. (C) RCS cells were treated with 20 ng/ml TGFβ1, 50 ng/ml IL6 or 50 ng/ml IFNγ for 10 minutes and analysed for the phosphorylation (p) of SMAD2, STAT1 and STAT3 by western blot. (D) 293T cells were treated with 20 or 50 ng/ml EGF alone or together with NDs for 5 minutes, transfected with vector expressing human wild-type TRKA for 24 hours, and treated with 20 ng/ml NGF alone or in the presence of **ND2** for 1 hour. Cells were analysed for ERK phosphorylation (p) with the total ERK serving as a loading control.

Figure 5

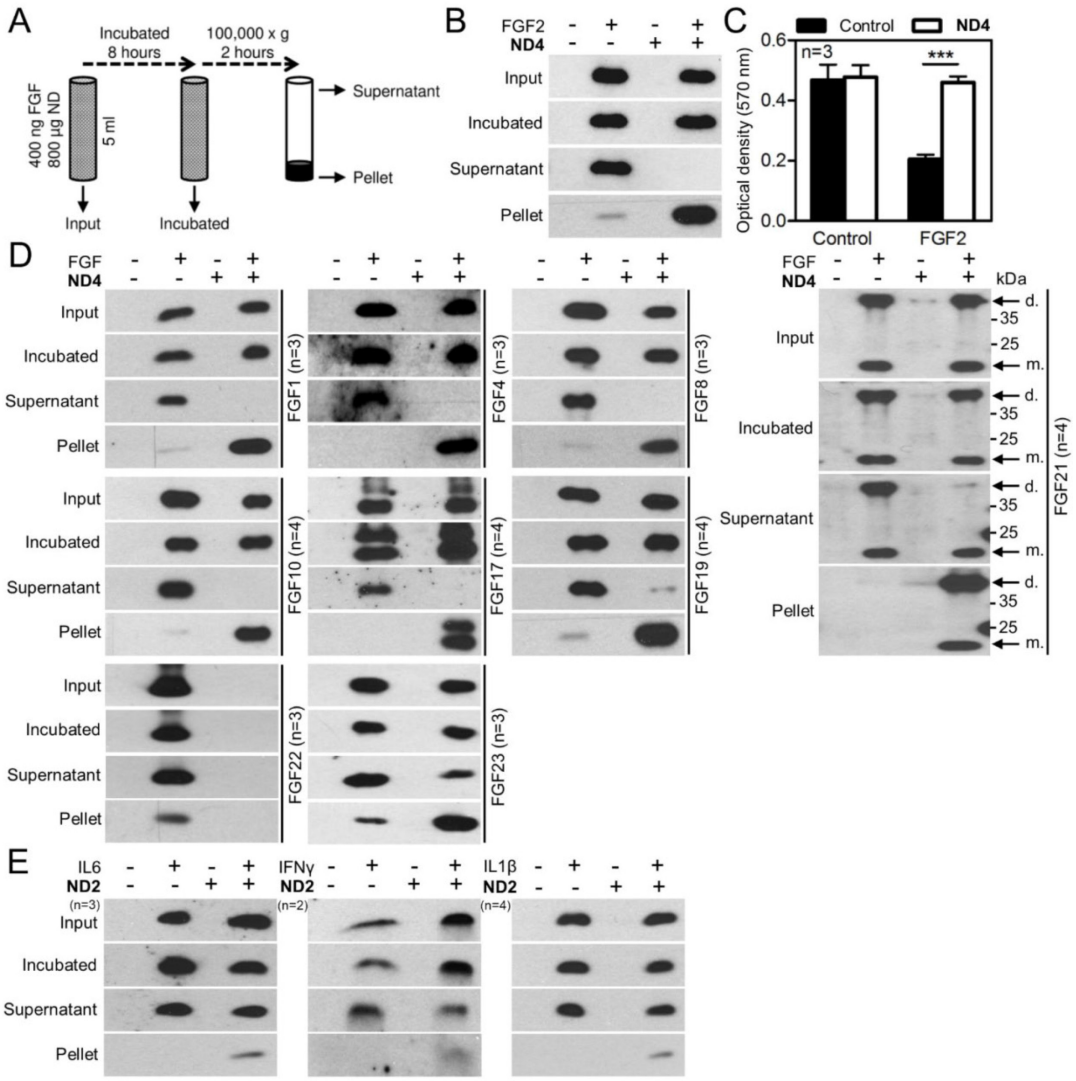

Figure 5 NDs sequester multiple FGF ligands.

(A) Outline of FGF pull-down experiments. Human recombinant FGFs were incubated with NDs in DMEM supplemented with 10% FBS for 8 hours, and the NDs were then collected by centrifugation (100,000 rfc, 2 h). Supernatant and pellet samples were analysed for the presence of FGF by western blot with specific antibodies. The input samples and samples taken after 8-

hour incubation but before centrifugation serve as controls. (B) Effective depletion of FGF2 from culture medium by **ND4**. Please note the lack of FGF2 signal in the medium supernatant after incubation with **ND4**. No growth arrest was detected in RCS cells grown in the latter medium supernatant for 72 h, in contrast to the media supernatant containing FGF2 only, which caused normal growth arrest (C). (D) Depletion of soluble recombinant FGF1, FGF4, FGF8, FGF10, FGF17, FGF19 and FGF21-23 by **ND4** in DMEM supplemented with 10% FBS. The depletion is demonstrated by the lack of FGF signals in the supernatant fraction in the medium containing **ND4**. Note the less effective clearance of FGF23 by **ND4** and the predominant clearance of dimeric (d.) FGF21, as opposed to FGF21 monomer (m.). Also note the complete disappearance of FGF22 from all analysed samples containing **ND4**, indicating the very strong binding of FGF22 to **ND4** and leading to the disappearance of detectable FGF22 from all tested fractions. (E) No significant depletion of recombinant IL6, IFNγ and IL1β by **ND2**. IL6, IFNγ and IL1β were detected by western blot with specific antibodies.

Figure 6

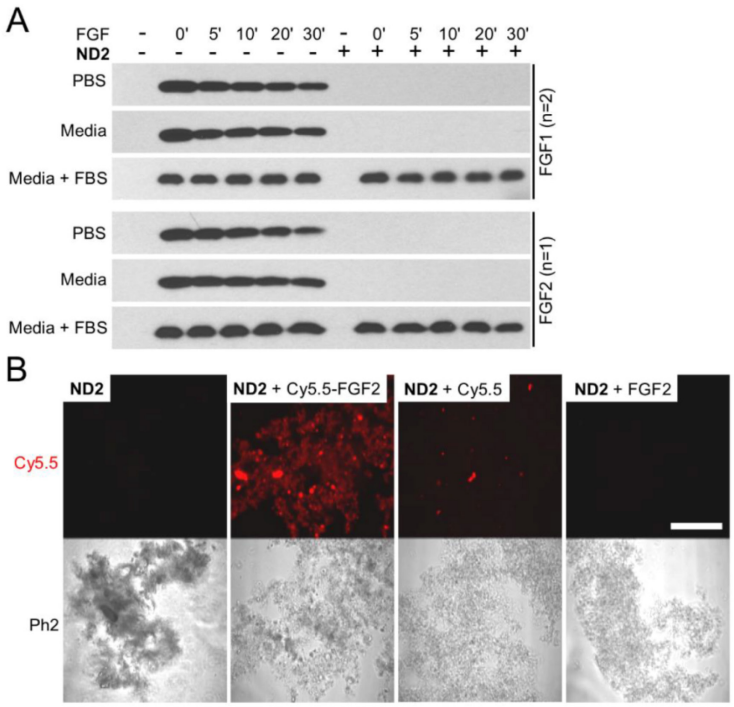

Figure 6 The dynamics of ND-FGF binding.

(A) Recombinant FGF1 and FGF2 were added for the indicated times to PBS, DMEM or DMEM supplemented with 10% FBS. The solution sample was taken after the indicated times and analysed for FGF expression by western blot. (B) **ND2** was incubated with FGF2 labelled with Cy5.5 (FGF2-Cy5.5), with non-labelled FGF2 or with free Cy5.5 for 8 hours, **ND2** was collected by centrifugation and analysed by confocal microscopy. Note the association of FGF2-Cy5.5 with **ND2** in contrast to no association with free Cy5.5. Corresponding phase contrast images are also shown (Ph2, lower panel), scale bar 50 μm.

Figure 7

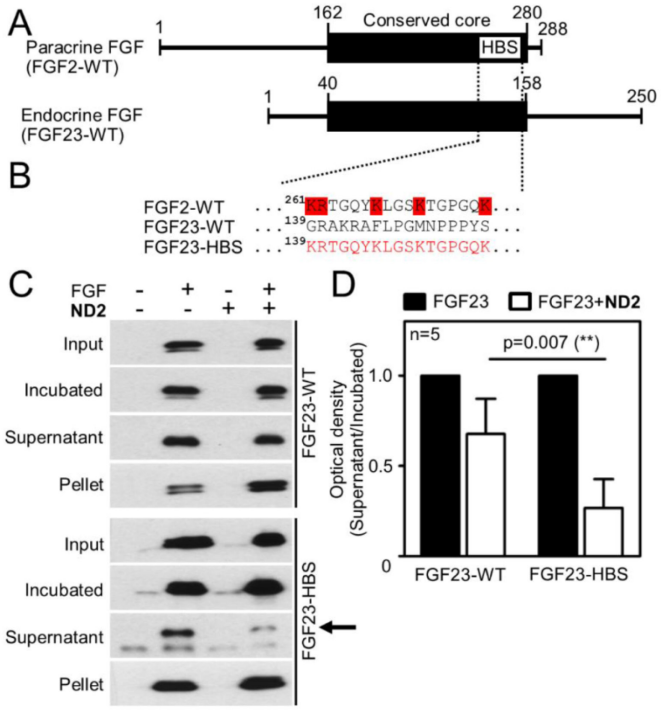

Figure 7 The heparin binding site (HBS) is involved in FGF interaction with NDs.

(A) Schematic representation of FGF2 and FGF23. Central core sequence (~120 amino acids) conserved among all members of the FGF family and HBS conserved among endocrine and paracrine FGFs. (B) Sequence alignment of human (paracrine) FGF2 and (endocrine) FGF23 at the location of the FGF2 HBS. Residues required for the binding of heparin to FGF2[75] are highlighted in red. In the chimeric FGF23-HBS protein, the GRAKRAFLPGMNPPPYS segment of the wild-type FGF23 was replaced by the KRTGQYKLGSKTGPGQK segment corresponding to the FGF2 HBS. (C) FGF23 and FGF23-HBS were expressed in 293T cells, released via freezing at -80°C and incubated with **ND2** for 8 hours. **ND2** was then collected by centrifugation. Supernatants and pellet samples were analysed for FGF23 by western blot (arrow). The input samples and samples taken after 8 hours of incubation but before centrifugation serve as controls. Note the more efficient depletion of FGF23-HBS by **ND2** (supernatant fraction) than that of wt

FGF23. (D) The FGF23 signal in supernatant samples obtained from five (n) independent experiments was quantified by densitometry and graphed. Data from individual western blots were expressed as a percentage of the control (FGF23 alone). Numbers represent averages from five experiments with the indicated standard deviation (SD). Statistically significant differences are indicated (** $p<0.01$, ANOVA).

Figure 8

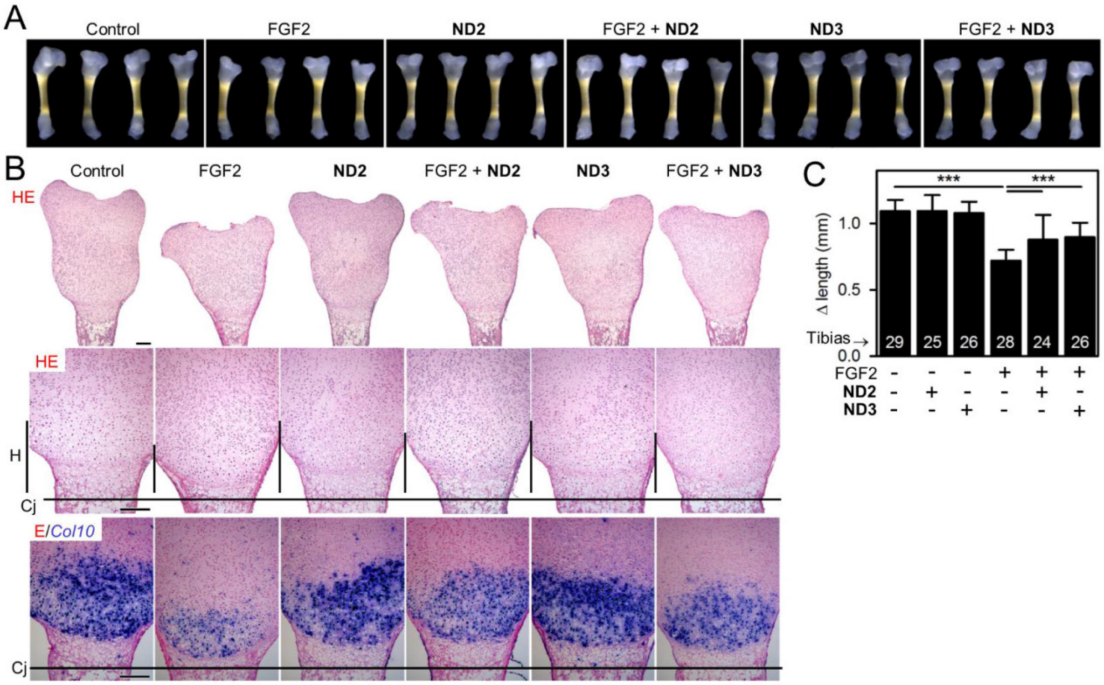

Figure 8 NDs inhibit FGF signalling in limb explant cultures.

(A) Tibias isolated from E18 mice embryos were cultured in medium containing 10% FBS, 50 ng/ml of FGF2, and 100 µg/ml of **ND2** or **ND3** for 8 days. (B) Histological sections of representative tibias were stained with haematoxylin/eosin (HE). Note the marked FGF2-mediated reduction in hypertrophic cartilage (H), visualized by collagen 10 *in situ* hybridization (sections counterstained with eosin, E). This phenotype is rescued by NDs. Cj, chondro-osseous junction. Scale bar, 100 µm. (C) The tibia length differences at isolation and after 8 days of incubation (Δ length) were determined and graphed. Note the partial rescue of the growth-inhibitory FGF2 phenotype mediated by NDs. Statistically significant differences are highlighted (Student's t-test, ***$p<0.001$). The results are a compilation of six independent experiments; n, the number of tibias analysed.

Appendix F

Appendix G

Rehor, I.; Raabova, H.; **Havlik, J.**; Fiserova, A.; Richter, J.; Turner, S.; Van Tendeloo, G.; Stursa, J.; Petrakova, V.; Dai, L.; Cigler, P.; Rounded monodisperse nanodiamonds: properties and mass production – **manuscript in preparation**.

Rounded monodisperse nanodiamonds: properties and mass production

Ivan Rehor[1], Helena Raabova[1,2], Jan Havlik[1,3], Stuart Turner[4], Gustaaf Van Tendeloo[4], Jan Stursa[5], Vladimira Petrakova[6], Petr Cigler[1,*]

[1] *Institute of Organic Chemistry and Biochemistry AS CR, v.v.i., Prague, Czech Republic*

[2] *University of Chemistry and Technology, Prague, Department of Inorganic chemistry, Technicka 5, Prague 16628 6, Czech Republic*

[3] *Faculty of Science, Charles University, Prague, Czech Republic*

[4] *EMAT, University of Antwerp, Antwerp, Belgium*

[5] *Nuclear Physics Institute AS CR, v.v.i., Rez near Prague, Czech Republic*

[6] *Faculty of Biomedical Engineering, Czech Technical University in Prague, Czech Republic*

Nanodiamond is a material which attracts a lot of scientific attention due to its outstanding physical properties. Fluorescent nanodiamonds (FNDs) are a recently introduced class of luminescent probes,[1–3] sensors,[4] parts of quantum computers, or other electronic nanodevices.[5] Fluorescence of a diamond originates from local disorders in a diamond crystal lattice – the nitrogen-vacancy (NV) centers.[6] NV center is completely resistant towards photobleaching and, apart from very small ND particles <5 nm, towards photoblinking[7,8] as well. The absolute stability of NV emission is unique among all fluorescent dyes and is essential in bioapplication of FND as a fluorescent probe, especially in applications where large laser powers are used, such as superresolution microscopy.[9,10]

In contrast to NDs, which are commercially available at reasonable price, bright FNDs still belong to valuable experimental materials. Vacancies in a diamond lattice are produced by irradiating of synthetic diamond nanocrystallites with charged particles. The vacancies are subsequently paired with inherent nitrogen impurities, present in diamond during annealing under inert atmosphere, giving rise to fluorescent NV centers.

High pressure high temperature (HPHT) synthesis is a well-established method for preparation of synthetic diamond.[11] Consecutive milling yields nanodiamond particles in sizes from 5 nm. HPHT nanodiamonds can be turned into fluorescent nanodiamonds of high brightness, much brighter than other types of diamond[12–14] (detonation, CVD). HPHT synthesis followed by milling produces polydisperse nanodiamonds of irregular shape bearing sharp edges and spiky vertexes. The nonuniformity in size and shape (accompanied by nonuniformity in fluorescence brightness) is limiting the applications of FNDs. For example in bioapplications – distribution of nanodiamonds in living

systems is as in the case of all other particles closely connected with their size.[15–17] Hence, polydisperse material exhibits less specific biodistribution, which limits its use as a diagnostic fluorescent probes or biosensors. Size separation of nanodiamonds using centrifugation[18–22] or gel permeation chromatography[23] was already described. The reduction of size of HPHT nanodiamonds by oxidative etching in air at 500 °C was also demonstrated[18] and allowed for construction of ND-based FRET sensors where small and uniform ND size is necessary. Not only size, but also nanoparticle shape is important factor, determining their biodistribution[24–29] and toxicity.[30,31] Spherical particles are generally considered biocompatible. It was described that a change of a nanoparticle shape from spherical to spiky, containing sharp vertexes, induced cytotoxicity in cells.[30] Although nanodiamonds are usually considered biocompatible, some recent studies indicate their possible harmful effects to living systems[32] and one can speculate, whether these are not in connection with their angular shape and highly curved surface. Spherical FNDs were prepared by milling from micrometer-sized crystals,[33] however this method described in 2009 did not spread among other ND research teams.

Here we present a new, simple and large-scale technique for preparation of pseudospherical monodisperse FNDs. Our etching method utilizes procedure, commonly used for polishing and etching of macroscopic diamonds – a high temperature treatment with potassium nitrate.[11] Effects of molten KNO_3 on diamond nanoparticles shape and behavior are studied and under optimum conditions particles of pseudospherical shape are prepared in a large scale. These particles are further separated by centrifugation in order to obtain rather monodisperse sample of rounded particles 35 nm in diameter.

Experimental:

Nanodiamonds of 0–50 nm diameter were purchased from Microdiamant Switzerland (MSY 0-0.05) and used as received. Sodium hydroxide, hydrochloric acid (35%) and nitric acid (65%) were purchased from Penta (Czech Republic). Hydrofluoric acid (40%) and potassium nitrate were purchased from Sigma-Aldrich. JetPEI® was purchased from PolyPlus-transfection. All chemicals were used as received without further purification. Deionized water was prepared with Millipore Synergy UV Ultrapure water system.

Methods:

Tube furnace

Tube furnace Nabertherm RT 50-250/13 was used for treatment of NDs with potassium nitrate. Small batches of NDs (2–4 mg) were treated in quartz vessels in a vertical setup. For large scale preparation, homebuilt insert was used. It consists of steel cylinder, copying the inner furnace diameter, a steel reaction vessel which accurately fits into the cylinder and a steel stirrer. All three components were inserted into the furnace in a vertical setup (**Suppl. Fig. 1**).

Electron microscopy

Bright field transmission electron microscopy (TEM) experiments were performed with a JEOL JEM-1011 electron microscope operated at 80 kV equipped with Tengra bottom-mounted camera. High resolution TEM, STEM, and spatially-resolved EELS experiments were carried out on a FEI Titan 80-300 "cubed" microscope fitted with an aberration-corrector for the imaging lens and the probe forming lens and a GIF Quantum energy filter for spectroscopy, operated at 80 kV to minimize knock-on damage to the sample. HRTEM imaging was carried out with an excited electron monochromator to extend the information transfer of the microscope. STEM-EELS experiments were performed using a convergence semi-angle α of ~21 mrad and a collection semi-angle β of ~75 mrad, using a beam current of approximately 80 pA. A fine electron probe (diameter ~1.5 Å) was scanned over a region of the sample, acquiring an EELS spectrum at each point. All spectra were acquired at the energy dispersion of 0.25 eV per pixel and with the energy resolution of approximately 1.2 eV. Chemical maps for the C signals (non-diamond carbon and diamond) were generated by fitting the carbon K-edge to known references for diamond and amorphous carbon. Samples for low-resolution TEM microscopy were prepared on carbon-coated copper grids (Pyser). In order to spread the particles evenly on the grid, following preparation procedure was established. Firstly, the grids were placed into a UV-ozonizing chamber (UV/Ozone Pro Cleaner Plus, Bioforce Nanosciences) for 15 min to hydrophilize the carbon layer. Secondly, a droplet of jetPEI® solution (diluted with water 1:2, vol:vol, equivalent of a pure PEI concentration 0,1 mg/ml) was placed on the grid and after 10 min incubation was removed with a piece of tissue. Afterwards the grid was washed by placing on a water droplet for 1 minute followed by water removal with a piece of tissue. Finally, a droplet of ND colloidal solution in water (0.1 mg/ml) was placed on the grid and after 3 min incubation was removed with a piece of tissue. For HR-TEM, STEM and EELS experiments, the ND particles were immobilized on the lacy carbon copper grids. Grids were placed on the filtration paper and approx. 50 uL of ND water solution (c = 0.1 mg/ml) was placed onto the grid.

Image Analysis

Particle size

Analysis of particle size distributions was performed as described in Ref.[34] Shortly, ImageJ software was used to process images from JEOL 1011 microscope. First, uneven illumination was removed by fitting of 3rd order polynomial. Then a background noise was removed by applying Gaussian blur and finally, threshold was applied to get binary image. Sporadic connections of particles were divided manually by line (2 pixel width) according to particle boundaries on the original images.

Size of an irregular particle can be expressed by its equivalent diameter. Here we use circular equivalent diameter (d_{eq}), defined as a diameter of a circular particle, having the same area as particle of interest (S) as described in equation (1).

$$d_{eq} = \sqrt{4S/\pi} \qquad (1)$$

These calculated equivalent circular diameters were used for a construction of two histogram types. In the number weighted distribution, each particle is given equal weighting irrespective of its size. In the volume weighted distribution, contribution of each particle is related to its volume. Here, this volume is calculated as a cube of particles equivalent circular diameter. Both types of particle size distributions include also the smallest fractions from supernatants (see the section Particle preparation).

Particle shape

Circularity was used to follow particle rounding. Circularity is defined as a squared ratio of the perimeter of particle of interest and the perimeter of an equivalent area circle. Circularity for each particle was obtained using the program ImageJ (NIH, USA) and an average value for each TEM image was calculated. Circularities of samples were evaluated without including the small and highly rounded fraction gained from supernatants (see the section Particles preparation). The error for each sample was derived from average circularities of 6 TEM images (approx. 200 particles per image) as a standard deviation. The circularities of samples differ significantly at a level $p<0.001$, calculated by ANOVA.

Calculations of particle dispersity

Dispersity (former polydispersity index) is typically used for expression of polymer uniformity in chain length. However, the same expression can be used to describe nanoparticle uniformity in size. Dispersity (D) of polymer is defined as the weight average molecular weight (M_w) divided by the number average molecular weight (M_n) as given in equation (2).

$$D = \frac{M_w}{M_n} \qquad (2)$$

Weight average molecular weight (M_w) is defined according to equation (3) while number average molecular weight (M_n) is defined in equation (4).

$$M_w = \frac{\sum M_i^2 N_i}{\sum M_i N_i} \qquad (3)$$

$$M_n = \frac{\sum M_i N_i}{\sum N_i} \qquad (4)$$

M_i is a molecular weight of a particle, while N_i is number of particles of this weight.

In system of inorganic nanoparticles, the molecular weight can be replaced by particle mass or particle volume (V_i), which was used in our case, yielding equation (5).

$$D = \frac{N\sum_{i=1}^{N} V_i^2}{\left(\sum_{i=1}^{N} V_i\right)^2} \qquad (5)$$

V_i is a volume of each particle and N is number of particles

Dynamic light scattering (DLS) and Zeta potential measurements

DLS and zeta potential measurements were recorded with a Zetasizer Nano ZS system (Malvern Instruments) at room temperature. Sample concentrations were 0.05 mg/ml for colloidal stability measurements and 0.5 mg/mL for others.

Raman and photoluminescence measurements

Raman and luminescence spectra were measured using a Renishaw InVia Raman Microscope; excitation wavelength was 514 nm (luminescence measurements) and 325 nm (Raman measurements)[35] with a 15 mW laser power. Spectra were taken at the room temperature and normalized to the diamond Raman peak.

Particle preparation

Rounded nanodiamonds (RNDs)

ND powder was used as-received. First 0.5 g was mixed and grinded with 25 g of KNO_3 in a ceramic mortar to get a fine powder. Powder was transferred within several seconds into reaction vessel already containing 75 g of molten KNO_3 preheated to 570 °C. Under optimum conditions, the mixture was kept in the furnace for 6 minutes while the temperature first dropped down to 500 °C. After the addition of NDs and KNO_3 mixture, it gradually increased to 556 °C. The temperature equilibrium was not reached. When studying the particles properties depending on etching level, the temperature was monitored during whole reaction to confirm the same reaction temperature profile for each sample. Because of the gradual heating of the reaction mixture, the final temperature was changing with reaction time (534; 547; 556; 560 and 562 °C for 3; 4.5; 6; 7 and 8.5 minutes resp.). Repeatedly measured temperature profiles were used to calculate temperature standard errors (e.g. 5 values for 3min sample, two values for 7min sample). Subsequently, the etching was quenched by pouring of the melt into 300 ml of cold water to cool down rapidly. The solution was centrifuged (4,000 rcf, 15 min, swinging bucket rotor, and 7000 rcf, 10 min, fixed angle rotor), the pellets were dispersed into a mixture of concentrated HF and HNO_3 (2:1 vol:vol, 21 ml) and heated and stirred for 48 hours at 160 °C in a 60ml PFA vessel (Savillex). Then NDs were centrifuged (4,000 rcf, 10 min), washed with 2M NaOH (50 ml, 1 h, shaking on vortex) and consequently with 2M HCl (50 ml, 1 h, shaking on vortex). Between treatments NDs were separated by centrifugation at 4,000 rcf for 15 min. After HCl treatment, diamonds were centrifuged 3 times with 50 ml of water (10,000 rcf, 20 min; 30,000 rcf, 30 min; 60,000 rcf, 30 min), sonicated in water by a sonication tip (750 W) for 10 minutes, filtered by 0.45µm GMF (glass microfiber membrane, Whatman) syringe filter and centrifuged twice (60,000 rcf, 40 min) with water (50 ml) to obtain stable colloid. Supernatants from washing containing the smallest particles were collected and precipitated with 1M HCl overnight, then concentrated to 3 ml and washed twice with water (30,000 rcf, 30 min; 40,000 rcf, 50 min). To isolate NDs as a powder, resulting main fraction colloids were concentrated to 5 ml by centrifugation (60,000 rcf, 40 min) and

freeze dried. The smallest fractions from supernatants were freeze dried separately and without further concentration. Under optimum conditions this procedure yields 86 mg (17%) of rounded nanodiamonds including both fractions and 73 mg (14.6 %) excluding the small fraction.

Angular nanodiamonds (control samples)

Control samples of angular particles were processed according to a procedure described above, except the etching step, which was substituted by simple oxidation in air – commonly used nanodiamond cleaning procedure [36,37] (air-oxidized control sample).

For air oxidation, the powder sample (100 mg) was placed in quartz tube and heated at 450 °C for 4 hours. NDs were then dispersed in HF and HNO_3 mixture (2:1 vol:vol, 21 ml in total) and heated for 2 days at 160 °C. Afterwards NDs were centrifuged (4,000 rcf, 10 min), washed with 2M NaOH (50 ml, 1 h, shaking on vortex) and consequently with 2M HCl (50 ml, 1 h, shaking on vortex). Between treatments, NDs were separated by centrifugation at 4,000 rcf for 15 min. After HCl treatment, diamonds were centrifuged 5 times with 50 ml of water (10,000 rcf, 20 min; 30,000 rcf, 30 min; 60,000 rcf, 30 min; 60,000, 40 min), with water (50 ml) to obtain a stable colloid. To isolate NDs as a powder, resulting colloid was concentrated to 5 ml by centrifugation (60,000 rcf, 40 min) and freeze dried. Sample of original not air-oxidized particles for TEM and HRTEM was processed with oxidizing acids and consequent washing with NaOH and HCl in a same manner as air-oxidized sample (acid-oxidized control sample).

Centrifugal fractionation

New RND sample prepared under optimum conditions with a yield of 75 mg (15%, excluding the small fraction, see the Particle preparation section) was used. A small amount (12 mg) of rounded or angular air-oxidized NDs were dispersed in 12 ml of water (sonication with 4 mm tip, 30 min). Resulting colloid was centrifuged in a swing rotor (2,000 rcf, 2 hours). Supernatant was collected and centrifuged (15,000 rcf, 2 hours). Sediment was collected and centrifuged (15,000 rcf, 2 hours). Collected sediment was dispersed into water. Colloid was freeze dried yielding 7.26 mg (60.6 %) of monodisperse RNDs and 4.91 mg (40.9 %) of angular NDs. Histograms of non-separated samples in **Fig. 4** do not include the small fraction remaining in supernatants after preparation of particles.

ND irradiation

Colloidal solutions of rounded and angular NDs were irradiated for 70 min with a proton beam extracted from the isochronous cyclotron U-120M (16 MeV, 6.10^{17} p^+/cm^3). The irradiated material was annealed at 900 °C for 1 hour in argon atmosphere, followed by air oxidation and mineral acid treatment as described above.

Results and Discussion

During industrial preparation, HPHT nanodiamonds are milled from larger particles, resulting in rather polydisperse material of irregular shape, determined by breaking crystals along crystal planes and defects. HPHT nanodiamonds are easily accessible commercially and can be turned into bright fluorescent emitters upon irradiation by high energy particles followed by thermal annealing. In order to control size and shape of this promising fluorescent material, we etched the original non-fluorescent particles in a molten potassium nitrate. We started with as-received commercially available nanodiamonds with given size below 50 nm. Even after standard cleaning procedure (see Particles preparation), these particles were irregular in shape and the majority of particles were smaller than 10 nm in diameter (**Fig. 1c, 2b**). By evaluation of TEM micrographs, we realized that exposition of ND sample to highly aggressive oxidative environment of molten potassium nitrate at temperatures above 500 °C leads to rounded NDs (RNDs) with shifted size distributions (**Fig. 1c, d**). To get deeper insight into the rounding process, we carried out a series of experiments.

Preliminary study with small samples (2-4 mg) focused on time and temperature dependence of etching effect shows that long etching times at lower starting temperatures (500 °C) result in particles aggregation and reaction termination, whereas high temperatures (580 °C) lead to rapid complete digestions of the sample (details in **Suppl. Fig. 1**). Therefore, higher temperatures and shorter etching times are favored which we further tested in up-scaled reaction series.

This large scale systematic study was designed to evaluate time dependence of etching effect at a fixed starting temperature and to find optimum conditions for maximum RNDs yield. This study concurrently revealed unexpected shift in colloidal stability of samples related to the particles´ etching level (details in **Suppl. Fig. 2**).

Large scale reactions were set up to process 0.5 g of raw NDs in one run. It was necessary to heat the KNO_3-ND mixture rapidly in order to suppress the above described ND particle aggregation in the melt. To achieve this task, three quarters of the potassium nitrate amount was first preheated in the furnace. Subsequently, NDs homogenized in the last quarter of KNO_3 amount were added directly into the melt.

The starting temperature of preheated KNO_3 melt was established to 567 °C, slightly above the KNO_3 decomposition temperature, where the rate of sample digestion is manageable. Reaction times were then set in a range from 3 to 8.5 min which lead to reasonable etching yields (**Fig. 1a**). Following the temperature diagram in the **Fig. 1a**, all reactions during this study had the same temperature profile according to particular times and each reaction time corresponds to specific final temperature. The starting temperature was not reached even after 8.5 mins of etching, where the reaction yield decreased to only 5.8 %.

To understand and optimize the etching procedure, several parameters were monitored in the etching time-dependence study. These are particles shape expressed as circularity (see experimental section for a definition), RNDs yield, particles size distribution, sp^2 carbon content, and samples colloidal

stability. The data were concurrently used to determine optimal etching conditions considering primarily particles circularity and reaction yield.

The rounding effect, easily observable in TEM images even with naked eye (**Fig. 2b, c**), was evaluated precisely using an image analysis. In order to allow image analysis, a method for preparation of TEM samples had to be developed,[34] gaining evenly spread particles on the grid and minimizing formation of agglomerates. The carbon grid surface was first hydrophilized using UV-ozone generator and its charge was reversed from negative using positively charged polymer. On such pretreated grid, negatively charged ND particles well adhere, and their agglomeration is minimized, so the TEM images can be easily thresholded and particle sizes and shapes automatically determined using appropriate software algorithms.

For small batches, an increase of etching time and temperature led to rapid reduction of the yield, while their decrease did not possess satisfactory rounding (see **Suppl. Fig. 1**). Thus, according to our expectations, the rounding effect is increasing in the expense of yield (**Figure 1a, b**). More unexpected fact is that particles´ circularity reaches its maximum and further etching prolongation causes only further material loss (**Fig. 1b**). Thus, the balanced yield to circularity compromise had to be found. In our experimental setup, these optimum conditions are etching time of 6 minutes and starting temperature of 567 °C. The yield under these conditions was 86 mg (17.2 %) with the sample average circularity 0.77. Notably, we do not see any obstacle for further reaction upscale as long as the rapid heating of reaction mixture can be achieved.

Etching is a surface reaction and its rate depends among others on particles surface curvature. Thus, the rounding is caused predominantly by etching of corners and edges of nanocrystals which react significantly faster. Concurrently the sample size distribution changes are the main result of higher reactivity of small particles in comparison with the bigger ones.[38] This is for our study well documented by image analysis of TEM micrographs, showing notable shift of distributions with etching time. Lowered number of small particles is especially pronounced in number-weighted distributions shown in **Fig. 1c**. On the other hand, volume-weighted histograms in **Fig. 1d** take into account particle sizes as a cube of their circular equivalent diameter and thus the effect of small particles on a distribution shape is suppressed. Decreasing number of small particles showing higher circularity can explain the stopping of circularity increase with etching time (**Fig. 1b**).

RNDs prepared under optimum conditions were studied by high resolution TEM (HRTEM), to see the detailed morphology of ND surface (**Fig. 3**). It is visible from the presented images that the original acid-oxidized material contains significant amounts of non-diamond carbon, both at the diamond surface and as separate graphite flakes. The HRTEM image in **Fig. 3b** shows that the flakes as well as a great deal of the surface carbon are removed by a 450 °C air oxidation step, a typical cleaning procedure for nanodiamond.[39,40] Even if the air oxidation may reduce the amount of very small particles in sample,[38,41] the appearance (shape, size distribution) of sample in TEM before and after air oxidation is the same. The TEM images and size distribution histograms of an original ND sample without air treatment can be found in **Suppl. Fig. S2**. **Figures 3c, d** are high resolution images of

the rounded nanodiamond material. The high-resolution image in **Fig. 3d** shows a rounded nanodiamond, imaged along the [011] zone axis orientation. The surface of the nanodiamond under study is extremely clean, only some small graphitic islands remain on the surface. The rounded nanodiamond surface consists of a multitude of atomic steps, with a preferential exposure of {111} planes. **Figure 3e** confirms the extremely low content of non-diamond content by the EELS diamond map on the RND surface. The images of both non-etched samples clearly display graphene sheets on the particle surface, which was confirmed by EELS. Significant reduction of the amount of sp^2 hybridized carbon was corroborated also for macroscopic samples. Raman spectra with 325 nm excitation were measured for etched (6 min), air-oxidized and acid-treated samples (**Fig. 3f**). At this excitation, a sharp band of diamond crystal grid at 1332 cm^{-1} appears, while band at 1580 cm^{-1} belongs to sp^2 hybridized carbon. The plot clearly shows reduction of sp^2 carbon amount in air treated sample and its disappearance in etched sample. Calculated diamond contents in samples are summarized it **Tab. 1**.

Table 1: Diamond content in RNDs and control samples.

Acid-treated NDs	91.4 %	91.4 %
Air-oxidized NDs	96.6 %	96.6 %
RNDs	99.3 %	99.6 %

The etching method apparently possessed RNDs with reduced non-diamond carbon content; however, the samples appeared polydisperse on the first sight. Getting monodisperse fraction was the next goal of this project. The sample contains two main populations of particles – particles between 20 and 50 nm in diameter and large fraction of sub 10 nm particles (for number weighted histogram see **Fig. 4a**). In general, brightness of a single FND particle is dependent on the number of NV centers it contains. It was described that the number of these centers dramatically decrease in sub 10-nm particles.[13] Particle brightness is a key parameter for its application as fluorescent probe. Therefore, we focused on isolation of presumably brighter fraction of particles with diameter around 40 nm. Centrifugation was used for RND size fractionation as a simple high-throughput method. To estimate the sizes and dispersities of separated NDs, image analysis of TEM images was used.

Several consecutive centrifugation separations were used to remove the fraction of impurities and large NDs in the first step and to remove the populated fraction of very small diamonds in consecutive two steps. The medium sized NDs were collected as the product of interest (TEM image in **Fig. 2d**) in yield 7.27 mg from starting 12 mg, representing 60.6 % yield (however, procedure can be up-scaled). Number weighted distribution histograms (where each particle is given equal weighting irrespective of its size) of spherical NDs before and after fractionation are plotted in **Fig. 4a**. The histograms show that the rounded NDs after separation have size population maximum at 35–40 nm (Average equivalent circular diameter 34 nm, SD 10.7) and the fraction of small particles <10 nm, present in rounded NDs before fractionation is almost completely removed. In order to express the size

uniformity of prepared sample, we used dispersity (former polydispersity index – *pdi*) which is commonly used in polymer chemistry. We adapted the formula by using volume of particle (proportional to the mass) instead of molecular mass (for more details see the Experimental section). The dispersity of sample after fractionation (1.6) is significantly lower, than dispersity of original rounded NDs (2.5).

To compare the behavior of non-rounded and rounded diamonds, non-rounded diamonds were fractionated according to the same procedure (**Fig. 4a**). Control non-rounded sample was treated by air oxidation. It is well visible from the plot that original non-rounded NDs before fractionation contain dominant fraction of sub 10nm particles in number weighted plot, much larger compared to rounded non-separated particles. This testifies that small particles are etched predominantly in etching step. After separation, sample of non-rounded NDs still contains significant fraction of small particles unlike sample of rounded NDs. The dispersities of non-rounded NDs confirm trends well visible from the plots and are 9.9 and 2.6 for particles before and after fractionation, respectively. Results show that only the combination of etching and subsequent fractionation is the effective way towards monodisperse material.

The size distribution data were also recalculated and plotted as volume weighted distributions (**Fig. 4b**) where contribution of each particle in the distribution relates to the volume/mass of that particle (for more details see the Experimental section). In volume weighted distributions the populations of small particles are less pronounced which is well visible in plots. After fractionation, the distributions became narrower and slightly shifted to the bigger particles. Considering the intended use of NDs as biological probes, optical sensors or microelectronic devices, we find number weighted distributions much more important than volume weighted. In these very fine applications, each particle of inappropriate size can cause severe problems or even failure of an experiment.

Recently, we demonstrated that oxidation of FNDs by potassium nitrate increase their fluorescence due to the effective removal of graphene-like structures.[14] Large scale synthesis of FNDs is still not available so FNDs represent a valuable material. The overall yield of etching and consecutive fractionation is 9.1 %. It is not reasonable to lose over 90 % of valuable FNDs, therefore we used RNDs as a substrate for proton irradiation leading to FNDs. Raman spectroscopy was used for brightness quantification. The relative brightness of rounded FNDs was comparable (ca 8 % higher) to non-rounded NDs irradiated under same conditions, so they can serve a source for a production of FNDs. After centrifugal separation, the brightness of monodisperse FNDs was comparable with original samples: 8 % higher for angular and 9 % lower for round diamonds. Since larger FNDs contain more NV centers, they contribute highly to the overall sample fluorescence contrary to the small ones. Because separation leads to reduction of both small and large ND fractions, their contributions to overall fluorescence intensity seem to cancel each other, resulting in monodisperse FND samples with brightness comparable to the polydisperse material.

Conclusions

Etching of HPHT nanodiamonds in molten potassium nitrate, originally used as a polishing method for macroscopic diamonds, leads to round diamond nanoparticles easily producible in gram-scales. Described methodology assures etching of individual, non-aggregated particles and results in increased particles circularity concurrently with a shift in particle size distributions to larger diameters. Rounding occurs in the expense of yield and thus optimum etching conditions had to be found based on compromise between the etching yield and particles circularity. Circularity and size distribution evaluation was enabled thanks to justified process of TEM samples preparation providing mostly separated particles on TEM micrographs and more precise and reproducible image analysis results. Samples dispersities were significantly decreased by centrifugal fractionation resulting in round diamonds of 34 ± 10.7 nm in diameter. In addition, all processes leading to round monodisperse diamond nanoparticles are feasible and can be easily up-scaled. Prepared round monodisperse nanodiamonds were finally transformed to fluorescent ones resulting in a novel promising material ready for studies in living systems.

FIGURES:

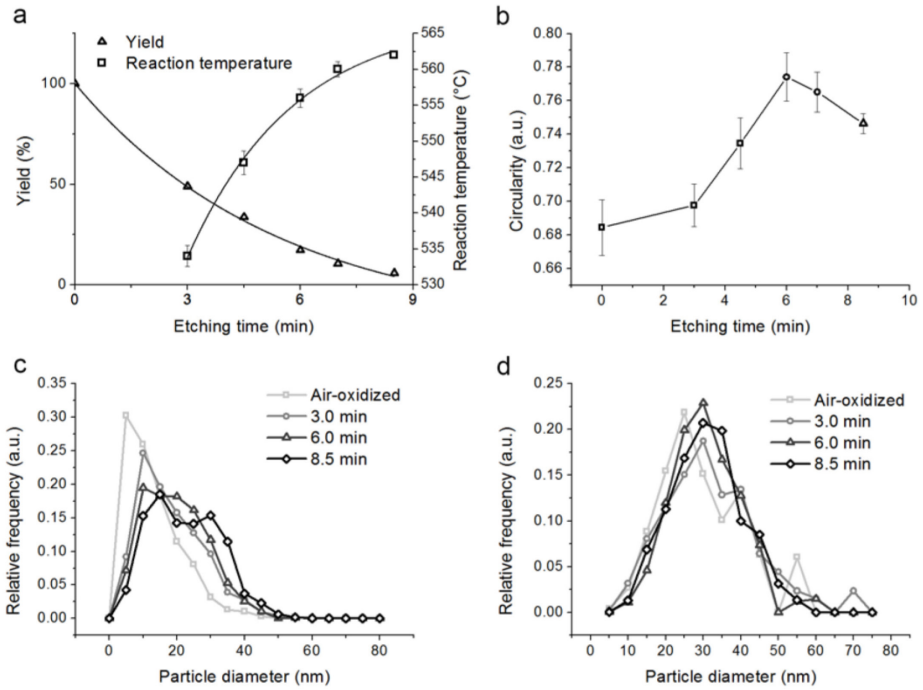

Figure 1 | Etching time influence on RNDs yield, shape and size. Polydisperse HPHT nanodiamonds are etched in molten potassium nitrate in order to round the particles and reduce the number of single-digit particles with maximum reaction yield. Whole etching process is illustrated by a series of etching times at a fixed starting temperature (567 °C), optimum etching time is found at 6 min. Increasing etching time leads to lower yields accompanied by higher final temperatures (**a**), the lines are a guide for eyes. Particles circularity reaches its maximum at 6 min and longer etching times cause only material loss (**b**). Mean values and standard errors of the means are reported; see the Experimental section for more details. Number (**c**) and volume (**d**) weighted particle size distributions are shifted to larger particles as the small particle fractions are reduced and digested by prolonged etching process. Particles sizes and circularities were obtained from image analysis of TEM micrographs.

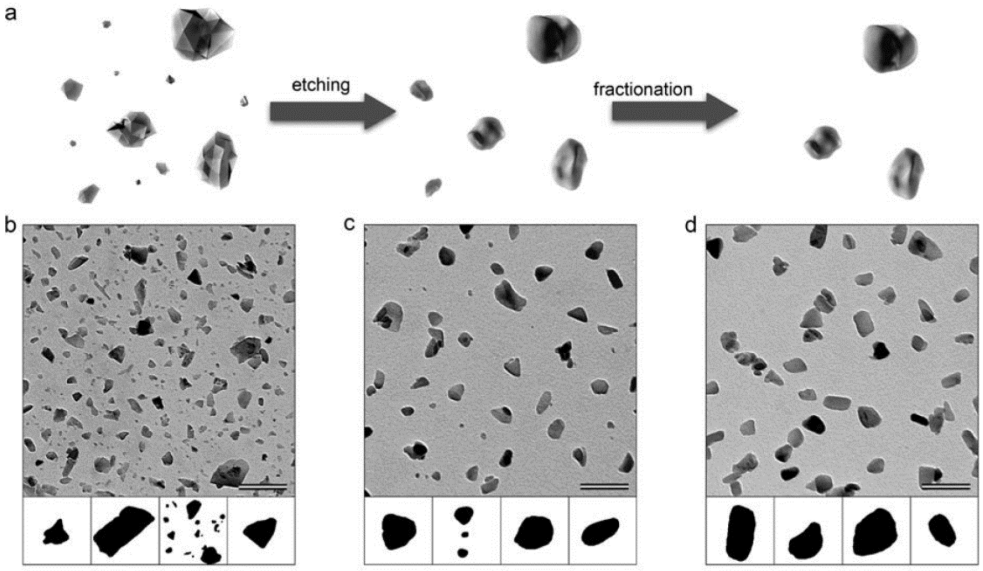

Figure 2 | Preparation and appearance of monodisperse RNDs. a, As received particles are rounded by etching and consequently separated by centrifugation to obtain particles of narrow size distribution around 40 nm. TEM micrographs of air-oxidized diamonds (**b**), rounded diamonds (**c**), and rounded separated diamonds (**d**) document well visible samples´ appearance changes. In insets are examples of particles in a form of a binary image, used for image analysis. Scale bar corresponds to 100 nm for TEM microphotography and to 50 nm for inset.

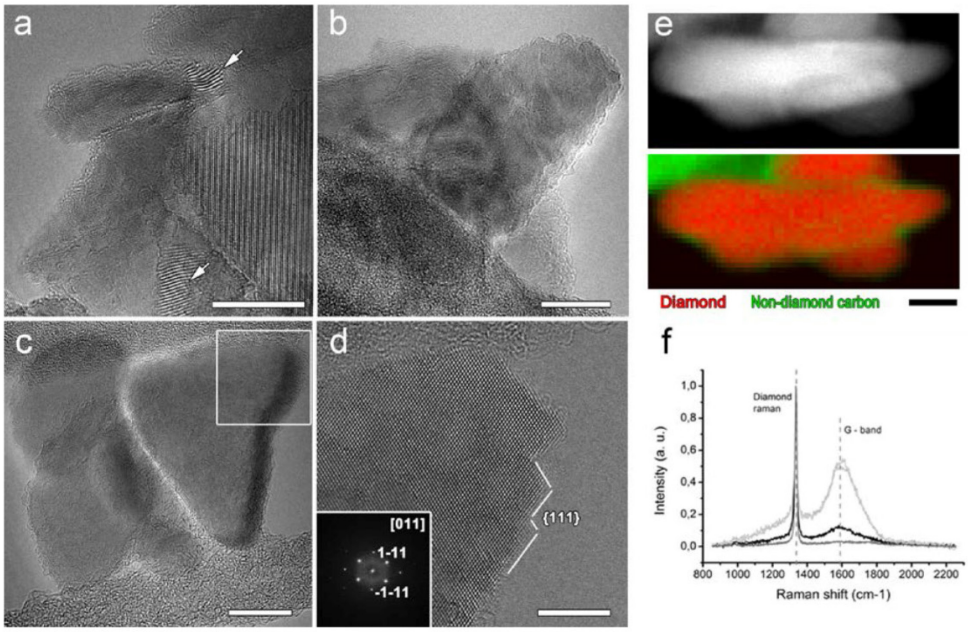

Figure 3 | Graphene on the surface of nanodiamonds. a, High resolution TEM image of the acid-oxidized ND sample showing disordered graphitic material on the nanoparticle surface as well as graphite flakes (arrows). **b**, HRTEM image of ND oxidized in air with graphitic structures on the surface. **c**, HRTEM image of potassium nitrate-etched NDs, showing their rounded geometry as well as reduced amount of graphene on the surface. **d**, detail of the etched ND nanoparticle, showing a clean surface etched 'atom-by-atom'. **e**, EELS map of the etched ND sample, with diamond carbon in red, and non-diamond carbon in green. **f**, Normalized Raman spectra of original (light grey), air-oxidized (black) and nitrate-etched (dark grey) NDs, G-band corresponds to of sp^2 hybridized carbon content. Scale bar: a–c: 10 nm, d–e: 5 nm.

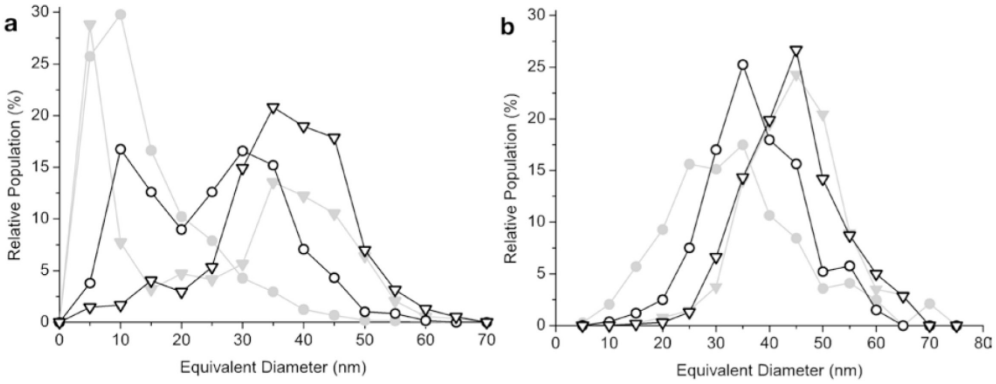

Figure 4 | Nanodiamonds separation – particle size distributions. Number weighted (**a**) and volume weighted (**b**) distribution diagram of rounded diamonds before (–○–) and after (–▽–) separation. Distribution diagrams of non-etched angular diamonds before (–●–) and after (–▼–) separation are given for comparison.

1. Mochalin, V. N., Shenderova, O., Ho, D. & Gogotsi, Y. The properties and applications of nanodiamonds. *Nat Nano* **7,** 11–23 (2012).
2. Xing, Y. & Dai, L. Nanodiamonds for nanomedicine. *Nanomedicine* **4,** 207–218 (2009).
3. Barnard, A. S. Diamond standard in diagnostics: nanodiamond biolabels make their mark. *Analyst* **134,** 1751–1764 (2009).
4. Maze, J. R. *et al.* Nanoscale magnetic sensing with an individual electronic spin in diamond. *Nature* **455,** 644–647 (2008).
5. Aharonovich, I., Greentree, A. D. & Prawer, S. Diamond photonics. *Nature Photonics* **5,** 397–405 (2011).
6. Davies, G., Lawson, S. C., Collins, A. T., Mainwood, A. & Sharp, S. J. Vacancy-related centers in diamond. *Phys. Rev. B* **46,** 13157–13170 (1992).
7. Jelezko, F. & Wrachtrup, J. Single defect centres in diamond: A review. *phys. stat. sol. (a)* **203,** 3207–3225 (2006).
8. Gruber, A. *et al.* Scanning Confocal Optical Microscopy and Magnetic Resonance on Single Defect Centers. *Science* **276,** 2012–2014 (1997).
9. Tzeng, Y.-K. *et al.* Superresolution Imaging of Albumin-Conjugated Fluorescent Nanodiamonds in Cells by Stimulated Emission Depletion. *Angew. Chem. Int. Ed.* **50,** 2262–2265 (2011).
10. Han, K. Y. *et al.* Three-Dimensional Stimulated Emission Depletion Microscopy of Nitrogen-Vacancy Centers in Diamond Using Continuous-Wave Light. *Nano Lett.* **9,** 3323–3329 (2009).
11. Chen, Y. & Zhang, L. C. *Polishing of diamond materials mechanisms, modeling and implementation*. (Springer, 2013).
12. Vaijayanthimala, V. & Chang, H.-C. Functionalized fluorescent nanodiamonds for biomedical applications. *Nanomedicine* **4,** 47–55 (2008).
13. Smith, B. R. *et al.* Five-Nanometer Diamond with Luminescent Nitrogen-Vacancy Defect Centers. *Small* **5,** 1649–1653 (2009).
14. Havlik, J. *et al.* Boosting nanodiamond fluorescence: towards development of brighter probes. *Nanoscale* **5,** 3208–3211 (2013).
15. Prokop, A. & Davidson, J. M. Nanovehicular intracellular delivery systems. *J Pharm Sci* **97,** 3518–3590 (2008).
16. Perrault, S. D., Walkey, C., Jennings, T., Fischer, H. C. & Chan, W. C. W. Mediating Tumor Targeting Efficiency of Nanoparticles Through Design. *Nano Lett.* **9,** 1909–1915 (2009).

17. Oh, E. *et al.* Cellular Uptake and Fate of PEGylated Gold Nanoparticles Is Dependent on Both Cell-Penetration Peptides and Particle Size. *ACS nano* (2011).
18. Mohan, N. *et al.* Sub-20-nm Fluorescent Nanodiamonds as Photostable Biolabels and Fluorescence Resonance Energy Transfer Donors. *Advanced Materials* **22,** 843–847 (2010).
19. Say, J. M., Bradac, C., Gaebel, T., Rabeau, J. R. & Brown, L. J. Processing 15-nm Nanodiamonds Containing Nitrogen-vacancy Centres for Single-molecule FRET. *Aust. J. Chem.* **65,** 496–503 (2012).
20. Komatsu, N. Novel and Practical Separation Processes for Fullerenes, Carbon Nanotubes and Nanodiamonds. *J. Jpn. Pet. Inst* **52,** 73–80 (2009).
21. Morita, Y. *et al.* A Facile and Scalable Process for Size-Controllable Separation of Nanodiamond Particles as Small as 4 nm. *Small* **4,** 2154–2157 (2008).
22. Peng, W. *et al.* Gram-scale fractionation of nanodiamonds by density gradient ultracentrifugation. *Nanoscale* **5,** 5017–5026 (2013).
23. Zhao, L. *et al.* Chromatographic Separation of Highly Soluble Diamond Nanoparticles Prepared by Polyglycerol Grafting. *Angewandte Chemie International Edition* **50,** 1388–1392 (2011).
24. Daum, N., Tscheka, C., Neumeyer, A. & Schneider, M. Novel approaches for drug delivery systems in nanomedicine: effects of particle design and shape. *Wiley Interdisciplinary Reviews: Nanomedicine and Nanobiotechnology* **4,** 52–65 (2012).
25. Herd, H. *et al.* Nanoparticle Geometry and Surface Orientation Influence Mode of Cellular Uptake. *ACS Nano* **7,** 1961–1973 (2013).
26. Decuzzi, P. *et al.* Size and shape effects in the biodistribution of intravascularly injected particles. *Journal of Controlled Release* **141,** 320–327 (2010).
27. Chithrani, B. D., Ghazani, A. A. & Chan, W. C. W. Determining the Size and Shape Dependence of Gold Nanoparticle Uptake into Mammalian Cells. *Nano Lett.* **6,** 662–668 (2006).
28. Chithrani, B. D. & Chan, W. C. W. Elucidating the Mechanism of Cellular Uptake and Removal of Protein-Coated Gold Nanoparticles of Different Sizes and Shapes. *Nano Letters* **7,** 1542–1550 (2007).
29. Chu, Z. *et al.* Rapid endosomal escape of prickly nanodiamonds: implications for gene delivery. *Scientific Reports* **5,** 11661 (2015).
30. Hutter, E. *et al.* Microglial Response to Gold Nanoparticles. *ACS Nano* **4,** 2595–2606 (2010).
31. Schaeublin, N. M. *et al.* Does Shape Matter? Bioeffects of Gold Nanomaterials in a Human Skin Cell Model. *Langmuir* **28,** 3248–3258 (2012).
32. Xing, Y. *et al.* DNA damage in embryonic stem cells caused by nanodiamonds. *ACS nano* **5,** 2376 (2011).
33. Boudou, J.-P. *et al.* High yield fabrication of fluorescent nanodiamonds. *Nanotechnology* **20,** 235602 (2009).
34. Rehor, I. & Cigler, P. Precise estimation of HPHT nanodiamond size distribution based on transmission electron microscopy image analysis. *Diamond and Related Materials* **46,** 21–24 (2014).
35. Fortunato, W., Chiquito, A. J., Galzerani, J. C. & Moro, J. R. Crystalline quality and phase purity of CVD diamond films studied by Raman spectroscopy. *J Mater Sci* **42,** 7331–7336 (2007).
36. Mohan, N., Chen, C.-S., Hsieh, H.-H., Wu, Y.-C. & Chang, H.-C. In Vivo Imaging and Toxicity Assessments of Fluorescent Nanodiamonds in Caenorhabditis elegans. *Nano Lett.* **10,** 3692–3699 (2010).
37. Vaijayanthimala, V. *et al.* The long-term stability and biocompatibility of fluorescent nanodiamond as an in vivo contrast agent. *Biomaterials* **33,** 7794–7802 (2012).
38. Osswald, S., Havel, M., Mochalin, V., Yushin, G. & Gogotsi, Y. Increase of nanodiamond crystal size by selective oxidation. *Diamond and Related Materials* **17,** 1122–1126 (2008).
39. Osswald, S., Yushin, G., Mochalin, V., Kucheyev, S. O. & Gogotsi, Y. Control of sp^2/sp^3 Carbon Ratio and Surface Chemistry of Nanodiamond Powders by Selective Oxidation in Air. *Journal of the American Chemical Society* **128,** 11635–11642 (2006).
40. Chang, Y.-R. *et al.* Mass production and dynamic imaging of fluorescent nanodiamonds. *Nat Nano* **3,** 284–288 (2008).
41. Gordeev, S. K. & Korchagina, S. B. On the stability of small-sized nanodiamonds. *J. Superhard Mater.* **29,** 124–125 (2007).

Supplementary information

Rounded monodisperse nanodiamonds: properties and mass production

Ivan Rehor[1], Helena Raabova[1,2], Jan Havlik[1,3], Stuart Turner[4], Gustaaf Van Tendeloo[4], Jan Stursa[5], Vladimira Petrakova[6], Petr Cigler[1,*]

[1] *Institute of Organic Chemistry and Biochemistry AS CR, v.v.i., Prague, Czech Republic*

[2] *University of Chemistry and Technology, Prague, Department of Inorganic chemistry, Technicka 5, Prague 16628 6, Czech Republic*

[3] *Faculty of Science, Charles University, Prague, Czech Republic*

[4] *EMAT, University of Antwerp, Antwerp, Belgium*

[5] *Nuclear Physics Institute AS CR, v.v.i., Rez near Prague, Czech Republic*

[6] *Faculty of Biomedical Engineering, Czech Technical University in Prague, Czech Republic*

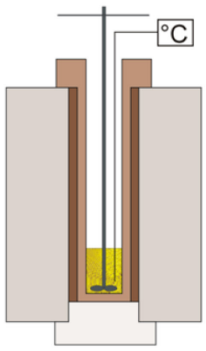

Figure S1. Homemade insert for tube furnace, used for melting NDs in KNO3. Outer steel cylinder accumulates heat and is responsible for even temperature distribution across sample. Inner cylindric bath is made of steel, which is passivated in molten nitrate.

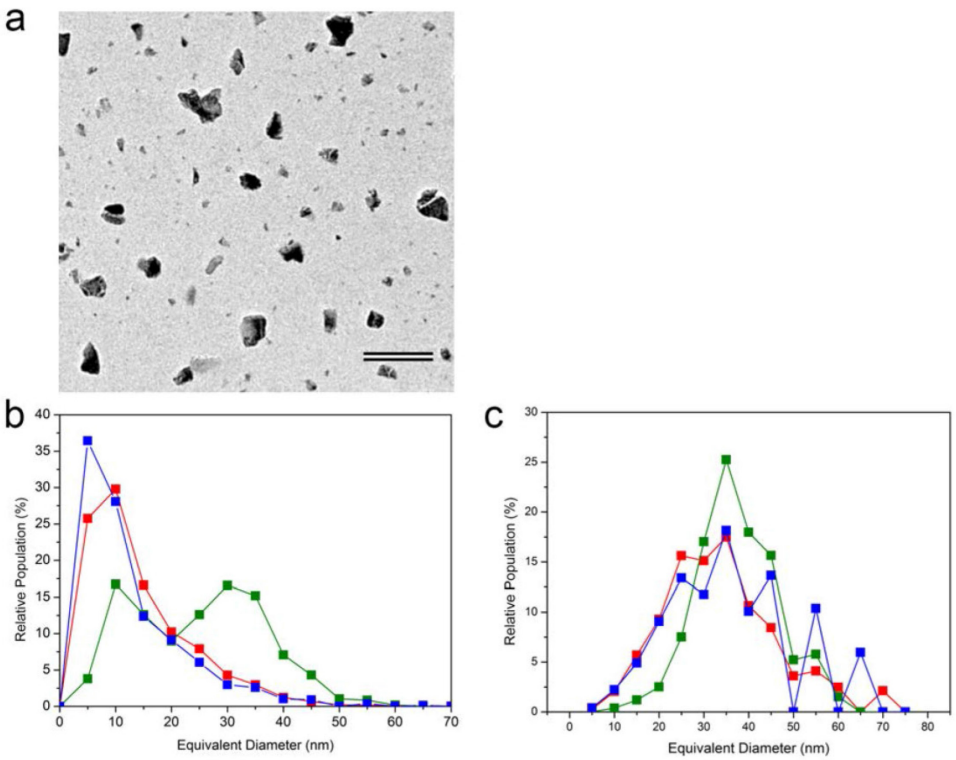

Figure S2. Particle characteristics of original nanodiamond sample which was neither air-oxidized nor nitrate-etched. a: TEM microphotography of commercial ND sample after treatment with mineral acids (scale bar corresponds to 100 nm). **b**, **c:** number weighted (**b**) and volume weighted (**c**) distribution diagram. Untreated NDs are in blue, air oxidized in red and nitrate etched in green. The oscillations at larger diameters in volume weighted histogram are caused by very low fraction of very large particles in original sample.

Supplementary Data 1. Small scale study of rounding effect dependence on melting time and temperature.

We performed a preliminary small-scale study revealing how the interplay between etching time and temperature influences the final sphericity of particles (expressed as circularity, calculated from TEM microphotographs). Results (**Table S1**) show increasing circularity with time and melting temperature. At long etching times and low temperatures, the ND dispersion in KNO_3 agglomerates, which results in termination of etching. Therefore, it was not possible to control the nanodiamond morphology sufficiently at these conditions. At temperatures above 520 °C, the reaction proceeds fast enough to obtain diamonds with higher circularity. On the other hand, the material is rapidly completely digested at high temperatures and therefore shorter etching times must be used. The results from this study were used for upscale reaction setup, in order to process larger quantities of NDs.

Table S1. Circularity values for samples etched at various time and temperature. The cross indicates a complete digestion and disappearance of particles in the sample.

	temperature (°C)				
etching time (min)	500	520	540	560	580
0	0.678				
5				0.705	0.761
10	0.701			0.746	x
15	0.711	0.715	0.730	x	
20	0.722				
50	0.672				

Supplementary Data 2: Decrease of colloidal stability of RNDs

Immediately after etching, before all analyses, samples were oxidized in strong acids and after washings yielded stable colloidal water dispersions, completely comparable to non-etched diamonds. Nevertheless, distinct differences in colloidal stability of etched samples were observed when increasing ionic strength of the solutions. To compare the samples colloidal stabilities, we measured the particle diameters over time in a solution of 10 mM NaCl in 5 mM phosphate buffer, pH 7.40. The diameters were recorded by dynamic light scattering as samples z-average. Against our expectations, longer etching times corresponding to more pronounced surface chemistry changes led to decreased colloidal stability (**Fig. S3**) - i.e. more etched particles were aggregating more readily even if having comparable and highly negative zeta potentials (-41 ± 2.1 mV). Such behavior is probably the effect of decreased roughness of particles surface, caused by elimination of non-diamond carbon sheets and clusters, leading to easier adhesion of smooth etched surfaces.

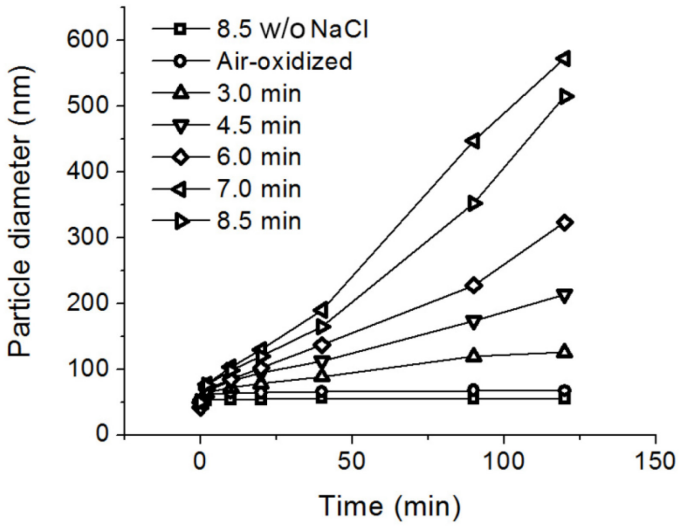

Fig. S3: NDs colloidal stability. Control samples are RNDs etched for 8.5 min in 5mM phosphate buffer without NaCl and air-oxidized NDs under the same conditions as the other etched samples. Both control samples are stable contrary to etched samples at increased NaCl concentration.